

SPATIALLY AND TEMPORALLY RESOLVED HARMONIC EMISSION
STUDIES OF LASER PLASMAS

Report No. 68

Steven M. Jackel

ACKNOWLEDGEMENT

The research reported on herein was supported by the following principal sponsors:

Exxon Research & Engineering Company
General Electric Company
Northeast Utilities Company
University of Rochester

Other contributors to the efforts of the work in the Laboratory for Laser Energetics include:

Empire State Electric Energy Research Company
U.S. National Science Foundation
New York State Energy Research & Development Administration
New York State Science & Technology Foundation
U.S. Air Force Office of Scientific Research

Such support does not imply endorsement of the content by any of the above parties.

DECEMBER 1977

ABSTRACT

Harmonic light emission from laser produced plasmas at the second and three-halves harmonics of the incident laser light frequency were spatially and temporally resolved to directly provide critical and quarter-critical electron density trajectories ($n_{e\ cr} = 10^{21}\text{ cm}^{-3}$ and $n_{e\ \frac{1}{4}cr} = 2.5 \times 10^{20}\text{ cm}^{-3}$ for $\lambda_{\text{LASER}} = 1.06\mu\text{m}$). The harmonic emissions were viewed from a direction perpendicular to the irradiation plane of a four beam laser.

The neodymium:glass laser, used to irradiate spherical-shell laser-fusion targets, provided focused $1.06\mu\text{m}$ wavelength light of intensity $I_{\text{LASER}} \lesssim 10^{15} \frac{\text{watt}}{\text{cm}^2}$ in pulses of durations $\tau_{\text{FWHM}} = 100\text{-}600$ psec and rise time $\tau_{\text{RISE}}(10\%\text{-max}) = 40\text{-}230$ psec.

The experimental data was applied to the study of laser light absorption and plasma energy transport. Absorption was found to vary by a factor of two for a factor of four increase in the measured distance between the critical and quarter-critical densities. Calculation of collisional plus resonant absorption gave a good fit. Moderate profile modification ($n_{\text{jump}}/n_{\text{cr}} \gtrsim .7$) was predicted to not substantially alter the scalelength dependence of absorption. The rate and nature of plasma energy transport was shown to affect the ablation region density profile, including the critical and quarter-critical density locations. Theory and experiment agreed in the prediction of a unique peak excursion relationship. Results suggested a laser pulse rise time dependence to the energy trans-

port contributing to ablation with longer rise time pulses giving larger values for the transport.

To obtain results with an accuracy necessary for the study of laser-plasma interaction physics, it was found that accuracy enhancement beyond the resolution of the optical system was needed. A simple image technique was devised to significantly enhance the accuracy of edge location measurements. Application of the image analysis technique required the determination of the optical system spatial resolution. The streak camera spatial resolution was studied and its point spread response was measured as a function of input intensity.

Publications

The following publications related to this study have appeared during the course of this report work.

Steven Jackel, James Albritton, and Edward Goldman "Critical-Density Scalelength Measurements in Laser Produced Plasmas" Phys. Rev. Letters 35, 514 (1975)

Steven Jackel, Bruce Perry, and Moshe Lubin "Dynamics of Laser Produced Plasmas through Time-Resolved Observations of the $2\omega_0$ and $(3/2)\omega_0$ Harmonic Light Emissions" Phys. Rev. Letters 37, 95 (1976)

W. Friedman, S. Jackel, W. Seka and J. Zimmermann "Dynamic Range and Spatial Measurements of Psec. Streak Cameras" in Proceedings of the 12th International Congress on High Speed Photography, (1977)

TABLE OF CONTENTS

	<u>Page</u>
Abstract	i
Publications	iii
Table of Contents.	iv
List of Tables	vii
List of Figures.	viii
1. Report Structure	1
2. Introduction	3
3. Data Acquisition and Accuracy.	10
3.1. Experimental Setup.	10
3.2. Resolution Requirements	18
3.2.1. Spatial Resolution	18
3.2.2. Temporal Resolution.	21
3.3. Sources of Spatial Error.	21
3.3.1. Theoretical Spatial Resolution	22
3.3.2. Actual Spatial Resolution.	24
3.3.3. Distortion Due to Refraction	29
3.3.4. Image Analysis	29
3.3.5. Precision and Accuracy of the Spatial Measurements	31
3.4. Temporal Resolution	31
4. Experimental Procedure	35

	<u>Page</u>
5. Experimental Results.	44
5.1. Experimental Data.	44
5.2. Experimental Correlations.	48
6. Theoretical Considerations.	69
6.1. Light Absorption By Spherical Plasmas.	69
6.1.1. Collisional Absorption.	69
6.1.2. Resonant Absorption	87
6.1.3. Combined Inverse Bremsstrahlung and Resonant Absorption	100
6.1.4. Effect of Profile Modification on Absorption.	105
6.1.5. Application of Absorption Theory to the Experimental Data	110
6.2. Refraction of Light Through a Plasma	120
6.2.1. Eikonal Equation.	120
6.2.2. Light Refraction Through a Spherical Plasma.	124
6.2.3. Light Refraction Through a Plane Plasma .	126
6.3. Ablation Region Dynamics	128
6.3.1. Steady-State Ablation	128
6.3.2. Computer Simulations.	131
7. Discussion of Results	158
References.	161
Appendix A - Spatial Resolution and Spatial Accuracy.	166

	<u>Page</u>
A.1. Finite Object Thickness	166
A.2. Diffraction Limited Resolution.	170
A.3. Resolution of a Diffraction Limited System for Viewing a Three-Dimensional Object.	172
A.4. Real Optical System Performance	176
A.5. Streak Camera Spatial Resolution.	178
A.6. Distortion Due to Refraction.	187
A.7. Image Analysis.	193
Appendix B - Density Dependence of the Harmonic Emissions	204

LIST OF TABLES

	<u>Page</u>
3-1. Error Bars on Spatial Measurements.	32
5-1. Summary of Data	45
6-1. Absorption Calculated from Streaked Data.	117
A-1. Flat Object Point Resolution for the Optical System . .	176

LIST OF FIGURES

	<u>Page</u>
2-1. Typical Electron Density and Temperature Profiles	4
2-2. Experimental Arrangement.	9
3-1. Harmonic Emission Viewing Optics.	11
3-2. Basic Two Lens Relay System of the Optical System	13
3-3. Streak Camera Schematic	17
3-4. Fractional Absorption: Inverse Bremsstrahlung + Resonant Absorption	20
3-5. Resolution of a Point at a Height x Above the Plane of Best Focus.	25
3-6. Resolution of an Edge for Emitting Surface with Radius r	26
3-7. Spatial Resolution of Streaked Data	28
4-1. Harmonic Emission Photographs	36
4-2. Time Integrated $2\omega_0$ Microdensitometer Trace	38
4-3. Streaked Data Microdensitometer Trace I	39
4-4. Streaked Data Microdensitometer Trace II.	40
4-5. Critical Surface Trajectory 11534 North.	42
4-6. Quarter - Critical Surface Trajectory 11534 North. . . .	43
5-1. Streaked Image Shot 11099.	47
5-2. Critical Surface Trajectory 11099 North.	49
5-3. Trajectories 11534 South	50
5-4. Time Resolved Scalelength 11534 South.	51
5-5. Trajectories 11534 North	52

	<u>Page</u>
5-6. Time Resolved Scalelength 11534 North.	53
5-7. Incident Pulse 11534	54
5-8. Critical Surface Trajectory 11570.	55
5-9. Incident Pulse 11570	56
5-10. Trajectories 11709 South	57
5-11. Time Resolved Scalelength 11709 South.	58
5-12. Incident Pulse 11709	59
5-13. Trajectories 11710 South	60
5-14. Time Resolved Scalelength 11710 South.	61
5-15. Trajectories 11710 North	62
5-16. Time Resolved Scalelength 11710 North.	63
5-17. Incident Pulse 11710	64
5-18. Experimental Scalelength Dependence of Absorption . . .	66
5-19. Peak Critical -- Quarter - Critical Surface Excursion Correlation	67
5-20. Peak Critical Surface Excursion -- Rise Time Dependence	68
6-1. Ray Path Geometry	76
6-2. Fractional Absorption Due to Inverse Bremsstrahlung . .	80
6-3. Laser Beam Intensity Profile.	82
6-4. Fractional Absorption Due to Inverse Bremsstrahlung Absorption.	84
6-5. Spatial Dependence of Oblique Incidence Inverse Bremsstrahlung Absorption	85
6-6. Fractional Resonant Absorption.	89

	<u>Page</u>
6-7. Geometries for Oblique Incidence Light on Spherical . . . and Plane Plasmas	91
6-8. Geometry of Linearly Polarized Light on a Spherical Plasma.	94
6-9. Absorption Efficiency of Resonant Absorption as a Function of Scalelength	96
6-10. Absorption Efficiency of Resonant Absorption as a Function of Critical Surface Location	97
6-11. Local Resonant Absorption as a Function of Initial Ray Height.	99
6-12. Total Fractional Absorption due to Inverse Bremsstrahlung and Resonant Absorption.	101
6-13. Comparison of Absorption With and Without Resonant Absorption.	102
6-14. Absorption Profiles I	103
6-15. Absorption Profiles II.	104
6-16. Steepened Density Profile for Absorption Calculations .	106
6-17. Effect of a Density Jump on Fractional Absorption - Normal Incidence.	108
6-18. Effect of a Density Jump on Fractional Absorption - Oblique Incidence	109
6-19. Absorption History / Beam 11534 South.	112
6-20. Absorption History / Beam 11534 North.	113
6-21. Absorption History / Beam 11709 South.	114

	<u>Page</u>
6-22. Absorption History / Beam 11710 South.	115
6-23. Absorption History / Beam 11710 North.	116
6-24. Scalelength Dependence of Absorption. Theory and Experiment.	119
6-25. Trajectories for Typical Conditions	133
6-26. Critical Surface Trajectories for Various Absorbed Energies.	135
6-27. Ablation Region Profiles During Peak Excursion Intervals	136
6-28. Peak Excursion Variation with Shell Thickness	138
6-29. Effect of Flux Limiter Variation on Critical Surface Trajectories.	139
6-30. Peak Critical Surface Excursion Dependence on Flux Limiter	140
6-31. Peak Critical Surface Excursion Dependence on Heat Front Thermal Energy and Corona Electron Temperature.	142
6-32. Peak Critical Surface Location Dependence on Heat Front Thermal Energy, Corona Temperature, and Ablating Material Source Location.	143
6-33. Peak Critical Surface Excursion Dependence on Ablation Rate and Corona Temperature	145
6-34. Peak Critical Surface Location Dependence on Ablation Rate, Corona Temperature, and Source Location	146
6-35. Critical -- 1/4 - Critical Surface Peak Excursion Relation.	148

	<u>Page</u>
6-36. Comparison of Theory and Experiment. Critical -- $1/4$ - Critical Surface Peak Excursion Relation	149
6-37. Effect of Supra - Thermal Electron Energy Transport on Peak Excursions.	151
6-38. Peak Critical Surface Excursion -- Laser Pulse Rise Time Dependence.	154
6-39. Flux Limiter -- Laser Pulse Rise Time Cross-Correlation.	155
6-40. Correlation Between Energy Transport and Laser Pulse Rise Time.	156
A-1. Geometry for Emitting Source with Finite Thickness . . .	168
A-2. Airy Diffraction Pattern	171
A-3. Resolution of an Edge for Emitting Surface with Radius r	174
A-4. Resolution of a Point at a Height x Above the Plane of Best Focus	175
A-5. Resolution Chart Photographed Through the Optical System	177
A-6. Test Object Images.	179
A-7. Streaked Crossed - Slit Image.	182
A-8. Dynamic Streak Camera Spatial Resolution	183
A-9. Sketch of $D - \log E$ Curve and Effect of Variable γ . . .	185
A-10. Spatial Resolution of Streaked Data.	188
A-11. Refraction of Plasma Emissions	190
A-12. Image Analysis Geometry.	194

	<u>Page</u>
A-13. Effect of Finite Resolution on Object Size Measurements	197
A-14. Out of Focus Image.	199
A-15. Correlation of Measured Edge Positions to the Actual Edge Position	201
A-16. Correlation for Corrected Data.	202

1. REPORT STRUCTURE

This report deals with the development and application of a new diagnostic technique that has provided new information for the study of laser-plasma interactions. Spatially and temporally resolved observation of light emissions from a plasma at the second and three-halves harmonics of the incident laser light frequency has directly yielded plasma density profile information. These results are applied to the study of fundamental plasma processes: laser light absorption, energy transport, and hydrodynamics.

Chapter 2 provides an introduction to the topic of laser produced plasmas and to their study through the observation of harmonic light emissions. Chapter 3 deals with the procedures for data acquisition. Data accuracy requirements are put forth. The experimental setup for spatially and temporally resolved microscopy of laser produced plasmas is described. System resolution is determined and an image analysis procedure is put forth for the enhancement of the accuracy of the results. (Resolution determination procedures and formulation of the image analysis technique are detailed in Appendix A.) The final accuracy of the results is tabulated.

In Chapter 4 typical data is taken and reduced according to standard procedures. In Chapter 5 the experimental results are presented. Chapter 6 deals with the topics to which the experimental results are applied. Chapter 7 gives a discussion of the results.

Appendix B indicates the source of the harmonic emission spatial inhomogeneity.

Equations are in cgs units with electro-magnetic quantities in Gaussian units. Exceptions to this rule are found when a unit of length may be expressed in microns ($1 \mu\text{m} = 10^{-4} \text{cm}$), a unit of time may be expressed in picoseconds ($1 \text{ psec} = 10^{-12} \text{ sec.}$), a unit of power may be expressed in watts ($1 \text{ watt} = 10^7 \frac{\text{erg}}{\text{sec}}$), and a unit of temperature may be expressed in kilo-electron volts or electron volts ($1 \text{ keV} = 10^3 \text{ eV} = 1.16 \times 10^7 \text{ }^\circ\text{k}$).

2. Introduction

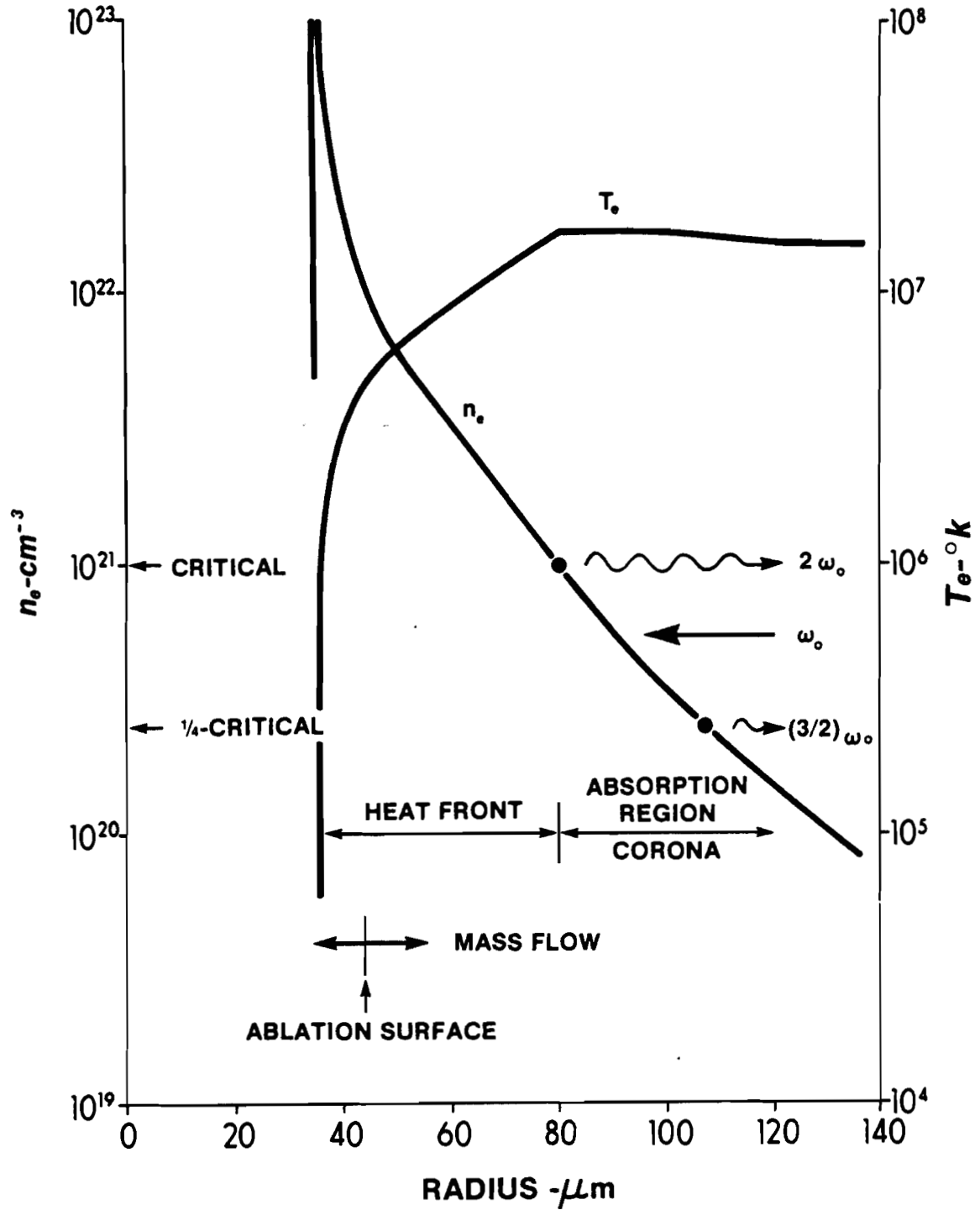
The interaction of laser light with matter produces plasma that is inherently spatially inhomogeneous. Plasma generated at the surface of a solid target expands, and decreases in density. The density of target material increases due to shock wave compression. Induced target motion may cause density variation effects.

Typical computer predicted electron density and temperature profiles are shown in figure 2-1. The plasma has been generated from a thin spherical glass shell target irradiated with 1.06 μm wavelength laser light. The laser light (ω_0), propagating parallel to the density gradient, penetrates up to the critical electron density and is there reflected. Energy is absorbed by the plasma in the zone of light penetration. Energy deposited by the laser heats the plasma in the sub-critical density region, the corona, to about 10^7 $^\circ\text{k}$. Energy transported inwards through the critical surface generates hot plasma from the shell material. Momentum transferred from the outward ablating plasma drives the shell inwards. Dividing the inward and outward moving material is a point of zero velocity known as the ablation surface.

Of importance in the study of laser produced plasmas is the characterization of the electron density profile in the region of the critical density. Processes such as laser light absorption and plasma energy transport depend on and affect the critical density region profile. Profile modification may occur through the deposition into the plasma of laser light momentum.

The important possible light absorption mechanisms are collisional,

FIGURE 2-1
**TYPICAL ELECTRON DENSITY AND
 TEMPERATURE PROFILES**



resonant, and plasma instability absorption. In collisional absorption, electrons driven by the laser light electric field collide with ions within the range of either a Debye shielding length (inverse bremsstrahlung absorption)^(2-1,2,3) or a turbulent ion structure (absorption off of ion turbulence).^(2-4,5,6,7) Collisional absorption is strongest where the frequency of collisions is largest. This occurs in the highest density region of light propagation, i.e., in the critical density region. Resonant absorption occurs when a component of the laser light electric field is converted directly into electron plasma waves.^(2-8,9,10,11,12) The point where the plasma waves build up is at the critical density. Plasma instabilities absorb energy by coupling light into plasma oscillations.⁽²⁻¹³⁻²²⁾ These instabilities are resonant at various densities and, therefore, depend on the shape of the sub-critical density profile.

Collisional and resonant absorption have significant and relatively straightforward density scalelength dependences. Measurement of scalelength and absorption can, and does, allow theory and experiment to be compared. The density profile dependence of plasma instabilities is complicated by the requirement of knowing not only thresholds and growth-rates but also saturation and energy dissipation mechanisms. Although the existence of finite amplitude plasma waves is supported by some of this thesis' experimental observations,⁽²⁻²²⁾ the energy absorbed into them is not studied here.

The principal modes of energy transport through the plasma are thermal electron heat conduction^(2-7,23,24) and supra-thermal electron transport.^(2-25,26) The two mechanisms are distinguished from one

another by the relative magnitudes of the electron collision length and the plasma thickness. When the distance between electron collisions is small compared to the density scalelengths, the electrons quickly become thermal and the transport is "diffusive". Suprathermal electron collision lengths are long compared to density scalelengths and the energy transport is "free-streaming". The magnitude and nature of energy transport manifests itself in the density profile shape and can be studied via analysis of experimentally determined profiles.

Laser light momentum deposition effects may manifest themselves in the density profile shape. These effects are generally localized to regions of strong laser light absorption, reflection, or refraction and are predicted to occur as localized steepening of the density gradients,^(2-6,20,21,27) as turbulence and rippling of the critical density surface⁽²⁻²⁸⁾, or as radial plasma filaments and laser beam self-focusing.⁽²⁻²⁹⁾ Profile modification effects may need to be considered when the ratio of the radiation pressure ' p_{rad} ' to the electron pressure ' p_e ' is of order .1 or greater.⁽²⁻²⁷⁾ For normal incidence light reflected from a surface

$$\frac{p_{\text{rad}}}{p_e} \approx \frac{2I}{c} \frac{1}{n_e k T_e} \quad (2-1)$$

where ' I ' is the laser intensity, ' n_e ' is the electron density, ' T_e ' is the electron temperature, ' c ' is the speed of light, and ' k ' is Boltzmann's constant. For 1.06 μm light reflected from the critical

surface of a 1×10^7 O_k plasma, $p_{\text{rad}}/p_e = .1$ at a laser intensity of $I = 2 \times 10^{21} \frac{\text{erg}}{\text{sec-cm}^2}$. Current experiments are conducted at laser intensities of $10^{22} \frac{\text{erg}}{\text{sec-cm}^2}$ or greater so that profile modification effects are predicted. At $10^{22} \frac{\text{erg}}{\text{sec-cm}^2}$ reference 2-27 predicts a density jump of $n_e = 3 \times 10^{20} \text{ cm}^{-3}$ to $1.35 \times 10^{21} \text{ cm}^{-3}$ and reference 2-28 predicts the existence of critical surface turbulence.

Of particular interest for the experimental determination of the electron density profile in the critical density region is the generation in the plasma of light at harmonics of the laser light frequency. The emission of these harmonics is strongly density dependent so that within an inhomogeneous plasma the harmonic light emissions are localized to narrow intervals of density and space. By following the sources of harmonic light emissions, particular densities can be followed in space and time.

Spatially resolved observation of harmonic light emissions is the technique developed in this thesis. The harmonics viewed are the second ($2\omega_0$) and three halves ($\frac{3}{2}\omega_0$) harmonics of the incident laser light (ω_0). For laser light at a wavelength of $1.064 \mu\text{m}$, the $2\omega_0$ occurs at $.5320 \mu\text{m}$ (green) and the $(3/2)\omega_0$ occurs at $.7093 \mu\text{m}$ (near infra-red). The $2\omega_0$ light is emitted at the critical density,^(2-30,31,32) $n_e = 1 \times 10^{21} \text{ cm}^{-3}$, and the $(3/2)\omega_0$ is emitted at the quarter-critical density^(2-17,33,34,35), $n_e = 2.5 \times 10^{20} \text{ cm}^{-3}$ (fig. 2-1). (See Appendix B)

As the plasma evolves, the critical and quarter-critical densities move in space and time. Spatially and temporally resolved $2\omega_0$ and $(3/2)\omega_0$ images provide critical and quarter-critical surface

trajectories (r_{cr} , $r_{\frac{1}{2}cr}$). Time resolved plasma density scalelengths are obtained as the difference between the quarter-critical and critical surface locations, i.e.,

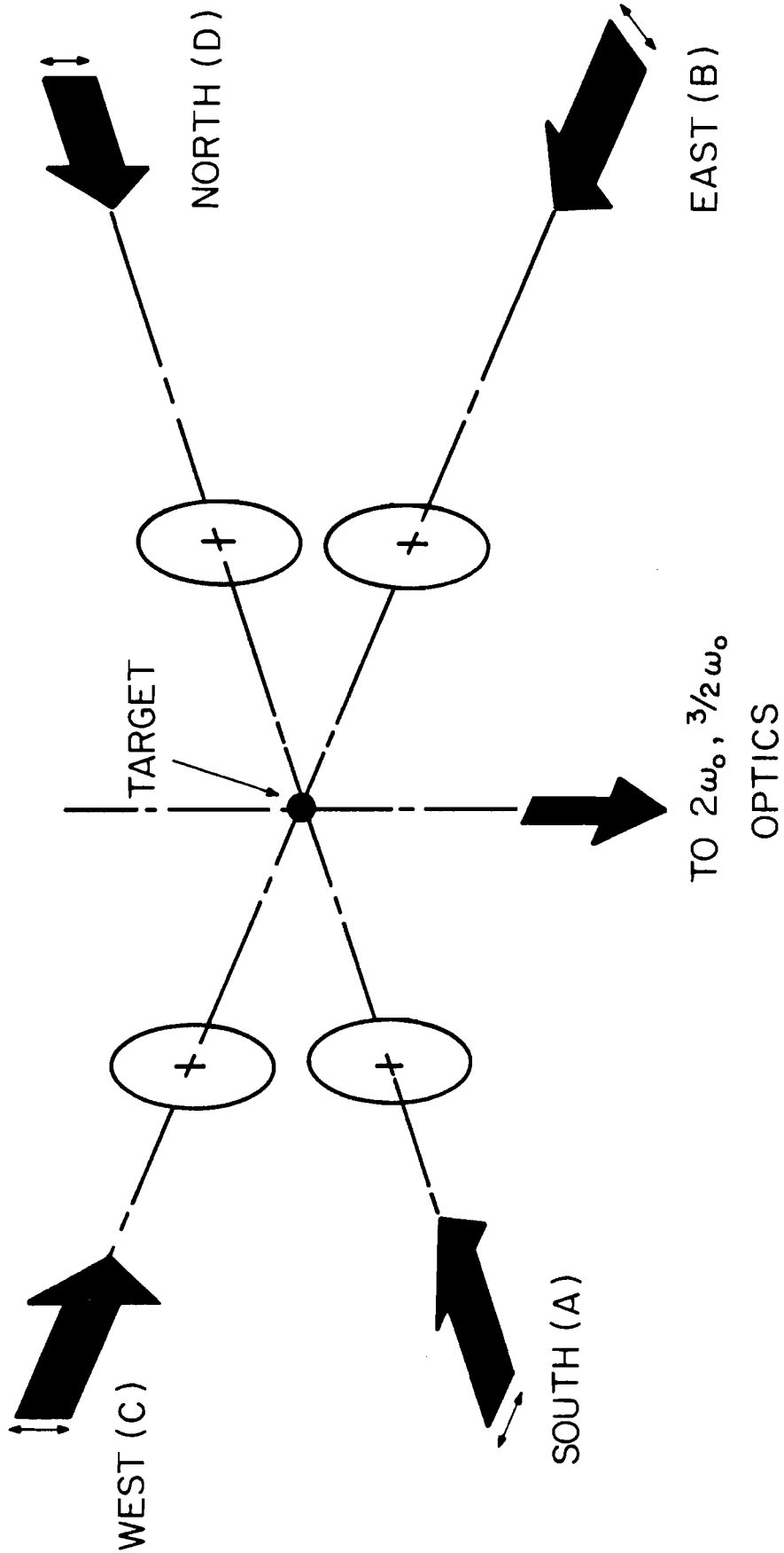
$$l \equiv r_{\frac{1}{2}cr} - r_{cr} \quad (2-2)$$

Time integrated $2\omega_0$ and $(3/2)\omega_0$ images provide critical and quarter-critical surface peak excursions and a "characteristic" plasma density scalelength given by

$$L \equiv r_{\frac{1}{2}cr \max} - r_{cr \max} \quad (2-3)$$

In the experimental arrangement, figure 2-2, the four beam output of a Nd:glass laser is focused within a plane onto glass microballoon targets.⁽²⁻³⁶⁾ The $2\omega_0$ and $(3/2)\omega_0$ plasma emissions are viewed from a direction perpendicular to the plane of irradiation. The time resolved images obtained with a streak camera (section 3.1) record plasma emissions along an axis through two opposing beams. For any shot, critical and quarter-critical surface trajectories are obtained on opposing sides of the plasma. The time integrated photographs record the plasma emissions from each of the four laser beams so that peak excursion data is obtained within each of the focal spots.

FIGURE 2-2
EXPERIMENTAL ARRANGEMENT



3. Data Acquisition and Accuracy

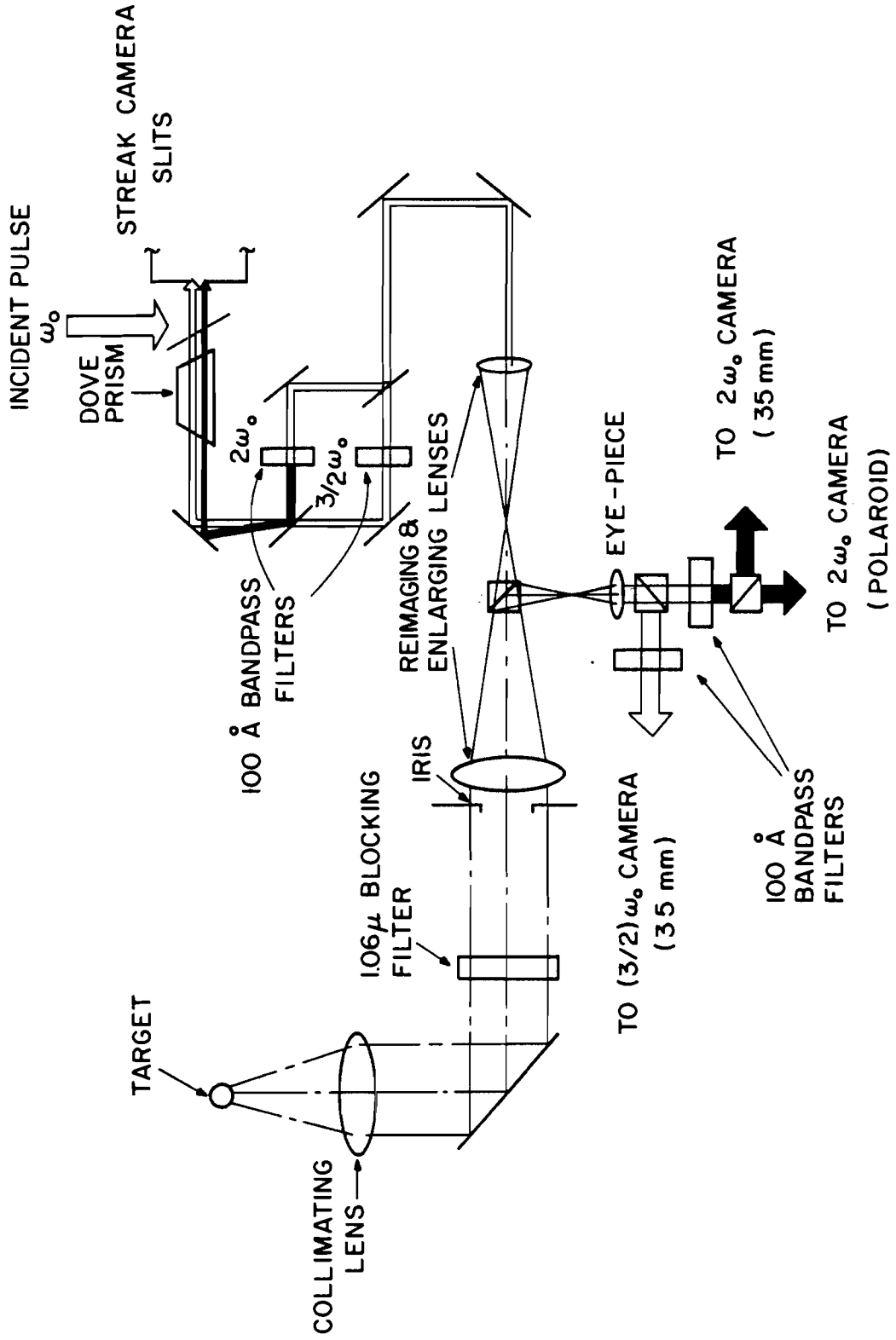
3.1 Experimental Setup

A schematic of the optical system is shown in figure 3-1. The system was designed to serve as an achromatic microscope for spatially and temporally resolved harmonic emission studies. Time integrated data with two dimensional spatial resolution was obtained by forming magnified images of the harmonic emissions on film. Temporal resolution was achieved by relaying the magnified images through a streak camera. The streak camera operated by displacing as a function of time the image of a slit located at the camera's entrance. Only the emission images falling on the entrance slit were relayed so that only one axis of the plasma was temporally and spatially resolved. Streaked data for the two harmonics was simultaneously obtained by placing the $2\omega_0$ and $(3/2)\omega_0$ images side-by-side on the streak camera entrance slit. The harmonic data was temporally multiplexed with the incident laser pulse via control of optical path lengths. The ω_0 light entered the streak camera earlier than the harmonic images so that the data was displaced in the output. (See figure 4-1.)

The hostile environment near the plasma necessitated the use of a long focal length lens to collect the light from the plasma. The necessity of imaging through a 1.3 cm thick vacuum chamber window required the placement of the first lens within the vacuum. To minimize spherical aberration caused by the window,⁽³⁻¹⁾ the first lens was placed one focal length from the target so that the light coming out was "collimated". The image produced by this lens was focused at

FIGURE 3-1

HARMONIC EMISSION VIEWING OPTICS



infinity. The collimating lens had a focal length of $F_c = 20$ cm and an f-number ($f \approx 1/\text{full acceptance angle of lens}$) of $f_c = 3.5$.

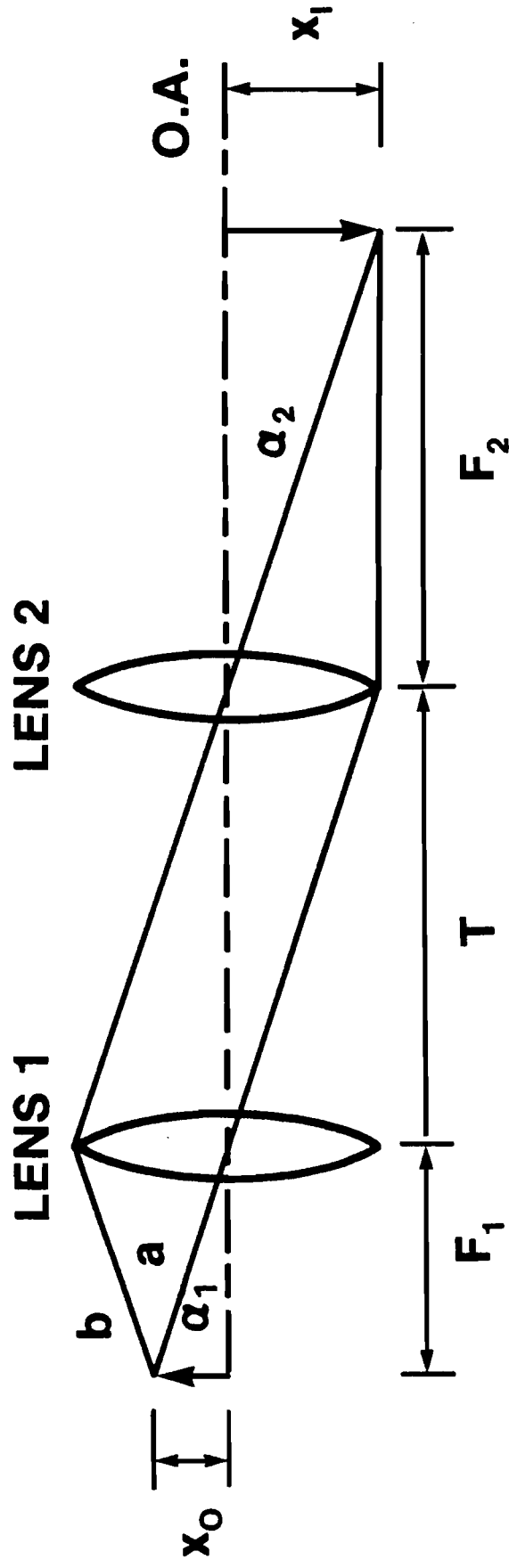
The collimated light was readily relayed with $\lambda/10$ aluminum coated mirrors to a reimaging lens. An astronomical telescope objective, designed to image the collimated light from infinitely distant objects, was well suited for reimaging the plasma emissions. A Unitron telescope objective was used having a focal length of $F_o = 150$ cm and an f-number = 15.

The magnification of a two lens system of the type used can be calculated with reference to figure 3-2. Consider two rays leaving an object at height x_o . The first ray, 'a', is chosen so that it passes through the center of lens 1. In the approximation of a thin lens its path is undeviated and it passes in a straight line from the object point to the second lens. At the second lens the ray is refracted and it then passes on to the image plane. For the second ray, 'b', a ray is chosen such that after refraction by lens 1 it passes through the center of lens 2. Ray 'b' passes from lens 1 to the image point in a straight line. Since both rays leave the same point on an object one focal length from lens 1, both rays are parallel in the interval between the two lenses.

The angle ' α_1 ' that ray 'a' makes with the optical axis before hitting lens 2 is given by

$$\tan \alpha_1 = \frac{x_o}{F_1} \quad (3-1a)$$

The angle ' α_2 ' that ray 'b' makes with the optical axis after pas-



**BASIC TWO LENS RELAY SYSTEM OF THE
OPTICAL SYSTEM**

FIGURE 3-2

ing through lens 1 is given by

$$\tan \alpha_2 = -\frac{x_I}{F_2} \quad (3-1b)$$

Since the two rays are parallel in the region between the lenses

$$\alpha_1 = \alpha_2$$

$$\frac{x_O}{F_1} = -\frac{x_I}{F_2}$$

The magnification 'm' is defined as the image height divided by the object height and for the two lens system is given by

$$m \equiv \frac{x_I}{x_O} = -\frac{F_2}{F_1} \quad (3-2)$$

At the telescope objective image plane the image was magnified by -7.5.

Additional magnification for the time integrated photographs was obtained with a second two lens system of the type just described. The two lenses were a telescope eye-piece with a focal length of $F_e = 2.5$ cm and a 35 mm camera lens with a focal length of $F_1 = 5.5$ cm. The total magnification of the system for the time integrated exposures was

$$m_{IO} = \frac{F_O}{F_C} \times \frac{F_1}{F_e} = 16.5 \text{ -- TIME INTEGRATED} \quad (3-3)$$

An advantage of the two lens arrangement was the magnification's independence to the distance between the lenses. The placement of the telescope objective and the camera lens was not critical. Another practical advantage was that the correct focus of the eye-piece in the two lens combination was also the proper focus for visual observations of the target through the eye-piece. The system could be visually aligned and focused, and a prefocused camera could then be put into place.

Space and alignment problems prohibited the use of a two lens system to relay a magnified image to the streak camera. A single $F_s = 30$ cm focal length Wray London Lustrar process lens was used. The system magnification to the streak camera was

$$m_{so} = \left(\frac{-F_o}{F_c} \right) \left[\frac{-L - (L^2 - 4LF_s)^{\frac{1}{2}}}{-L + (L^2 - 4LF_s)^{\frac{1}{2}}} \right] = 19.5 \text{ -- ONTO STREAK CAMERA SLITS} \quad (3-4)$$

where $L = 160$ cm was the distance from the telescope objective focus to the streak camera slits and $F_s = 30$ cm. Since the magnification in equation (3-4) was sensitive to changes in L it was checked by photographing a test object of known size through the viewing optics-streak camera system.

A rule of thumb in optics is that the introduction of elements into an optical system, generally, only degrades the final image quality. If elements must be introduced into a microscope system then they should be placed after as much magnification as possible has

been done so as not to magnify the aberrations introduced by the elements. With the exception of a 1.06 μm blocking filter this rule was followed for all beam splitters and filters. The effect of the 1.06 μm blocking filter was checked and found to be minimal.

The 1.06 μm blocking filter was a .2 cm thick Schott KG3 grade A filter. It had a transmission of 10^{-3} at 1.06 μm , .45 at .71 μm , and .88 at .53 μm . The interference filters were a Ditric .01 μm bandwidth .53 μm bandpass filter and a Bausch & Lomb .01 μm bandwidth .71 μm bandpass filter. Both filters had quoted rejection ratios of 10^4 and were measured to have rejection ratios of greater than the 10^2 sensitivity of the Cary 14 spectrometer on which they were tested.

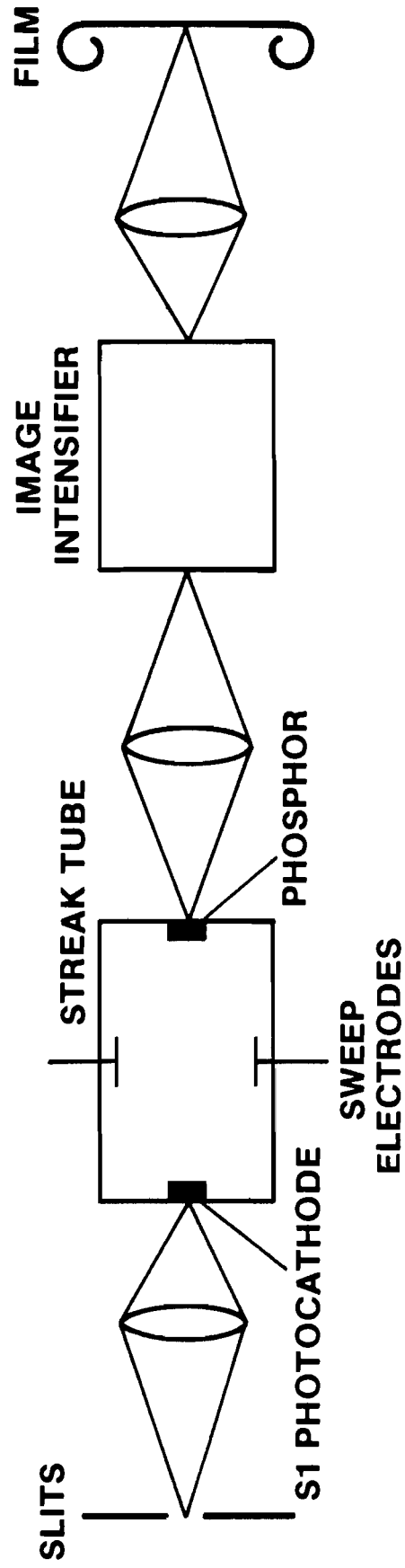
The two remaining optical components were a variable aperture size iris and a dove prism. The iris was used to control aberrations through adjustment of the system f-number. (See section 3.3) The dove prism, a device used to rotate an image about the optical axis, was used to control the plasma axis being imaged through the streak camera.

Films used were chosen to have high sensitivity at the $2\omega_0$ and $(3/2)\omega_0$ frequencies. Kodak Tri-X Panchromatic and Kodak High Speed Infra-Red film⁽³⁻²⁾ were chosen respectively for the $2\omega_0$ and $(3/2)\omega_0$ time integrated observations. Both films were developed in D-19 developer at 20°C. The tri-X was developed for 4 minutes and the HSIR was developed for 9 minutes.

The streak camera was a model 512 Electro-Photonics electro-optic streak camera. A schematic is shown in figure 3-3. Its use

FIGURE 3-3

STREAK CAMERA SCHEMATIC



provided time resolved data with spatial resolution in one dimension. To briefly describe its operation; an entrance slit was optically imaged onto a photocathode within the streak tube. Electrons were emitted from the photocathode according to the intensity distribution of the light on its surface. The electrons were relayed through the streak tube and onto a phosphor output with electron optics. The output image was displaced in space (the input image in time) by applying a time varying electric field across the electron beam. At different times the slit image fell at different positions along the phosphor and a time resolved image of the input slit was obtained. The phosphor converted the electron image into a photon image. This image was optically coupled to a 4 stage magnetically focused image intensifier with a gain of 10^6 . The output was placed onto photographic film to form a permanent record. Details on streak camera characteristics can be found in references (3-3) to (3-5).

3.2 Resolution Requirements

A primary consideration in the design of the experimental equipment was the required resolution. The resolution requirements were based on a consideration of the accuracy necessary to study the physics of light absorption and ablation region hydrodynamics, and of the accuracy of the other diagnostics to which the experimental results were compared. Resolution breaks down into two categories: spatial resolution and temporal resolution.

3.2.1 Spatial Resolution

There are two spatial length scales of interest. They are the

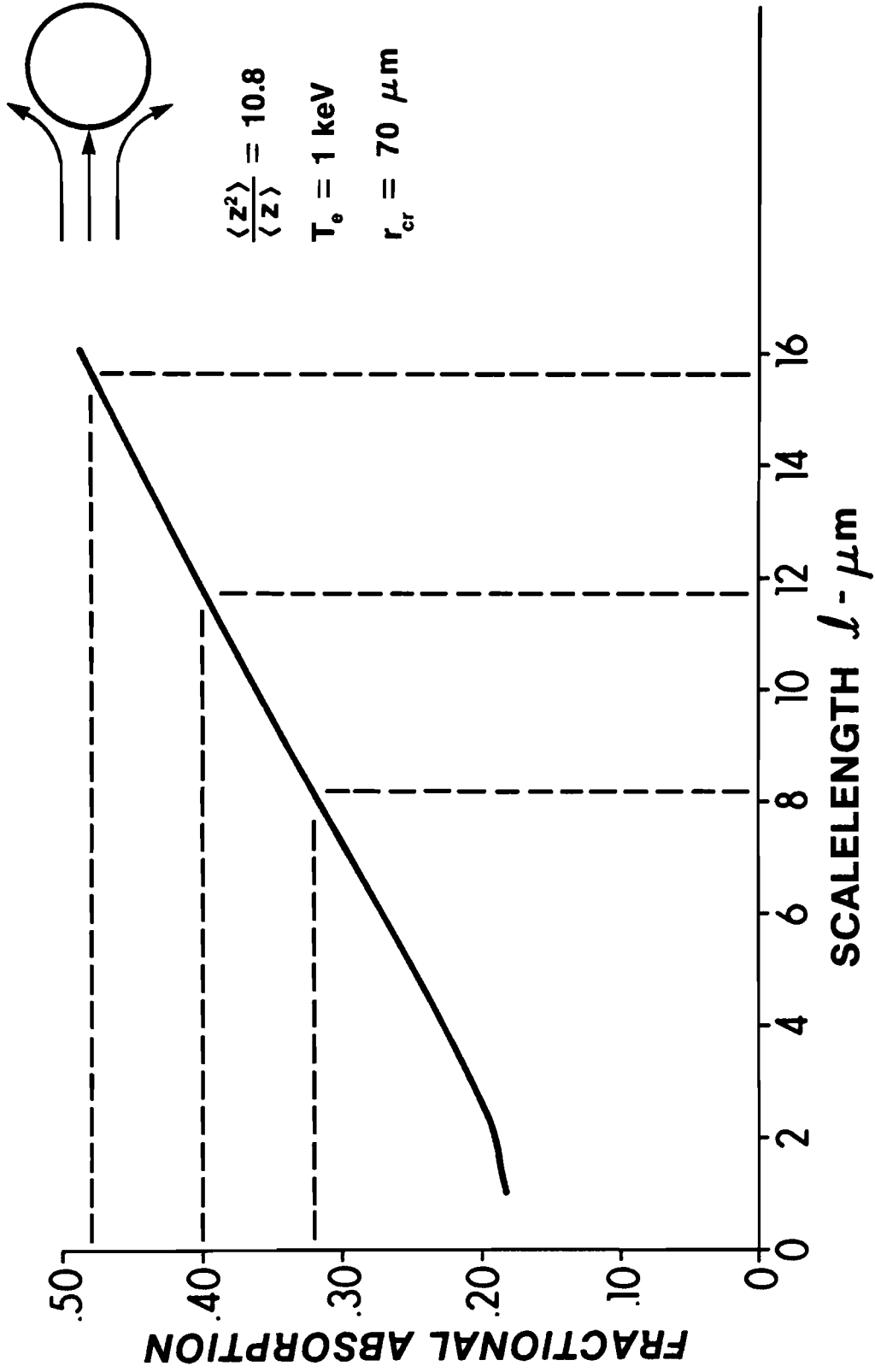
radius of the critical surface and the distance between the critical and quarter-critical surfaces.

To compare the experimental results to hydrodynamic codes and analytic models of plasma expansion it is sufficient to know the critical surface location to $\pm 5\%$. The critical surface position varies from the initial target radius ($\approx 50 \mu\text{m}$) to a maximum excursion of about $80 \mu\text{m}$ so that the accuracy requirement on the critical surface position is approximately $\pm 3 \mu\text{m}$.

An important use of scalelength information is to examine the mechanisms for light absorption by a plasma. This is done by taking the measured scalelengths and calculating with the possible absorption mechanism theories, the energy fraction absorbed. This quantity is compared to the experimentally measured value of the fractional absorption (energy absorbed/energy on target). To accomplish this comparison, the accuracy of the scalelength measurement should be such that the calculated fractional absorption is at least as accurate as the measured fractional absorption.

Typical experimental values for the fractional absorption of $1.06 \mu\text{m}$ laser light, measured using a variety of techniques, is about .40 with measuremental accuracy of $\pm .08$.^(3-6,7,8,9) Figure 3-4 shows the theoretical scalelength dependence of inverse bremsstrahlung plus resonant absorption for the conditions of this experiment (see Chapter 6). To study the absorption's scalelength dependence with the accuracy of the absorption measurement, figure 3-4 shows that it is necessary to have a scalelength accuracy of approximately $\pm 4 \mu\text{m}$.

FIGURE 3-4
**FRACTIONAL ABSORPTION : INVERSE
 BREMSSTRAHLUNG + RESONANT ABSORPTION**



3.2.2 Temporal Resolution

For the time-resolved results the desired temporal resolution is fixed by the spatial resolution and the maximum observed critical and quarter-critical surface expansion velocities.

The relationship between spatial and temporal resolution requirements can be seen by noting that if a position 'z' is measured at time 't' then the next measurement should be made by the time the position has changed by one resolution element ' λ '. At a velocity 'v', the position will have changed by ' λ ' in a time ' δt ' given by:

$$\delta t = \frac{\lambda}{v} \quad (3-5)$$

The most stringent requirement on temporal resolution occurs when v is a maximum. The maximum velocity observed is on the order of 5×10^7 cm/sec. This leads to a temporal resolution requirement of $\delta t = \pm 6$ psec.

3.3 Sources of Spatial Error

Principal sources of error in making spatial measurements are the finite thickness of the object, the finite diffraction limited resolution of the optical system, the aberrations present in the optics and streak camera, and distortion produced by refraction of light as it passes out of the plasma. Error due to the first three sources results from the necessity of analyzing photographs that contain blurred images. The effect of the last source of error,

refraction, is the production of an emitting surface image that is possibly distorted from the actual emitting surface shape lying within the plasma.

Finite object thickness and diffraction limited resolution produce an upper limit on the theoretical resolution of the optical system. Real lens and streak camera aberrations degrade the actual resolution from the theoretical value.

In this section the effect of each source of error on the system resolution is characterized. Theoretical and actual resolutions are compared. Bounds are placed on the possible error due to light refraction by the plasma. The section concludes with a description of a simple image analysis technique that accounts for and eliminates most of the systematic error introduced by the finite system resolution.

Only results as they pertain to the accuracy of the $2\omega_0 - (3/2)\omega_0$ measurements are described in this section. Detailed derivations and general aspects of spatial resolution measurements are described in the appendix. Included in the appendix are new results on the intensity dependence of the streak camera spatial resolution.

3.3.1 Theoretical Spatial Resolution

Limitations on the ultimate resolution of any optical system are imposed by the finite thickness of the object being viewed and by the diffraction limited performance of the optics used to collect and reimage the light.

Finite object thickness effects arise from the fact that a well corrected optical system images a plane object into a plane image.

The image of a three-dimensional object can have only a single plane in sharp focus. The rest of the object appears blurred to some extent. Even if only a single plane is being studied, the effect of the entire object must be considered since, in general, light from out-of-focus points overlaps the in-focus points.

The amount of blurring due to the finite object thickness is a function of the object thickness parallel to the optical axis, the object shape, and the angular spread in the rays leaving the object and collected by the optics. The effect can be expressed in terms of a point or edge resolution. Point resolution gives the blur in individual out-of-focus points and can be quantified as the blur circle radius. Edge resolution gives the blur observed at the outer edge of a three-dimensional object and can be expressed as the difference between the actual edge location and the location in the image of the outermost blurred light.

Diffraction limited performance is a consequence of the limited collection angle of the optics. To form a perfect image of a point, all of the emitted light must be collected and reimaged. The inability to do so results in an emitting point image consisting of an "Airy diffraction pattern".⁽³⁻¹⁰⁾ The image spot size, quantified as the diffraction pattern radius at the first intensity minimum, is a function of the angular spread in the light collected and of the light wavelength.

The resolution of a diffraction limited system viewing a spherical object is given by equation (3-6) for the point resolution ' r_p '

and equation (3-7) for the edge resolution ' κ_E '.

$$\kappa_p = \left[\left(\frac{x}{2f_c} \right)^2 + (1.22\lambda f_c)^2 \right]^{\frac{1}{2}} \quad (3-6)$$

$$\kappa_E = \left[\left(\frac{r}{8f_c^2} \right)^2 + (1.22\lambda f_c)^2 \right]^{\frac{1}{2}} \quad (3-7)$$

' λ ' is the light wavelength, ' f_c ' is the dimensionless f-number of the collecting optics, ' x ' is the distance parallel to the optical axis from the object point to the plane of best focus, and ' r ' is the radius of the emitting surface. The first term in equations (3-6) and (3-7) gives the contribution due to the finite object thickness and the second term gives the contribution due to diffraction limited performance.

Figures 3-5 and 3-6 show plots of equations (3-6) and (3-7) for conditions of experimental interest. At low f-numbers (large collection angles) finite object thickness effects dominate while at high f-numbers diffraction limitation effects dominate. Optimum resolution can be achieved via adjustment of f_c although the optimum point and edge resolutions do not coincide. The point resolution is relatively insensitive to the source location (x) for $f_c \geq 12$ while edge resolution is independent of the emitting object radius (r) for $f_c \geq 5$. (The independence of κ on object parameters shall prove to be of importance when image analysis is considered.)

3.3.2 Actual Spatial Resolution

The actual optical system was run at an f-number of $f_c=13$. This

FIGURE 3-5

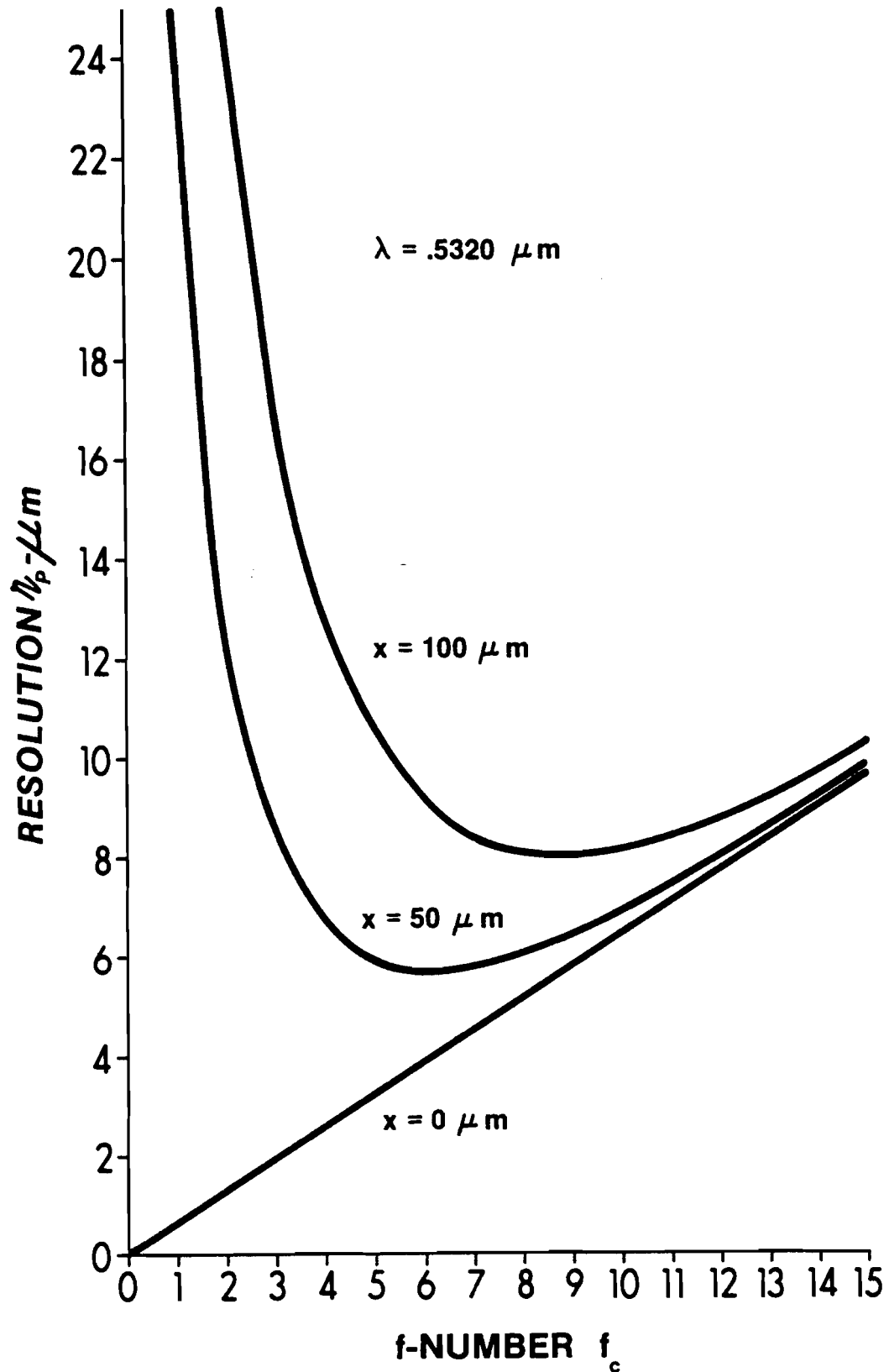
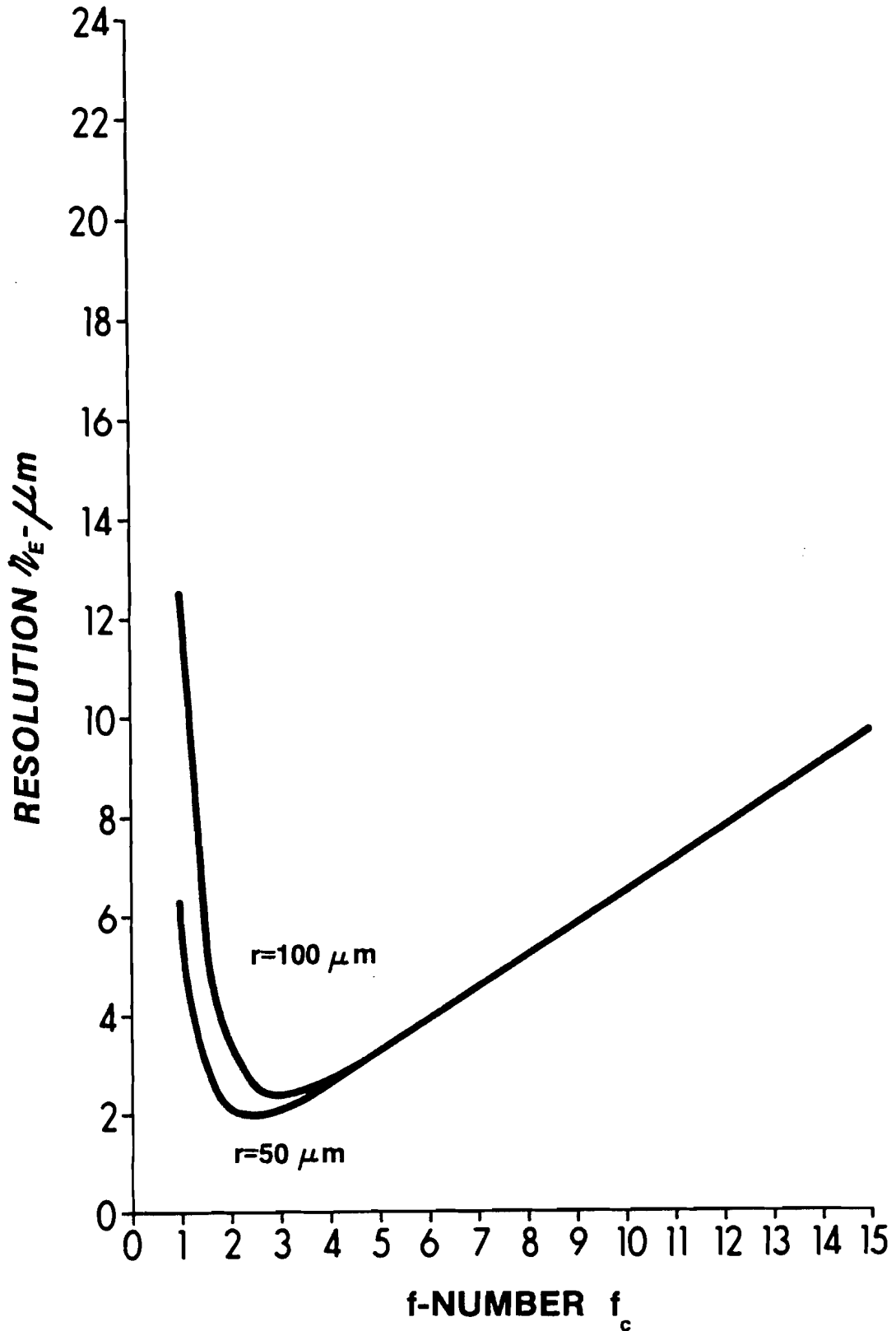
**RESOLUTION OF A POINT AT A HEIGHT x
ABOVE THE PLANE OF BEST FOCUS**

FIGURE 3-6

RESOLUTION OF AN EDGE FOR EMITTING SURFACES WITH RADIUS r .

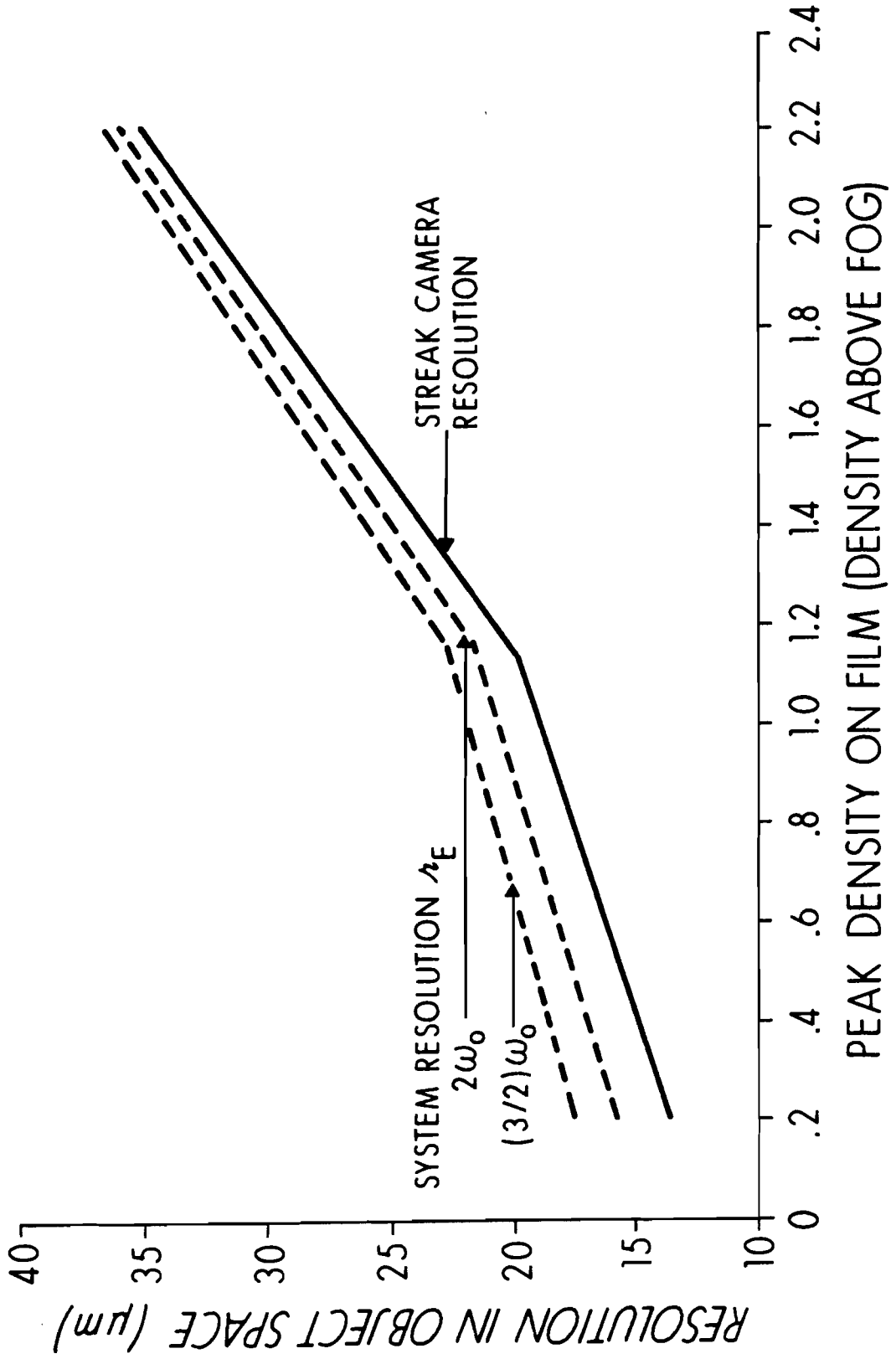
was the lowest collimating lens f-number for which the non-symmetrical aberration of coma was eliminated,⁽³⁻¹¹⁾ and for which the symmetrical aberrations of spherical and axial chromatic aberration⁽³⁻¹¹⁾ were reduced to the point where a point source Airy diffraction pattern could be clearly observed.⁽³⁻¹²⁾ The resolution, exclusive of the streak camera, was determined by photographing resolution charts and test objects and was found to be 8 to 9 μm with green light ($\lambda = .53 \mu\text{m}$) illumination. This is in good agreement with the 8 μm prediction of near diffraction limited performance. White light illumination revealed no significant axial or lateral chromatic aberration.

Using equation (3-6), the flat object resolution for the two wavelengths of interest are: 8 μm at $\lambda = .5320 \mu\text{m}$ and 11 μm at $\lambda = .7093 \mu\text{m}$.

Relaying the images through the streak camera degraded the resolution from that of the passive optical system. Resolution measurements were made in static and streaked modes and the principal results are: the intensity distribution of the point response shows only a weak broadening with increasing input intensity, the width of the point response at the noise level increases but that this broadening is due to a minimum detection level so that more of the point response is seen for more intense inputs, and the streak camera spatial resolution degrades by 25% in going from static to streaked mode.

The width of the point response at the noise level is the important measure of resolution for the experimental results. A plot of the streaked data resolution as measured by the point response half width at base density, as a function of the peak film exposure is shown in figure 3-7. The resolution is referenced back to the plasma.

FIGURE 3-7
 SPATIAL RESOLUTION OF STREAKED DATA



3.3.3 Distortion Due to Refraction

An inhomogeneous plasma has a variable index of refraction and causes light passing through it to bend. If the goal of an observation is to locate a source of emissions within the plasma, then the effect of light refraction must be considered.

Refraction through a smooth spherical plasma is studied in appendix A.6 via a ray trace computer code and an analytic model. The results are that the apparent emitting surface size is smaller than that of the actual emitting surface and that the apparent critical and quarter-critical surface radii, and the apparent scalelength are in possible error by amounts:

$$\Delta r_{\text{cr-REF}} \equiv r_{\text{cr}} - r_{\text{cr APP}} = .15 r_{\text{cr APP}} \quad (3-8)$$

$$\Delta r_{\frac{1}{4}\text{cr-REF}} \equiv r_{\frac{1}{4}\text{cr}} - r_{\frac{1}{4}\text{cr APP}} = .06 r_{\frac{1}{4}\text{cr APP}} \quad (3-9)$$

$$\Delta \ell_{\text{REF}} \equiv \ell - \ell_{\text{APP}} = .06 \ell_{\text{APP}} - .09 r_{\text{cr APP}} \quad (3-10)$$

When compared to experimental results equations (3-8) - (3-10) appear to over-estimate the error due to refraction. A plausible explanation is that the plasma does not have smooth isodensity surfaces but that there exist local structures or turbulence.

3.3.4 Image Analysis

The results of the preceding sections show that the system resolution is substantially larger than the maximum tolerable error required for physical interpretation of the results. The error introduced by finite system resolution turns out to be systematic and is

correctable by a simple image analysis technique.

In the experiment, the system magnification is determined by measuring the diameter of a test object and dividing by the known object diameter. The measured magnification contains the finite resolution effects and differs from the theoretical ideal system magnification. Nevertheless, if a subsequent measurement is made with the system of an object the same size as that of the test object, then the image sizes will be the same. Use of the measured magnification accurately gives the object size and the measurement contains no systematic error. For objects with sizes different from the test object, use of the measured magnification leaves a residual systematic error. This error can be much less than the system resolution. If an estimate of the resolution is available, then most of the residual error can be eliminated.

It is shown in appendix A.7 that the actual size of any object s is related to the measured size of any object s' by the relation

$$s = \left(1 + \frac{\lambda}{h}\right) s' - \lambda \quad (3-11)$$

s' is calculated using the measured system magnification m' obtained by dividing the measured image dimension of a test object H' by the test object size h , i.e., $m'=H'/h$. λ is the system resolution.

The validity of the image analysis technique has been experimentally confirmed. The accuracy of the final results is limited by the

accuracy and constancy of the measured resolution to about $\pm 2 \mu\text{m}$, and by the consistency of the data reduction procedure.

3.3.5 Precision and Accuracy of the Spatial Measurements

Once the data has been corrected for systematic errors the remaining measurement error is random and is a measure of the precision of the measurement technique. The major contribution to random error in the streaked results comes from a low signal to noise ratio and from a variation in the noise level from point to point on the streak photographs. Selecting the standard deviation of the r_{cr} and $r_{\frac{1}{4}cr}$ data points from the polynomial least square curve fits (Chapter 4) as the measure of the statistical fluctuations, a precision of $\pm 4 \mu\text{m}$ is obtained. This value is conservative since part of the standard deviation is due to short time scale variations averaged out by the curve fitting procedure.

The spatial accuracy of the measurements, exclusive of refraction considerations, is equal to the combination of residual systematic error and statistical error. For the streaked results, the total spatial error is $\pm 4 \mu\text{m}$ and for the time integrated results, it is $\pm 3 \mu\text{m}$. If the bounds on the refraction error, as obtained in section 3.3.6, are used then the maximum error bars for the spatial data are obtained. The results are tabulated in table 3-1. Refraction effects are calculated for a critical surface at $70 \mu\text{m}$ and a $10 \mu\text{m}$ scalelength.

3.4 Temporal Resolution

The two factors limiting the temporal resolution are the time resolution of the streak camera and the low signal to noise ratio of

	<u>MEASUREMENTAL ERROR *1</u>	<u>TIME RESOLVED</u>	
		<u>UPPER BOUND ON REFRACTION</u>	<u>COMBINED *2</u>
r_{CR}	± 4	+11	+12 -4
$r_{\frac{1}{4}CR}$	± 4	+5	+6 -4
ℓ	± 6	-6	+6 -8
<u>TIME INTEGRATED</u>			
r_{CR}	± 3	+11	+11 -3
$r_{\frac{1}{4}CR}$	± 3	+5	+6 -3
ℓ	± 4	-6	+4 -7

*1 These error bars are displayed in the data.

*2 $COMBINED = \sqrt{(MEASUREMENTAL)^2 + (REFRACTION)^2}$

ERROR BARS ON SPATIAL MEASUREMENTS

TABLE 3-1

the streaked $2\omega_0$ and $(3/2)\omega_0$ images. The temporal resolution of the streak camera in the mode it was run during the experiment is approximately 10 psec.

Low signal to noise ratios affect the results in that to obtain an adequate signal for the trajectory and scalelength data, the region scanned on the photograph has to have a certain area. To avoid reducing spatial resolution, the signal to noise ratio can be increased only at the expense of temporal resolution. Adequate signal to noise ratios are achieved at the equivalent of 15 psec temporal resolution. The overall temporal resolution of the trajectory and scalelength measurements is 18 psec so that the error bars on the measurement are ± 9 psec.

Since the $2\omega_0$ and $(3/2)\omega_0$ signals are focused onto the streak camera along different optical paths it is necessary to check the timing difference. This is done by replacing the $(3/2)\omega_0$ filter with a $2\omega_0$ filter so that for a test shot two $2\omega_0$ streaks are obtained. The timing difference can then be measured to within approximately ± 3 psec.

When the data was first analyzed it was found that the critical surface always started at the initial target radius. From this it was assumed that the start of the plasma emissions coincided with the start of the laser pulse. Later on, when the intensity histories of the plasma emissions were compared to the incident pulse it was found that the best correlation did not always occur when the start of plasma emissions was made to coincide with the start of the laser

pulse. A maximum discrepancy of 40 psec delay for the start of the plasma emission was observed when the data was positioned for optimum intensity correlation.

4. Experimental Procedure

In this chapter a particular shot, #11534, is taken and reduced according to the procedure applied to all of the experimental $2\omega_0$ and $(3/2)\omega_0$ data.

Prior to a series of shots the four laser beams are focused onto a CD_2 test target. Once the laser system is aligned, the CD_2 sphere is illuminated with a high pressure mercury arc lamp. The target appears as a bright sphere and it is on this that the $2\omega_0 - (3/2)\omega_0$ optical system is aligned and focused.

An absolute spatial reference is provided for in the $2\omega_0$ and $(3/2)\omega_0$ time integrated photographs with a graticule in the eyepiece prior to the $2\omega_0 - (3/2)\omega_0$ beam-splitter (fig. 3-1). For the time resolved data, the plasma axis to be spatially resolved is centered on the streak camera slits and a picture of the two CD_2 target images is taken with the streak camera in focused mode. It is also found that the $2\omega_0$ streaked image, and the $(3/2)\omega_0$ streaked image when the emissions start within 25 psec of one another, has an initial diameter equal to that of the target. Individual critical and quarter-critical surface trajectories can, therefore, be obtained.

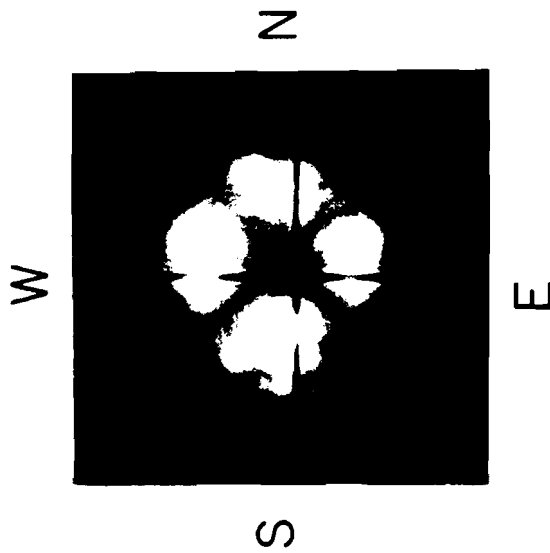
Figure 4-1 shows the plasma emission data obtained for the shot. The time integrated photograph shows the $2\omega_0$ plasma emission generated from each of the four laser beams. The streak photograph shows the incident pulse (ω_0) followed by the $2\omega_0$ and $(3/2)\omega_0$ images. The streaked plasma emission images correspond to a $5\ \mu\text{m}$ wide strip of plasma along the south-north laser beam axis.

FIGURE 4-1

HARMONIC EMISSION PHOTOGRAPHS

SHOT 11534

SN SN



150 μm

TIME INTEGRATED

$2\omega_0$



150 μm

TIME RESOLVED

$\omega_0, 2\omega_0, (3/2)\omega_0$

TIME

$(3/2)\omega_0$

500 psec

$2\omega_0$

INCIDENT PULSE

ω_0

The data is reduced using a one-dimensional "flying spot" microdensitometer. Figure 4-2 is a microdensitometer scan of the $2\omega_0$ time integrated photograph along the south-north axis. The microdensitometer slit dimensions correspond at the plasma to $2\ \mu\text{m}$ by $4\ \mu\text{m}$ parallel and perpendicular to the scan direction. To within the accuracy of the measurement ($\pm 3\ \mu\text{m}$) each point along the scan corresponds to a point at the plasma. The outer edges of the $2\omega_0$ emission pattern are the peak critical surface excursions. The steep density fall-off near the outer edges is limited by the system spatial resolution. In this scan, the steep fall-off occurs over a $9\ \mu\text{m}$ distance and is almost equal to the $8\ \mu\text{m}$ spatial resolution of the system (section 3.3.2). Peak excursion measurements are calculated according to the image analysis procedure of section 3.3.4.

The time resolved trajectories are obtained by making multiple scans (~ 100 per shot) along the spatial axis of the streak photograph. The scans are separated by 6 psec. The microdensitometer slit dimensions corresponded to $5\ \mu\text{m}$ by 15 psec.

Figure 4-3 shows a typical scan and the procedure for data reduction. With the scans along the spatial dimension, an arbitrary but absolute reference axis for the spatial coordinate is affixed to the traces with the microdensitometer. This reference axis corresponds, in figure 4-3, to the left hand edge of the trace. All spatial measurements are made with respect to this axis. With the target center locations on the $2\omega_0$ and $(3/2)\ \omega_0$ streaked image known, the critical and quarter-critical surface locations are computed (figure 4-4).

FIGURE 4-2
**TIME INTEGRATED $2\omega_0$
MICRODENSITOMETER TRACE**

11534

SOUTH

NORTH

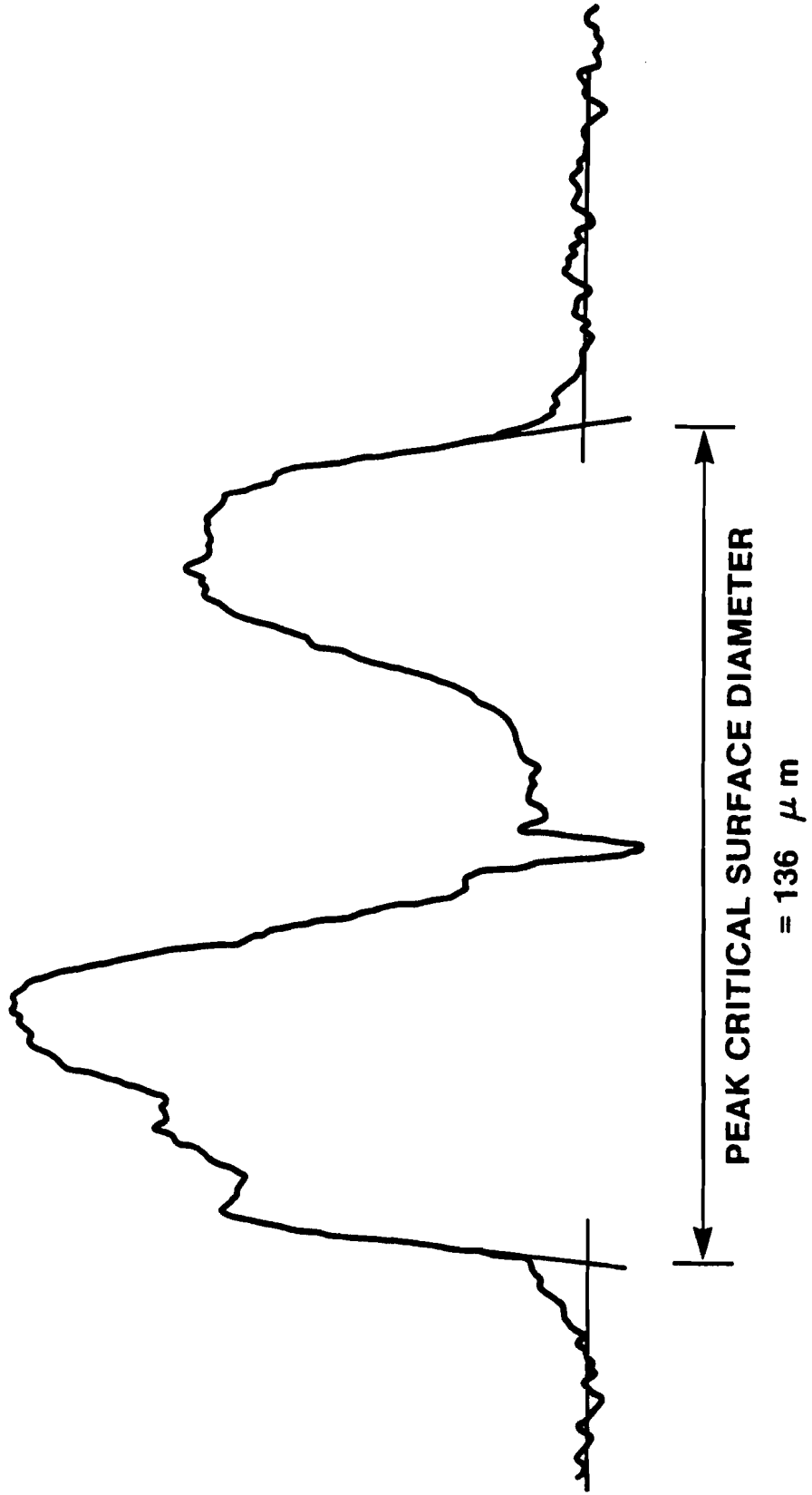


FIGURE 4-3
STREAKED DATA MICRODENSITOMETER TRACE

SCAN #36 $t_{2\omega} = 98$ psec, $t_{3/2\omega} = 55$ psec

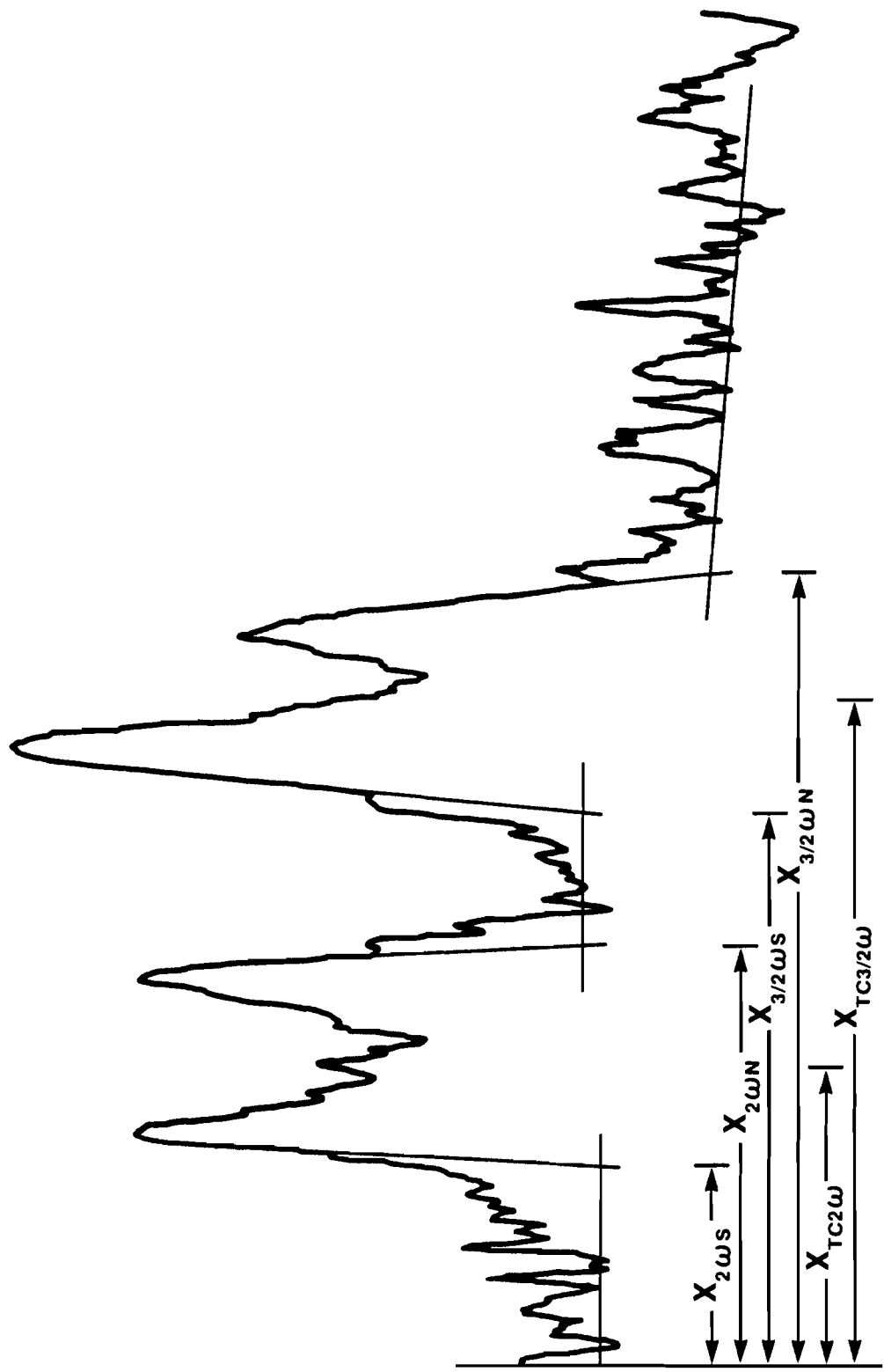
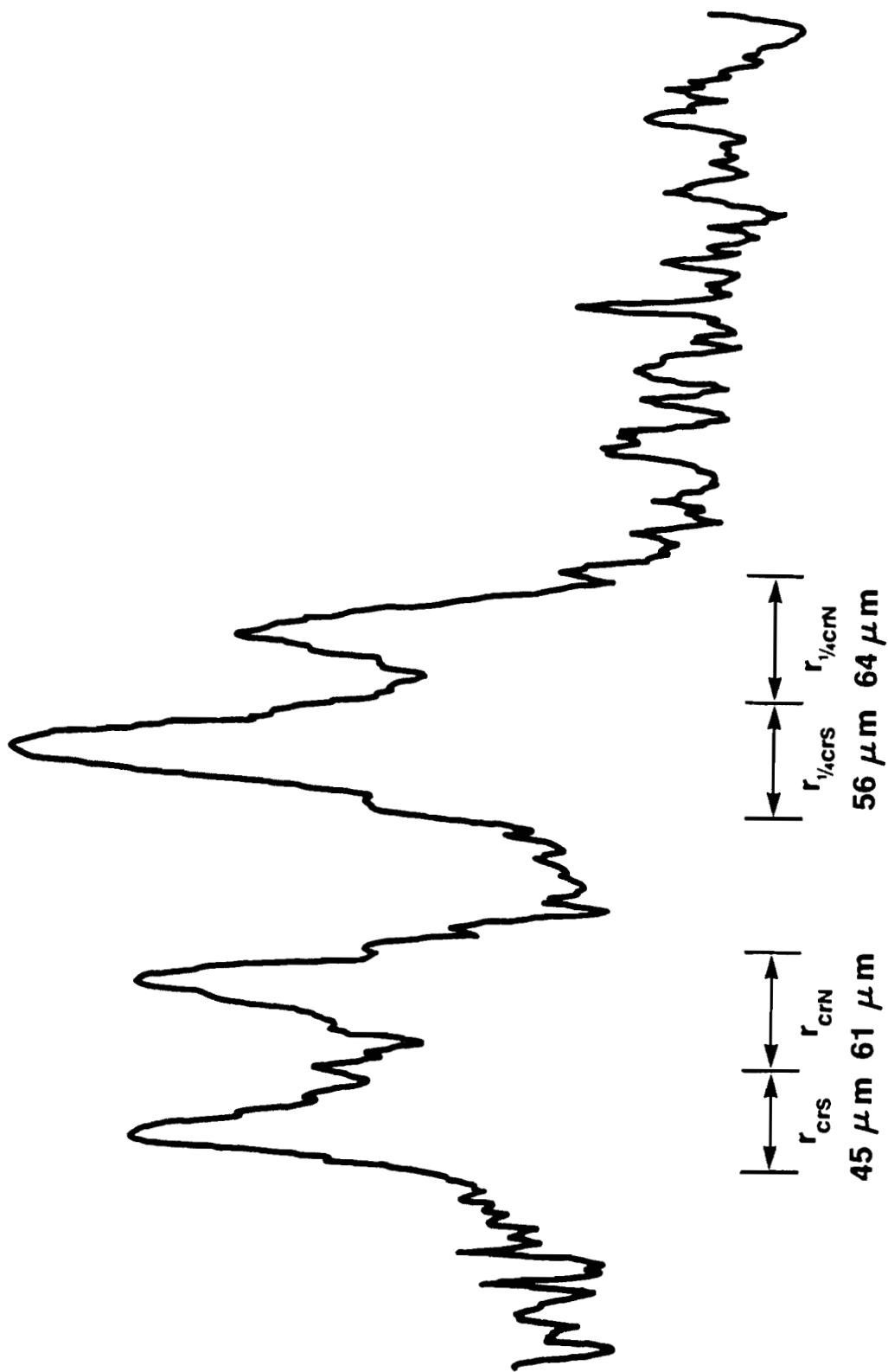


FIGURE 4-4
STREAKED DATA MICRODENSITOMETER TRACE

SCAN #36 $t_{cr} = 98$ psec, $t_{1/4cr} = 55$ psec



It should be noted that a significant amount of noise and base density shift is present in the streak photographs. These are the significant sources of error that remain in the results after image analysis has been performed.

Time along the streaks at each microdensitometer scan is different for the $2\omega_0$ and $(3/2)\omega_0$ images. This is because of a path length difference in the $2\omega_0$ and $(3/2)\omega_0$ arms (figure 3-1). The time difference is determined during a test shot when the $(3/2)\omega_0$ filter is replaced by a $2\omega_0$ filter and two identical images are photographed through the streak camera.

Data from the scans is collated and reduced according to the image analysis procedure of section 3.3.4. A polynomial least squares curve fit to the data is then made. Fourth order fits appear to give good results (figures 4-5,6). Only a small decrease in the curve fit standard deviation occurs for fits between fourth and tenth orders. The standard deviation is typically around $\pm 4 \mu\text{m}$. Scale-lengths are computed as the difference between the critical and quarter-critical surface trajectory curve fits.

FIGURE 4-5
CRITICAL SURFACE TRAJECTORY
11534 NORTH

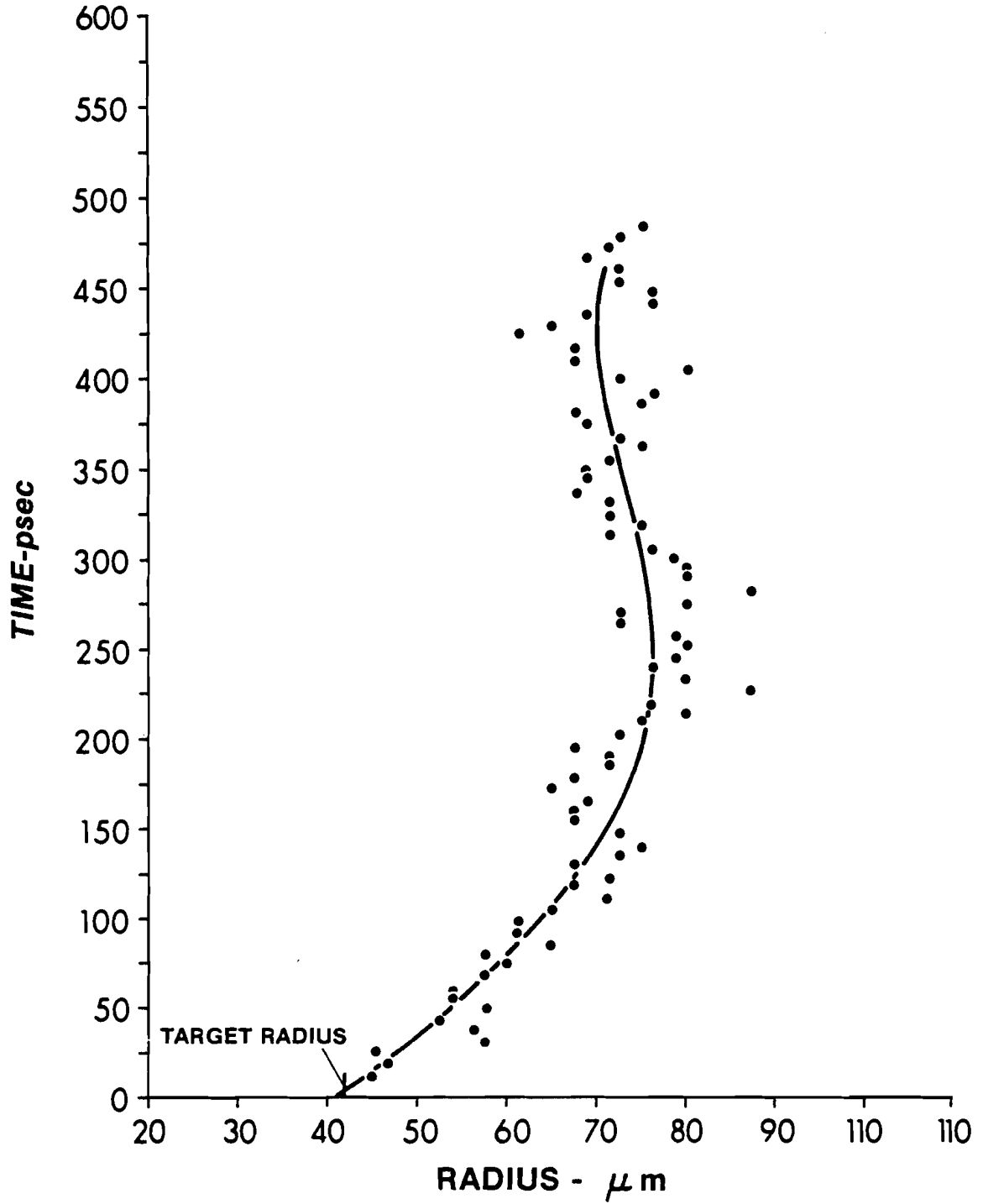
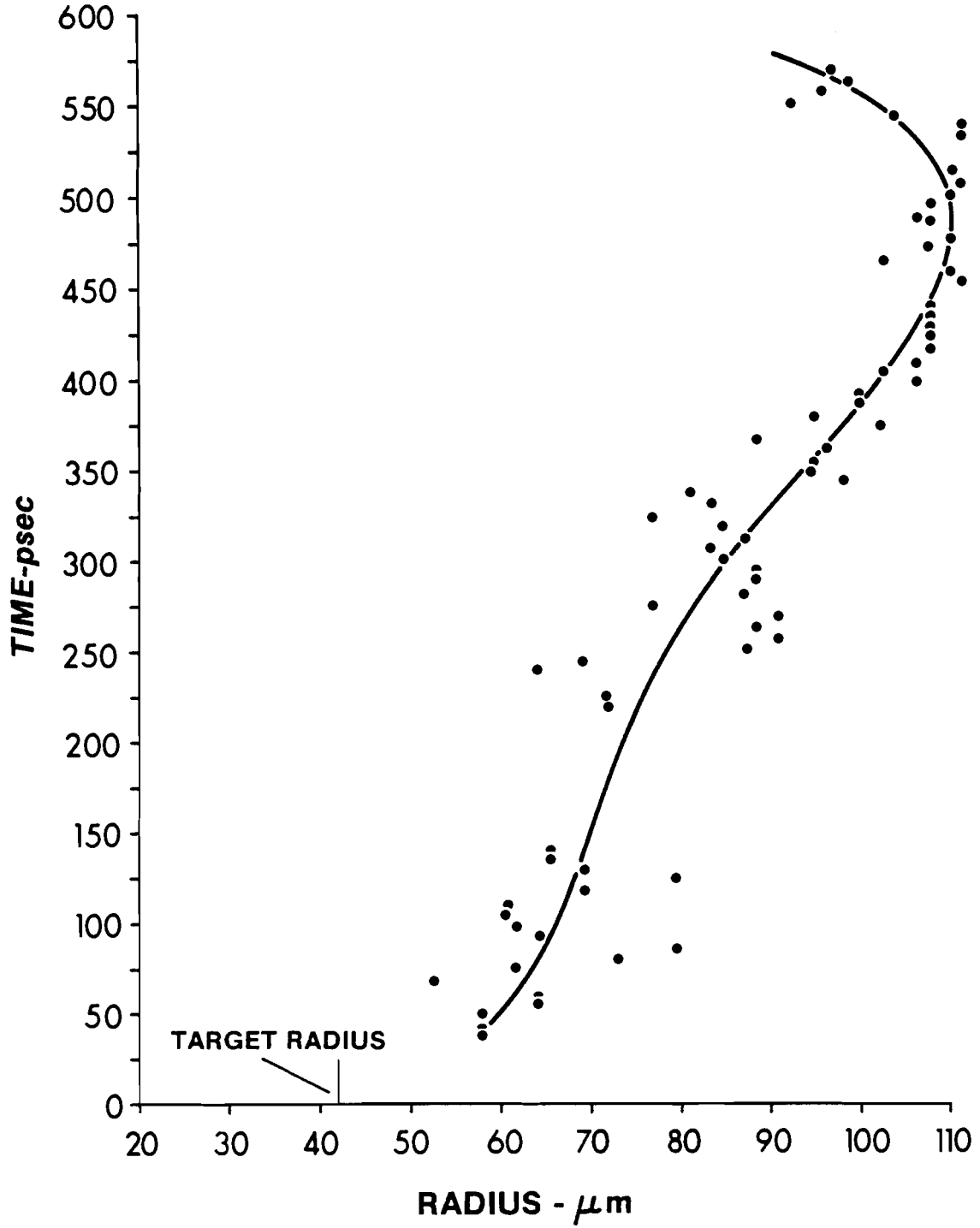


FIGURE 4-6
QUARTER-CRITICAL SURFACE TRAJECTORY
11534 NORTH



5. Experimental Results

Data obtained in the experiment is presented in this chapter. The $2\omega_0 - (3/2)\omega_0$ data is of two kinds: time integrated with two-dimensional spatial resolution from which peak excursion information is obtained, and time resolved with spatial resolution along one plasma dimension from which critical and quarter-critical surface trajectories are determined. The data is presented in section 5.1. In section 5.2 are shown the correlations between experimental parameters used in chapter 6.

5.1 Experimental Data

Table 5.1 summarizes the data obtained in the experiment. Included are the $2\omega_0 - (3/2)\omega_0$ results and the results of other diagnostics. All of the shots show, from the $2\omega_0$ data, well focused beams on target. The data is split up into four groups: A, B, C, and D.

Group A consists of shots in which $2\omega_0 - (3/2)\omega_0$ time integrated data was obtained and for which the laser was not severely overdriven ($P_{\text{Laser}} \lesssim .2 - .25 \text{ tw}$). At these power levels the laser beam was not subject to significant breakup.⁽⁵⁻¹⁾ The energy on target was approximately a constant fraction of the laser output, i.e., $E_{\text{Target}} \approx .7 E_{\text{Laser}}$.⁽⁵⁻²⁾ Energy absorbed by the plasma was measured and the fractional absorption was calculated. This group provided experimental data for absorption studies.

Group B consists of shots where $2\omega_0 - (3/2)\omega_0$ time integrated data was obtained but for which the laser was overdriven and the un-

Shot	T _{FWHM}	T _{RISE} 10%-Max	Single Pulse	E _{Laser}	P _{Laser}	E _{ABS}	n _{ABS}	T _e	r _{Target}	Δr _{Target}	<p _{cr} >	<p _{3cr} >	<L>
9902	470±20psec	~20psec	*	73±.5joules	.16TW	18joules	.35	.8±.1kw	52μm	1.3μm	14.5±3μm	29.5±3μm	15.0±4μm
9904	276	-	*	64	.23	13	.29	.9	52	1.4	16.0	26.0	10.0
9905	~350	-	*	87	.25	23	.38	1.0	60	1.0	15.0	27.5	12.5
9912	414	-	*	59	.14	20	.48	.8	52	1.0	8.0	25.5	17.5
9914	480	-	*	91	.19	36	.57	.8	52	1.6	13.0	37.0	24.0
9915	235	-	*	83	.17	14	.24	.8	55	1.4	7.0	13.0	6.0
9916	550	-	*	83	.15	31	.53	.8	46	1.3	9.5	33.0	23.5
10321	440	-	*	119	.20	38	.46	1.0	56	-	18.0	37.0	19.0
9901	~350	-	-	114	.33	23	.9	.9	47	1.0	23.5	40.0	16.5
10039	250	-	*	90	.36	9	.29	1.0	38	-	4.0	9.0	5.0
10040	270	-	*	107	.40	11	.9	.9	42	-	5.0	13.0	8.0
10041	380	-	*	103	.27	9	.40	.9	40	-	11.5	19.5	8.0
10355	340	-	*	120	.35	17	.20	-	48	1.4	9.5	24.5	15.0
10356	250	-	*	120	.39	20	.52	.8	52	1.3	7.5	16.5	9.0
10359	356	-	*	120	.34	22	.46	-	52	-	20.0	37.0	7.0
11482	332	60	2 beams	20	.06			-	42	1.3	15.0	-	-
11534	355	232	*	78	.22			.9	42	.8	24.0	-	-
11546	470	135	*	30	.073			1.0	44	.8	23.0	-	-
11550	160	200	*	30	.19			-	42	.8	25.0	-	-
11564	235	80	*	27	.11			.8	41	.7	15.0	-	-
11565	110	80	*	36	.33			1.2	42	.8	18.0	-	-
11566	218	80	*	13	.060			1.2	42	.8	14.0	-	-
11568	238	170	*	35	.15			-	42	1.0	19.0	-	-
11570	258	180	*	46	.18			1.0	44	.8	20.0	-	-
11571	275	100	*	58	.21			1.0	42	.8	14.0	-	-
11709	250	45	*	31	.12			1.0	36	1.0	8.0	-	-
11710	240	120	*	35	.15			.8	49	1.0	22.0	-	-
11711	230	35	*	48	.21			.8	43	1.6	6.0	-	-
11713	260	65	*	37	.14			.9	40	1.0	12.0	-	-
11051	370	250	*	40	.11			.7	47	1.0	21.0	-	-
11862	490	110	*	94	.19			.8	45	.8	18.0	-	-
11951	300	90	*	67	.22			.8	44	1.1	13.0	-	-
11963	250	100	*	46	.18			1.0	50	1.1	15.0	-	-
11099	480	2 beams	*	40	.08			1.0	53	.8	27.0	-	-

SUMMARY OF DATA
TABLE 5 - 1

certainty in the energy on target was large. Time integrated $2\omega_0 - (3/2)\omega_0$ data from groups A and B was used to obtain a correlation between the peak critical and quarter-critical surface excursions.

Group C consists of shots in which accurate laser pulse rise time and peak critical surface excursion data was obtained. A correlation between these two quantities was observed. Streaked $2\omega_0 - (3/2)\omega_0$ data was also obtained for shots within group C. The shots where complete trajectories were determined are 11534, 11570, 11709, and 11710.

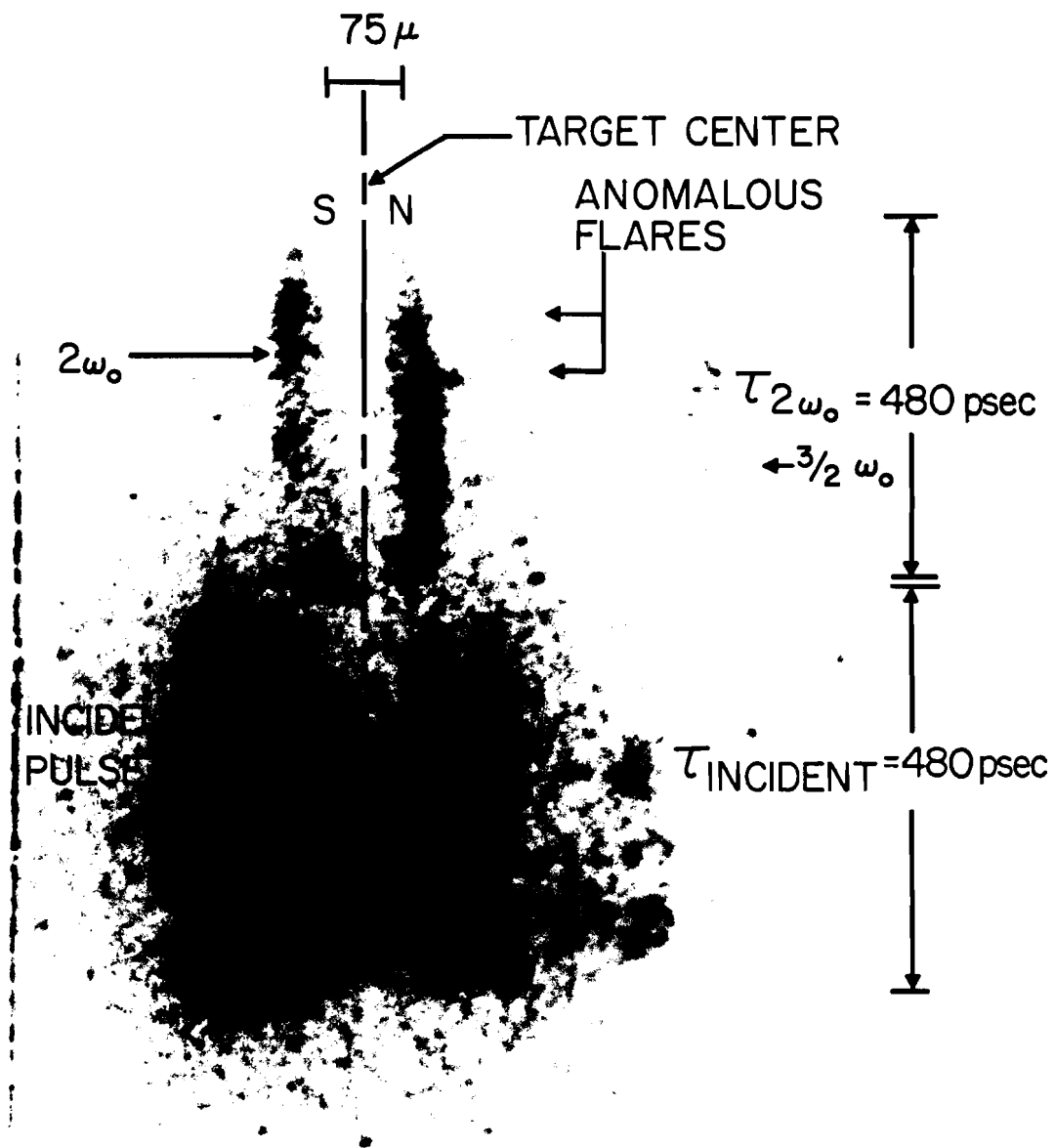
Group D consists of a single shot in which a $2\omega_0$ trajectory was determined but for which accurate rise time data was not obtained. It is included because "flares" occurred during this shot. (See figure 5-1.)

Flares in the $2\omega_0$ and $(3/2)\omega_0$ emissions were observed during two shots: 11099 (group D) and 11709 (in group C). These were short duration extensions of the light patterns beyond the relatively smooth outer edges of the emitting surface trajectories. The flares lasted for less than 50 psec and had lengths of up to 50 μm . Flares did not occur simultaneously in the plasma emissions recorded from opposing beams nor were they observed to simultaneously occur at the two harmonic frequencies.

To briefly explain the column headings of table 5-1: 'Shot' gives the standard laser shot reference number for data from the Laboratory for Laser Energetics four beam laser system. ' T_{FWHM} ' is the laser pulse duration given by the pulse full-width at the

FIGURE 5-1

STREAKED IMAGE SHOT 11099



half-maximum intensity level. ' $T_{\text{Rise 10\%-Max}}$ ' is the time it takes for the laser pulse intensity to increase from the 10% of maximum intensity level to the peak intensity point. 'Single Pulse' indicates whether only a single pulse was switched out of the laser oscillator. Shots with other than four beams on target are so indicated in this column. ' P_{Laser} ' is the laser power calculated by $P_{\text{Laser}} = E_{\text{Laser}}/T_{\text{FWHM}}$. ' E_{ABS} ' is the energy absorbed by the plasma as determined from Faraday cup ion collectors⁽⁵⁻³⁾ but normalized to charge calorimeters.⁽⁵⁻⁴⁾ ' η_{ABS} ' is the fractional absorption calculated by $\eta_{\text{ABS}} = E_{\text{ABS}}/(.7E_{\text{Laser}})$. ' T_e ' is the corona plasma temperature obtained from x-ray measurements.⁽⁵⁻⁵⁾ ' r_{Target} ' is the shell radius and ' Δr_{Target} ' is the thickness of the shell wall. ' $\langle p_{\text{cr}} \rangle$ ' and ' $\langle p_{\frac{1}{4}\text{cr}} \rangle$ ' are the critical and quarter-critical surface peak excursions obtained for each shot by averaging the peak excursions along the four laser beam axis. ' $\langle L \rangle$ ' is the characteristic plasma density scalelength defined as $L \equiv p_{\frac{1}{4}\text{cr}} - p_{\text{cr}}$.

Figures 5-2 to 5-17 show the streaked data for shots 11099, 11534, 11570, 11709, and 11710. Where data was obtained, streaked critical and quarter-critical surface trajectories, scalelengths, and laser pulse histories are shown. In examining the trajectories and scalelengths the accuracy of the measurement should be kept in mind. In particular, small scalelength (positive or "negative") of several microns are zero scalelength to within the accuracy of the measurement ($\Delta l = \pm 6 \mu\text{m}$).

5.2 Experimental Correlations

Figures 5-18,19,20 show correlations between experimental parame-

FIGURE 5-2
CRITICAL SURFACE TRAJECTORY
11099 NORTH

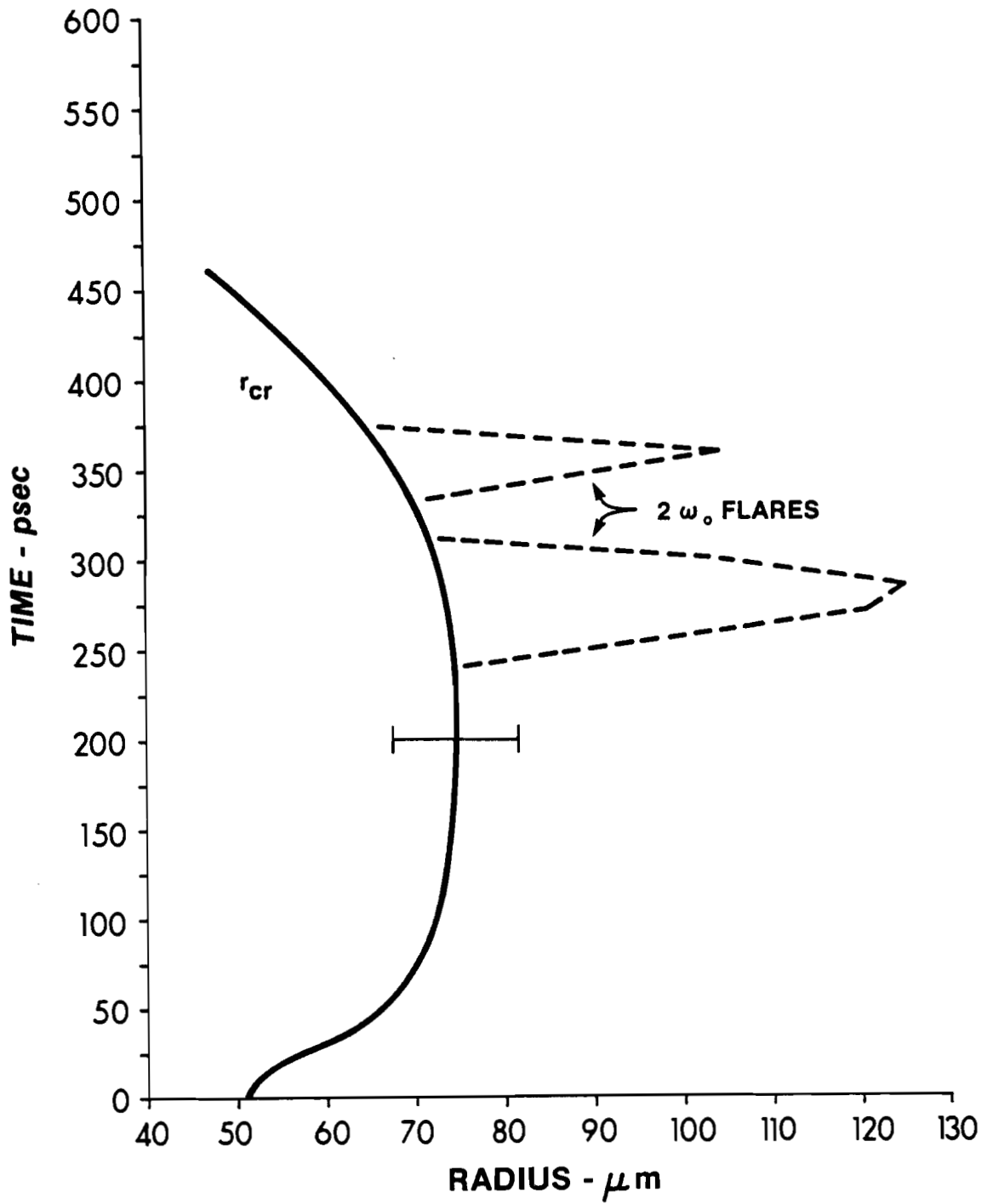


FIGURE 5-3
TRAJECTORIES
11534 SOUTH

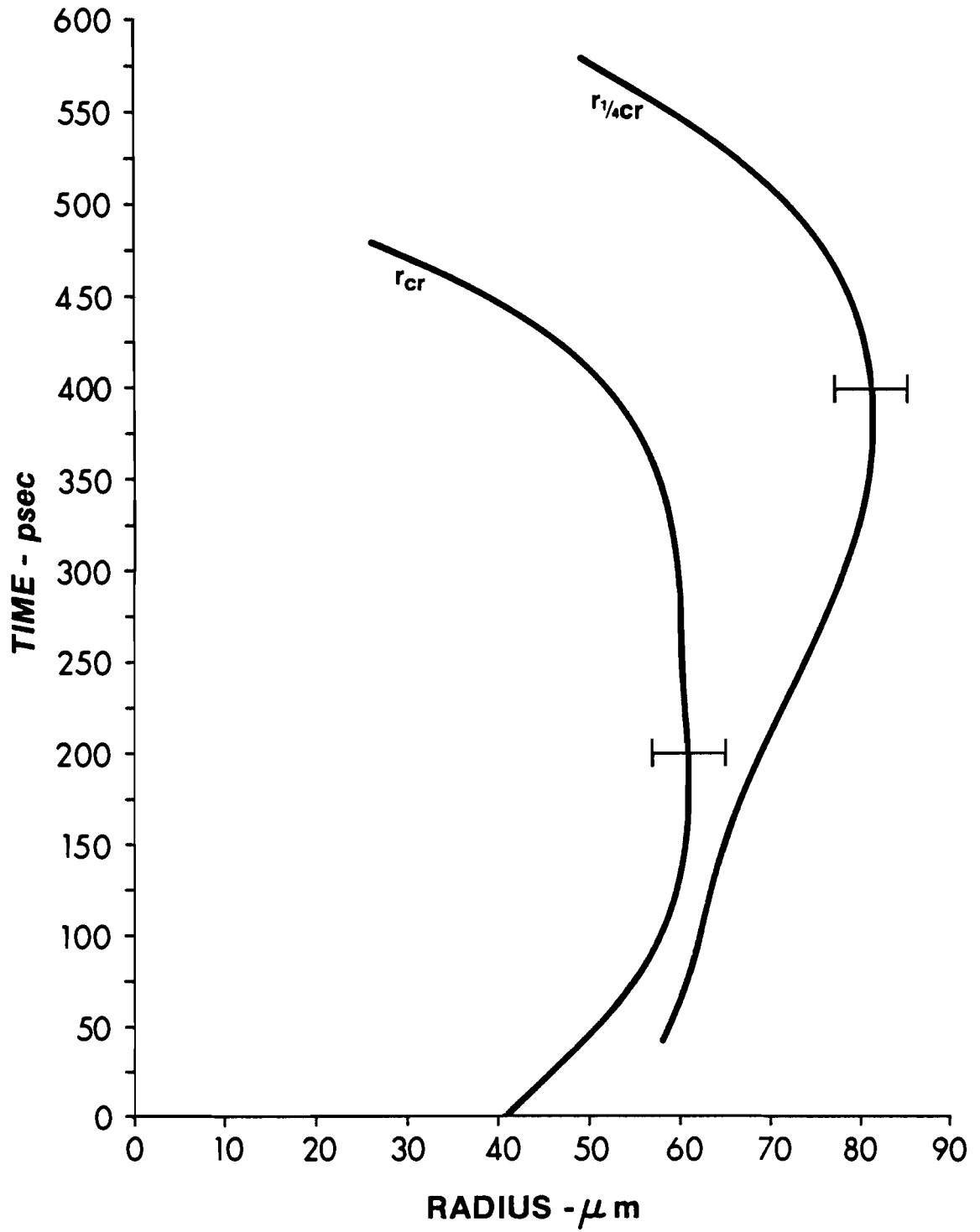


FIGURE 5-4

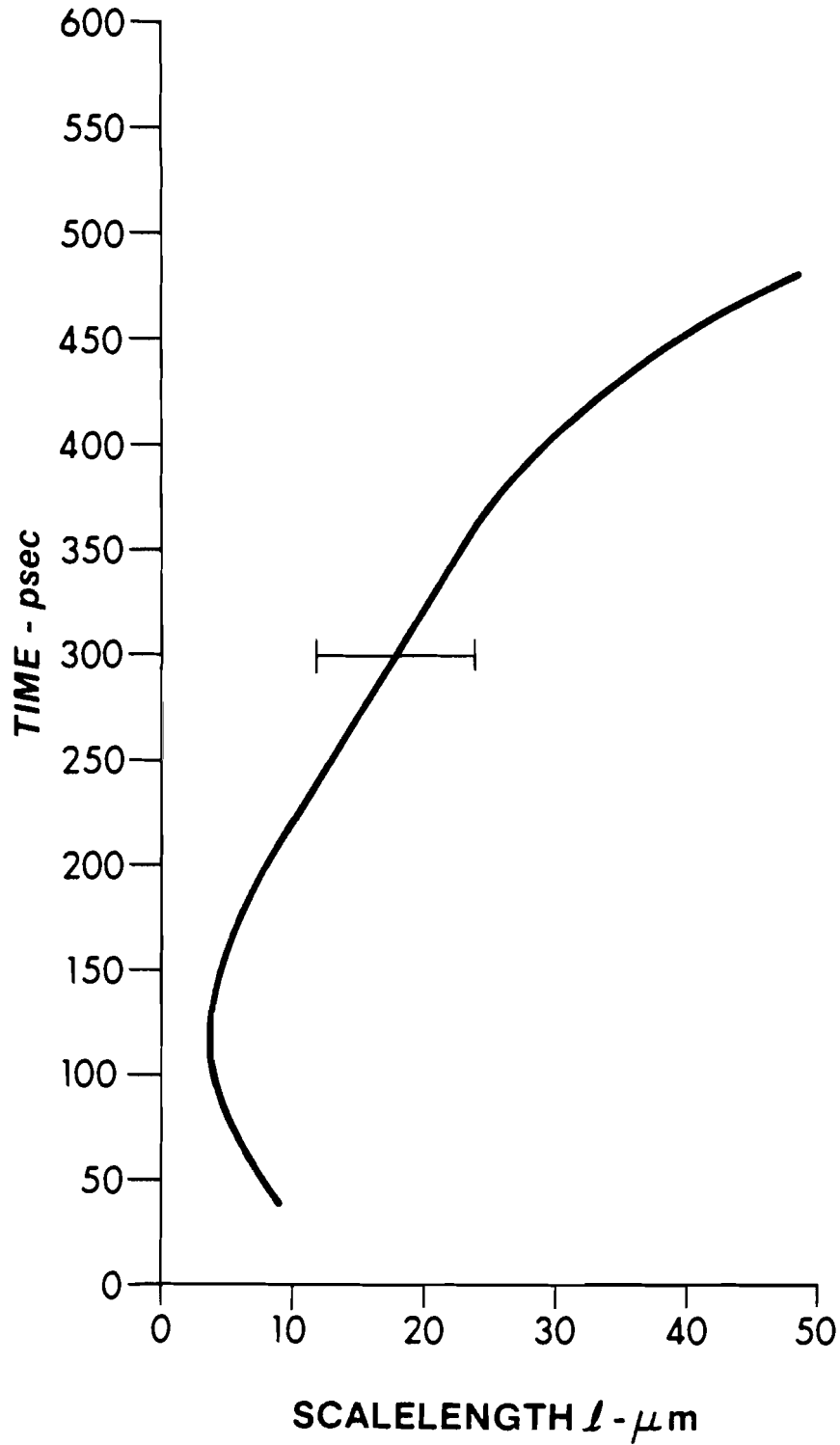
**TIME RESOLVED SCALELENGTH
11534 SOUTH**

FIGURE 5-5
TRAJECTORIES
11534 NORTH

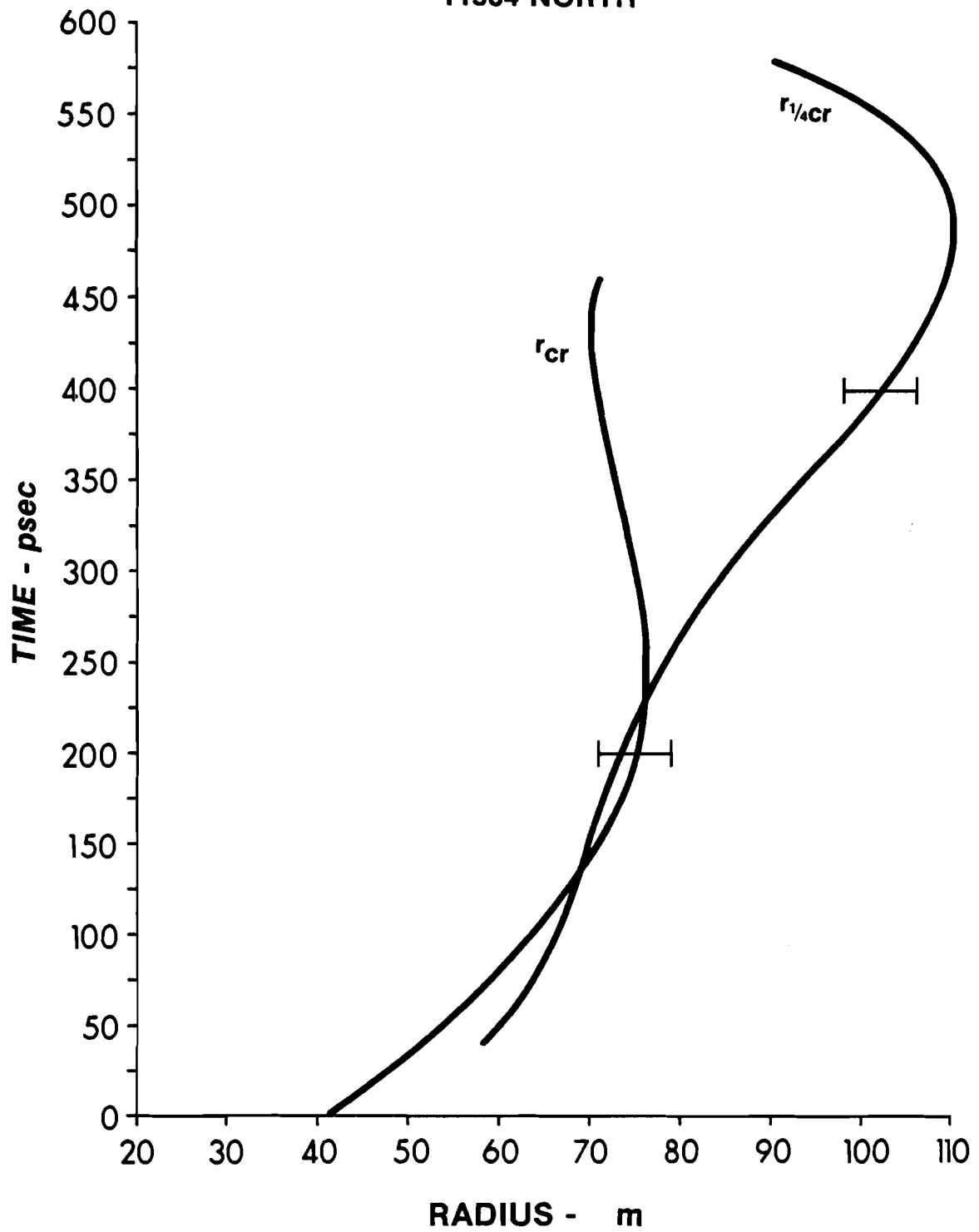


FIGURE 5-6

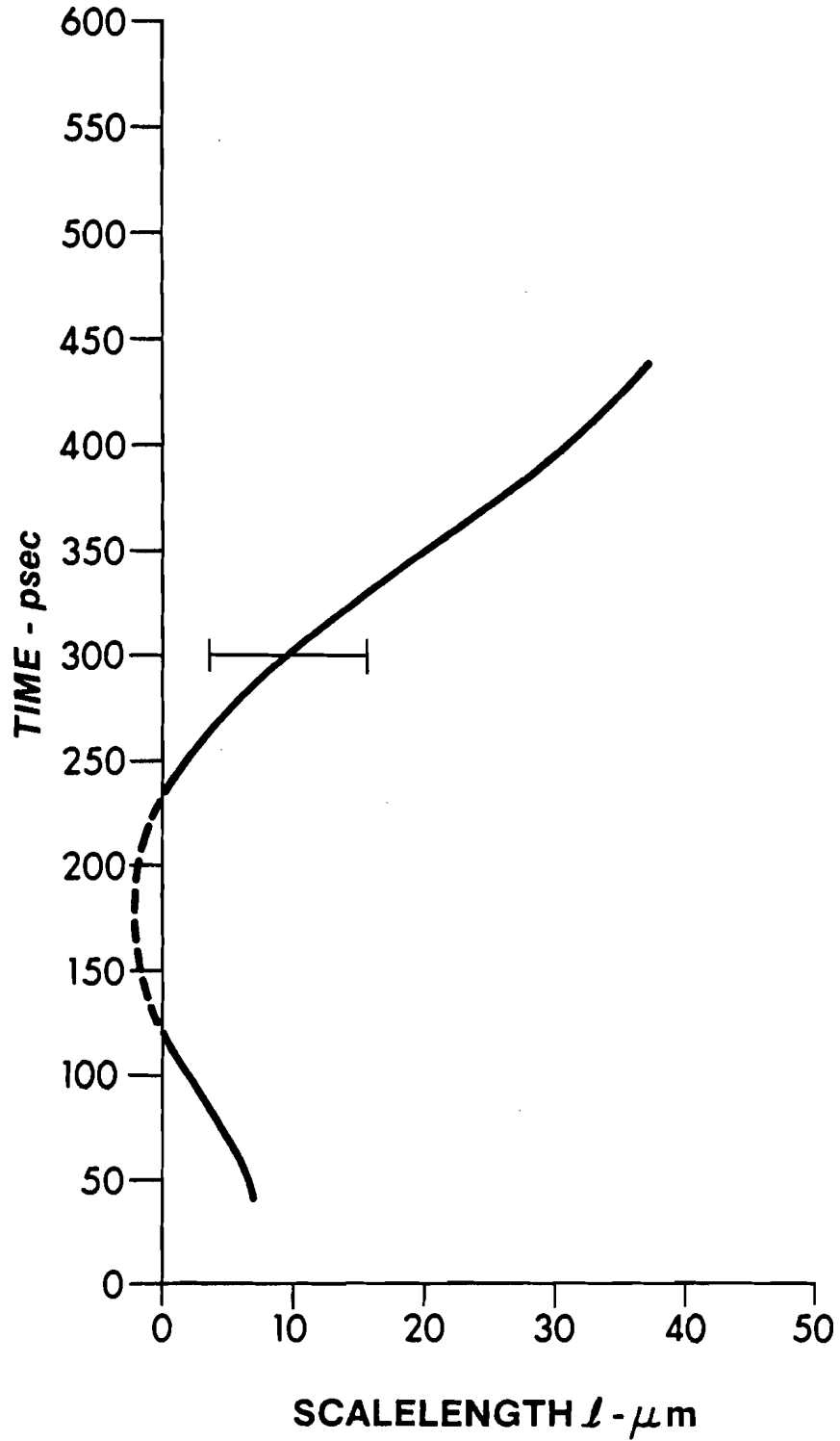
**TIME RESOLVED SCALELENGTH
11534 NORTH**

FIGURE 5-7
INCIDENT PULSE
11534

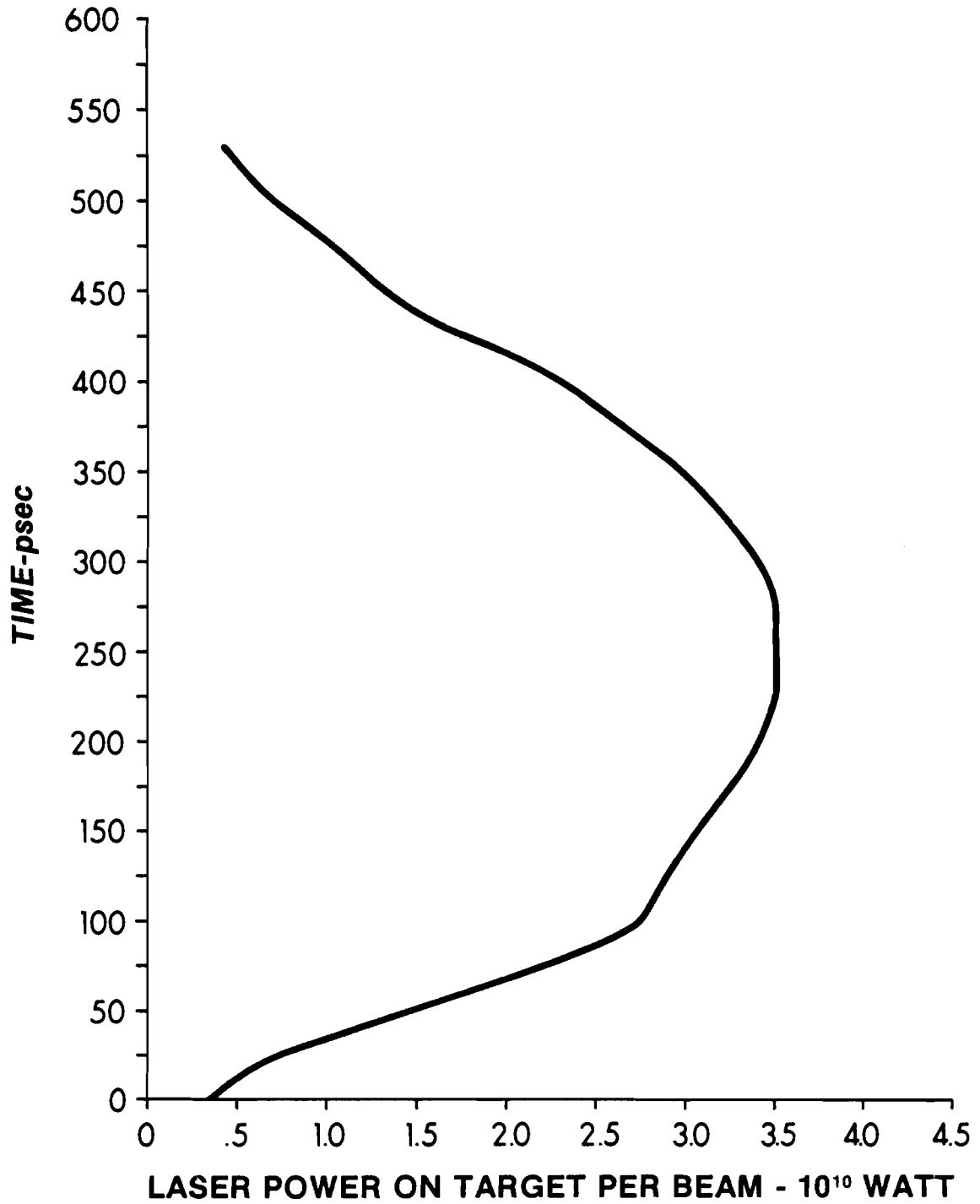


FIGURE 5-8

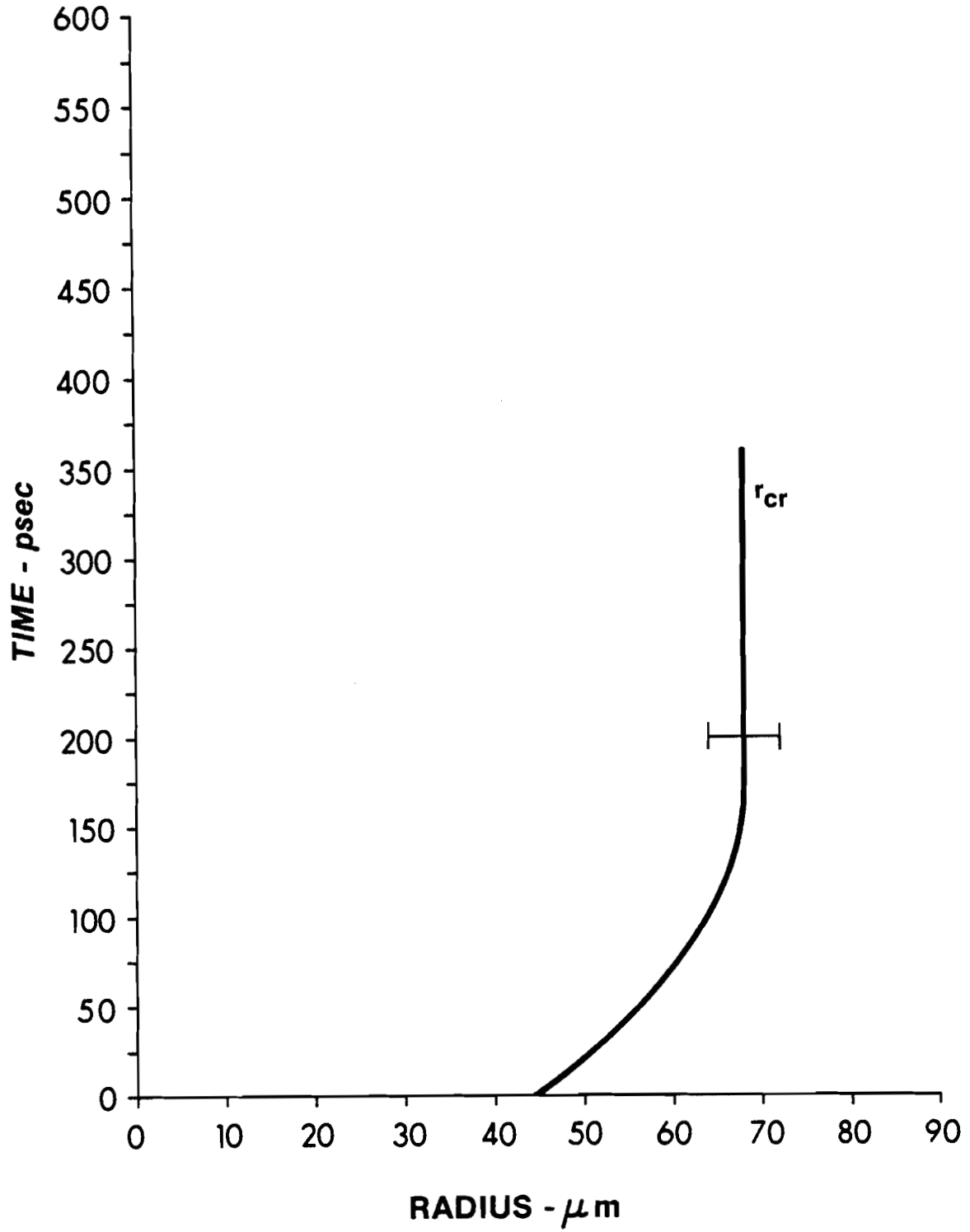
**CRITICAL SURFACE TRAJECTORY
11570 SOUTH-NORTH AVERAGE**

FIGURE 5-9
INCIDENT PULSE
11570

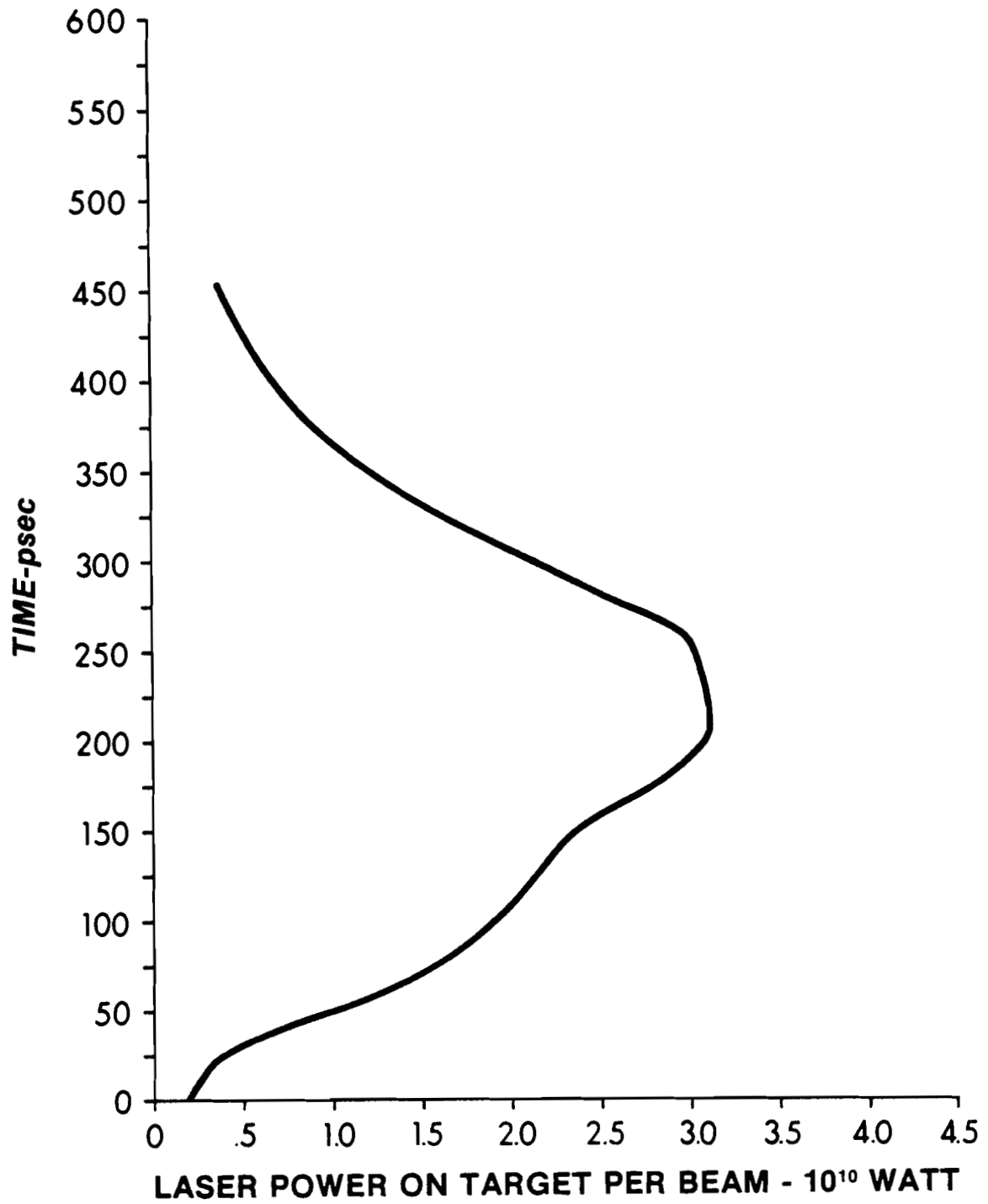


FIGURE 5-10
TRAJECTORIES
11709 SOUTH

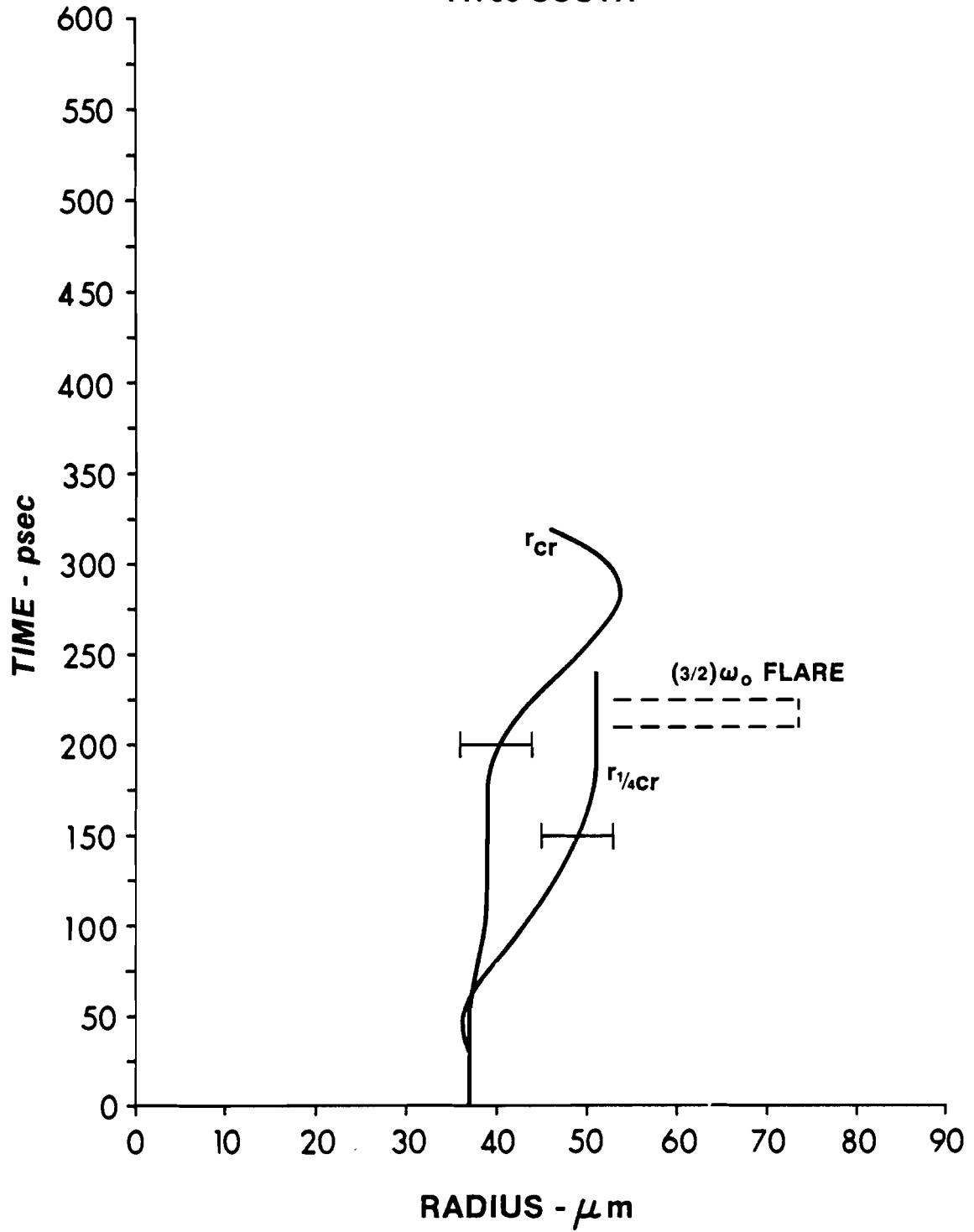


FIGURE 5-11
TIME RESOLVED SCALELENGTH
11709 SOUTH

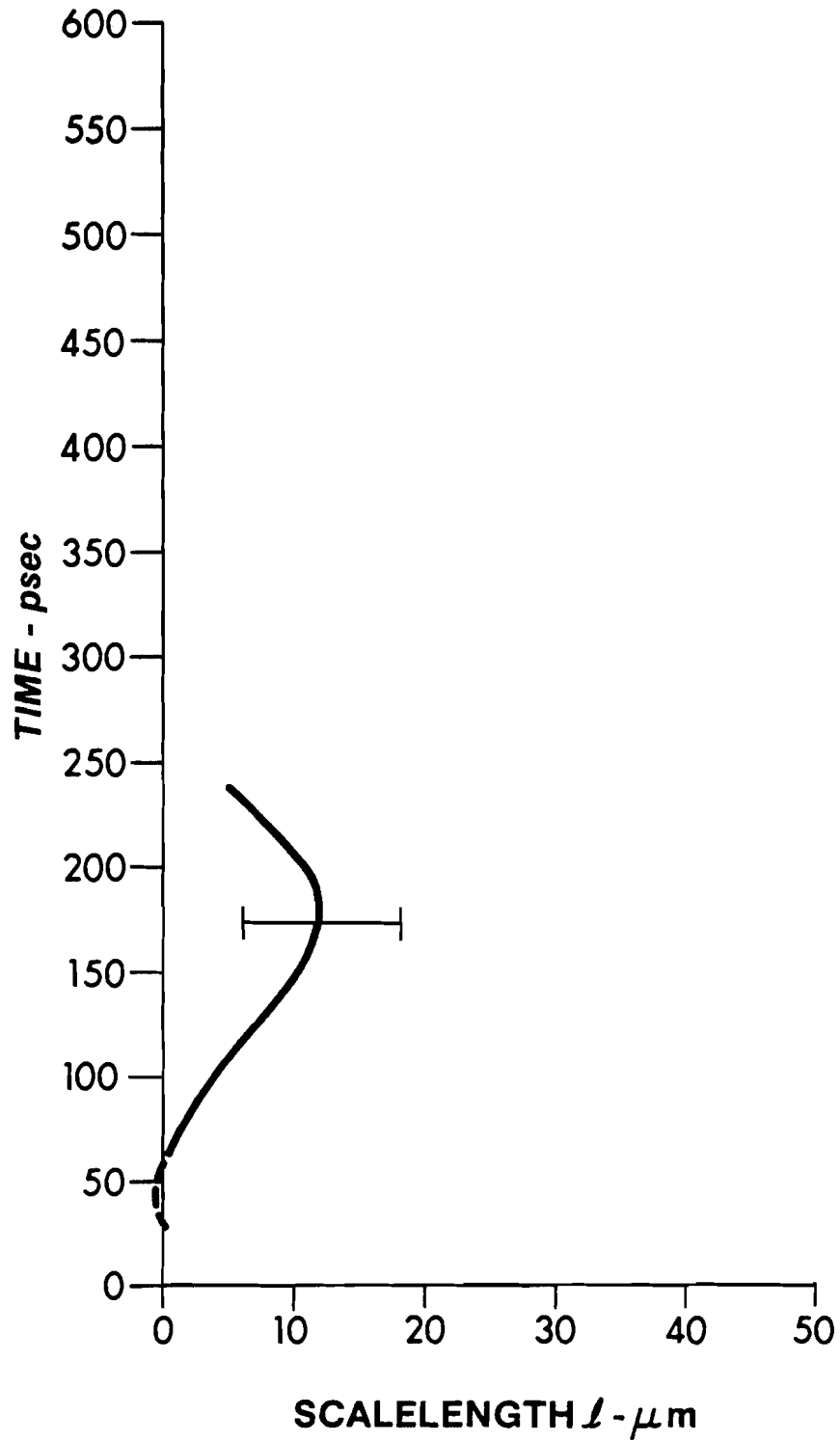


FIGURE 5-12
INCIDENT PULSE
11709

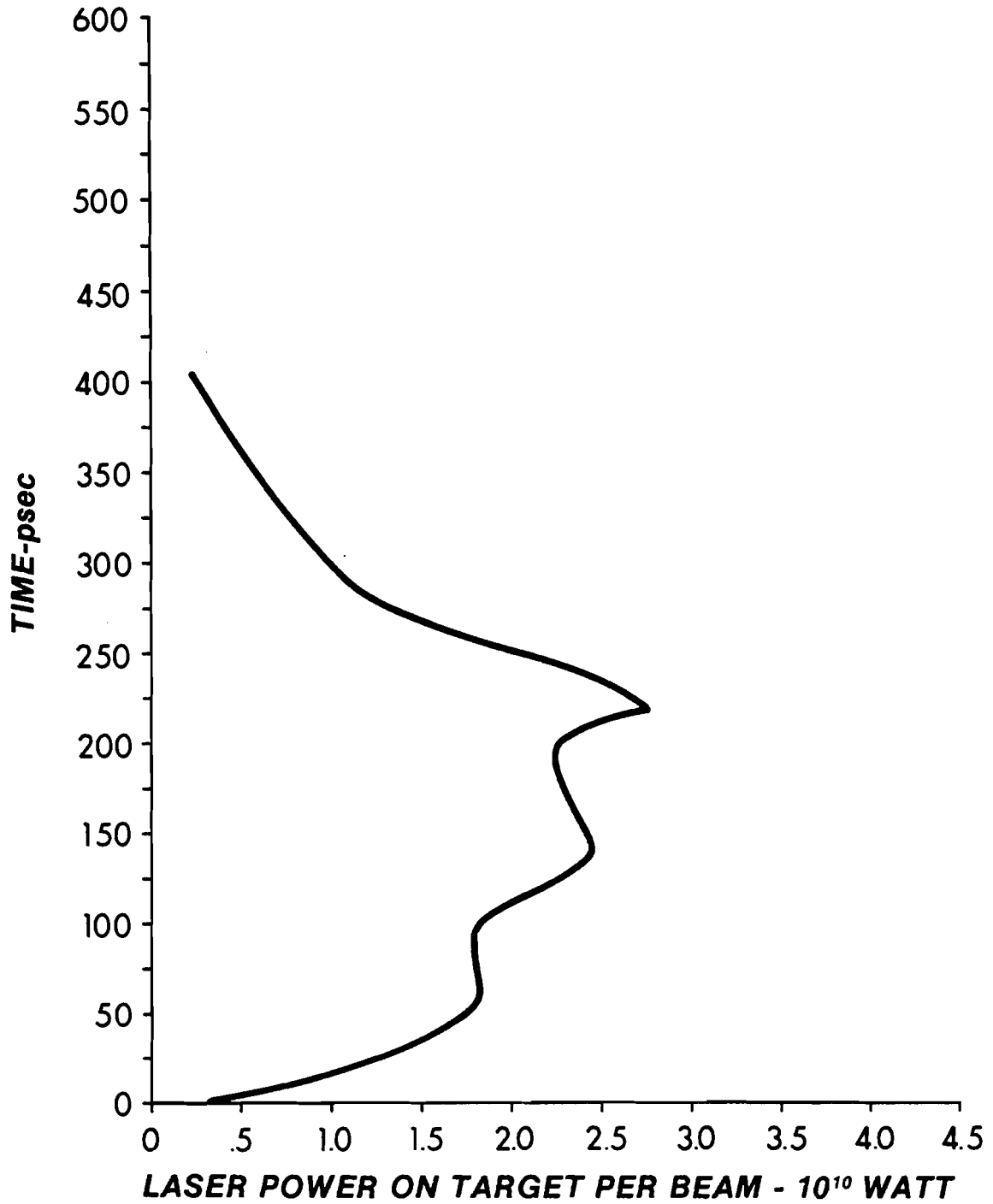


FIGURE 5-13
TRAJECTORIES
11710 SOUTH

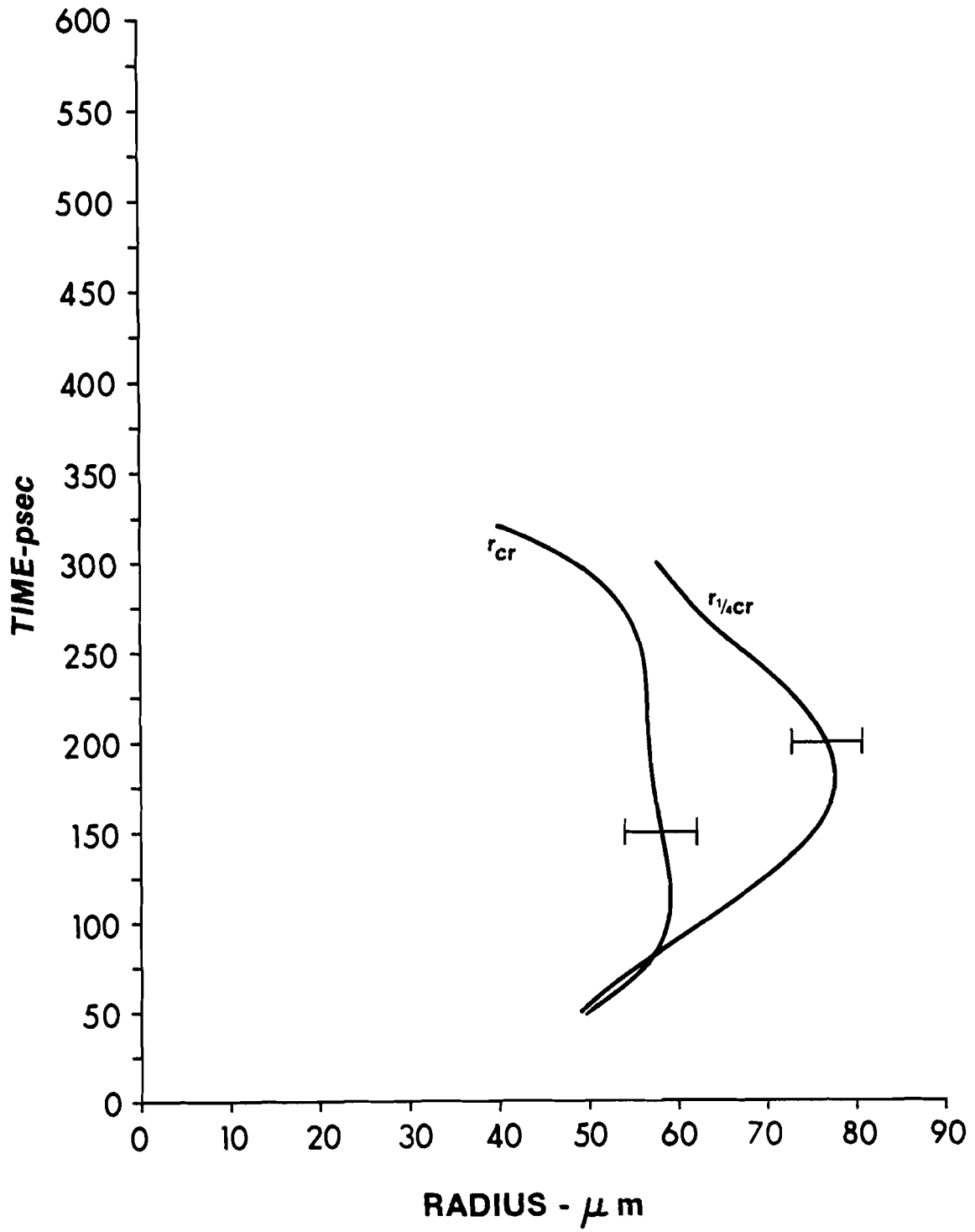


FIGURE 5-14
TIME RESOLVED SCALELENGTH
11710 SOUTH

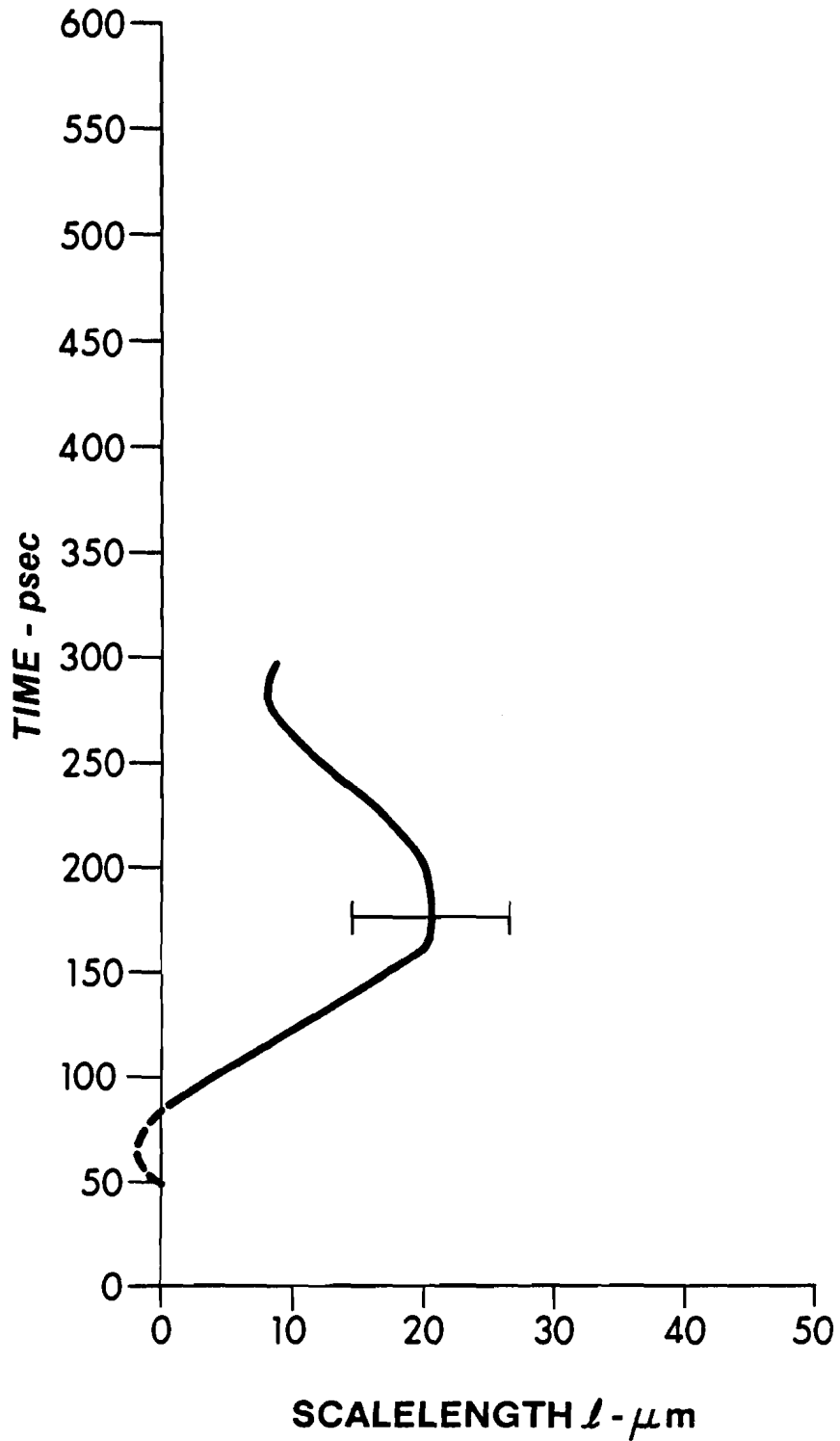


FIGURE 5-15
TRAJECTORIES
11710 NORTH

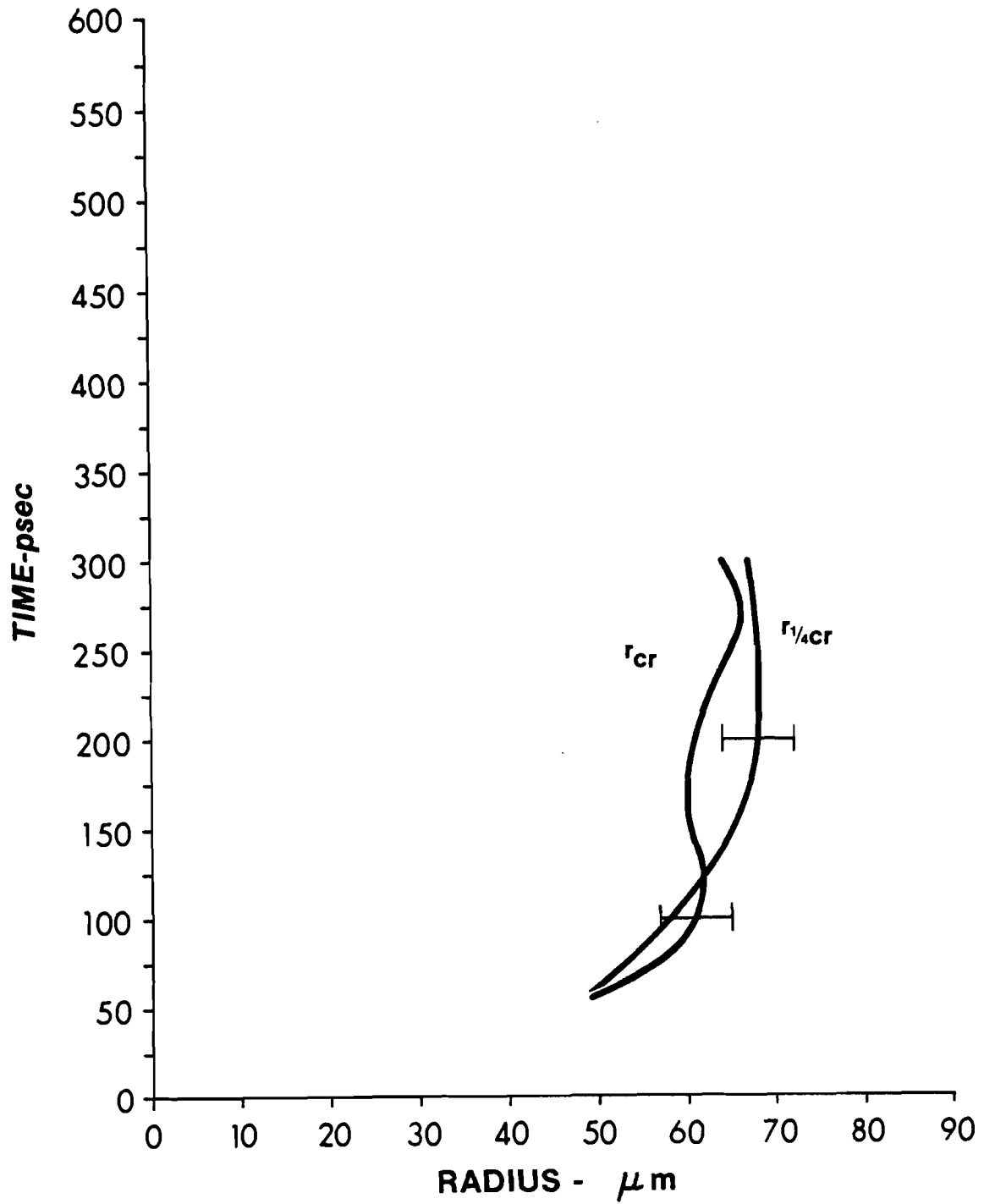


FIGURE 5-16
TIME RESOLVED SCALELENGTH
11710 NORTH

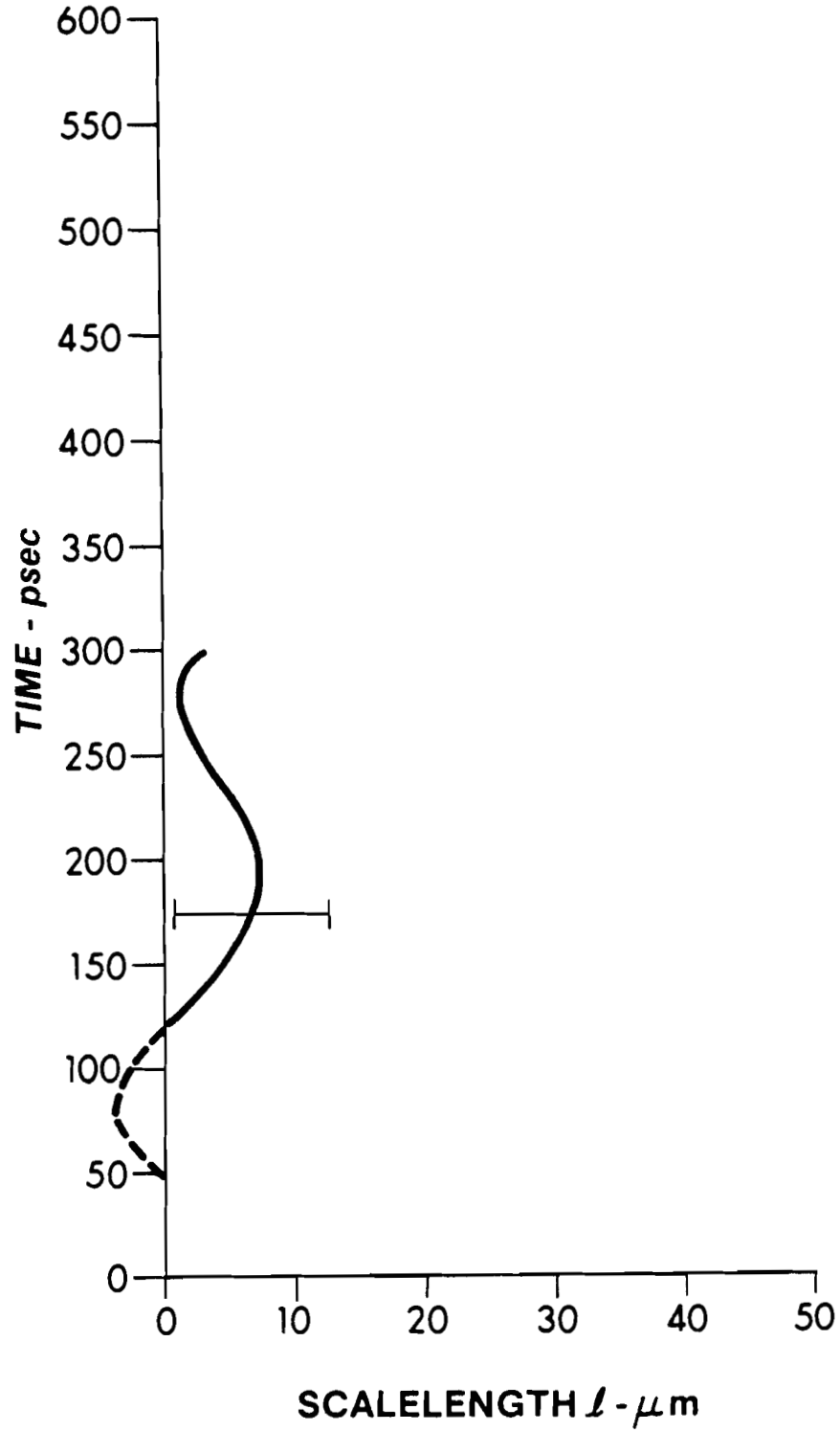
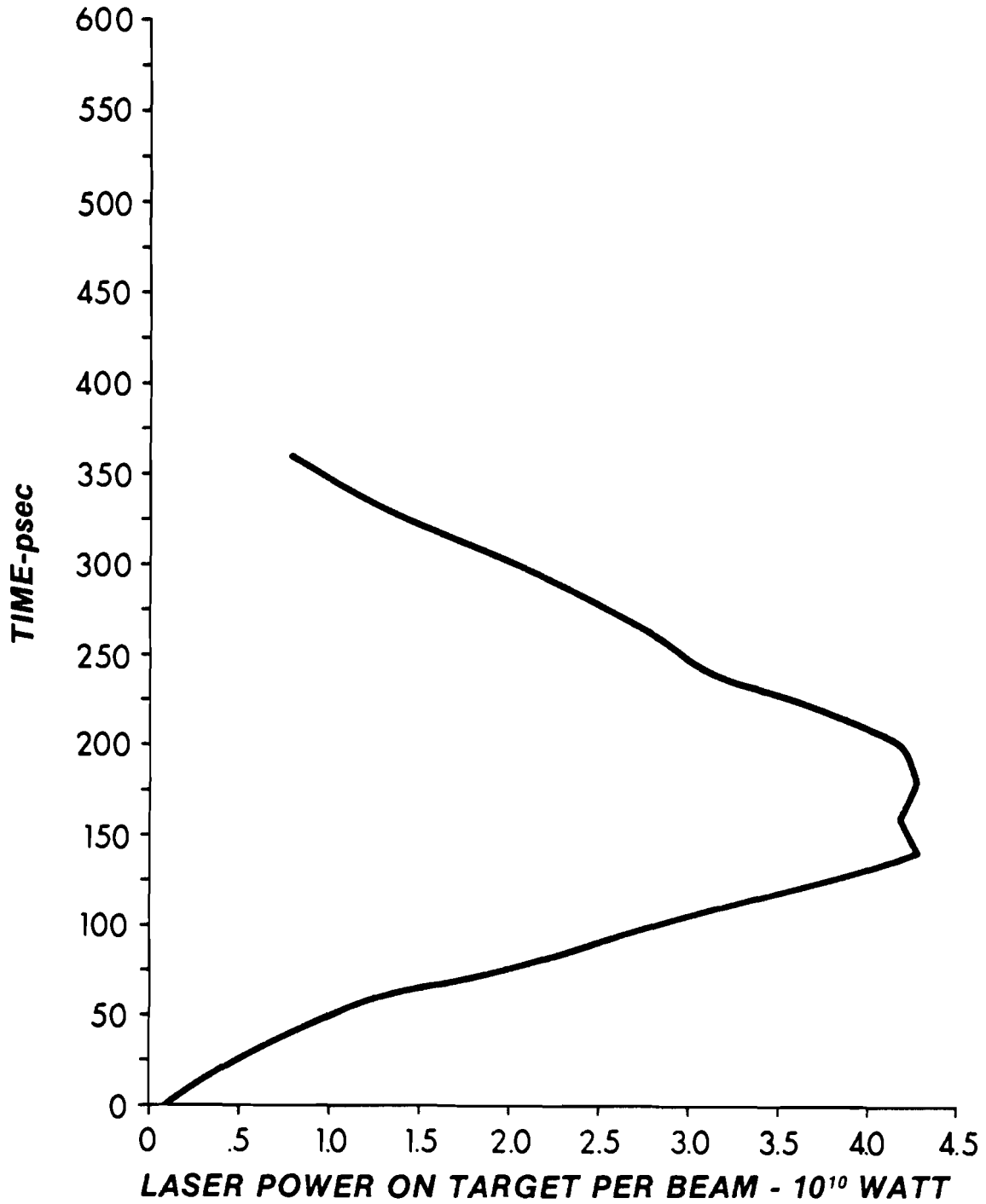


FIGURE 5-17
INCIDENT PULSE
11710



ters that are of importance to the interpretation of the experimental results. Figure 5-18 reveals a scalelength dependence to the fractional absorption. This is discussed in section 6.1. Figure 5-19 shows a correlation between the peak critical and quarter-critical surface peak excursions. Figure 5-20 indicates a rise time dependence to the peak excursions. Figures 5-19,20 are used in section 6.3 to study the hydrodynamics of microballoons and energy transport in laser produced plasma.

FIGURE 5-18
EXPERIMENTAL SCALELENGTH DEPENDENCE
OF ABSORPTION

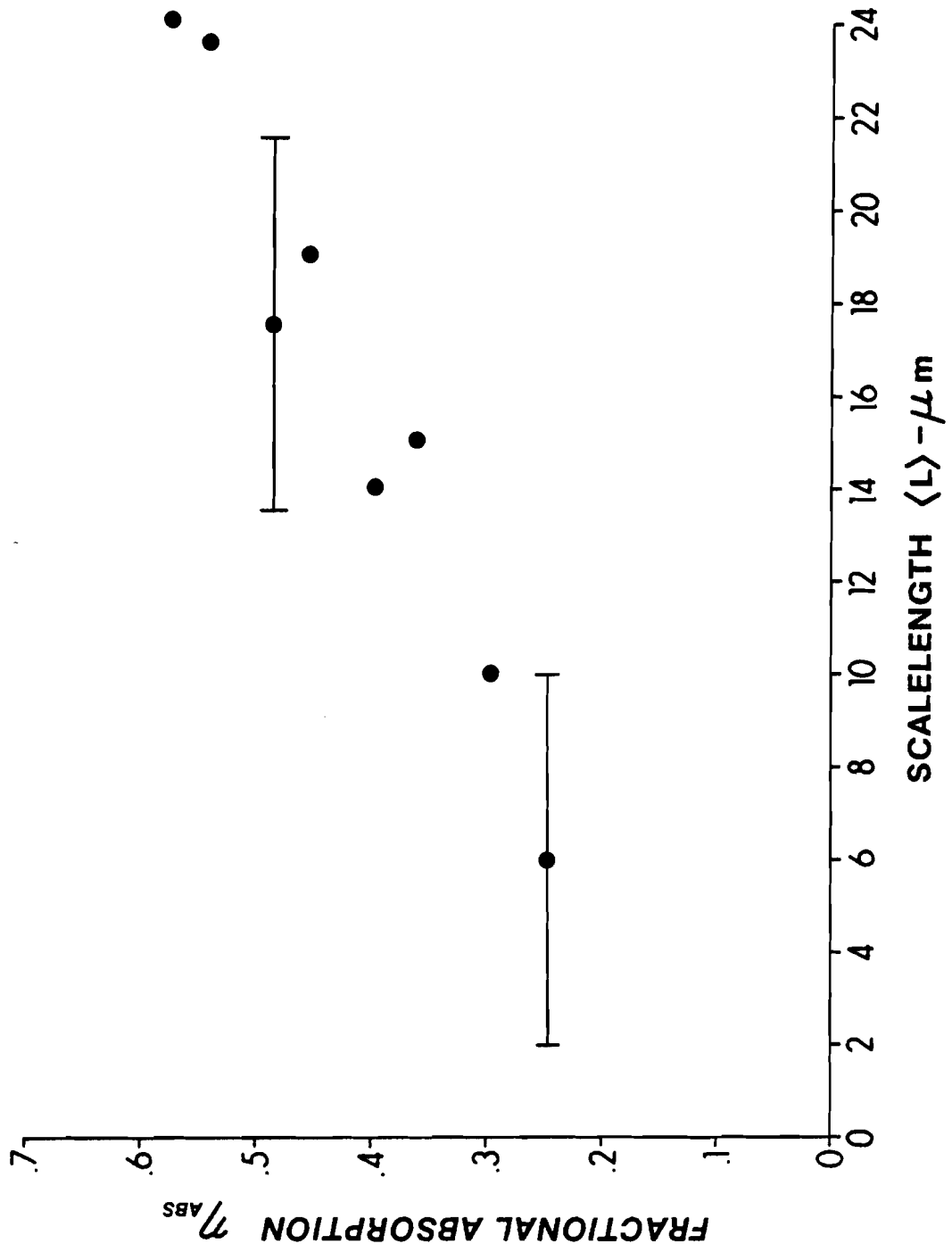


FIGURE 5-19

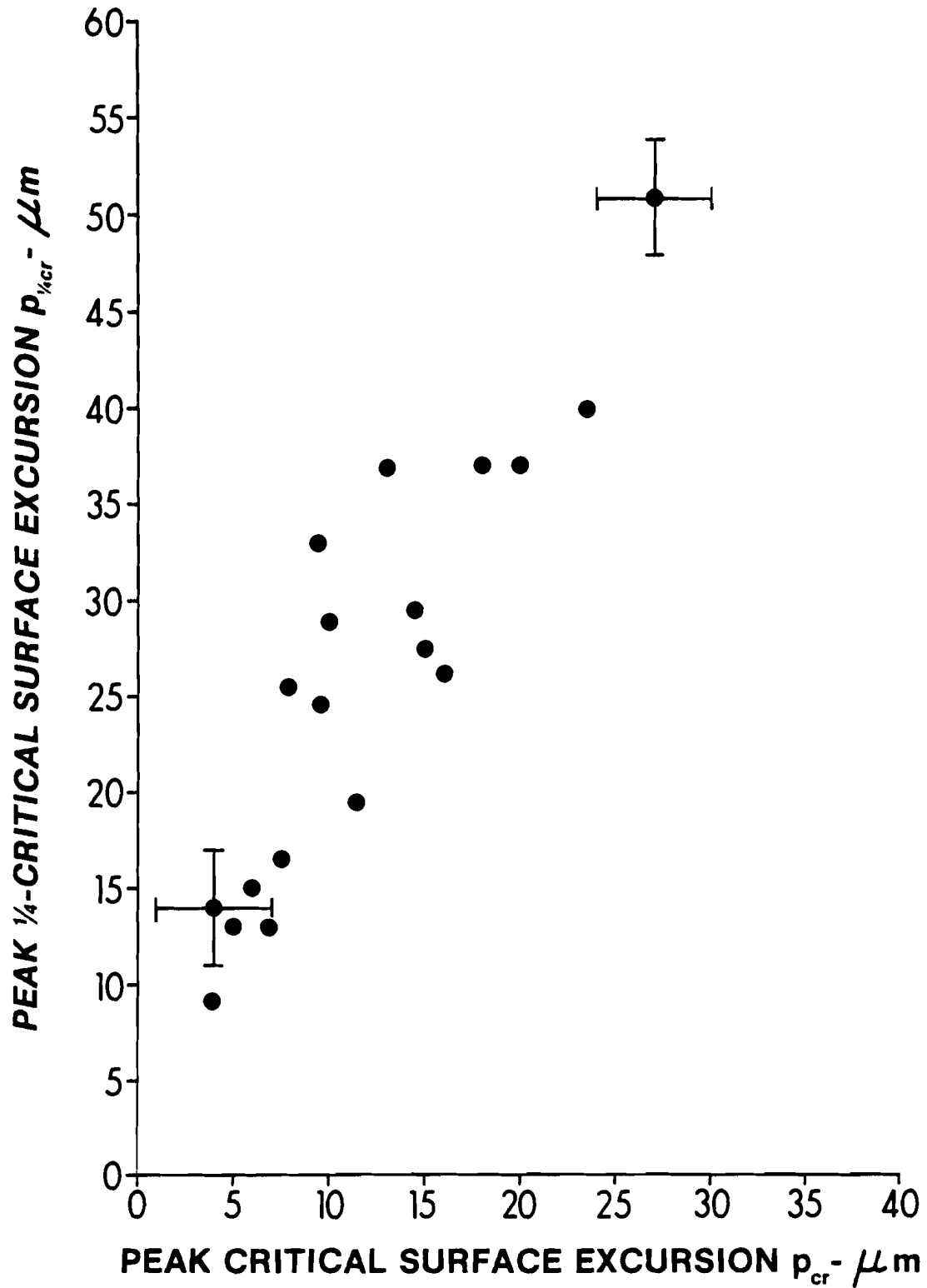
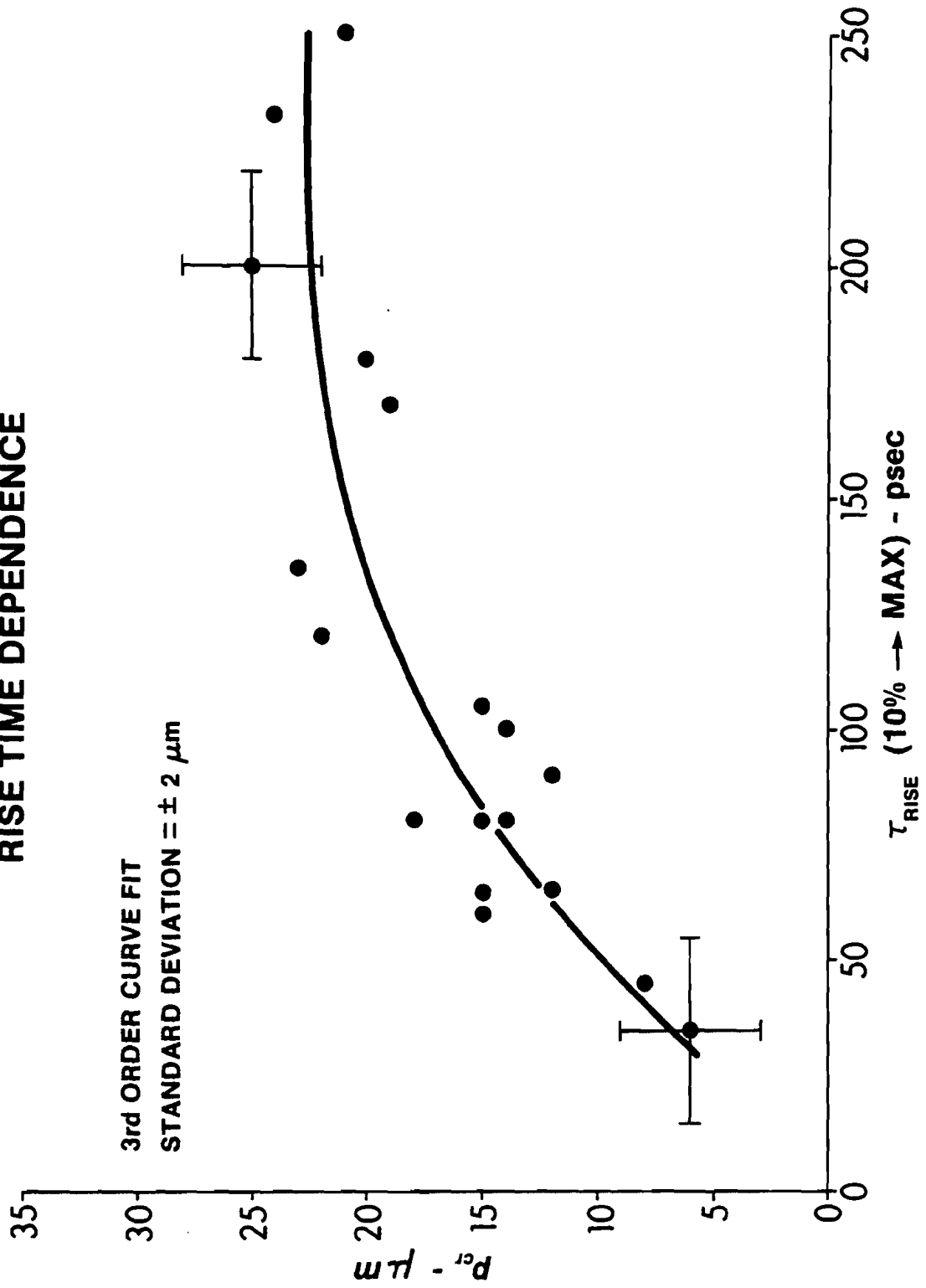
PEAK CRITICAL - QUARTER-CRITICAL SURFACE EXCURSION CORRELATION

FIGURE 5-20
**PEAK CRITICAL SURFACE EXCURSION
RISE TIME DEPENDENCE**



6. Theoretical Considerations

This chapter treats topics for which physics can be learned from a knowledge of the critical and quarter-critical surface motion. The areas studied are: laser light absorption, plasma energy transport, and hydrodynamics of thin spherical shells. Also studied, because of its importance to absorption and to plasma emission observations, is the refraction of light by a plasma.

6.1 Light Absorption By Spherical Plasmas

A significant use of the scalelength and trajectory measurements is found in the study of light absorption by the plasma. It is important to know not only how much of the laser light was absorbed, but also when it was absorbed and in what regions of the plasma.

In this section the theories of "collisional" and "resonant" absorption are reviewed and applied to spherical plasmas. Absorption, which is dependent upon the laser beam focal spot geometry, is analyzed for two situations: normal incidence of spherical waves concentric with the spherical plasma, and oblique incidence of plane waves onto the spherical plasma.

6.1.1 Collisional Absorption

Collisional absorption describes the process by which energy in the laser light electric field is transferred to the plasma through ion-electron collisions. In the absence of ion-electron collisions, electrons oscillate in the electric field of the laser and except for the energy expended in setting up the oscillations, no energy is transferred to the plasma. When electrons randomly collide with ions

the ordered electron motion, derived from the applied fields, is randomized. The laser energy, thus, goes into heating of the plasma constituents.

Because the Coulomb forces acting between the charged particles are long-range, the amount of scattering per encounter tends to be small and the number of particles participating in the scattering process tends to be large. The effect of collisions can, then, be lumped into a single factor that expresses the rate of electron velocity dispersal due to ion-electron collisions. This factor is called the ion-electron collision time ' τ_c ' or the ion-electron collision frequency ' ν_{ei} ', where $\nu_{ei} = 1/\tau_c$.

To obtain an expression for the absorbed energy, the equation of motion for a single electron is used. (6-1)

$$\Sigma \bar{F}_e = m \frac{d\bar{V}}{dt} = -e\bar{E} - \frac{m}{\tau_c} \bar{V} \quad (6-1)$$

'm' is the electron mass, ' \bar{V} ' is the electron velocity, ' \bar{E} ' is the electric field felt by the electron, and ' τ_c ' is the ion-electron collision time. In the absence of a driver field ' \bar{E} ', the electron velocity would decay by .368 in a time τ_c .

Equation (6-1) together with Maxwell's equations forms a complete set. To obtain a solution, a transverse electromagnetic wave is imposed on the plasma of the form:

$$\bar{E} = \bar{E}_0 e^{i(\bar{k} \cdot \bar{r} - \omega t)} \quad , \quad \bar{B} = \bar{B}_0 e^{i(\bar{k} \cdot \bar{r} - \omega t)} \quad (6-2)$$

A linearized analysis is conducted with a plasma response assumed to be proportional to $e^{i(\vec{k}\cdot\vec{r}-\omega t)}$. A dispersion relation is then obtained.

$$k = \pm \frac{\omega}{c} \left[1 - \frac{\omega_p^2}{\omega^2} \frac{1}{(1+i/\tau_c\omega)} \right]^{\frac{1}{2}}, \quad \omega_p^2 = \frac{4\pi e^2 n_e}{m} \quad (6-3)$$

' ω_p ' is known as the plasma frequency.

To determine the absorption, the imaginary part of k needs to be computed where:

$$k = k_R + i k_I \quad (6-4)$$

The real and imaginary parts of ' k ' turn out to be (for $\tau_c\omega \gg 1$):

$$k_R = \frac{\omega}{c} \left[1 - \frac{\omega_p^2}{\omega^2} \right]^{\frac{1}{2}} \quad (6-5)$$

$$k_I = \frac{\omega_p^2}{2c\omega^2 \left[1 - \omega_p^2/\omega^2 \right]^{\frac{1}{2}}} \frac{1}{\tau_c} \quad (6-6)$$

The light intensity at any point within the plasma is given by the time averaged ' $\langle \rangle$ ' magnitude ' $| \cdot |$ ' of Poynting's vector ' \vec{S} '.

$$I = |\langle \vec{S} \rangle| = \left| \frac{c}{4\pi} \text{Re } \vec{E} \times \text{Re } \vec{B} \right| = I_0 e^{-2k_I \hat{k} \cdot \vec{r}} \quad (6-7)$$

' $\text{Re } \vec{E}$ ' and ' $\text{Re } \vec{B}$ ' denote the real parts of \vec{E} and \vec{B} , ' I_0 ' is the light intensity at $r=0$, and ' \hat{k} ' is a unit vector pointing in the direction

of light propagation.

Equation (6-7) is strictly correct only for a homogeneous plasma. If the plasma parameters vary slowly compared to the wavelength of the light then a WKB analysis can be performed and (6-7) becomes:

$$I = I_0 \exp \left[-2 \int_0^s k_I ds \right] \quad (6-8)$$

where the integral is taken along the trajectory of each ray of light.

At this point it is necessary to determine ' τ_c ' that appears in equation (6-6). ' τ_c ' is obtained through use of the kinetic equation and the problem has been solved by Silin for the case of only thermal ion-electron density fluctuations from charge neutrality.⁽⁶⁻²⁾ Absorption in such a situation is known as "inverse bremsstrahlung" absorption. Only the results are presented here. The collision time ' τ_c ' can be written as

$$\frac{1}{\tau_c} = \nu_{ei} = \frac{16\pi^2 \text{emc}^{9/2} Z n_e}{\lambda^3 I^{3/2}} \left[Q \left(\frac{e \lambda I^{1/2}}{c^{3/2} (2\pi m k T_e)^{1/2}} \right) \right] \text{Ln} \Lambda \quad (6-9a)$$

$$Q(\xi) = \int_0^\xi dZ Z^2 e^{-Z^2} [\mathcal{J}_0(Z^2) - \mathcal{J}_1(Z^2)] \quad (6-9b)$$

$$\Lambda = \frac{b_{\max}}{b_{\min}} = \frac{3}{2\pi^{1/2} e^{3/2} Z n_e^{1/2}} \left[k T_e + \frac{2e^2 \lambda^2 I}{3\pi m c^3} \right]^{3/2} \quad (6-9c)$$

' \mathcal{J}_0 ' and ' \mathcal{J}_1 ' are modified Bessel functions. ' b_{\min} ' and ' b_{\max} ' are

the minimum and maximum impact parameters for ion-electron collisions taken respectively to be the impact parameter for 90° scattering and the electron Debye radius, at which the force on an electron due to the electric field of an isolated charge within the plasma equals the force due to the electron pressure. The pressure is taken as due to the electron's random thermal velocity and the electron's quiver velocity in the light's electric field.

It has been shown by Catto and Speziale⁽⁶⁻³⁾ that $Q(\xi)$ can be expressed by the series:

$$Q(\xi) = \frac{\xi^3}{\pi^{1/2}} \sum_{n=0}^{\infty} \frac{(-2\xi^2)^n}{(n+3/2)} \frac{\Gamma(n+3/2)}{\Gamma(n+1)\Gamma(n+2)} \quad (6-10)$$

Inserting equation (6-10) into equation (6-9a) and retaining only the first three terms in the series

$$\frac{1}{\tau_c} = \frac{8\pi^2 e^4 m Z n_e}{(2\pi m k T_e)^{1/2}} \left\{ \frac{2}{3} - \frac{3\xi^2}{5} + \frac{5\xi^4}{21} \right\} \text{Ln}\Lambda \quad (6-11)$$

Note that

$$\xi = \frac{e\Lambda I^{1/2}}{c^{3/2} (2\pi m k T_e)^{1/2}} = \frac{1}{2} \frac{v_{osc}}{v_T} \quad (6-12)$$

where v_{osc} is the oscillatory velocity of the electrons in the electric field and v_T is the electron thermal velocity. For the conditions of experimental interest $I \approx 10^{15}$ watt/cm² and $T_e \approx 1$ keV so that $\xi \approx .3$. It suffices to retain only the first two terms in the

expansion. The collision frequency can, therefore, be written as

$$\frac{1}{\tau_c} = \nu_{ei} = \frac{16\pi^2 e^4 m Z n_e}{3(2\pi m k T_e)^{3/2}} \left\{ 1 - \frac{9}{10} \frac{e^2 \lambda^2 I}{c^3 (2\pi m k T_e)} \right\} \text{Ln} \Lambda \quad (6-13)$$

Inserting numerical values for the constants in (6-13) and (6-9c)

$$\frac{1}{\tau_c} = \nu_{ei} = 3.626 \frac{Z n_e}{T_e^{3/2}} \left\{ 1 - (9.723 \times 10^{-9}) \frac{\lambda^2 I}{T_e} \right\} \text{Ln} \Lambda \quad (6-14a)$$

$$\Lambda = (1.241 \times 10^4) \frac{[T_e + (1.440 \times 10^{-8}) \lambda^2 I]^{3/2}}{Z n_e^{1/2}} \quad (6-14b)$$

The appropriate units are ' n_e ' in particle/cm³, ' λ ' in cm, ' I ' in erg/(sec-cm²), and ' T_e ' in ⁰K.

Using equation (6-8) together with equations (6-6) and (6-13), the absorption can be computed for various plasma density profiles and focal spot geometries. There is, in general, no analytic solution for the problem of obliquely incident light. Answers can be obtained numerically using equation (6-6), but calculation of the ray trajectories must first be obtained. In addition, equation (6-6) is singular (an integrable singularity) at $n_e/n_{cr} = 1$ so that the numerical accuracy of the results is affected for near-normal incidence rays. Both these problems can be solved with further analysis.

Let the absorption be calculated for a plasma that is isothermal in the subcritical region of the plasma. Such a situation has been predicted to develop within 50 psec of the start of the laser

pulse. (6-4) Let it also be assumed that the plasma profile is smooth and that it is linear in the subcritical region of the plasma.

Following the ray trajectory into the plasma, the intensity of light at a point is given by

$$I = I_0 e^{-\sigma} \quad (6-15)$$

$$\sigma = \int_0^{\Delta} \frac{n_e/n_{cr}}{c(1-n_e/n_{cr})^{1/2}} \frac{16\pi^2 e^4 mZ n_e}{3(2\pi m k T_e)^{3/2}} \left\{ 1 - \frac{9e^2 \lambda^2 I}{10c^3 (2\pi m k T_e)} \right\} \text{Ln}\Lambda \, d\Delta \quad (6-16)$$

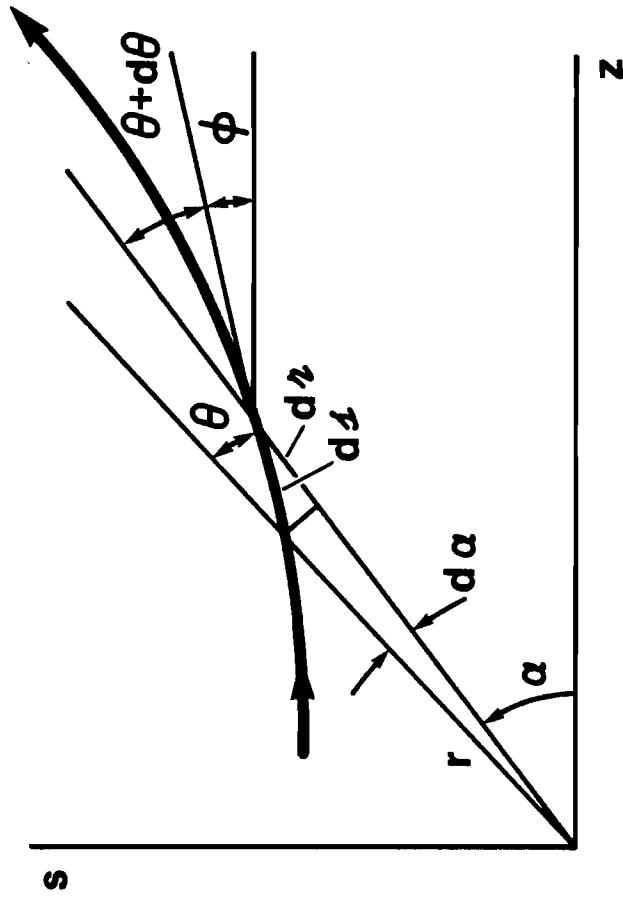
To simplify evaluation of the integral let the laser intensity in the field correction terms be assumed constant and equal to the vacuum laser beam intensity at some representative value within the focal spot. Let the slowly varying $\text{Ln}\Lambda$ be assumed constant and equal to its value at the critical surface. Equation (6-16) then becomes:

$$\sigma = \frac{1}{c\tau_{cr}} \int_0^{\Delta} \frac{(n_e/n_{cr})^2}{(1-n_e/n_{cr})^{1/2}} \, d\Delta \quad (6-17)$$

where ' τ_{cr} ' is the ion-electron collision time at the critical surface.

To incorporate the ray tracing, Bouguer's formula (section 6.2) is used. Figure 6-1 shows the geometry of the problem. It can be seen that

FIGURE 6-1
RAY PATH GEOMETRY



$$ds = \frac{dr}{\cos(\theta+d\theta)} \approx \frac{dr}{\cos \theta}$$

Using Bouguer's formula ($\mu r \sin\theta = K$) derived in Section 6.2:

$$\cos \theta = \pm \left[1 - \frac{K^2}{\mu^2 r^2} \right]^{\frac{1}{2}}$$

For rays travelling inwards $\frac{\pi}{2} \leq \theta \leq \pi$ so that the minus sign is appropriate. Since $\mu = (1 - n_e/n_{cr})^{\frac{1}{2}}$ the incremental path length along the ray can be written as

$$ds = -(1 - n_e/n_{cr})^{\frac{1}{2}} \frac{dr}{\left[\left(1 - \frac{K^2}{r^2}\right) - n_e/n_{cr} \right]^{\frac{1}{2}}} \quad (6-18)$$

Equation (6-17) becomes:

$$\sigma = -\frac{1}{c\tau_{cr}} \int_0^{r_{TP}} \frac{(n_e/n_{cr})^2}{\left[\left(1 - K^2/r^2\right) - n_e/n_{cr} \right]^{\frac{1}{2}}} dr \quad (6-19)$$

Equation (6-19) incorporates the ray tracing and follows the ray through the plasma to its turning point (r_{TP}). It is valid for any density profile of the form $n_e = n_e(r)$ but does contain a singularity (integrable) at what turns out be the ray turning point.

To eliminate the singularity we proceed with the particular case of a linear density profile of the form

$$n_e/n_{cr} = 1 - \frac{3}{4\ell} (r-r_{cr}) \quad r \leq r_{cr} + \frac{4\ell}{3} \quad (6-20)$$

For this density profile equation (6-19) becomes

$$\sigma = \frac{1}{c_{\tau cr}} \int_{r_{TP}}^{r_{cr} + \frac{4\ell}{3}} \frac{\left[1 - \frac{3}{4\ell} (r-r_{cr})\right]^2 r dr}{\left[\frac{3}{4\ell} r^3 - \frac{3r_{cr}}{4\ell} r^2 - K^2\right]^{\frac{1}{2}}} \quad (6-21)$$

If Bouguer's formula is used to determine where the turning point occurs, then an equation identical to the cubic equation appearing in the denominator of equation (6-21) is obtained. One root of the cubic equation is real and gives the radius of the turning point. The other two roots are complex. Factoring out the real root from the square-root, and changing variables by $w \equiv (r-r_{TP})^{\frac{1}{2}}$ a well-behaved integral is obtained. The result is:

$$\sigma = \frac{1}{c_{\tau cr}} \left(\frac{16\ell}{3}\right)^{\frac{1}{2}} \int_0^{\left[\frac{2}{3} (r_{cr} + 2\ell) - (A+B)\right]^{\frac{1}{2}}} \frac{\left[1 - \frac{3}{4\ell} (w^2 - \frac{2}{3} r_{cr} + A+B)\right]^2 (w^2 + \frac{1}{3} r_{cr} + A+B) dw}{\left[w^4 + 3(A+B)w^2 + 3(A^2 + AB + B^2)\right]^{\frac{1}{2}}} \quad (6-22)$$

$$w = \left[r - r_{TP}\right]^{\frac{1}{2}} = \left[r - \frac{1}{3} r_{cr} - A - B\right]^{\frac{1}{2}} \quad (6-23)$$

$$A = \left\{ \frac{r_{cr}^3}{27} + \frac{2\ell k^2}{3} + \frac{2}{3} \ell k^2 \left[1 + \frac{r_{cr}^3}{9\ell k^2} \right]^{\frac{1}{2}} \right\} \quad (6-24)$$

$$B = \left\{ \frac{r_{cr}^3}{27} + \frac{2\ell k^2}{3} - \frac{2}{3} \ell k^2 \left[1 + \frac{r_{cr}^3}{9\ell k^2} \right]^{\frac{1}{2}} \right\} \quad (6-25)$$

Use of equation (6-22) in equation (6-15) gives the energy reaching the turning point. The intensity after the ray leaves the plasma is given by

$$I_{out} \approx (I_0 e^{-\sigma})(e^{-\sigma}) = I_0 e^{-2\sigma}.$$

The fractional absorption due to inverse bremsstrahlung is then

$$\eta_{IB} \equiv 1 - \frac{I_{out}}{I_0} = I_0 e^{-2\sigma} \quad (6-26)$$

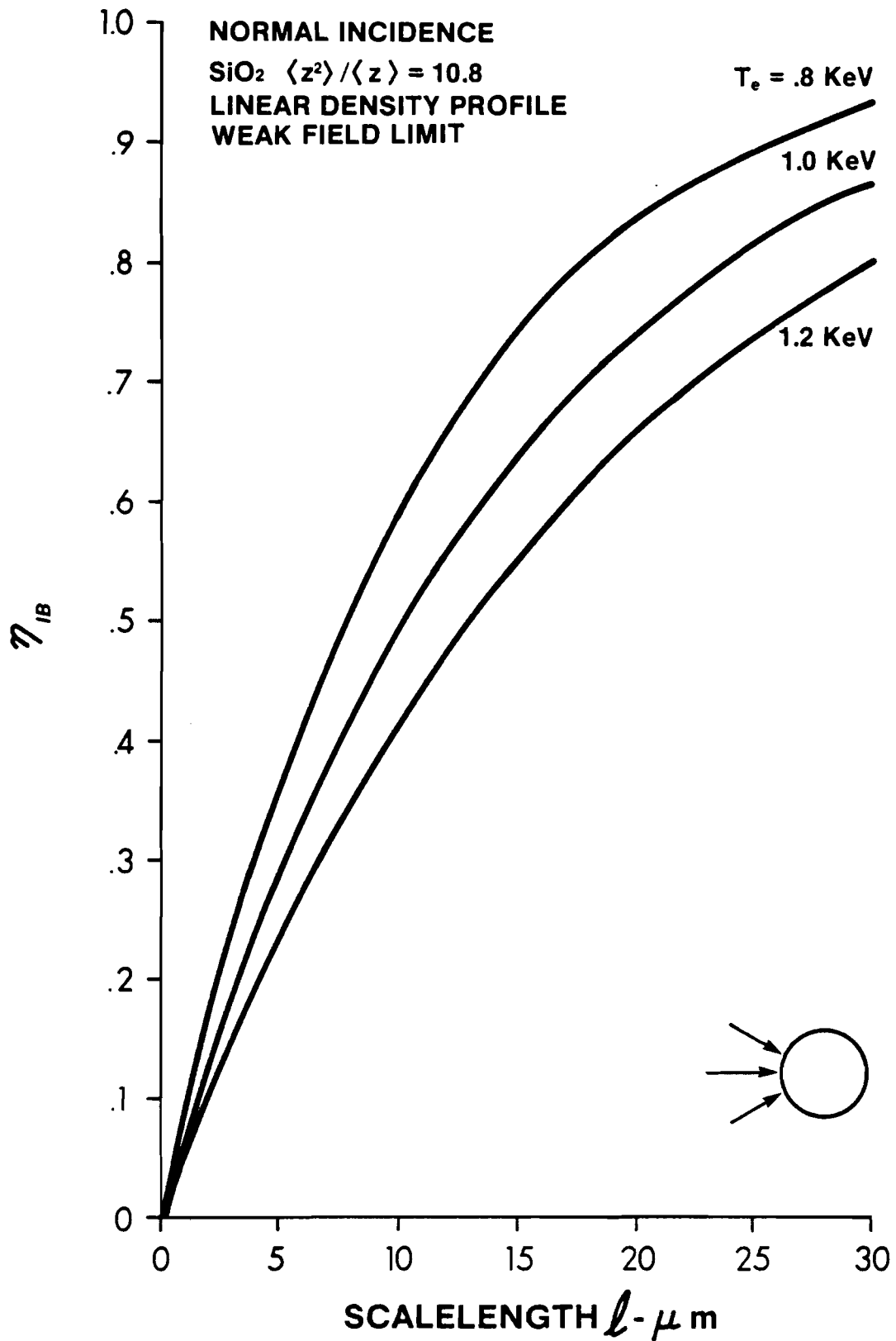
Equation (6-22) can easily be integrated numerically. All that is needed are the plasma parameters ' r_{cr} ' and ' ℓ ', and the initial ray trajectory parameter ' K '. For normal incidence an analytic solution exists. To obtain it note that at normal incidence $K=0$. $A=B=\frac{1}{3} r_{cr}$ and $r_{TP}=r_{cr}$. σ can then be integrated analytically with the result that

$$\sigma = \frac{64\ell}{45c\tau_{cr}} \quad - \text{NORMAL INCIDENCE} \quad (6-27)$$

Figure 6-2 shows a plot of the fractional inverse bremsstrahlung

FIGURE 6-2

FRACTIONAL ABSORPTION DUE TO INVERSE BREMSSTRAHLUNG



absorption as a function of scalelength for the range of electron temperatures encountered. The calculations are done in the weak field limit, for which the finite light intensity effects have not been included. At 10^{15} watt/cm² the fractional absorption is reduced by about 5% from the fractional absorption calculated in the weak field limit.

The increase of absorption with scalelength increase is due to the increasing number of particles available to collisionally absorb energy. The absorption decrease with increasing electron temperatures is due to a fractionally smaller velocity change per collision as the initial velocity increases.

To investigate oblique incidence absorption it is necessary to specify the focal spot geometry; not only the intensity distribution, but also the ray trajectories or a phase front within it. The information experimentally available is the focal spot intensity distribution and the fact that it doesn't change substantially along an axial distance of 100 μm in the focal region (focal spot waist). The transverse dimension of the beam is characterized by a radius of 70-80 μm within which lies 80% of the focused energy. The intensity distribution is approximately Gaussian.⁽⁶⁻⁵⁾

Since the focal spot is much larger than the diffraction limited ($r_D \approx 3 \mu\text{m}$) and since the focal spot waist is long, it is assumed that the rays are parallel to the optical axis as they enter the plasma. The intensity distribution across the focal spot is assumed to be Gaussian with 80% of the energy within a 40 μm radius (Figure 6-3).

FIGURE 6-3

LASER BEAM INTENSITY PROFILE

GAUSSIAN PROFILE WITH 80% OF ENERGY IN A 40 μm RADIUS FOCAL SPOT

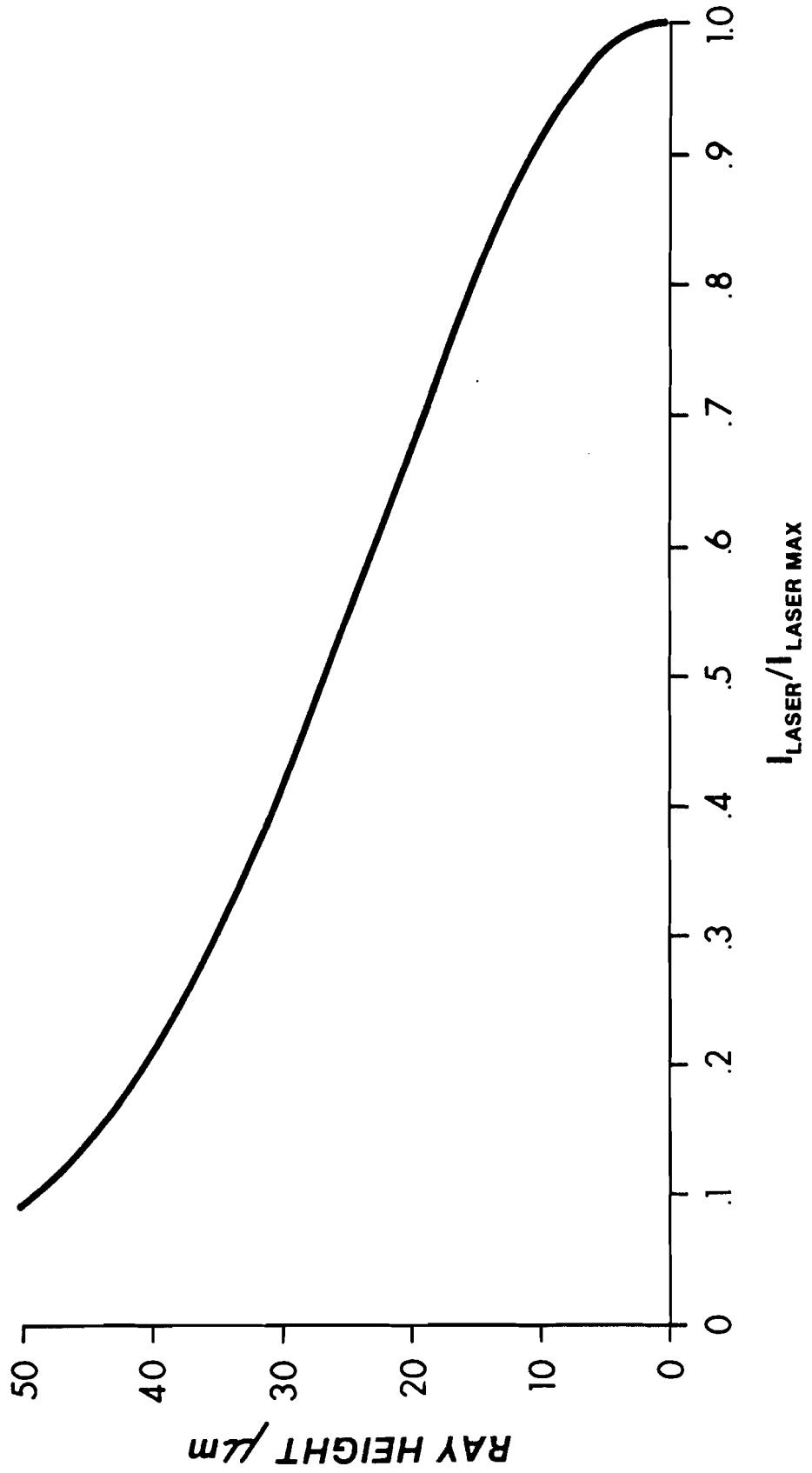


Figure 6-4 shows the fractional inverse bremsstrahlung absorption (absorbed power/laser power - $P_{\text{ABS}}/P_{\text{LASER}}$) for the case of a laser with power 7.8×10^{14} watt/cm² (50 joules in 500 psec) incident on a $T_e = 1$ keV, Si O₂; $\langle Z^2 \rangle / \langle Z \rangle = 10.8$ plasma. For the oblique incidence focal spot previously described, normal incidence is treated as the limiting case of large radius of curvature where $r_{\text{cr}} \gg \lambda$ and $r_{\text{cr}} \gg r_{\text{FOCAL SPOT}}$.

Obliquely incident light penetrates less deeply into the plasma and is absorbed less efficiently. For a fixed oblique incidence focal spot, smaller plasmas absorb less efficiently. This is the trend seen in Figure 6-4 and also in Figure 6-5.

Figure 6-5 shows the local inverse bremsstrahlung fractional absorption (absorbed intensity/laser intensity - $I_{\text{ABS}}/I_{\text{LASER}}$) plotted as a function of the initial ray height. The effect of the Gaussian intensity profile appears only in the moderate field correction terms. The field correction is revealed in the normal incidence curves where the fractional absorption is lowest on axis where the laser beam intensity is highest. The consequence of oblique incidence is readily evident by the drop in absorption efficiency as the initial ray height increases.

If non-charge-neutral structures exist within the plasma, electrons can collide with the ions of a structure and not just those ions within a Debye sphere. Silin's results then inadequately explain the absorption. Such a situation was investigated by Faehl and Kruer in a study of light absorption by short wavelength ion turbulence.⁽⁶⁻⁶⁾ Using an estimation of ion turbulence strength ($\delta n/n$) and wavenumber

FIGURE 6-4

FRACTIONAL ABSORPTION DUE TO INVERSE BREMSSTRAHLUNG ABSORPTION

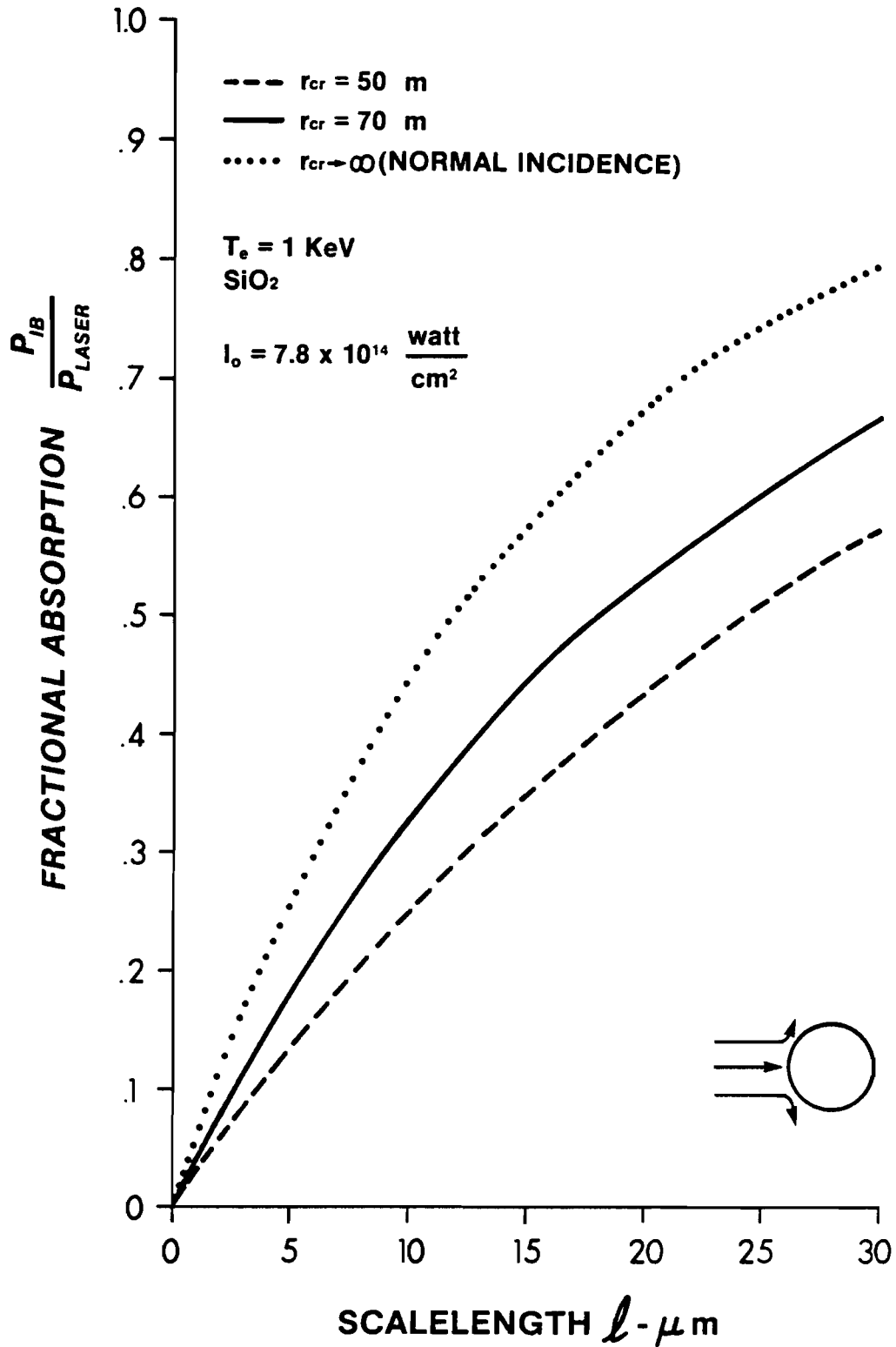
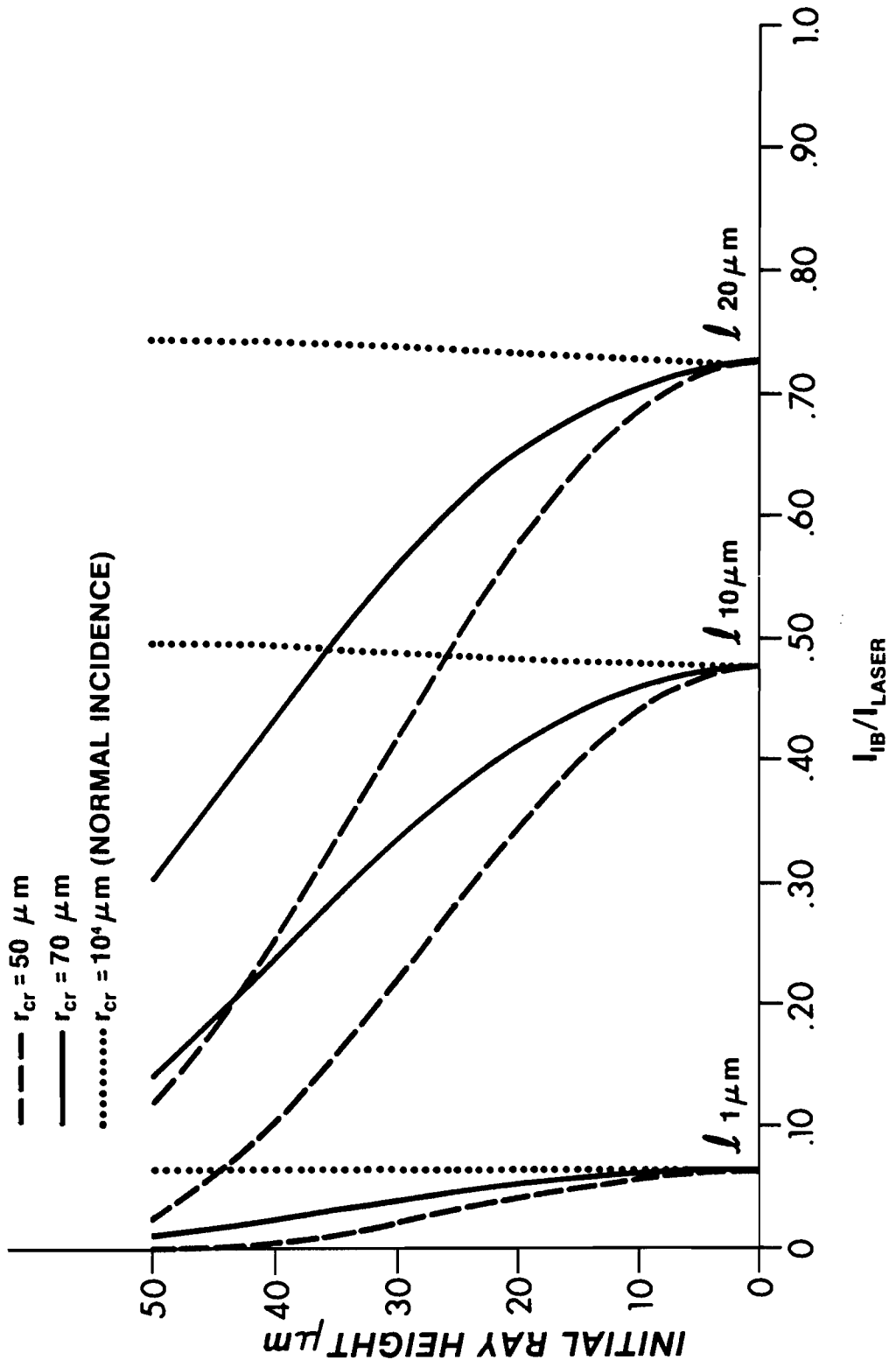


FIGURE 6-5
**SPATIAL DEPENDENCE OF OBLIQUE INCIDENCE
 INVERSE BREMSSTRAHLUNG ABSORPTION**



(k_T) obtained from particle-in-cell code simulations, an effective collision time (τ_T) as a function of density was calculated. The result was that for modest density fluctuations ($\delta n/n \approx .1$, $k_T = \frac{1}{2} (4\pi e^2 n_e / kT_e)^{\frac{1}{2}}$), the collision time was found to be approximately equal to

$$\tau_T \approx \begin{cases} 2 \times 10^2 / \omega_p & \frac{1}{2} \lesssim n_e / n_{cr} \lesssim 1 \\ \infty & n_e / n_{cr} \lesssim \frac{1}{2} \end{cases} \quad (6-28)$$

Comparing τ_T to the inverse bremsstrahlung collision time τ_c given by eq. (6-17) for 1 keV glass yields:

$$\frac{\tau_c}{\tau_T} = \frac{3.91 \times 10^{10}}{n_e^{\frac{1}{2}}} \quad (6-29)$$

This ratio is greater than one but of order one in the region of strong absorption. Absorption within turbulent structures is clearly important. It should be noted that when turbulence exists the absorption due to it does not necessarily supplement inverse bremsstrahlung absorption but rather supplants it. Inverse bremsstrahlung absorption is obtained as the limit of weak turbulence when the density fluctuations approach the thermal fluctuation level.

In 1 keV glass, turbulent and inverse bremsstrahlung absorption are approximately equal and have a similar scalelength dependence. To see this, equation (6-28) is used to obtain an absorption

coefficient. Equations (6-6) and (6-8) are used along with the assumption of normal incidence to trace a ray through the plasma. The fractional absorption is then given by

$$\eta_T = 1 - e^{-2\sigma} \quad \sigma = 3.68 \times 10^{-2} \frac{\ell}{\lambda} \quad (6-30)$$

This can be compared to equations (6-26,27). The important distinction is that (6-30) contains no explicit ionization state (Z) or electron temperature (T_e) dependence. These appear only indirectly through their effect on $\delta n/n$ and k_T in the possible turbulence generation mechanisms. The Z and T_e dependences of collisional absorption may not be as apparent and important as the inverse bremsstrahlung theory indicates.

6.1.2 Resonant Absorption

When light is polarized in the plane of incidence, the electric field vector becomes parallel to the plasma density gradients at the ray turning point. The longitudinal electric field generates an electron density perturbation which propagates as a longitudinal electrostatic electron wave of frequency ω . (The electric field of the wave is parallel to the direction of propagation.)

The electron wave can travel in the direction of higher densities. At the critical density a resonance exists and the wave energy is deposited. Large electron density fluctuations and electric fields are produced which, through nonlinear interaction, transport energy into the plasma.

This process of laser light absorption is referred to as res-

onant absorption. It is linear in the sense that the absorption coefficient is not a function of intensity. The process does not have an intensity threshold. It should be distinguished from the parametric processes which involve three wave interactions.

Resonant absorption for the case of plane waves incident upon a plane one-dimensional plasma with a linear density profile has been studied in the past through analytical models and computer simulations.^(6-7,8,9,10) A computer study for the case of spherical plasmas and diffraction limited focal spots has also been performed.⁽⁶⁻¹¹⁾

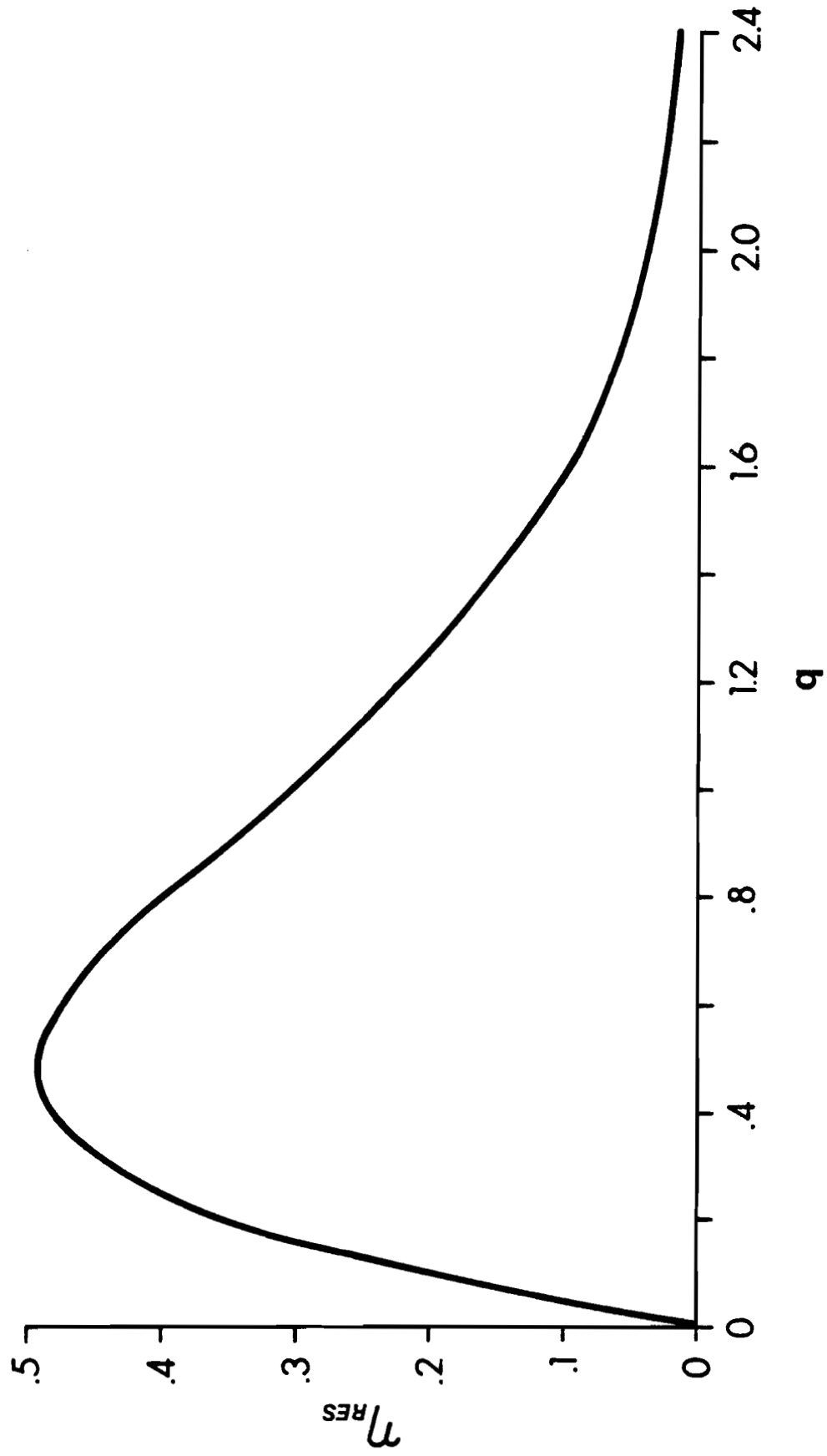
The result of interest from the plane plasma solutions is the determination of the absorption coefficient ' η_{RES} ' as a function of the parameter 'q'

$$q \equiv \left(\frac{8\pi}{3} \frac{\ell}{\lambda_0} \right)^{2/3} \sin^2 \alpha_0 \quad (6-31)$$

where ' ℓ ' is the distance between the critical and quarter-critical densities, ' λ_0 ' is the vacuum laser light wavelength, and ' α_0 ' is the initial angle of incidence in the plane geometry. Figure 6-6 shows ' η_{RES} ' as a function of 'q'. The plot is taken from reference (6-9). It is valid for $\frac{8\pi}{3} \frac{\ell}{\lambda_0} \gg 1$ and is insensitive to changes in electron temperature.

Although figure 6-6 was obtained for a plane plasma it is here applied to spherical plasmas. The procedure used gives results in agreement with reference (6-11).

FIGURE 6-6
FRACTIONAL RESONANT ABSORPTION



To obtain results applicable to spherical plasmas note that although 'q' is expressed as a function of the initial angle of incidence, it can equally well be expressed as a function of the light's point of deepest penetration into the plasma; i.e., the ray turning point. This latter representation emphasizes the importance of the distance travelled by the longitudinal electrostatic wave to reach the resonance point.

The ray is determined which in the plane plasma penetrates as deeply as the ray passing through the spherical plasma. With the distances travelled by the longitudinal electrostatic waves equal, the resonant absorptions should be approximately equal.

The two geometries are depicted in figure 6-7. In the plane plasma geometry Snell's law states that between all points on a ray

$$\mu \sin \alpha = \text{const.} \quad (6-32)$$

Before the ray enters the plasma $\mu=1$ and $\alpha=\alpha_0$. At the turning point $\mu=\mu_{TP}$ and $\alpha=\pi/2$. The initial angle of incidence in the plane geometry is, therefore related to the index of refraction at the turning point (and to r_{TP} since $\mu_{TP} = \mu(r_{TP})$) by:

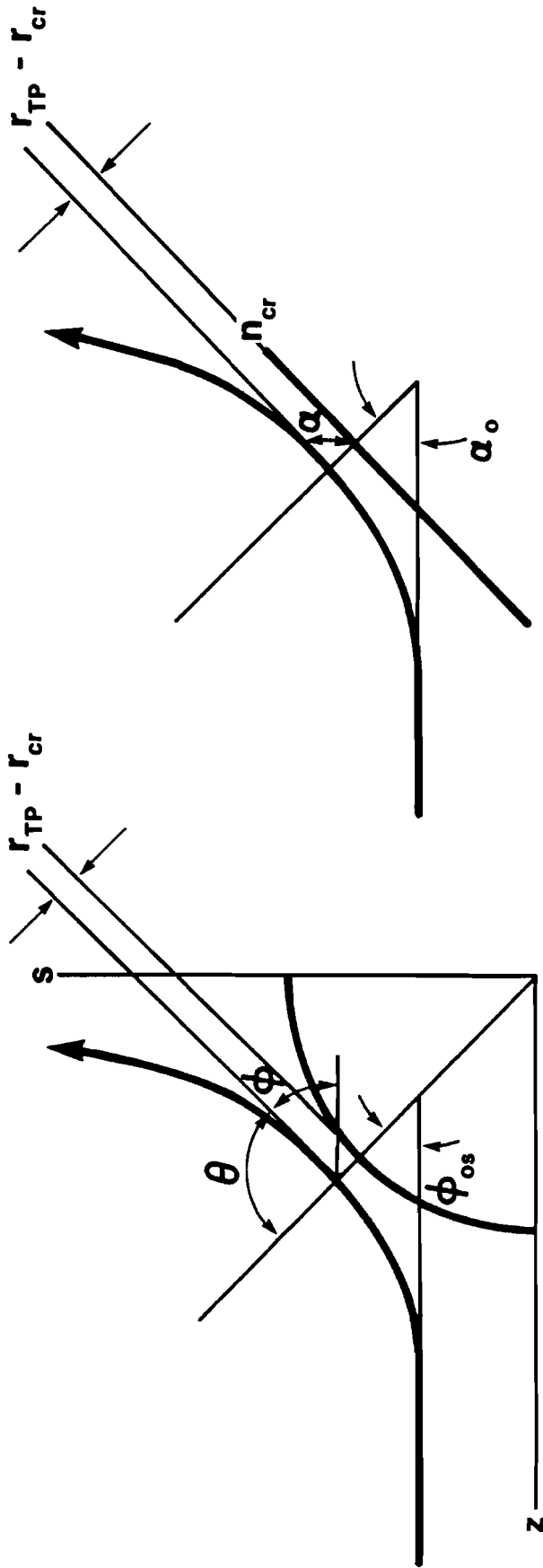
$$\mu_{TP} = \sin \alpha_0 \quad (6-33)$$

In the spherical geometry Bouguer's law states that along a ray (See figure 6-7)

$$\mu(s \cos \phi - z \sin \phi) = \mu r \sin \theta = \text{const.} \quad (6-34)$$

FIGURE 6-7

GEOMETRIES FOR OBLIQUE INCIDENCE LIGHT ON SPHERICAL AND PLANE PLASMAS



SPHERICAL PLASMA

PLANE PLASMA

Before the ray enters the plasma $\mu=1, \phi=0$, and $s=s_0$. At the turning point $\mu=\mu_{TP}$, $r=r_{TP}$, and $\theta=\pi/2$. The result is that

$$s_0 = \mu_{TP} r_{TP} \quad (6-35)$$

For the linear density profile, equation (6-20), one has that

$$\mu_{TP} = \left[1 - \frac{n_{TP}}{n_{cr}} \right]^{1/2} = \left[\frac{3}{4} \frac{(r_{TP} - r_{cr})}{\ell} \right]^{1/2}$$

Solving for r_{TP} and putting the result into equation (6-35):

$$s_0 = \frac{4\ell}{3} \mu_{TP}^3 + r_{cr} \mu_{TP} \quad (6-36)$$

Equating μ_{TP} in both the plane and spherical geometries allows equations (6-33) and (6-36) to be combined. The result is a cubic equation in $\sin \alpha_0$, the solution to which gives the relationship between the initial conditions in plane and spherical plasmas for equivalent ray penetrations into the plasmas.

$$\sin^3 \alpha_0 + \frac{3}{4} \frac{r_{cr}}{\ell} \sin \alpha_0 - \frac{3}{4} \frac{s_0}{\ell} = 0 \quad (6-37)$$

$$\sin \alpha_0 = \left\{ \frac{3s_0}{8\ell} \left[\left(1 + \frac{1}{9} \frac{r_{cr}^3}{s_0^2 \ell} \right)^{1/2} + 1 \right] \right\}^{1/3} - \left\{ \frac{3s_0}{8\ell} \left[\left(1 + \frac{1}{9} \frac{r_{cr}^3}{s_0^2 \ell} \right)^{1/2} - 1 \right] \right\}^{1/3} \quad (6-38)$$

'q' for spherical plasmas can then be expressed by:

$$q = 2.145 \left\{ (\zeta + \beta)^{1/3} - (\zeta - \beta)^{1/3} \right\}^2 \quad (6-39a)$$

$$\zeta = \left(\frac{s_0^2}{\lambda_0^2} + \frac{r_{cr}^3}{9\lambda_0^2 \ell} \right)^{1/2} \quad (6-39b)$$

$$\beta = s_0 / \lambda \quad (6-39c)$$

Equation (6-39) used in conjunction with figure 6-6 forms the basis for resonant absorption studies in spherical plasmas.

With ' η_{RES} ' specified, it remains to do a convolution across the laser beam profile. Not only must the laser light spatial intensity variation be considered, but the resonant absorption dependence on polarization must also be included.

The laser beam in the experiment is linearly polarized so that the electric field vector lies in a single plane. Only the electric field component in the plane of incidence (p-polarization) can be absorbed resonantly.

With reference to figure 6-8 it is seen that the p-component is given by:

$$E_p = E \cos \psi \quad (6-40)$$

The local intensity component that is resonantly absorbed is:

$$I_p = I \cos^2 \psi \quad (6-41)$$

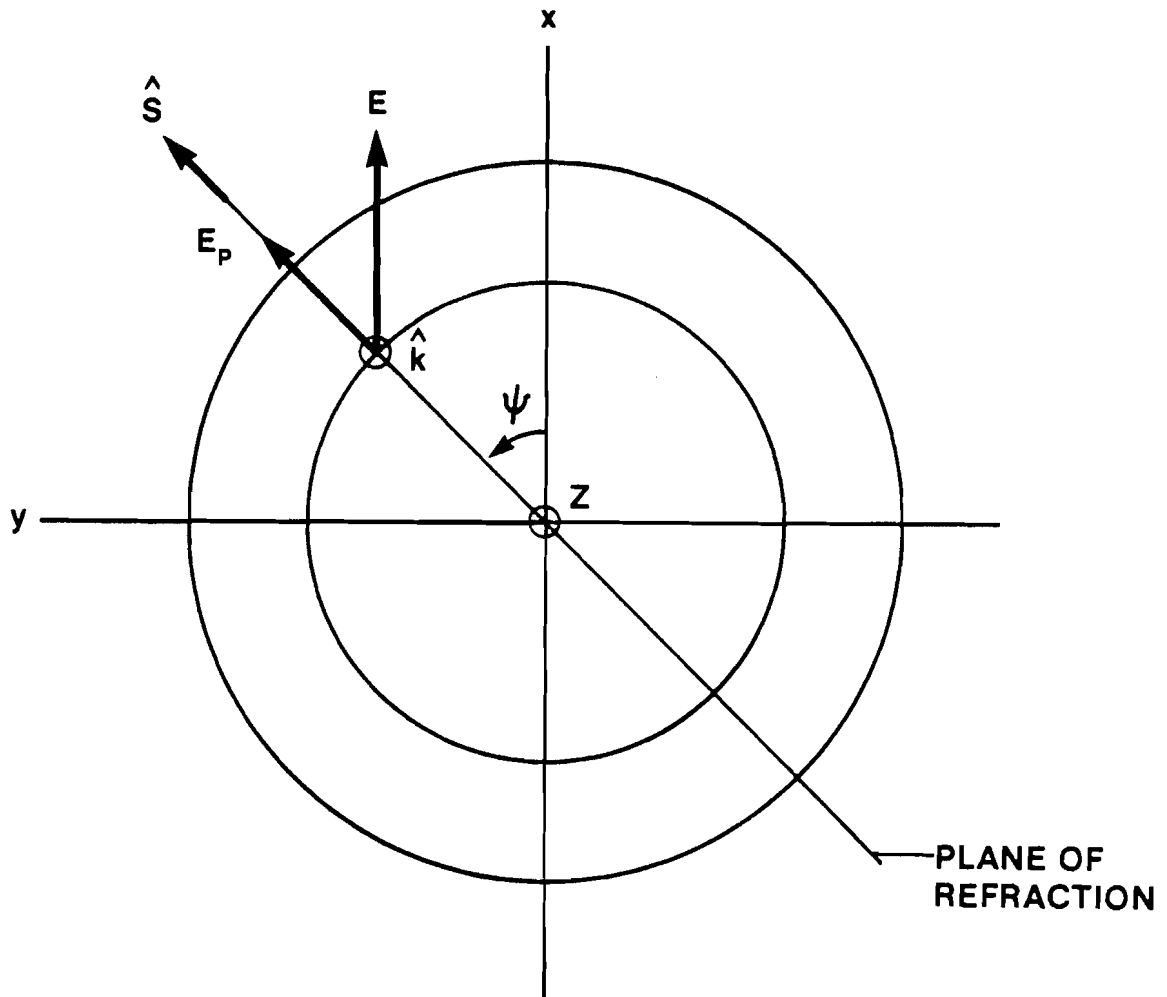
At any point within the laser beam focal spot the power of the p-component is

$$dP_p = I \cos^2 \psi \, d\psi \, s \, ds \quad (6-42)$$

For a Gaussian intensity profile

$$dP_p = \frac{P(t)}{\pi S^2} s e^{-s^2/S^2} \cos^2 \psi \, d\psi \, ds \quad (6-43)$$

'P(t)' is the power in the laser beam and 'S' is the focal spot radius within which 63% of the laser power is contained.



**GEOMETRY OF LINEARLY POLARIZED LIGHT
INCIDENT ON A SPHERICAL PLASMA
(VECTORS SHOWN PRIOR TO REFRACTION)**

FIGURE 6-8

The power absorbed is given by

$$P_{\text{RES}} = \int_{\text{FOCAL SPOT}} \eta_{\text{RES}} dP_p \quad (6-44)$$

Integrating over ψ results in the final equation

$$P_{\text{RES}} = \frac{P(t)}{S^2} \int_0^{S_{\text{max}}} \eta_{\text{RES}} s e^{-s^2/S^2} ds \quad (6-45)$$

For computational purposes ' S_{max} ' is taken as the value of ' S ' large enough so that the integrand effectively equals zero.

Figure 6-9 shows a plot of the fractional resonant absorption (absorbed power/laser power) as a function of scale length. Each curve is for a different critical surface location. The range of parameters covers those encountered in the experiment. The curves are cut off at $\lambda=1\mu\text{m}$ where the validity of the theory becomes questionable. Figure 6-10 shows the fractional resonant absorption as a function of critical surface location for several different scale-lengths. Both figures are for a focal spot with a gaussian intensity distribution with 80% of the energy within a $40\mu\text{m}$ radius. All the rays enter the plasma parallel to the optical axis.

Figure 6-10 shows the existence of a maximum in the possible resonant absorption. This value is about .16. For a given laser focal spot the maximum occurs with the proper combination of scale-length and critical surface radius. The solutions from references (6-11), done for a diffraction limited focal spot, reveal a quite similar behavior with a maximum possible resonant absorption of about .15 to .20. The maximum possible resonant absorption, thus, appears

FIGURE 6-9
**ABSORPTION EFFICIENCY OF RESONANT
 ABSORPTION AS A FUNCTION OF
 SCALELENGTH**

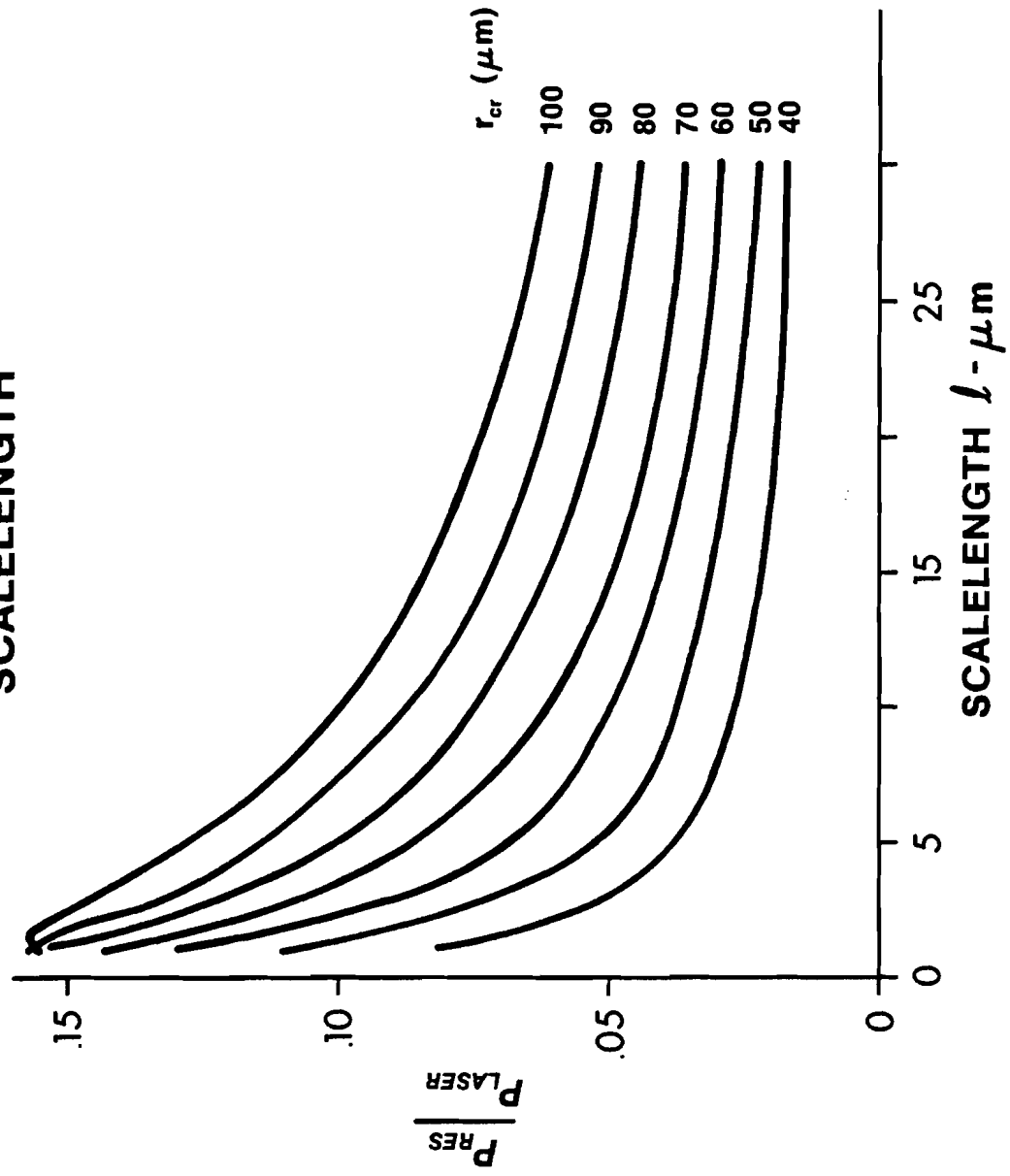
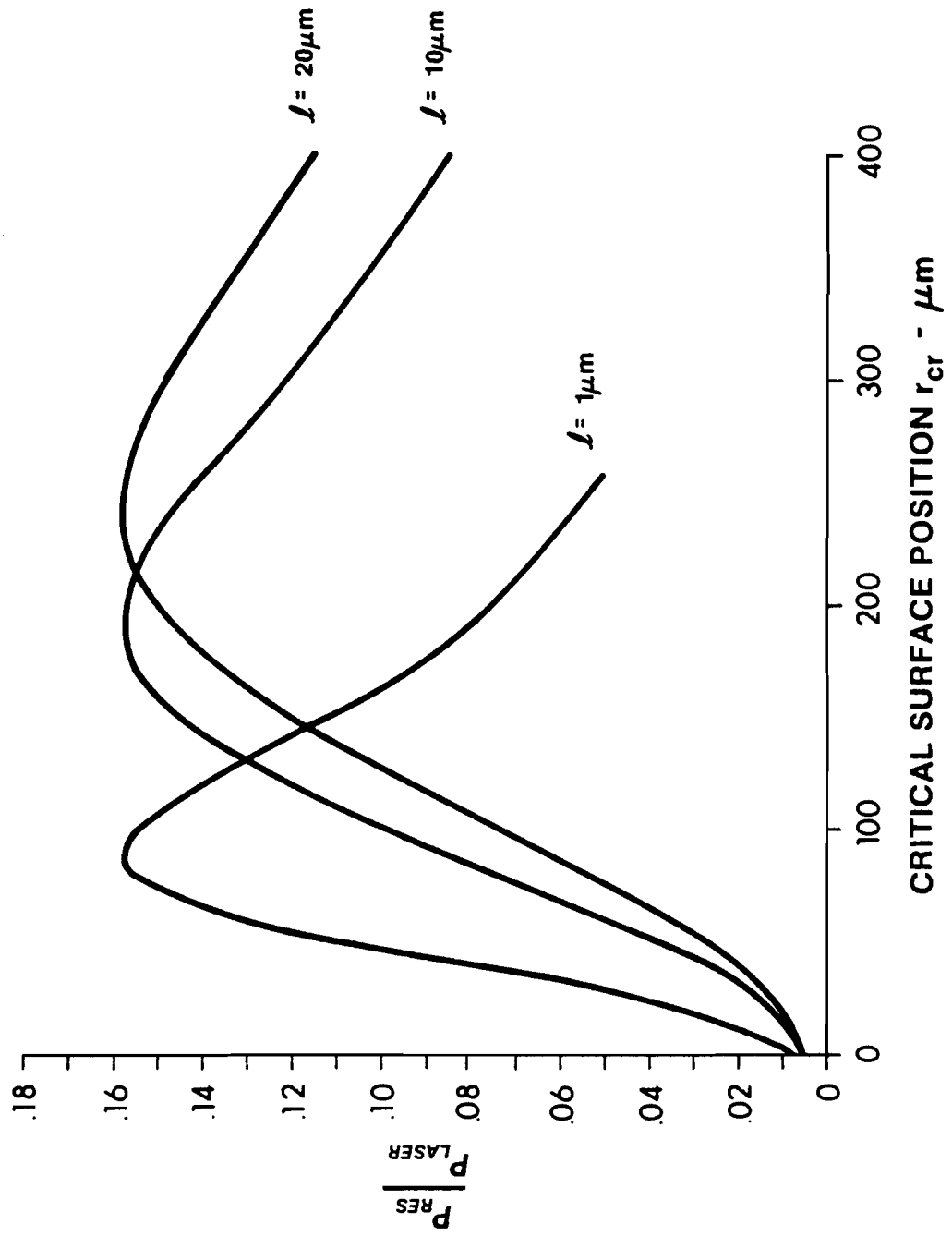


FIGURE 6-10
**ABSORPTION EFFICIENCY OF RESONANT
 ABSORPTION AS A FUNCTION OF CRITICAL
 SURFACE LOCATION**



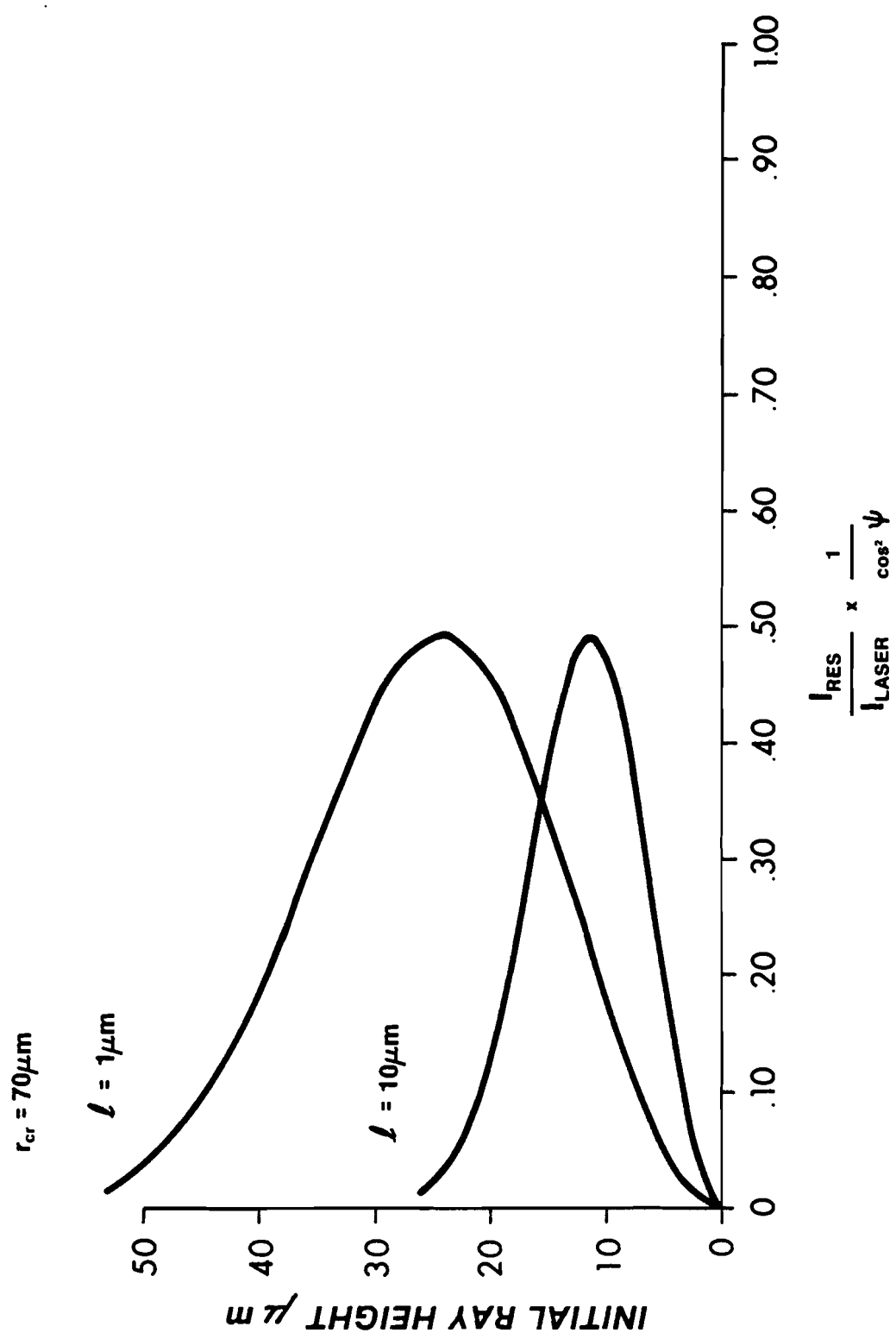
to be relatively insensitive to the focal spot geometry. The plasma conditions at peak absorption do, of course, vary.

Comparison of figures 6-4 and 6-9 reveals an opposite scalelength dependence between inverse bremsstrahlung and resonant absorption. Inverse bremsstrahlung increases and resonant absorption decreases as the scalelength increases. They are about equal, for $T_e = .8-1.2$, at $\ell \approx 3\mu\text{m}$. (The combined absorption will be computed in the next section.)

Examination of the spatial absorption profile is warranted by the concern for absorption symmetry in laser-fusion experiments. The first source of non-uniformity is the $\cos^2 \psi$ polarization dependence of resonant absorption for those rays entering the plasma with equal height (equation 6-41).

The other source of spatial variation is the resonant absorption dependence on initial ray height. Figure 6-11 shows the typical local resonant absorption dependence on initial ray height. At normal incidence there is no resonant absorption so that $I_{\text{RES}}/I_{\text{LASER}} = 0$ on axis. The curves peak off axis at $(I_{\text{RES}}/I_{\text{LASER}})_{\text{max}} \approx .5 \cos^2 \psi$. The peak occurs farther off axis for smaller scalelengths and larger critical surface radii. The areas under the curves $I_{\text{RES}}/I_{\text{LASER}}$ and $2\pi s \cdot (I_{\text{RES}}/I_{\text{LASER}})$ are larger for smaller ' ℓ ' and larger ' r_{cr} ', with ' ℓ ' and ' r_{cr} ' in the range of experimental interest. In determining total absorption, the area under the ' $I_{\text{RES}}/I_{\text{LASER}}$ ' resonant absorption curve weighs more heavily than the location of the peak resonant absorption. This can be seen by referring to figure 6-11 then back to figures 6-9 and 6-10.

FIGURE 6-11
**LOCAL RESONANT ABSORPTION AS A
 FUNCTION OF INITIAL RAY HEIGHT**



6.1.3 Combined Inverse Bremsstrahlung and Resonant Absorption

With the results of sections 6.1.1 and 6.1.2, the total inverse bremsstrahlung and resonant absorption can be calculated. This is done by calculating the inverse bremsstrahlung for the ray up to the turning point, the resonant absorption at the turning point, and the inverse bremsstrahlung as the ray leaves the plasma.

Figure 6-12 shows typical absorption behavior as a function of scalelength. Only at short scalelengths is there a significant departure from the oblique incidence inverse bremsstrahlung results. The comparison is shown in figure 6-13. It should be again noted that even at the optimum plasma conditions the peak resonant absorption is only 16%.

The absorption spatial profiles are again of interest. Examples are shown in figures 6-14 and 6-15. The plots show the local absorption intensity normalized to the on axis laser intensity. The gaussian laser beam profile has been convolved with the local fractional absorption. Curves 3 and 4 show the absorption perpendicular and parallel to the plane of polarization. Curves 1 and 2 show the resonant absorption and inverse bremsstrahlung components of the absorption in the plane of polarization. Resonant absorption produces an off-axis absorption peak which is clearly visible within the total absorption profile. The polarization dependence and spatial non-uniformity of resonant absorption can be used to experimentally confirm the presence of this absorption mechanism.

FIGURE 6-12

TOTAL FRACTIONAL ABSORPTION DUE TO INVERSE BREMSSTRAHLUNG AND RESONANT ABSORPTION

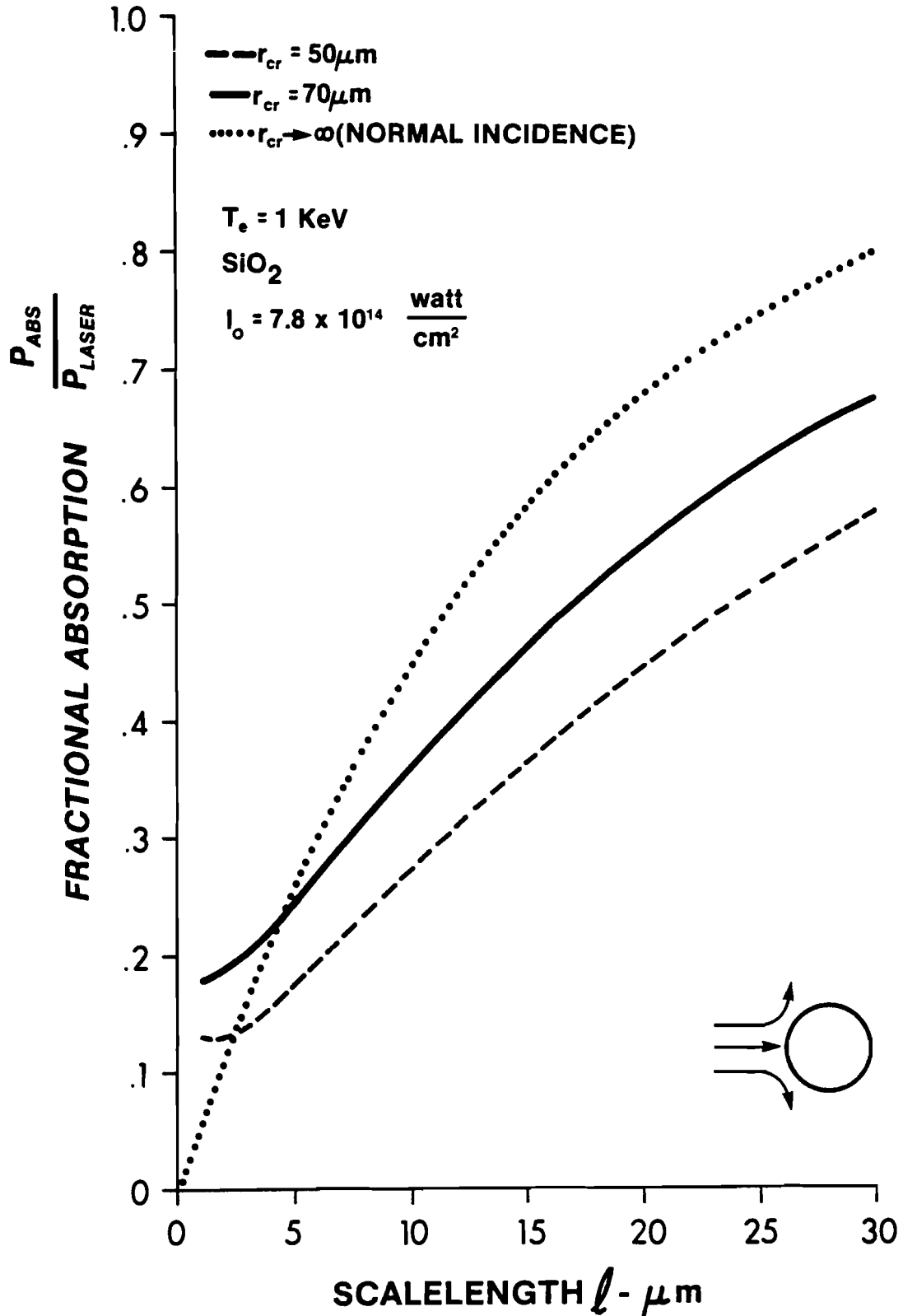


FIGURE 6-13

COMPARISON OF ABSORPTION WITH AND WITHOUT RESONANT ABSORPTION

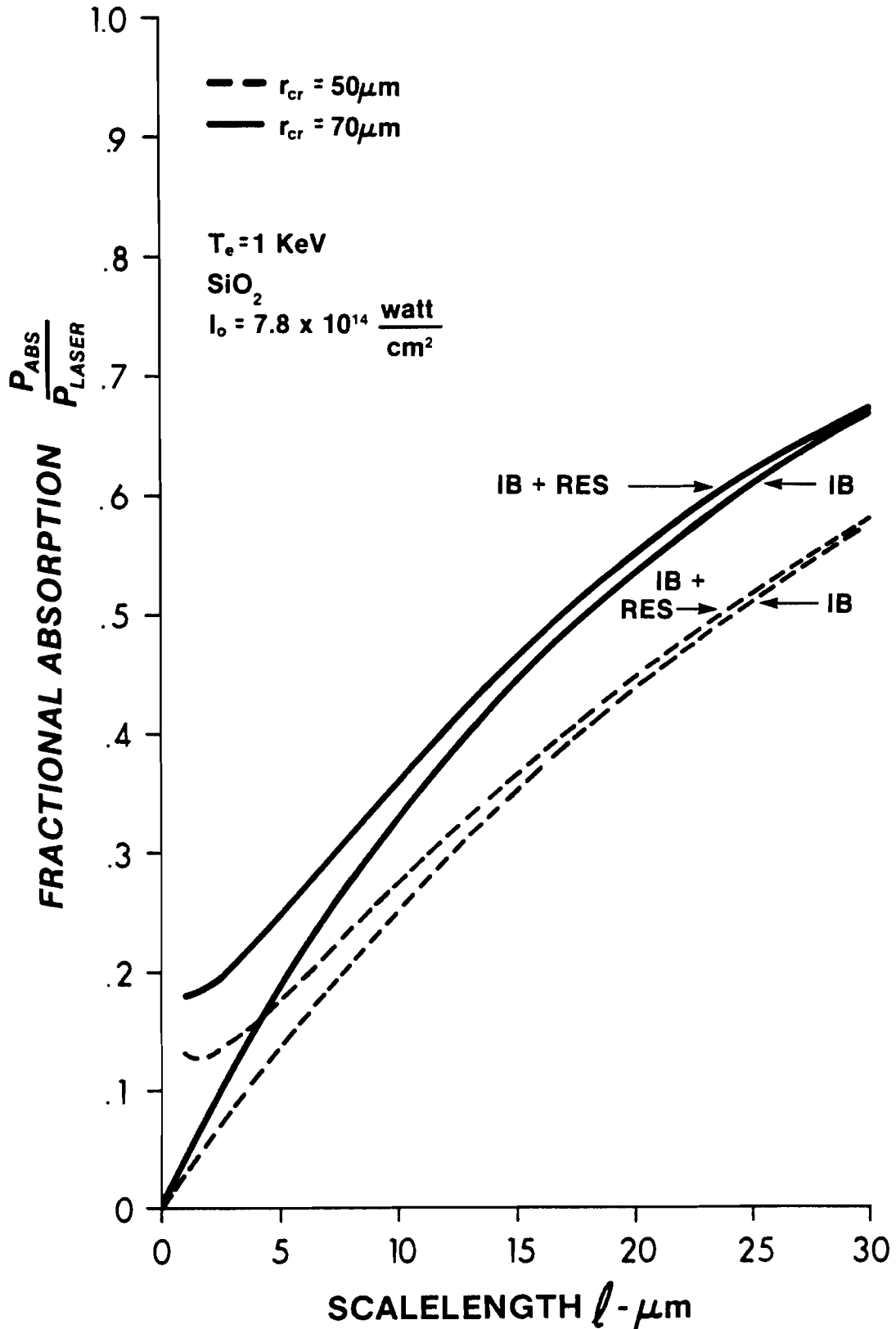


FIGURE 6-14
ABSORPTION PROFILES

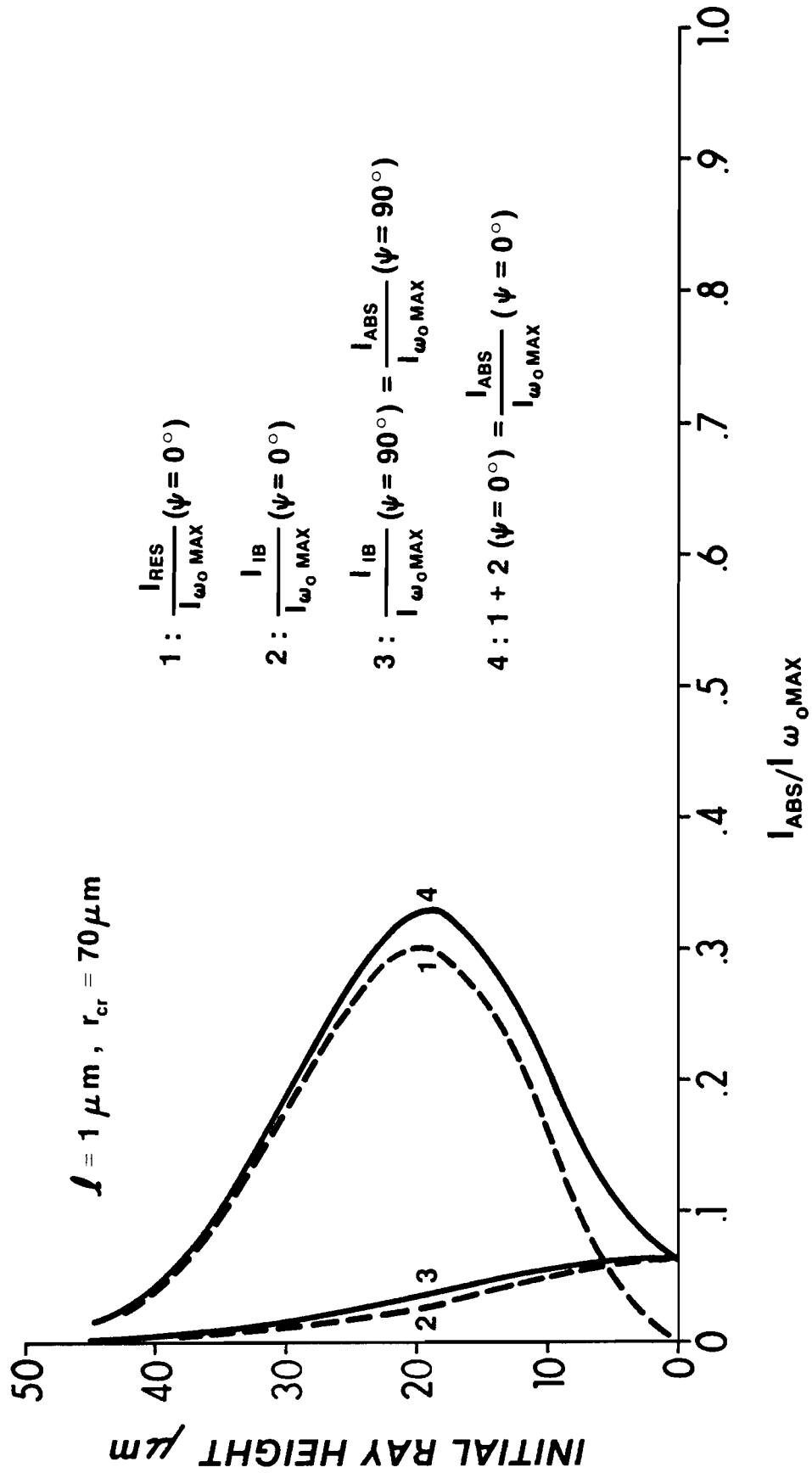
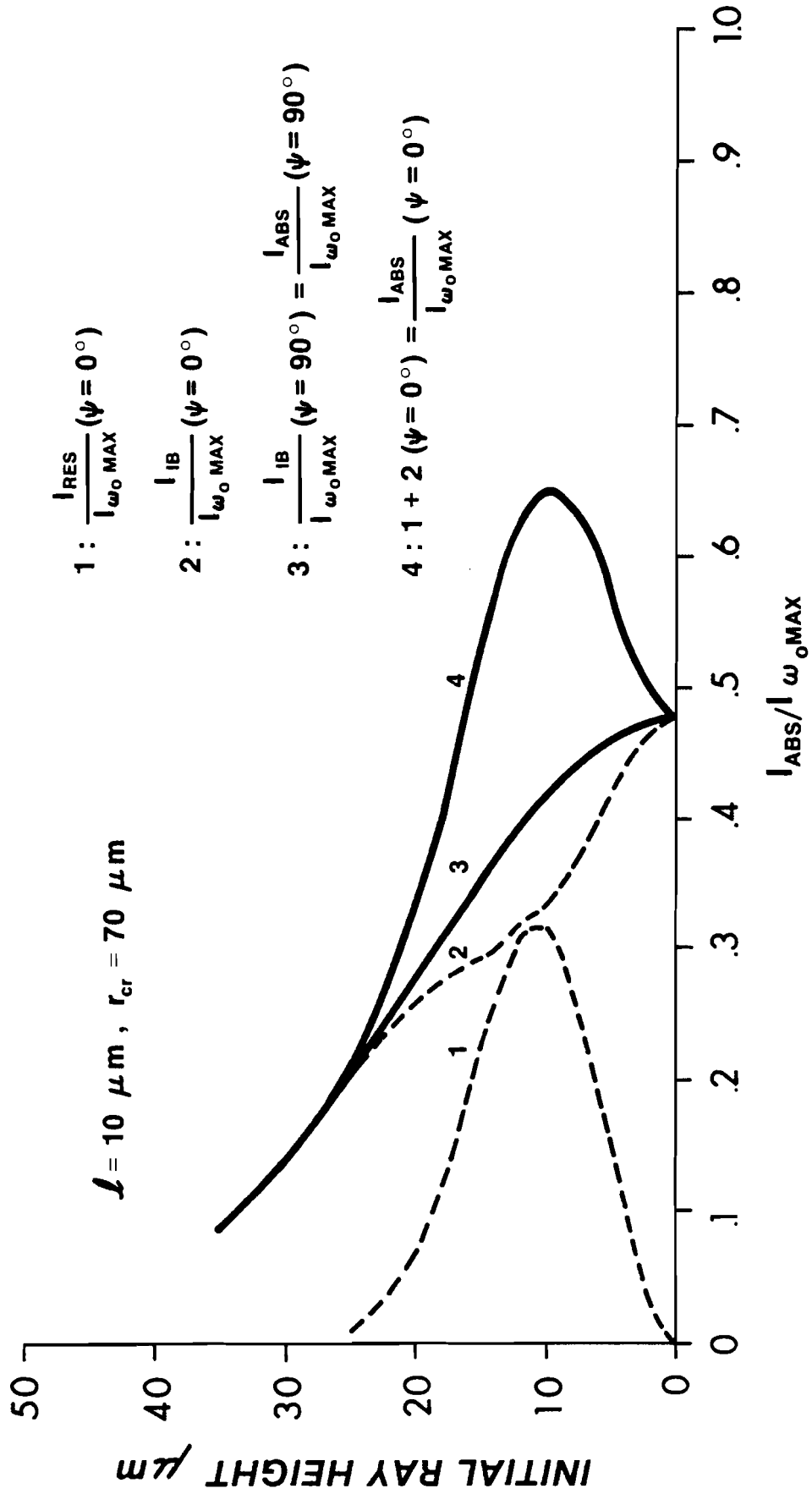


FIGURE 6-15

ABSORPTION PROFILES



6.1.4 Effect of Profile Modification on Absorption

The results of the previous absorption analysis were derived with the assumption of a smooth (linear) density profile. Modification of the plasma density profile in the critical density region is possible through the action of ponderomotive forces. The long term effect of such profile modification may be a steepening of the density profile. Such a steepening would affect the absorption.

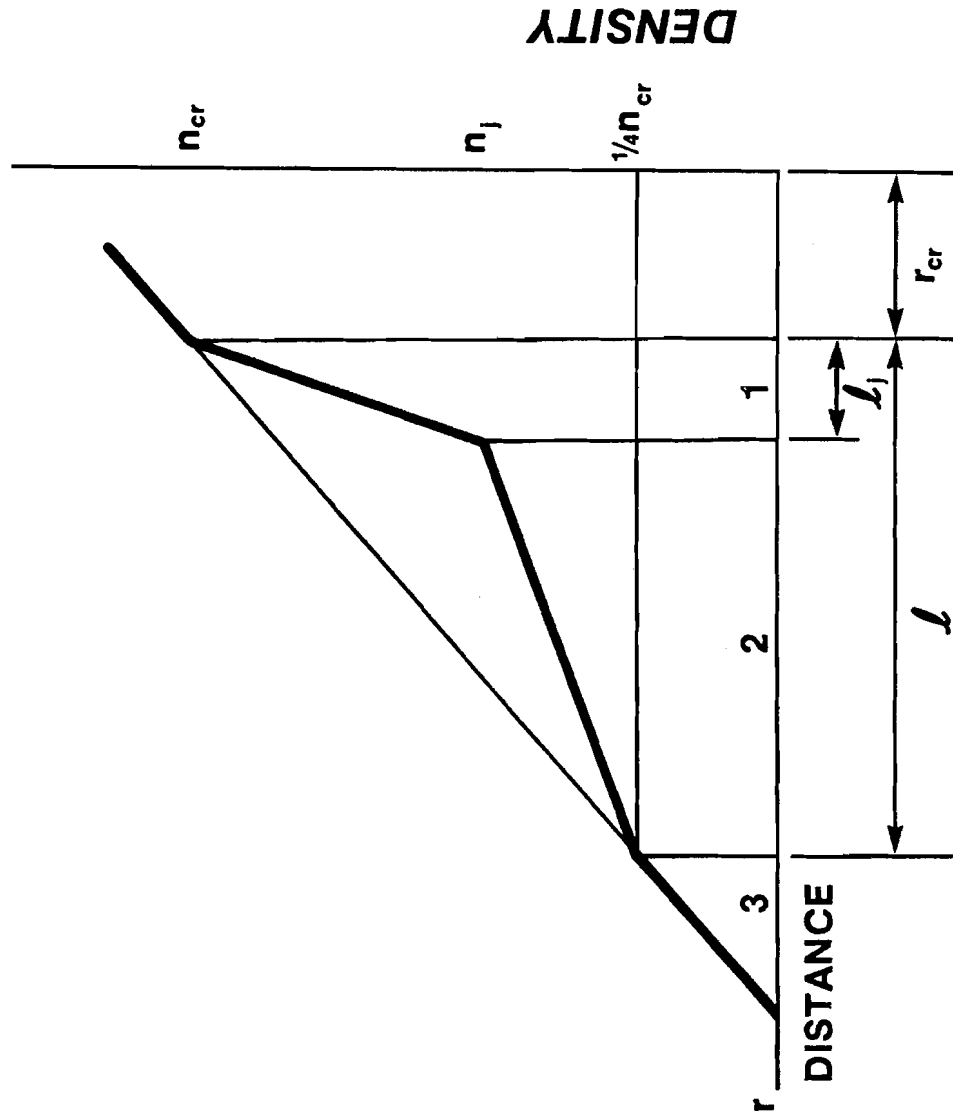
The $2\omega_0 - (3/2)\omega_0$ observations give the critical and quarter-critical density locations. Profile modification affects the results of the absorption calculations if the steepening does not extend to the quarter-critical density and is not detected.

To study the consequences of this sort of local steepening a profile of the form shown in figure 6-16 is studied. The critical and quarter-critical density locations are fixed. At the critical density, a steep gradient is assumed so that the density drops from ' n_{cr} ' to ' n_j ' in a distance ' l_j '. From ' n_j ' the density drops linearly to ' $\frac{1}{4}n_{cr}$ '. The slope of the profile below ' $\frac{1}{4}n_{cr}$ ' is assumed equal to that of the unmodified profile.

With such a density profile the absorption can be calculated according to the techniques of sections 6.2.1 and 6.2.2. Inverse bremsstrahlung is calculated using equations (6-15), (6-22) - (6-25) with the integral evaluated within each region of continuity

$$\sigma = \sum_{i=1}^3 \frac{1}{c\tau_{cr}} \left(\frac{16l_j}{3} \right) \int_{w_{min_i}}^{w_{max_i}} \left\{ \right\} dw \quad (6-46)$$

FIGURE 6-16
**STEEPENED DENSITY PROFILE FOR ABSORPTION
 CALCULATIONS**



The limits of integration are determined using the definition of w , the bounding values of 'r' for each region, and the ray turning point radius in each region. Unless the turning point exists within the bounds of a particular region the turning point is "virtual" and is never reached. A "real" turning point must exist for each ray within one of the three regions, and this point demarks the lower limit of integration.

Resonant absorption solutions are available only for linear density profiles. Reasonable agreement can be expected for those rays which have their turning point in region 1. There the profile between the turning point and the critical surface is linear. For rays with turning points in regions 2 and 3 there is no direct analogy to the linear profile solutions. To obtain an estimate of resonant absorption for the rays with turning points in regions 2 and 3 an equivalent linear density profile is determined such that the ray turning point and critical surface locations are equal. The resonant absorption is then calculated using equations (6-38, 39, 45) and Figure 6-6.

The results are shown in figures 6-17 and 6-18. Figure 6-17 shows the effect of a density jump on absorption in the normal incidence geometry. Absorption is due only to inverse bremsstrahlung. The density jump magnitude is given by the ratio of the density at the jump to the critical density ($\xi_j \equiv n_j/n_{cr}$). $\xi_j = 1$ corresponds to an unmodified density profile. ' λ_j ' has been assumed equal to zero in this example.

FIGURE 6-17

EFFECT OF A DENSITY JUMP ON FRACTIONAL ABSORPTION-NORMAL INCIDENCE

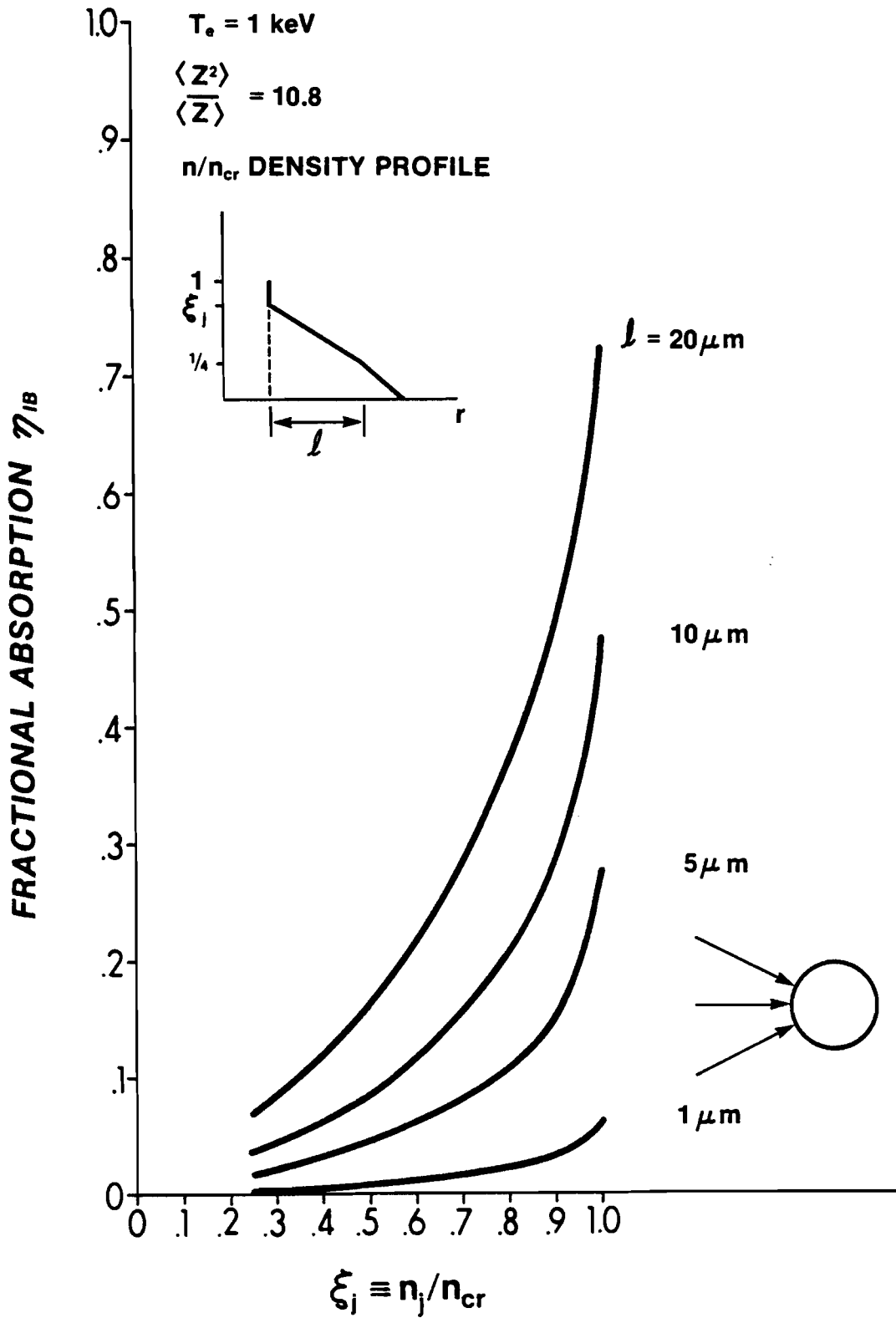
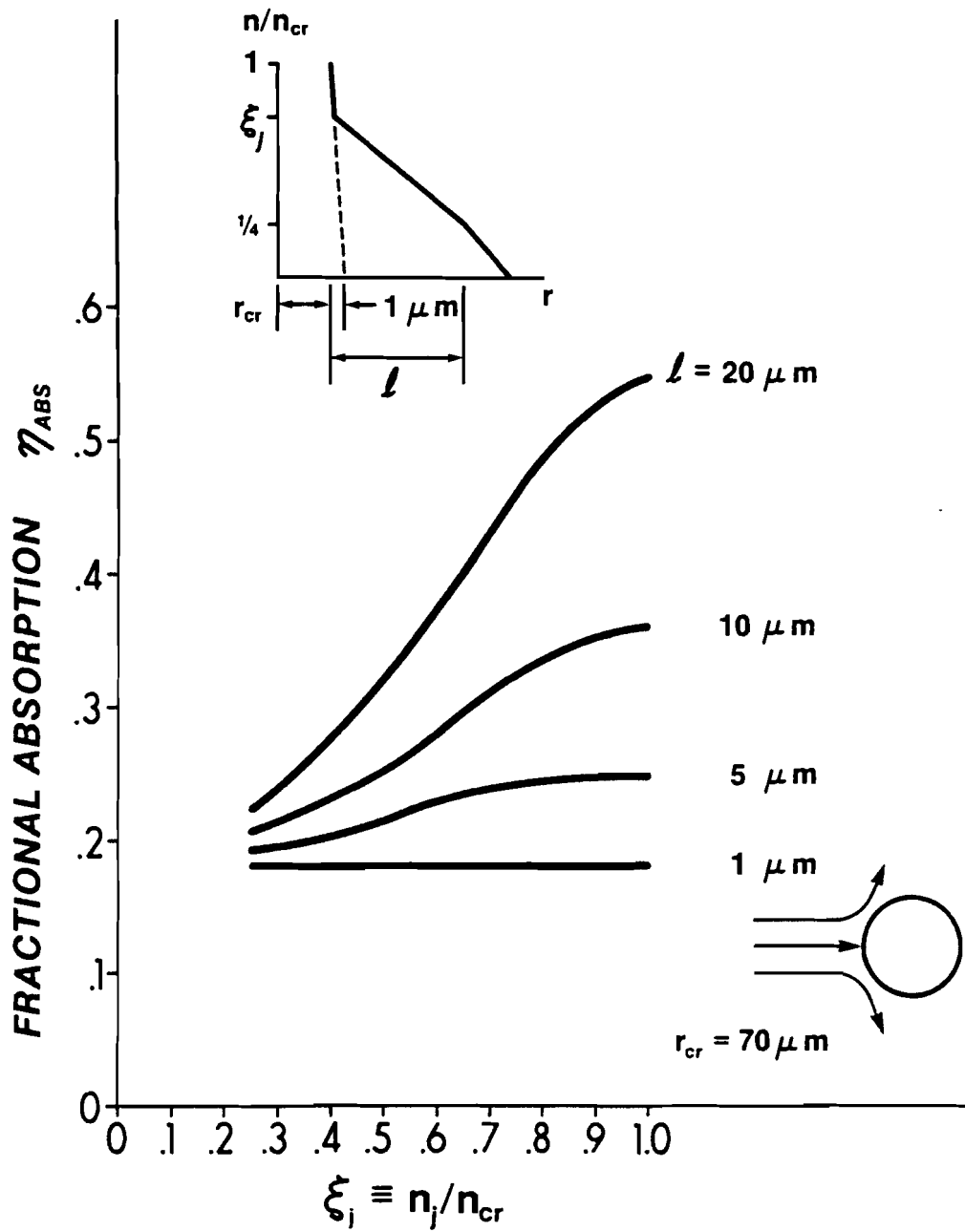


FIGURE 6-18
**FRACTIONAL ABSORPTION FOR OBLIQUELY INCIDENT
 LIGHT IN THE PRESENCE OF A DENSITY JUMP**



The steep slope of the ' η_{IB} ' curves for large ' ξ_j ' shows the importance to inverse bremsstrahlung absorption of the plasma at densities near critical. A density jump of $\xi_j \approx .8-.9$ reduces the absorption by a factor of two. Large density jumps (smaller ξ_j) would reduce the absorption to low values.

Figure 6-18 shows the absorption in the oblique incidence geometry. The resonant absorption theory used here requires that for meaningful analysis the density jump scalelength is finite. For the example shown the slope in the steepened region was assumed constant and of a value such that the density dropped from $n=n_{cr}$ to $n=0$ in $1\mu m$. ' ξ_j ' was varied.

As the density jump increases the absorption decreases but not as rapidly as in the normal incidence geometry. In the oblique incidence geometry the interpretation of the experimental results would not be substantially modified unless a large undetected density jump were present. The absorption dependence on ' ξ_j ' is determined by the counterbalancing inverse bremsstrahlung decrease and resonant absorption increase with decreasing ' ξ_j '. Note that the minimum possible absorption is always greater than or equal to the absorption of a plasma with a slope equal to that of the steepened region.

6.1.5 - Application of Absorption Theory to the Experimental Data

The absorption theory developed in the previous sections of this chapter can be applied to the experimental data obtained in the experiment. In this section absorption histories are obtained by convolving the time resolved scalelengths and laser pulse histories, using the absorption theory for oblique incidence light upon spherical plasmas

with linear density gradients. After the absorption histories are presented and the general features pointed out, the total fractional absorptions obtained from the streaked data are computed and compared to the fractional absorptions obtained from time integrated peak excursion data. The calculated fractional absorptions are then compared with values obtained simultaneously by independent measurements.

Figures 6-19, 20, 21, 22, 23 show the time resolved absorption histories per beam for the shots in which complete critical and quarter-critical trajectories were obtained. Shown are the incident pulse, the total absorbed power, and the components of the absorption due to inverse bremsstrahlung and resonant absorption.

The first thing to notice is that for about the first 100 psec, the absorbed power per four beams is relatively low at about .01 - .02 tw. A significant fraction of the absorption during this period is due to resonant absorption. After about one laser pulse rise time the plasma scalelength develops (Chapter 5). Absorption due to inverse bremsstrahlung increases and dominates over the resonant absorption contribution.

Table 6-1 shows the absorbed energies per beam computed for the duration of the time resolved scalelength data. Also shown are the fractional absorptions. For these shots the absorption can be characterized as being typically from 20% to 40%.

Since time integrated data is easier to obtain, it is of interest to determine the accuracy of absorption fractions calculated from peak excursion data. Comparing η'_{ABS} from table 6-1 to the

FIGURE 6-19

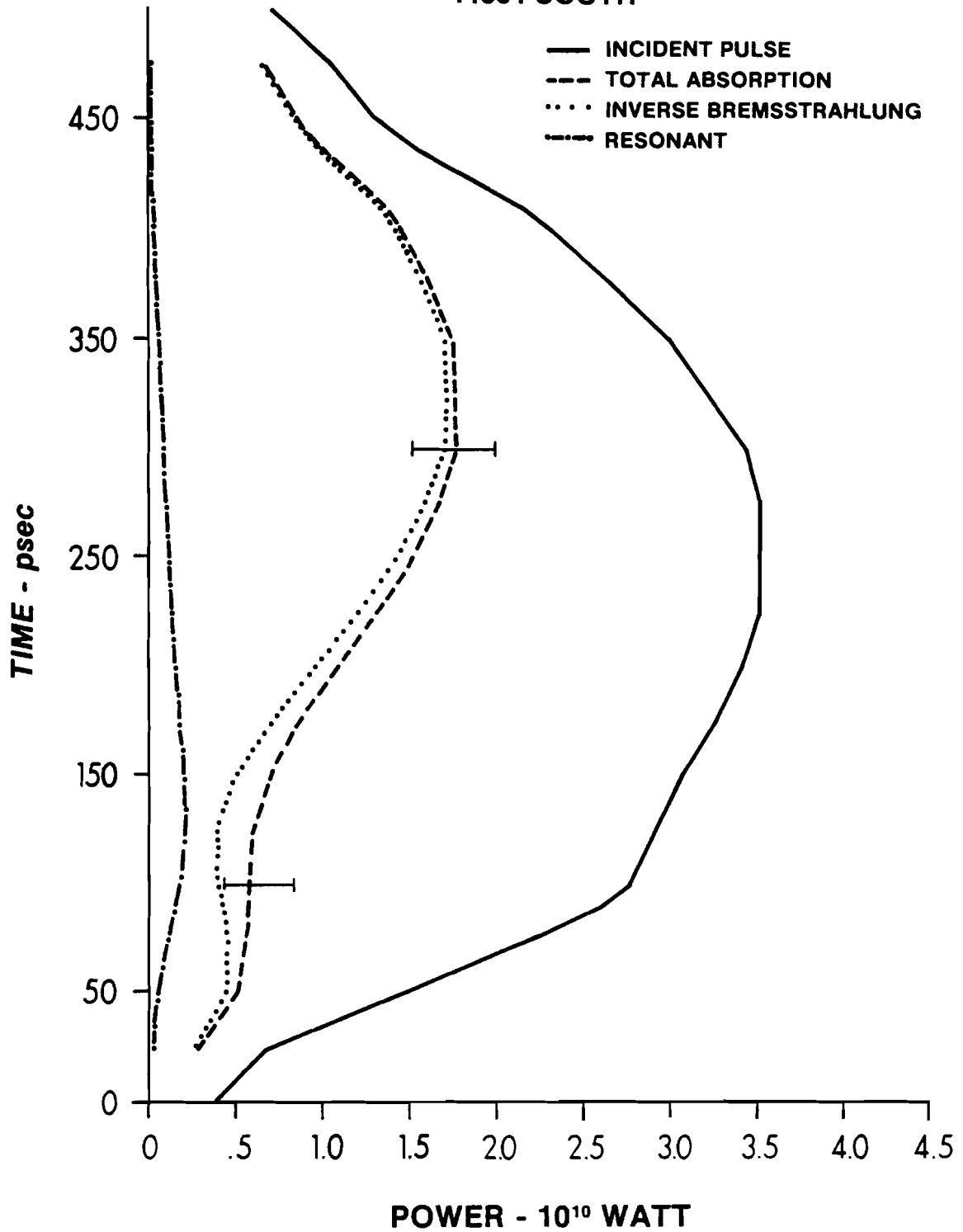
ABSORPTION HISTORY/BEAM**11534 SOUTH**

FIGURE 6-20

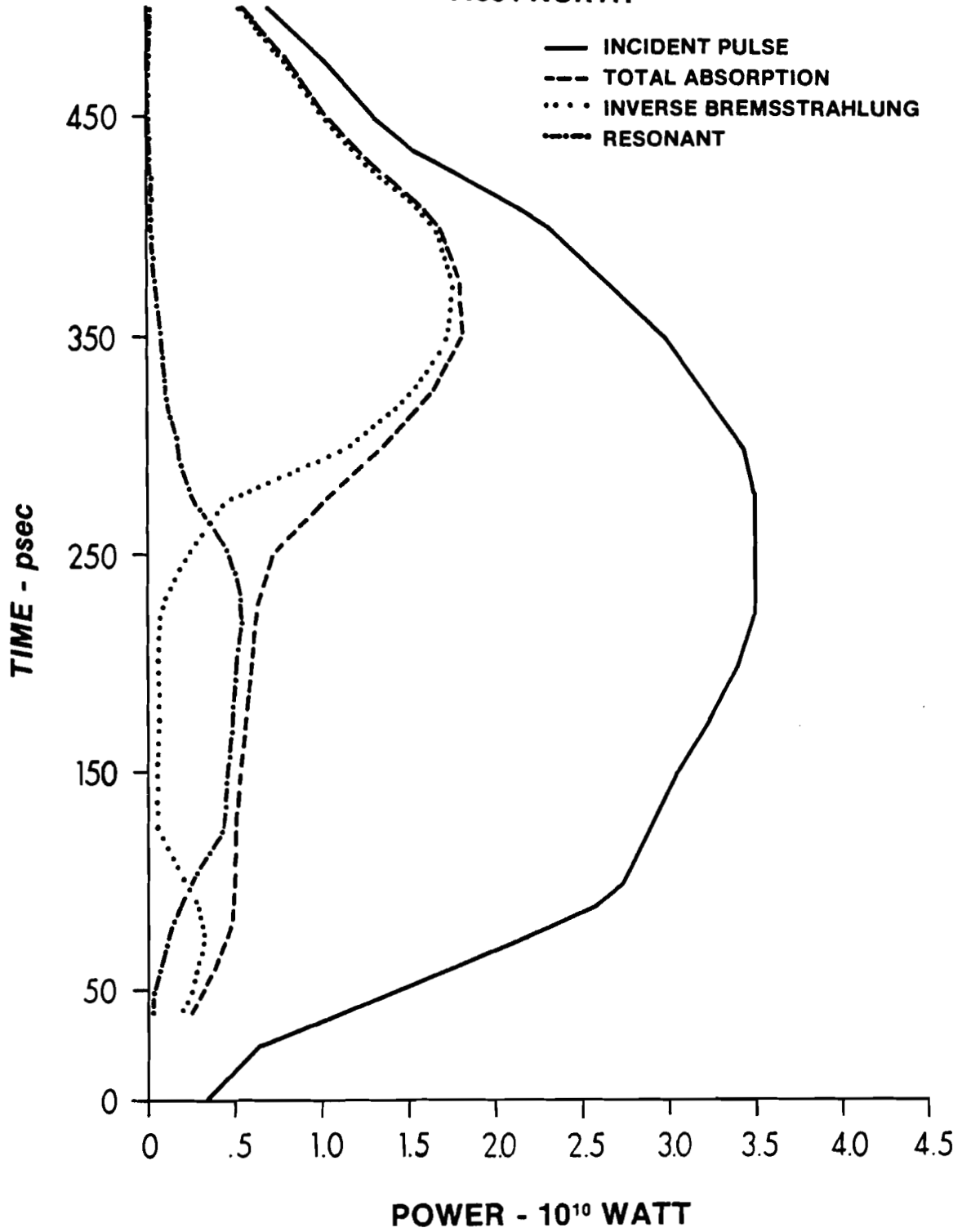
ABSORPTION HISTORY/BEAM**11534 NORTH**

FIGURE 6-21

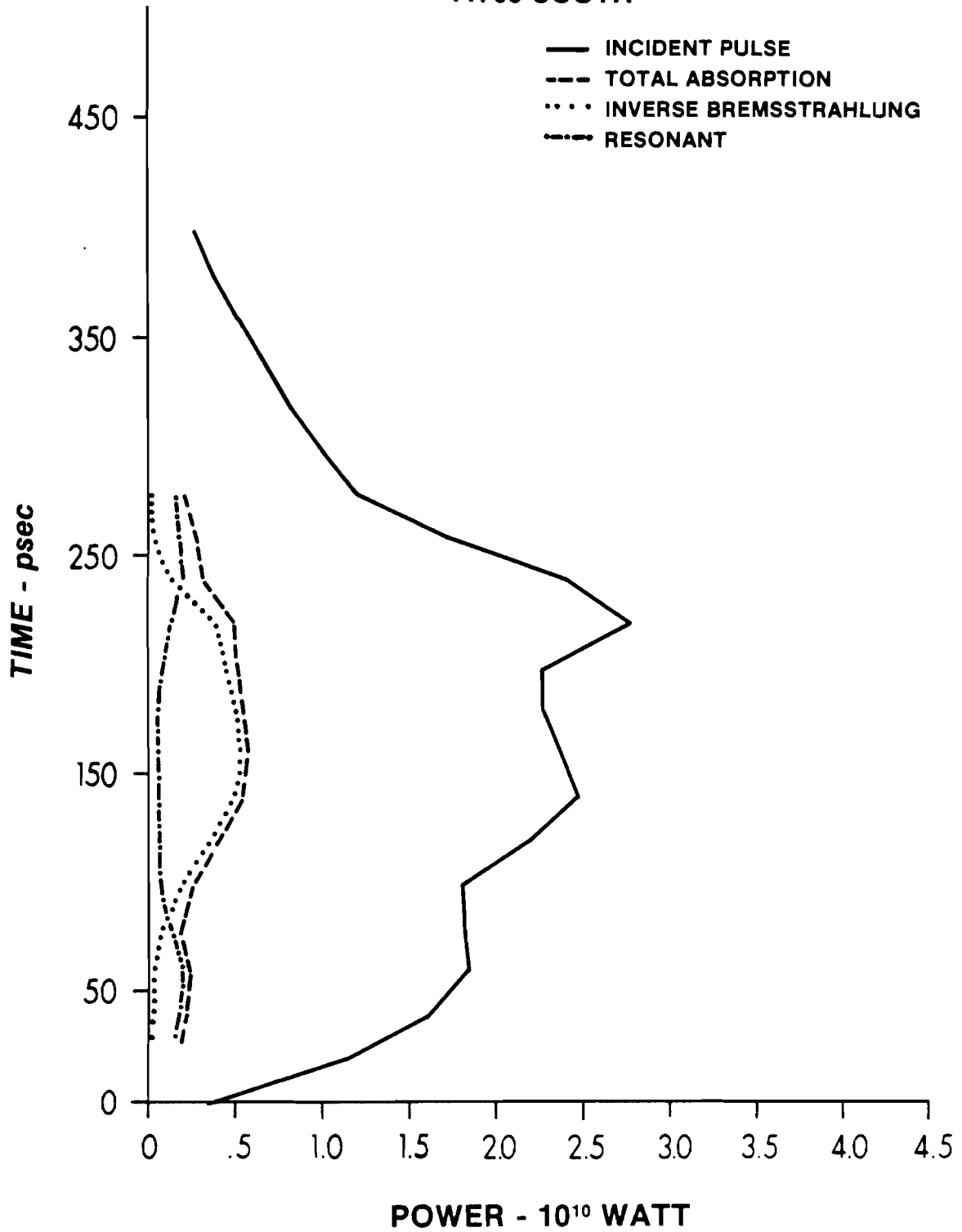
ABSORPTION HISTORY/BEAM**11709 SOUTH**

FIGURE 6-22

ABSORPTION HISTORY/BEAM

11710 SOUTH

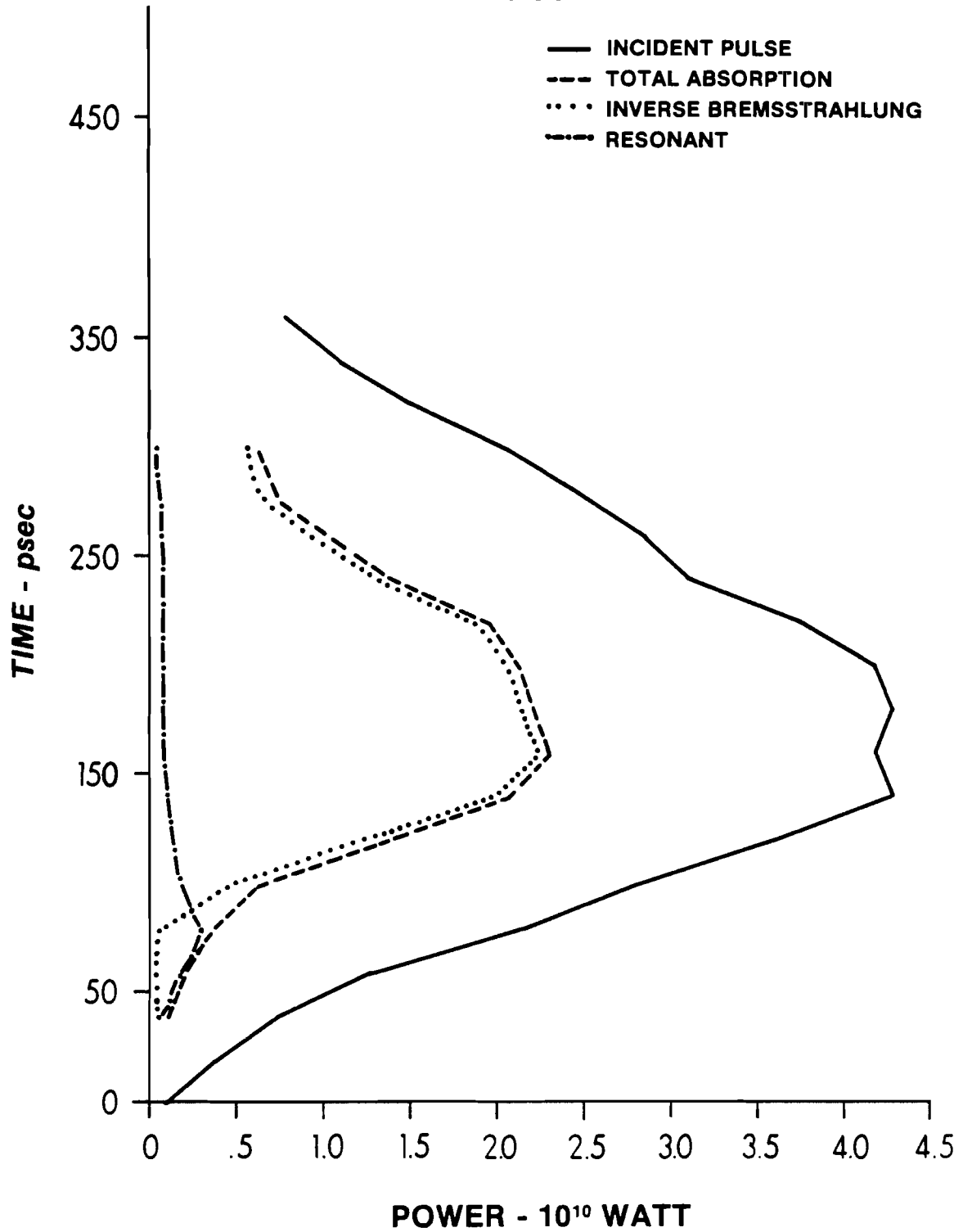
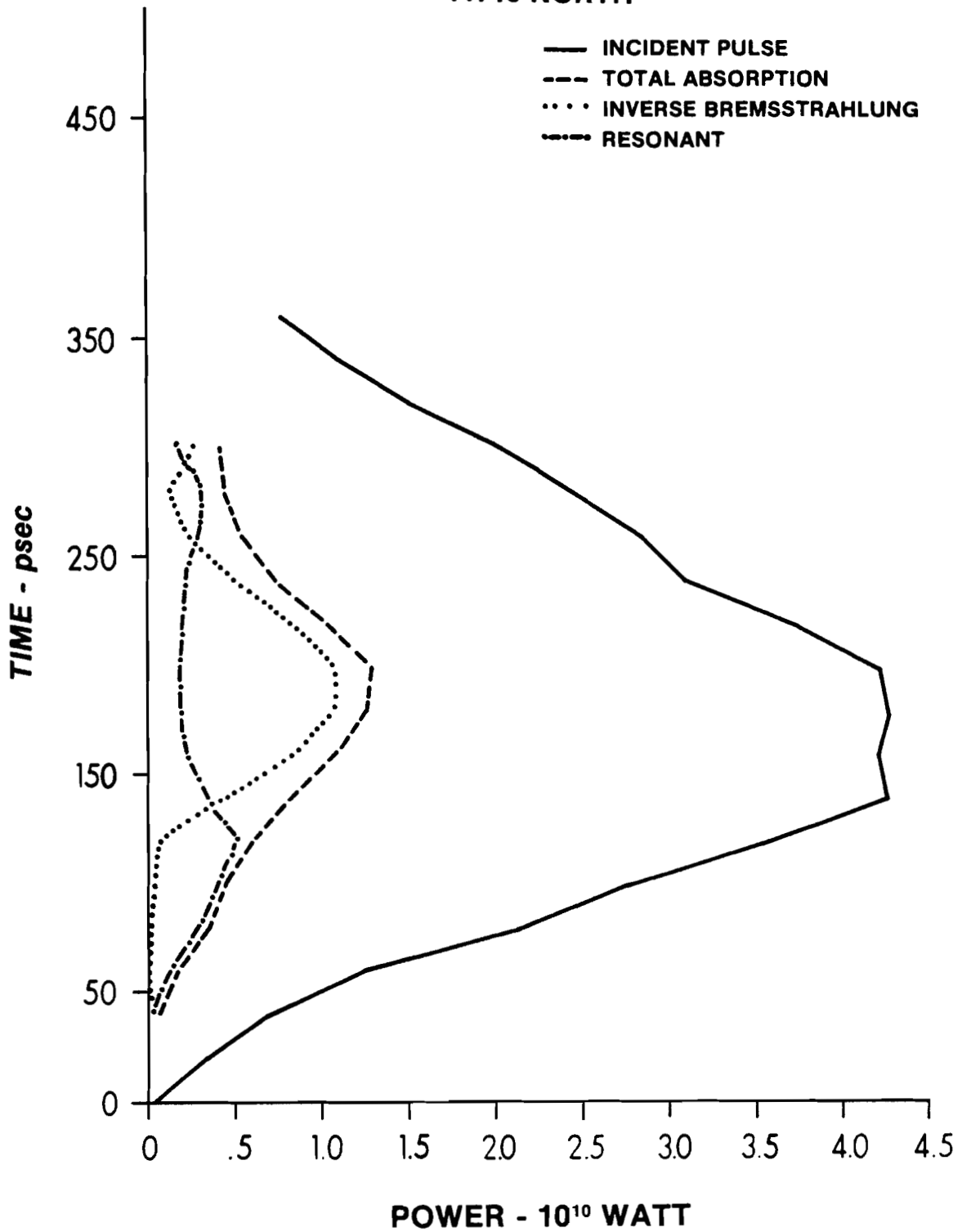


FIGURE 6-23

**ABSORPTION HISTORY/BEAM
11710 NORTH**

CALCULATED PER BEAM FOR DURATION OF STREAKED SCALE LENGTH DATA

Shot	E_{Target}	E_{Target}^1	E_{ABS}^1	E_{IB}^1	E_{RES}^1	η_{ABS}^1	η_{IB}^1	η_{RES}^1
11534 South	12.5joules	12.2 joules	5.3joules	4.8joules	.5joules	.43	.39	.04
11534 North	12.5	12.2	4.3	3.3	1.0	.35	.27	.08
11709 South	6.2	5.2	.8	.5	.2	.15	.10	.05
11710 South	9.0	8.0	3.5	3.3	.2	.44	.41	.03
11710 North	9.0	8.0	2.0	1.2	.8	.25	.15	.10

ABSORPTION CALCULATED FROM STREAKED DATA

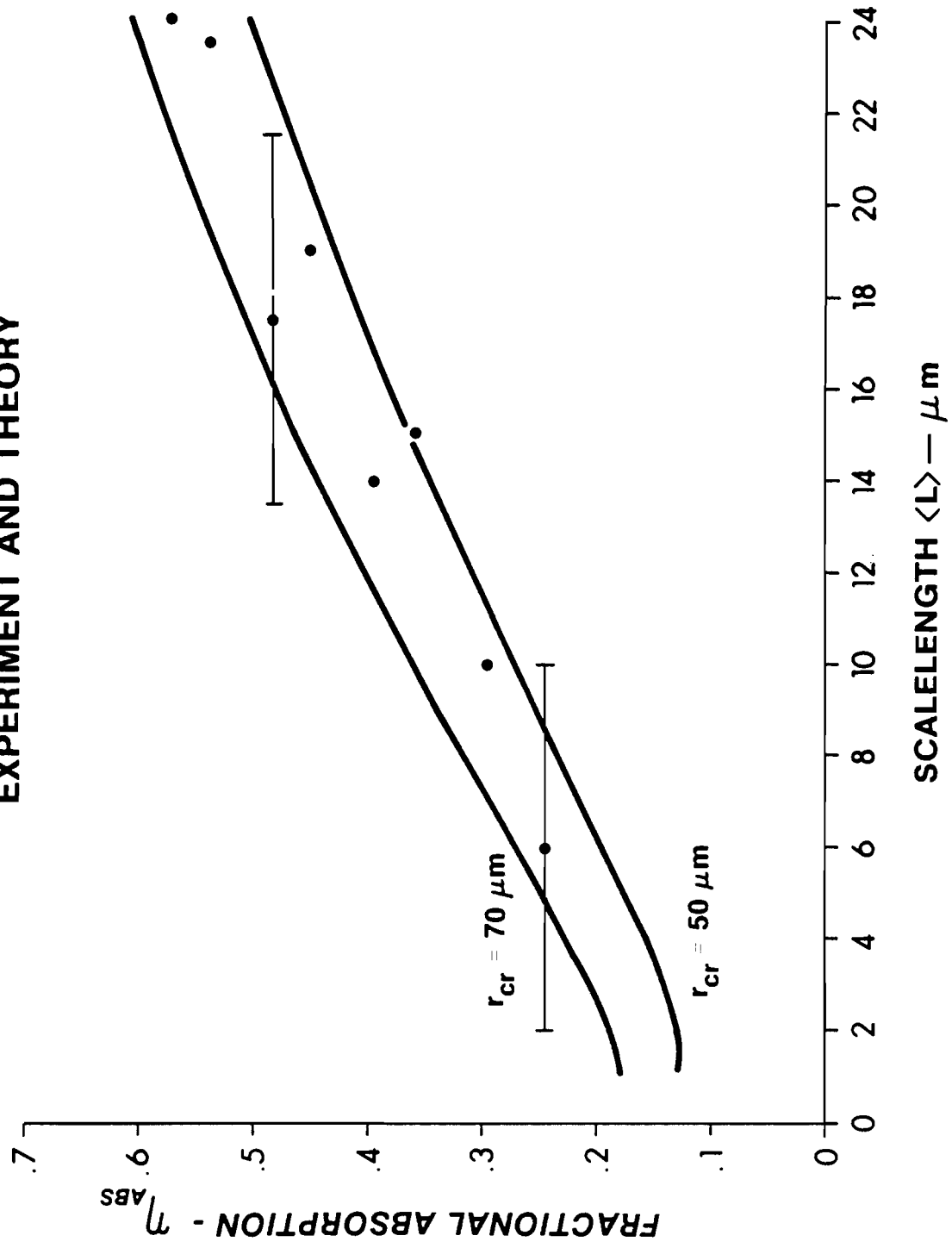
TABLE 6 - 1

fractional absorptions computed from the peak excursions it is found that the time integrated data can overestimate the calculated absorption by $40\% \pm 20\%$. The size of this factor indicates that, although a detailed calculation using time integrated data might not be justified, many aspects of absorption physics can be studied just with peak excursion data.

One question that can be answered through use of the peak excursion data is whether the theoretical scalelength dependence of absorption (figure 6-13) agrees with the experimental observation. Figure 6-24 shows the result. The fractional absorption has been plotted as a function of scalelength. The points are the experimental data of GROUP A (Chapter 5) and the solid lines correspond to the theoretical bounds within which the data is expected to lie. The fractional absorption is observed to vary by a factor of two for a factor of four variation in the scalelength. The good agreement shows a scalelength dependence of absorption as predicted by the theory of inverse bremsstrahlung plus resonant absorption. In terms of total energy absorbed, inverse bremsstrahlung dominates for the laser pulses of this experiment.

$$(I_{\text{TARGET}} \lesssim 10^{15} \frac{\text{watt}}{\text{cm}^2}, \quad \tau_{\text{FWHM}} = 200 - 500 \text{ psec.})$$

FIGURE 6-24
SCALELENGTH DEPENDENCE OF ABSORPTION
EXPERIMENT AND THEORY



6.2 Refraction of Light Through a Plasma

Light refraction in a plasma is a fundamental process in this study. In the previous section refraction was shown to strongly influence the laser light absorption of the plasma. In Chapter 3, refraction was shown to possibly distort the images of the critical and quarter-critical density surfaces produced by the $2\omega_0$ and $(3/2)\omega_0$ emissions.

In this section light refraction is studied through the use of ray tracing techniques. The methods developed here follow those used by Born and Wolf in the study of ray propagation through dielectric media.⁽⁶⁻¹²⁾ This procedure obviates the need for solving the complete wave equation by making the assumption that over the period of one free space optical wavelength ' λ_0 ' the plasma parameter variation, characterized by ' ℓ ', is small i.e., $\lambda_0/\ell \ll 1$. Taking the limit of $\lambda_0/\ell \rightarrow 0$ the wave equation is greatly simplified. Solution of the resulting equation, "the eikonal equation", yields the trajectories of transverse electromagnetic waves in inhomogeneous media.

6.2.1 Eikonal Equation

The eikonal equation is derived by using the electron equation of motion and Maxwell's equations. Instead of looking for plane wave solutions as was done in Section 6.1, solutions are sought for the propagation of waves of the more general form:

$$\bar{E} = \bar{E}_0(\bar{r}) e^{i(k_0 L(\bar{r}) - \omega t)} , \bar{B} = \bar{B}_0(\bar{r}) e^{i(k_0 L(\bar{r}) - \omega t)}$$

where $k_0 \equiv \omega/c$. Let the plasma response be assumed to be:

$\vec{v} = \vec{v}_1(\vec{r})e^{i(k_0 L(\vec{r}) - \omega t)}$ and $n_e = Zn_i + n_1 e^{i(k_0 L(\vec{r}) - \omega t)}$ for the electron velocity and density. Substituting these wave and particle response forms into equation (6-1) and Maxwell's equation, and solving for a single equation in \vec{E}_0 results in the wave equation:

$$i \left\{ \nabla L \times (\nabla L \times \vec{E}_0) + \left[1 - \frac{1}{(1+i/\tau_c \omega)} \frac{n_e}{n_{cr}} \right] \vec{E}_0 \right\} + \frac{1}{k_0} \left[\nabla \times (\nabla L \times \vec{E}_0) + \nabla L \times (\nabla \times \vec{E}_0) \right] - \frac{i}{k_0^2} \left[\nabla \times (\nabla \times \vec{E}_0) \right] = 0 \quad (6-47)$$

The plasma parameter variation appears in ' $\vec{E}_0(\vec{r})$ ', ' $L(\vec{r})$ ', their spatial derivatives, and in the position dependence of ' n_e ' and ' τ_c '. Assuming that the characteristic scalelength of these variations is of order ' ℓ ' and that this length is long compared to the vacuum wavelength, then $k_0 \ell = \frac{\lambda_0}{2\pi \ell} \ll 1$. For this situation, the terms in the first bracket predominate. Equation (6-47) reduces to

$$\nabla L \times (\nabla L \times \vec{E}_0) + \left[1 - \frac{1}{(1+i/\tau_c \omega)} \frac{n_e}{n_{cr}} \right] \vec{E}_0 = 0 \quad (6-48)$$

In the limit of weak collisions, the limit of experimental interest, $\tau_c \omega \ll 1$. If $L = L_R + i L_I$ this limit implies that $L_R/L_I \gg 1$ and that for ray trace purposes $L \approx L_R$ except in the vicinity of the critical surface. (This is the same as the conclusion reached from the plane wave analysis of Section 6.1.1 where $k_R/k_I \gg 1$ for $\tau_c \omega \gg 1$

except near the critical surface.) Equation (6-48) reduces to the "eikonal equation"

$$(\nabla L)^2 = \mu^2 \quad (6-49)$$

where $(\nabla L)^2 \equiv \nabla L \cdot \nabla L$ and $\mu^2 = 1 - n_e/n_{cr}$.

To obtain a vector form of the eikonal equation note that a unit vector parallel to the direction of propagation ' \hat{e} ' is also perpendicular to a surface of constant phase $L(\vec{r}) = \text{CONST.}$ ' \hat{e} ' is given by

$$\hat{e} = \frac{d\vec{r}}{ds} = \frac{\nabla L}{|\nabla L|} \quad (6-50)$$

so that

$$\nabla L = \mu \frac{d\vec{r}}{ds} = \mu \hat{e} \quad (6-51)$$

' \hat{e} ' is commonly known as the "ray vector".

It is convenient to express equation (6-51) in a form that contains only ' μ ', ' \hat{e} ' and their derivatives. For this purpose equation (6-51) is differentiated with respect to the path length

$$\frac{d}{ds} (\mu \hat{e}) = \frac{d}{ds} (\nabla L) = \frac{d\vec{r}}{ds} \cdot \nabla (\nabla L)$$

Using equation (6-51)

$$\frac{d}{ds} (\mu \hat{e}) = \frac{1}{\mu} \nabla L \cdot \nabla (\nabla L) = \frac{1}{2\mu} \nabla [(\nabla L)^2]$$

and using equation (6-49)

$$\frac{d}{ds} (\mu \hat{e}) = \nabla \mu \quad (6-52)$$

This "ray trace" equation can be used to trace any sort of transverse electromagnetic wave through any sort of plasma as long as the ray trace conditions remain satisfied.

To determine the ray trace validity limits of equation (6-52), an order-of-magnitude estimate of the wave equation, equation (6-47), is performed. Denoting a spatial derivative by ('), the wave equation, equation (6-47), becomes in this estimate:

$$i \left(2\mu^2 E_0 \right) + \frac{1}{k_0} \left(\mu' E_0 + 2\mu E_0' \right) - \frac{i}{k_0^2} \left(E_0'' \right) = 0 \quad (6-53)$$

where $|\nabla L|$ has been set equal to μ . The ray trace analysis holds if the first bracketed term predominates. This is true if:

$$\frac{\mu'}{k_0 \mu^2} \ll 1 \quad (6-54)$$

$$\frac{E_0'}{k_0 \mu E_0} \ll 1 \quad (6-55)$$

$$\frac{E_0''}{k_0^2 \mu^2 E_0} \ll 1 \quad (6-56)$$

These conditions break down near the critical surface where $\mu \rightarrow 0$ and near the turning point where E_0' and E_0'' may be large. Even if

the theory breaks down at these points, a complete trajectory can be obtained since the ray can be traced to the vicinity of the breakdown and the point of breakdown is also approximately known. What cannot be obtained is the structure of the fields.

6.2.2 Light Refraction Through a Spherical Plasma

Plasmas generated in the experiment are to a first approximation spherical. To study refraction in such plasmas an integral form of equation (6-52) can be obtained that gives a constant along the ray path. This result, known as Bouguer's formula, is valid for spherical or cylindrical plasmas where the index of refraction is a function only of the radial distance from the point or axis of symmetry.

To obtain Bouguer's formula the cross-product of the ray trace equation, equation (6-52), is taken with the radial position vector \bar{r} .

$$\bar{r} \times \frac{d}{ds} (\mu \hat{e}) = \bar{r} \times \frac{d\mu}{dr} \hat{r} = 0$$

The right hand side equals zero and the left hand side can be rewritten so that

$$\frac{d}{ds} (\mu \bar{r} \times \hat{e}) - \frac{d\bar{r}}{ds} \times \mu \hat{e} = 0$$

If a ray trajectory is followed then $\frac{d\bar{r}}{ds} \times \hat{e} = \hat{e} \times \hat{e} = 0$. The resulting differential equation is:

$$\frac{d}{ds} (\mu \bar{r} \times \hat{e}) = 0$$

Integrating along the ray trajectory gives Bouguer's formula

$$\mu \bar{r} \times \hat{e} = \overline{\text{CONST.}} \quad (6-57a)$$

or

$$\mu r \sin \theta = \text{CONST.} \equiv K \quad (6-57b)$$

' θ ' is the angle between ' \bar{r} ' and ' \hat{e} '.

Note, from equation (6-57a), that since the vector formed by ' $\bar{r} \times \hat{e}$ ' points in the same direction for all points along the ray, ' \bar{r} ' and ' \hat{e} ' always define the same plane. The ray trajectory lies in the plane determined by the initial orientations of ' \bar{r} ' and ' \hat{e} '.

For numerical ray tracing the form of Bouguer's formula in equation (6-57) is often inconvenient. It can be rewritten as (see figure 6-1):

$$\mu(s \cos \phi - z \sin \phi) = \text{CONST} \equiv K \quad (6-58)$$

where ϕ is the angle between an axis orthogonal to the symmetry axis and the local rayvector. Solving for ' $\sin \phi$ '

$$\sin \phi = -\frac{Kz}{\mu(z^2+s^2)} + \frac{z}{|z|} \left\{ \frac{s^2}{(z^2+s^2)} \left[1 - \frac{K^2}{\mu^2(z^2+s^2)} \right] \right\}^{\frac{1}{2}} \quad (6-59)$$

To do numerical ray tracing equation (6-59) is used in conjunction with the two incremental formulas:

$$z_{I+1} = z_I + \Delta z \quad (6-60)$$

$$s_{I+1} = s_I + \Delta z \tan \phi_I \quad (6-61)$$

where I+1 and I denote adjacent grid points.

An important point on the ray trajectory is the point of deepest penetration or the ray turning point. To locate this point consider a density profile that increases monotonically as 'r' decreases. ' μ ' and 'r' decrease monotonically as the ray penetrates into the plasma. The turning point occurs where 'r' is a minimum along the ray path and this point is found in equation (6-57) where $\frac{\partial}{\partial \theta} (\mu r) = 0$. This occurs when

$$\theta_{TP} \equiv \theta(\mu r = \text{minimum}) = \pi/2 \quad (6-62)$$

6.2.3 Light Refraction Through a Plane Plasma

Ray tracing through a plane plasma is necessary in this study because it is by comparing refraction in plane and spherical plasmas that resonant absorption is calculated.

A simple formula, equivalent to Snell's law, is obtained by a technique analogous to that used in deriving Bouguer's formula. The ray trace equation, equation (6-52), is crossed with a unit vector parallel to the density gradient. The result is that

$$\mu \sin \theta = \text{CONST.} \quad (6-63)$$

where ' θ ' is the angle between the ray vector and the density

gradient vector $\hat{e} = \frac{\nabla\mu}{|\nabla\mu|}$.

As for spherical plasmas, the turning point occurs at $\theta = \pi/2$.

The ray trajectory position dependence appears only through ' μ ' in the plane plasma situation whereas it is explicit in spherical plasmas. This implies that to specify plasma parameters for refraction in plane plasmas only the scalelength need be known. With a spherical plasma the scalelength and one density point location (r_{cr}) must be specified.

6.3 Ablation Region Dynamics

In section 6.1 it was shown that the critical and quarter-critical surface trajectories strongly affected the absorption of laser light. The plasma density profile was assumed to be known, as from the experiment, and the absorption was then calculated. Factors that affected the density profile were not considered.

In this section the physical parameters that most strongly influence the density profile are determined. Those aspects of the data that can be most readily used to study the selected parameters are isolated.

In particular, it is shown that the energy transport from the laser light absorption region to the region of plasma generation sensitively determines the peak critical and quarter-critical surface excursions. When only classical transport mechanisms are present, i.e., no supra-thermal electron or radiation transport, the peak excursions are insensitive to the amount and history of energy absorption and that they depend only on the energy transport coefficients. The rates at which the hydrodynamics evolve are, however, sensitive functions of the absorption rates. It is also shown that the hydrodynamic variables of ablation rate, ablating material source location, and corona temperature at the time of peak excursion uniquely define the extents of the peak excursions.

6.3.1 Steady-State Ablation

To see the density profile dependence on ablation parameters it is useful to consider a simple steady-state ablation model. The model is based on the single fluid plasma equations of mass and momentum conservation for spherical flows.

$$\frac{\partial \rho}{\partial t} + \frac{1}{r^2} \frac{\partial}{\partial r} (r^2 \rho v) = 0 \quad (6-64a)$$

$$\frac{\partial v}{\partial t} + v \frac{\partial v}{\partial r} + \frac{1}{\rho} \frac{\partial}{\partial r} (Z \rho R T) = 0 \quad (6-64b)$$

' ρ ' is the plasma mass density which is approximately equal to the ion mass density, ' v ' is the plasma velocity, ' T ' is the electron temperature, ' Z ' is the ionization state, and ' R ' is the ion ideal gas constant.

Assuming steady-state flow ($\frac{\partial}{\partial t} = 0$) and an isothermal plasma, ($T = \text{const}$), integrating equations (6-64 a,b) with respect to ' r ', and solving for the constants of integration in terms of the mass flow through a sphere (\dot{m}) and the density at the plasma source (r_s, ρ_s) yields two equations in ' r ', ' ρ ', and ' v '.

$$r^2 \rho v = \frac{\dot{m}}{4\pi} \quad (6-65a)$$

$$\frac{v^2}{2} + ZRT \ln \rho = \frac{\dot{m}^2}{32\pi^2 r_s^4 \rho_s^2} + ZRT \ln \rho_s \quad (6-65b)$$

Eliminating ' v ' and solving for ' r ' in terms of ' ρ ' provides a single equation for the location of a density point.

$$r \approx \left\{ \frac{1}{32\pi^2 ZR\rho^2 \ln|\rho_s/\rho|} \left(\frac{\dot{m}}{T^{1/2}} \right)^2 \right\}^{1/4} \quad (6-66)$$

The important thing to note in equation (6-66) is the dependence of the density point location on the parameter $\dot{m}/T^{1/2}$. This dependence

is confirmed by computer simulations (next section).

If the critical and quarter-critical surface excursions ($p_{cr} \equiv r_{cr} - r_t$, $p_{\frac{1}{4}cr} \equiv r_{\frac{1}{4}cr} - r_t$) are computed using equation (6-66), then a correlation is obtained that is independent of $\dot{m}/T^{\frac{1}{2}}$. (Also insensitive to energy transport since ablation rates depend on energy transport rates.)

$$p_{\frac{1}{4}cr} = 2 \left[\frac{\text{Ln}|\rho_s/\rho_{cr}|}{\text{Ln}|4\rho_s/\rho_{cr}|} \right]^{\frac{1}{4}} p_{cr} + \left\{ 2 \left[\frac{\text{Ln}|\rho_s/\rho_{cr}|}{\text{Ln}|4\rho_s/\rho_{cr}|} \right]^{\frac{1}{4}} - 1 \right\} r_t \quad (6-67)$$

For a source density equal to that of solid glass $\rho_s/\rho_{cr} = 750$, equation (6-67) becomes:

$$p_{\frac{1}{4}cr} = 1.91p_{cr} + .91r_t \quad (6-68)$$

Equation (6-68) can be compared to the experimentally observed $p_{cr} - p_{\frac{1}{4}cr}$ correlation (figure 5-19). The slope of equation (6-68) agrees well with the data. The intercepts disagree.

The important conclusions to be drawn from this model are that the density profile shape is a function of the outwards mass flow and corona temperature ($\dot{m}/T^{\frac{1}{2}}$) and that once one density point location is known, the rest of the ablation region profile is uniquely determined. These conclusions are confirmed and quantified in the next section with computer simulations of the experiment.

6.3.2 Computer Simulations

The principal tools used in this computer study are the codes SIMSUP and SUPER.^(6-13,14,15,16,17) Both are one-dimensional hydrodynamic Lagrangian codes for a one velocity two temperature plasma. SUPER contains real equation of state, radiation transport, and supra-thermal electron production and transport. SIMSUP (SIMPLIFIED SUPER) contains ideal gas equation of state and energy transport only by heat conduction. Except for the effect of supra-thermals, little difference is noticed in the ablation region hydrodynamics calculated by the two codes.

Laser light absorption is handled in the codes by normal incidence inverse bremsstrahlung plus a constant value dump that deposits at the critical surface a specified fraction of the reflected laser energy. In SIMSUP the dump is set at 15% to simulate the effect of peak resonant absorption in smooth spherical plasmas. This energy is deposited in the thermal electron distribution. In SUPER the absorption history is specified. 100% of the reflected energy is deposited at the critical surface with 90% of this energy going into a 10 KeV temperature supra-thermal electron distribution.

Because the codes do not self-consistently treat absorption, parameters insensitive to absorption rates are sought.

Energy transport in SIMSUP is handled by electron thermal conduction. The heat conduction is calculated according to Fourier's Law

$$Q = K \nabla T \quad K\text{-Spitzer Conductivity} \quad (6-69)$$

up to the point where the heat transported across an interface equals the net electron free-streaming energy flux. From that point on, the energy transport across an interface is given by the net electron free-streaming energy flux:

$$Q \approx \frac{\sqrt{3}}{4} \left[\left(\frac{kT_{e2}}{m_e} \right)^{1/2} \frac{3}{2} n_{e2} kT_{e2} - \left(\frac{kT_{e1}}{m_e} \right)^{1/2} \frac{3}{2} n_{e1} kT_{e1} \right]$$

$$\approx FL \frac{k}{m_e} n_e T_e^{1/2} \Delta T_e \quad (6-70)$$

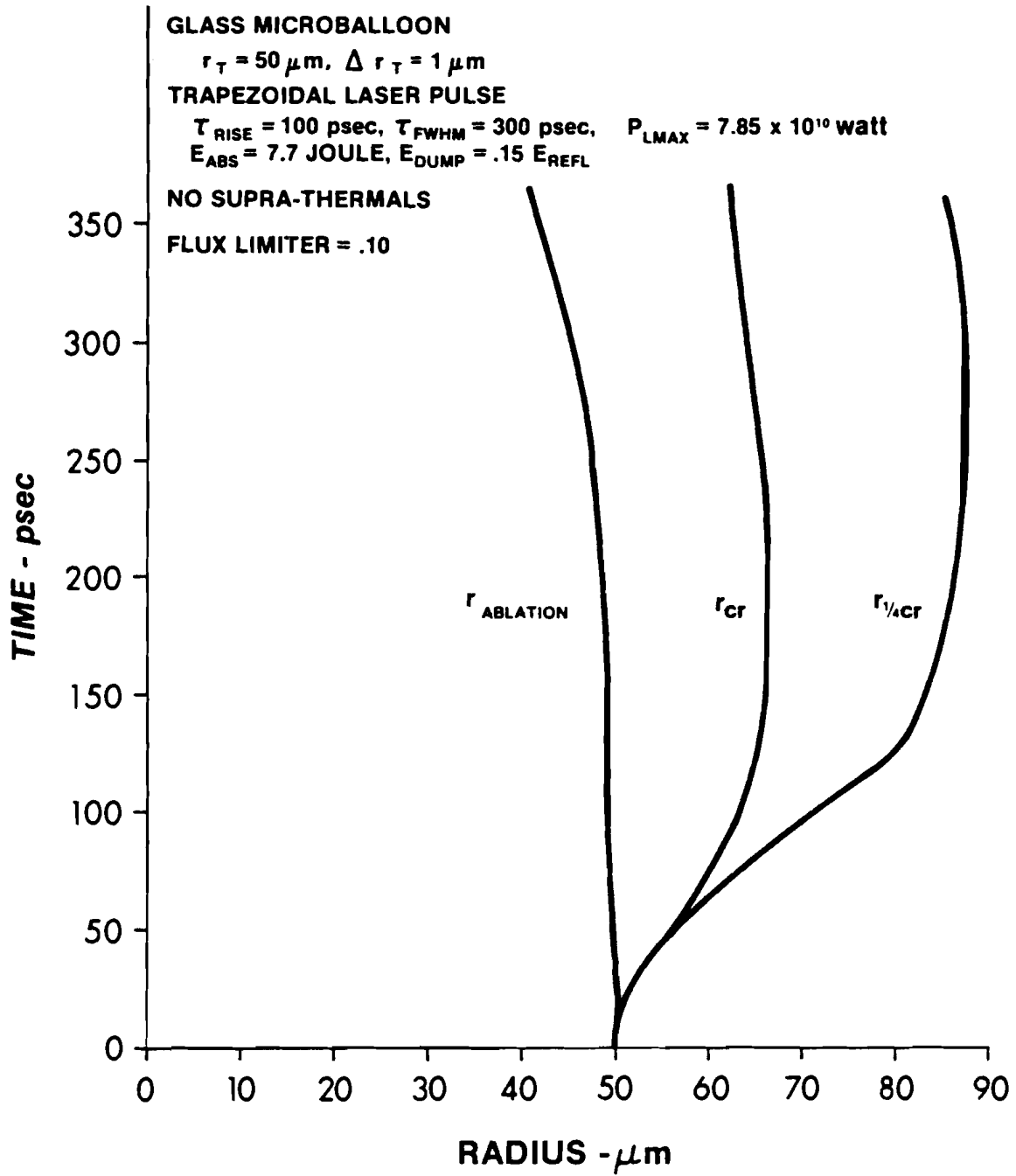
The flux limiter 'FL' equals .65 for classical flux limiting and is less than .65 if an anomalous flux inhibition mechanism is assumed.

For SUPER, energy transport by thermal electrons is the same as in SIMSUP. Additional energy transport occurs via supra-thermal electrons and radiation. Details on these mechanisms and other aspects of the code can be found in the references. (6-13,14,15,16,17)

The situation in which supra-thermals do not exist is analyzed first. Typical critical, quarter-critical, and ablation surface trajectories for a thin shell heated by a laser are shown in figure 6-25. As the laser pulse turns on and the shell absorbs energy, the heated plasma expands and the critical and quarter-critical densities move toward increasing radius. The bulk of the shell, including the ablation surface, is driven inward by the momentum imparted from the outward flowing material. Following a period of rapid expansion the density points slow down, reach a peak excursion, and remain near

FIGURE 6-25

TRAJECTORIES FOR TYPICAL CONDITIONS



that position for most of the laser pulse duration. The peak excursions are, thus, characteristic of the critical and quarter-critical surface locations for most of the laser pulse.

Input parameters can be selectively varied to determine which ones affect the critical and quarter-critical surface trajectories. The free parameters can be grouped into three categories: laser pulse, target configuration, and energy transport. The first choice is to vary laser pulse parameters and figure 6-26 shows the effect of peak power variation on the critical surface trajectory. Of particular importance is the equality of the peak critical surface excursions. Plotting the ablation region electron density profiles during the times of peak excursion, figure 6-27, reveals that the density profiles are almost identical and that heat fronts have penetrated to the same point! This occurs despite a factor of ten variation in the absorbed energy and a factor of five variation in the corona electron temperature. It should be noted, figure 6-26, that the hydrodynamic time scales do vary with the absorption rates.

Varying the pulse shape with constant peak power produces similar results. The codes predict no peak excursion dependence on pulse shape.

These considerations indicate that not only are the peak excursions characteristic of the density point locations during most of the laser pulse but that they are also insensitive to the only approximately known rate of energy absorption. For these reasons special attention is paid to the peak excursions.

When target parameter dependences are considered, for a fixed shell

FIGURE 6-26
**CRITICAL SURFACE TRAJECTORIES FOR
 VARIOUS ABSORBED ENERGIES**

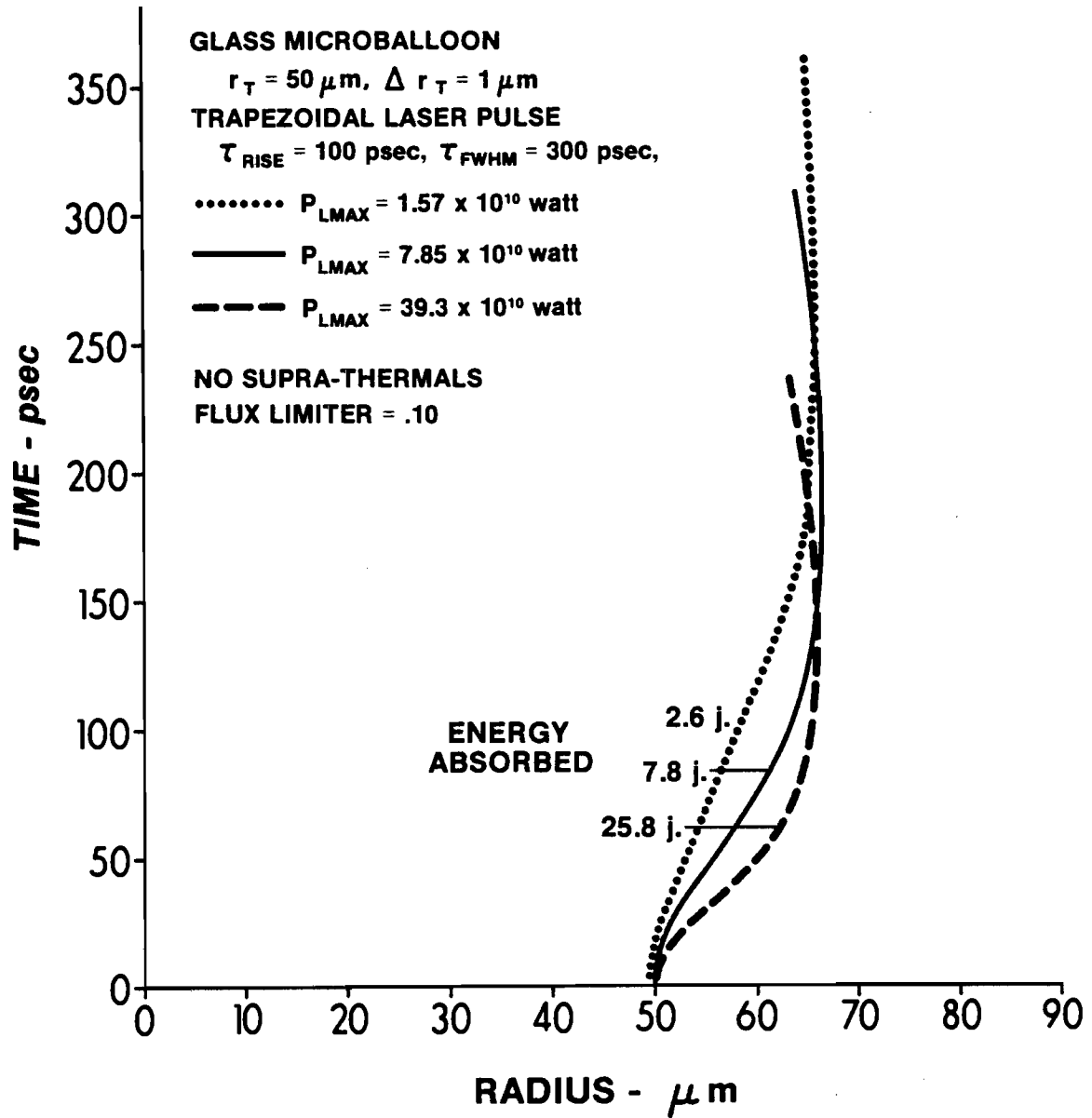
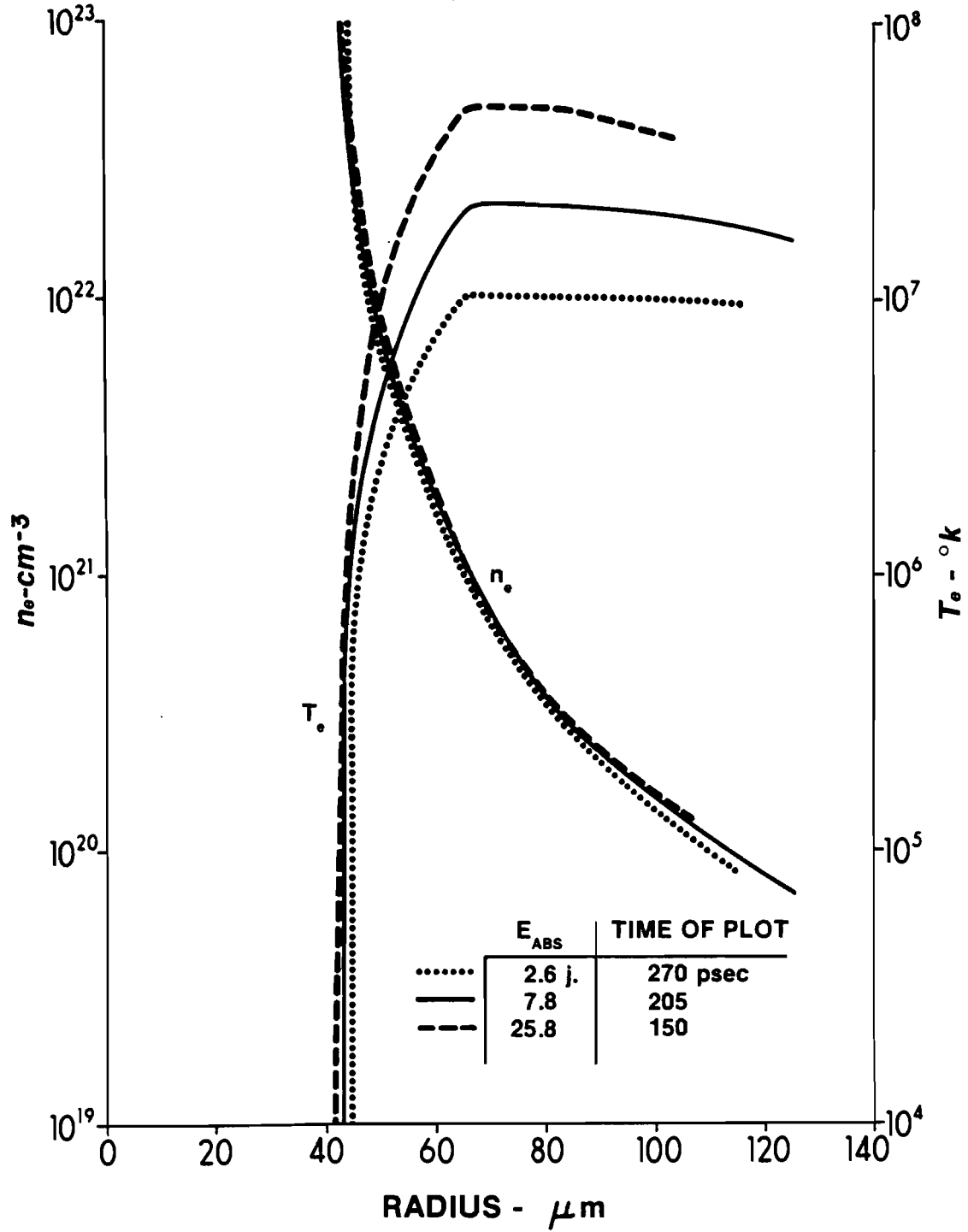


FIGURE 6-27
**ABLATION REGION PROFILES DURING PEAK
 EXCURSION INTERVALS**



thickness it is found that the difference between the maximum density point location ' r_{\max} ' and the original target radius ' r_t ' is insensitive to the target radius. Intending to not study target radius variation effects it is convenient to define the peak excursion by

$$p \equiv r_{\max} - r_t \quad (6-71)$$

The effect of shell thickness on the peak critical surface excursion is shown in figure 6-28. The relationship is a consequence of variation in the motion of the imploding shell (the source of ablating material) with shell thickness. The dependence will be quantified later on in terms of an effective source location for the ablating material.

The remaining free parameter is the energy transport coefficient: the flux limiter. Its magnitude strongly influences the amount of energy transported from the absorption region to the region of hot plasma generation and so controls the rate of shell ablation. The effect on the density point trajectories is pronounced, as seen in figure 6-29, and the dependence is clearly revealed in the magnitude of the peak excursion, figure 6-30.

To see the dependence of the peak excursions on the energy transported in the heat front, 'p' could be plotted as a function of the maximum thermal energy in the heat front ' $E_{\text{TH HF}}$ ' (the thermal energy in the heat front is a maximum at the time of peak excursion) but it would also be a function of the absorption rates. The absorption de-

FIGURE 6-28

PEAK EXCURSION VARIATION WITH SHELL THICKNESS

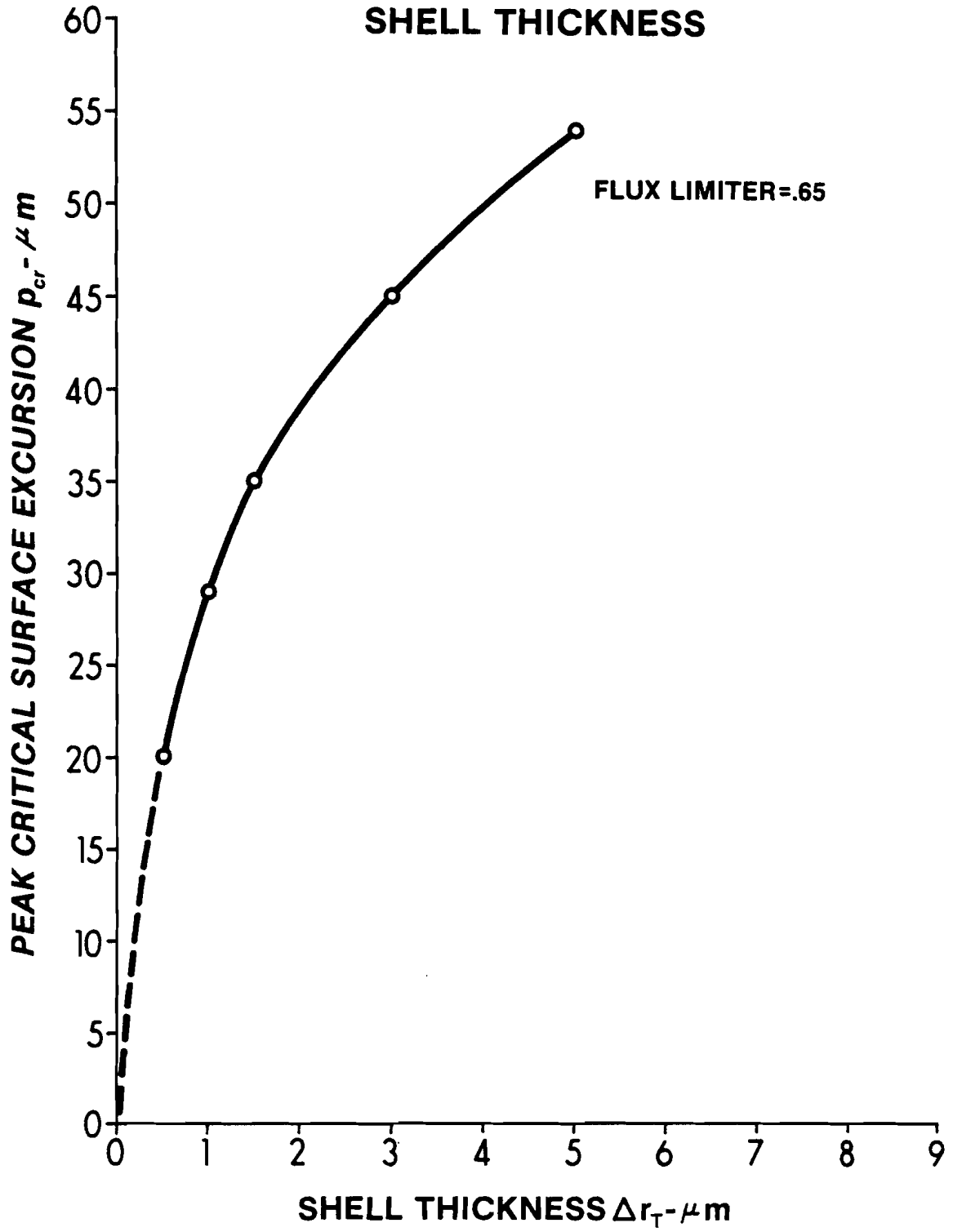


FIGURE 6-29
**EFFECT OF FLUX LIMITER VARIATION ON
CRITICAL SURFACE TRAJECTORIES**

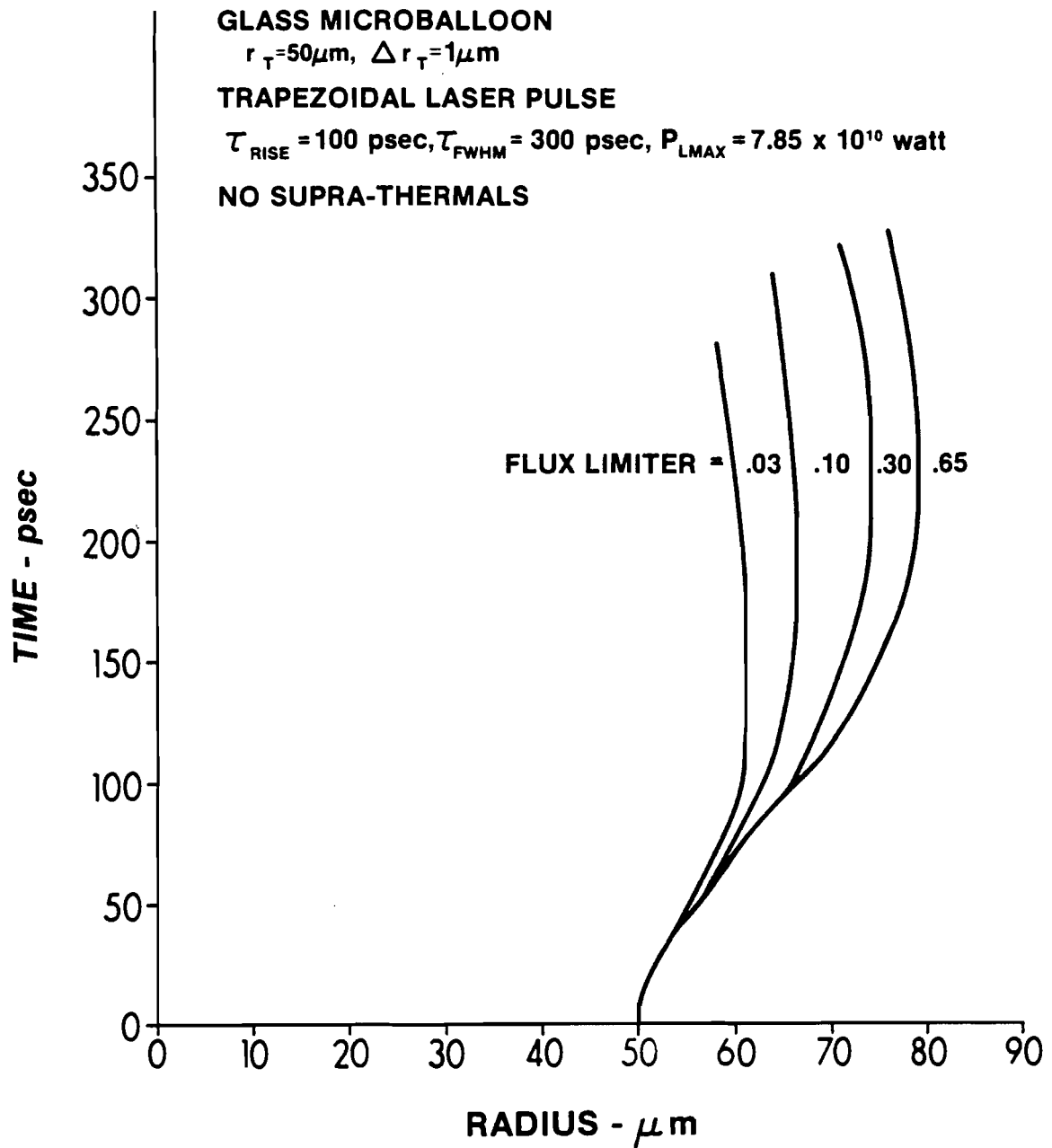
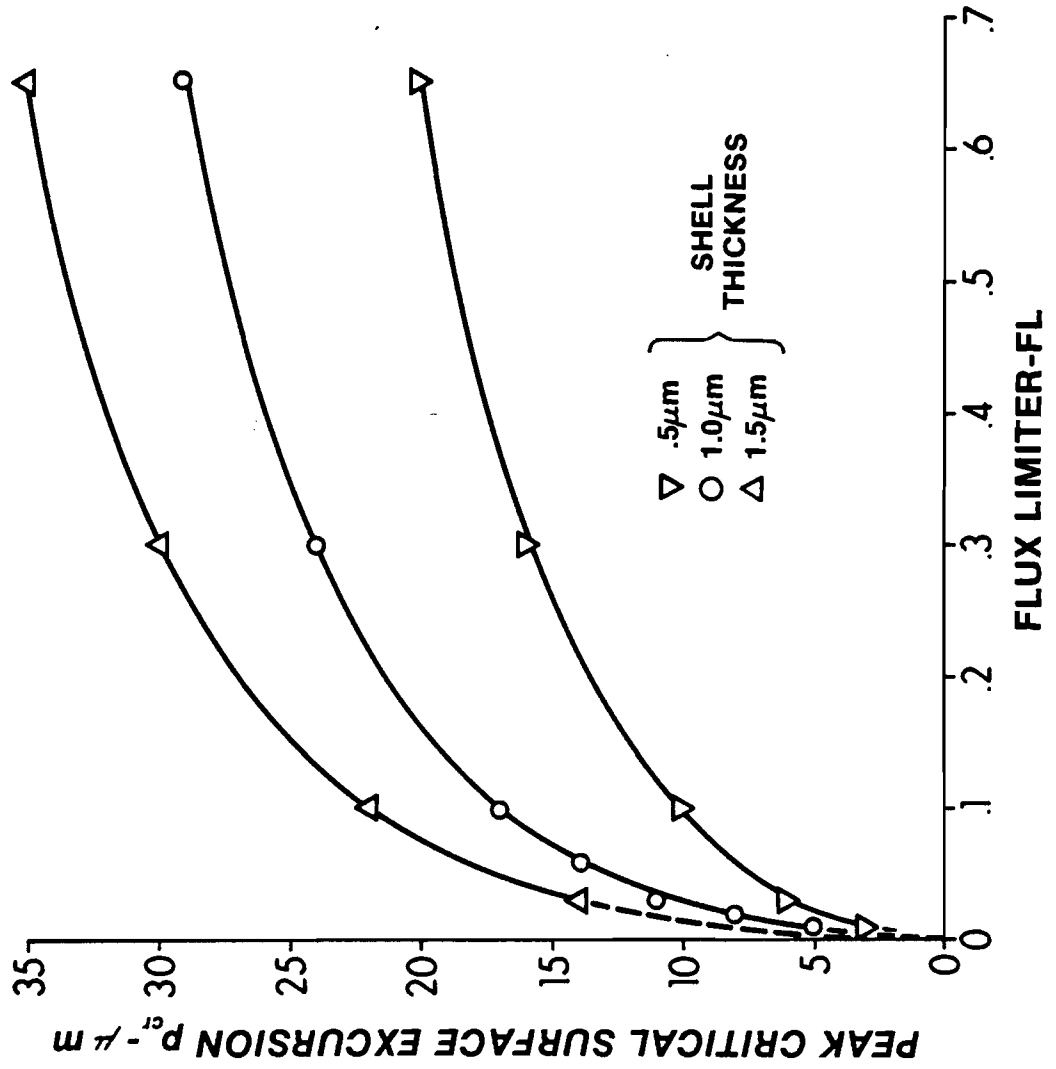


FIGURE 6-30
PEAK CRITICAL SURFACE EXCURSION
DEPENDENCE ON FLUX LIMITER



pendence can be eliminated by dividing by the corona electron temperature which is approximately equal to the critical surface electron temperature ' $T_{e\ cr}$ '. The resulting quantity ' $E_{TH\ HF}/T_{e\ cr}$ ' is a maximum at the time of peak excursion and the relationship between it and ' p ' is independent of absorbed energy. For the cases shown in figure 6-26 the peak excursions are the same as are the values of $(E_{TH\ HF}/T_{e\ cr})_{max}$. A plot of ' p_{cr} ' as a function of $(E_{TH\ HF}/T_{e\ cr})_{max}$ is shown in figure 6-31.

The physical significance of the quantity $E_{TH\ HF}/T_{e\ cr}$ can be seen by noting that the thermal energy of the heat front is given by $(3/2 k T_e) N_e$ where ' T_e ' is a characteristic temperature and ' N_e ' is a characteristic number of particles. Taking $T_e = T_{e\ cr}$, then $N_e = \tilde{N}_e$ is a characteristic number of particles that can be heated to the corona temperature. The quantity $E_{TH\ HF}/T_{e\ cr}$ then gives

$$\frac{E_{TH\ HF}}{T_{e\ cr}} \approx \frac{(3/2 k T_{e\ cr}) \tilde{N}_e}{T_{e\ cr}} \sim \tilde{N}_e \quad (6-72)$$

and is, thus, characteristic of a peak ablation rate.

The dependence on shell thickness is accounted for by noting that the total shell mass, via the principle of momentum conservation, affects the imploding shell's motion, and, thus, the motion of the ablating material's source. Characterizing the source location for the ablating material by the ablation surface ' r_{ABL} ', i.e., the point where the particle velocity equals zero, it is found that the difference between the source location and the peak density point location,

FIGURE 6-31
**PEAK CRITICAL SURFACE EXCURSION DEPENDENCE
 ON HEAT FRONT THERMAL ENERGY AND CORONA
 ELECTRON TEMPERATURE**

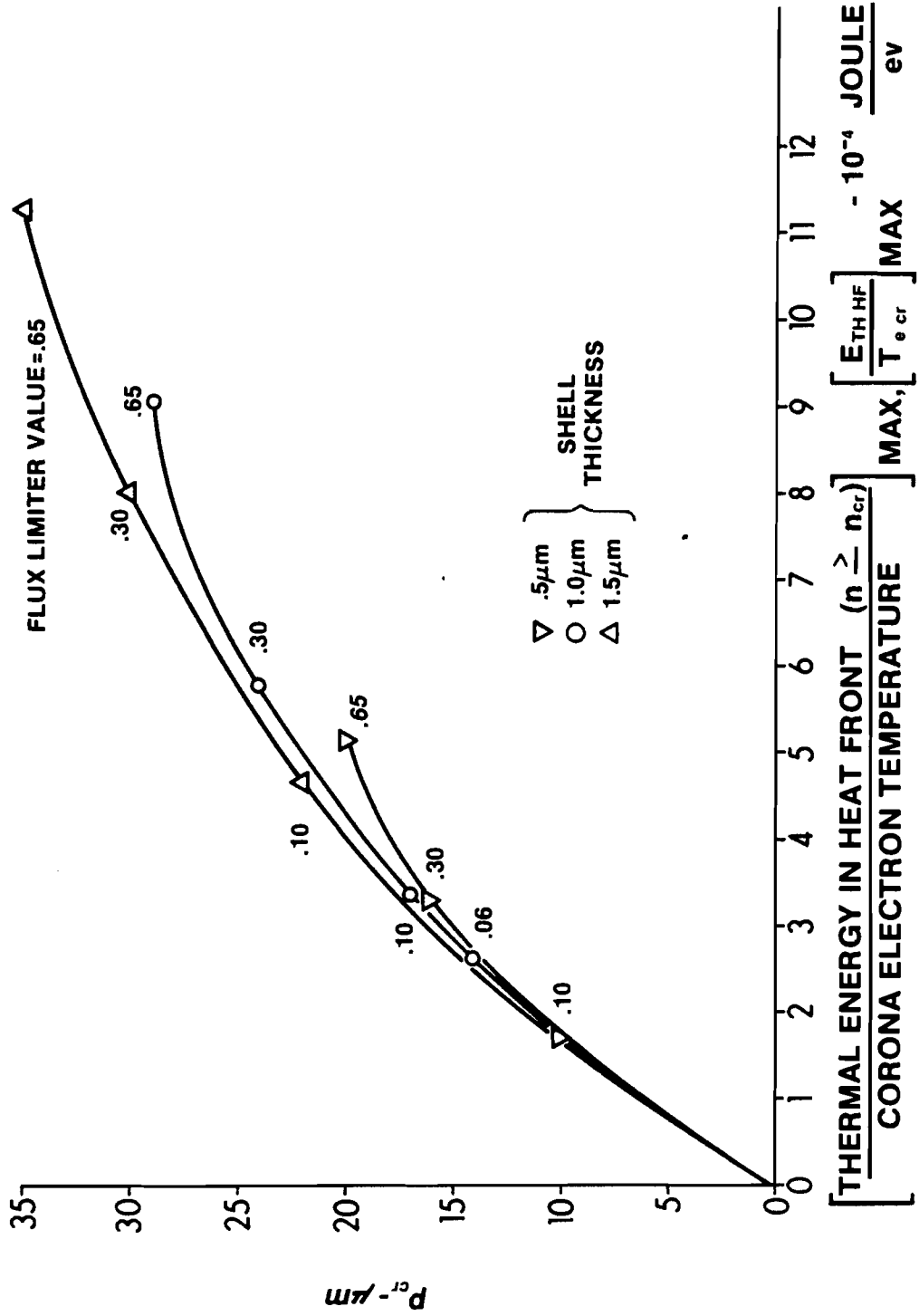
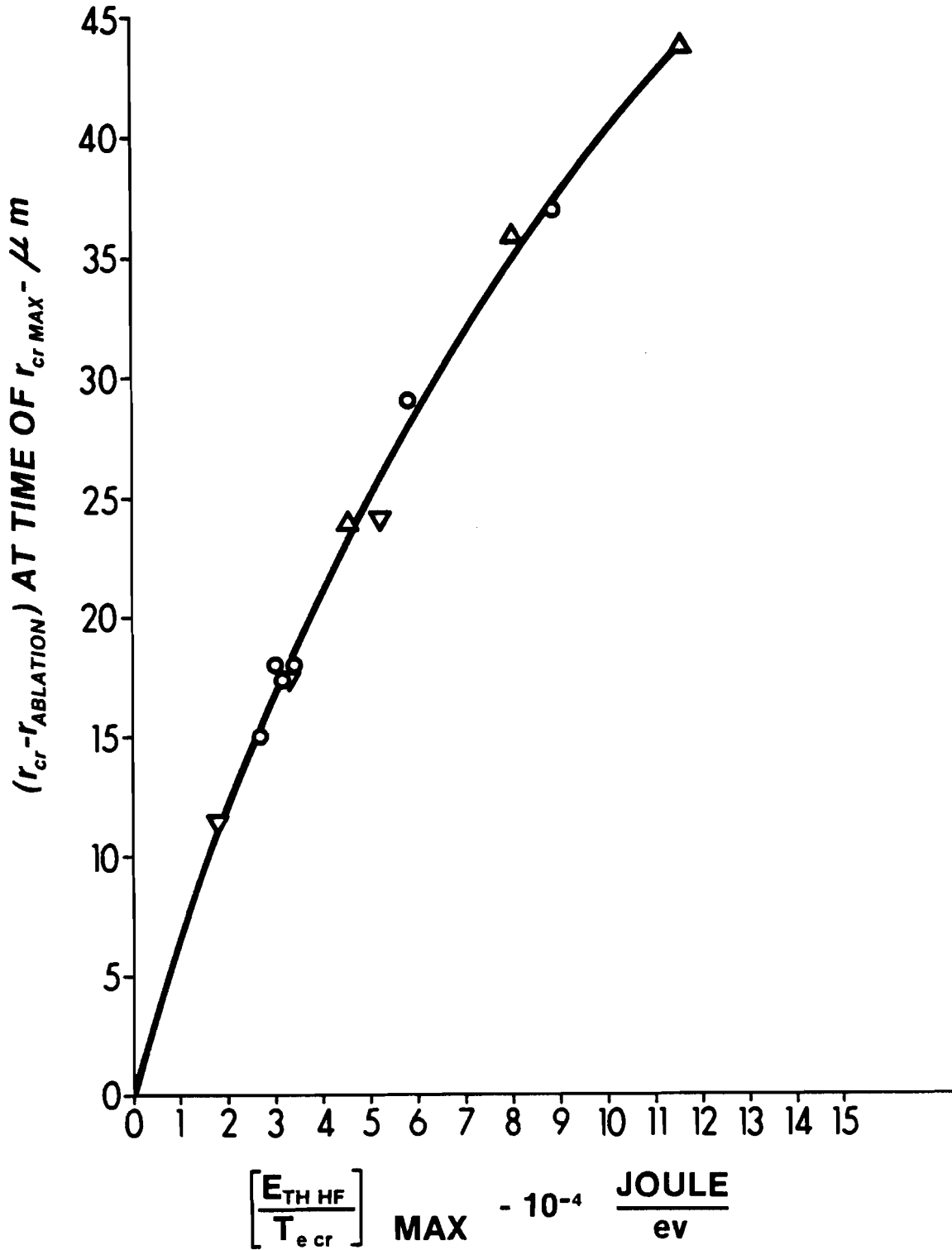


FIGURE 6-32

**PEAK CRITICAL SURFACE LOCATION DEPENDENCE
ON HEAT FRONT THERMAL ENERGY, CORONA
TEMPERATURE, AND ABLATING MATERIAL
SOURCE LOCATION**



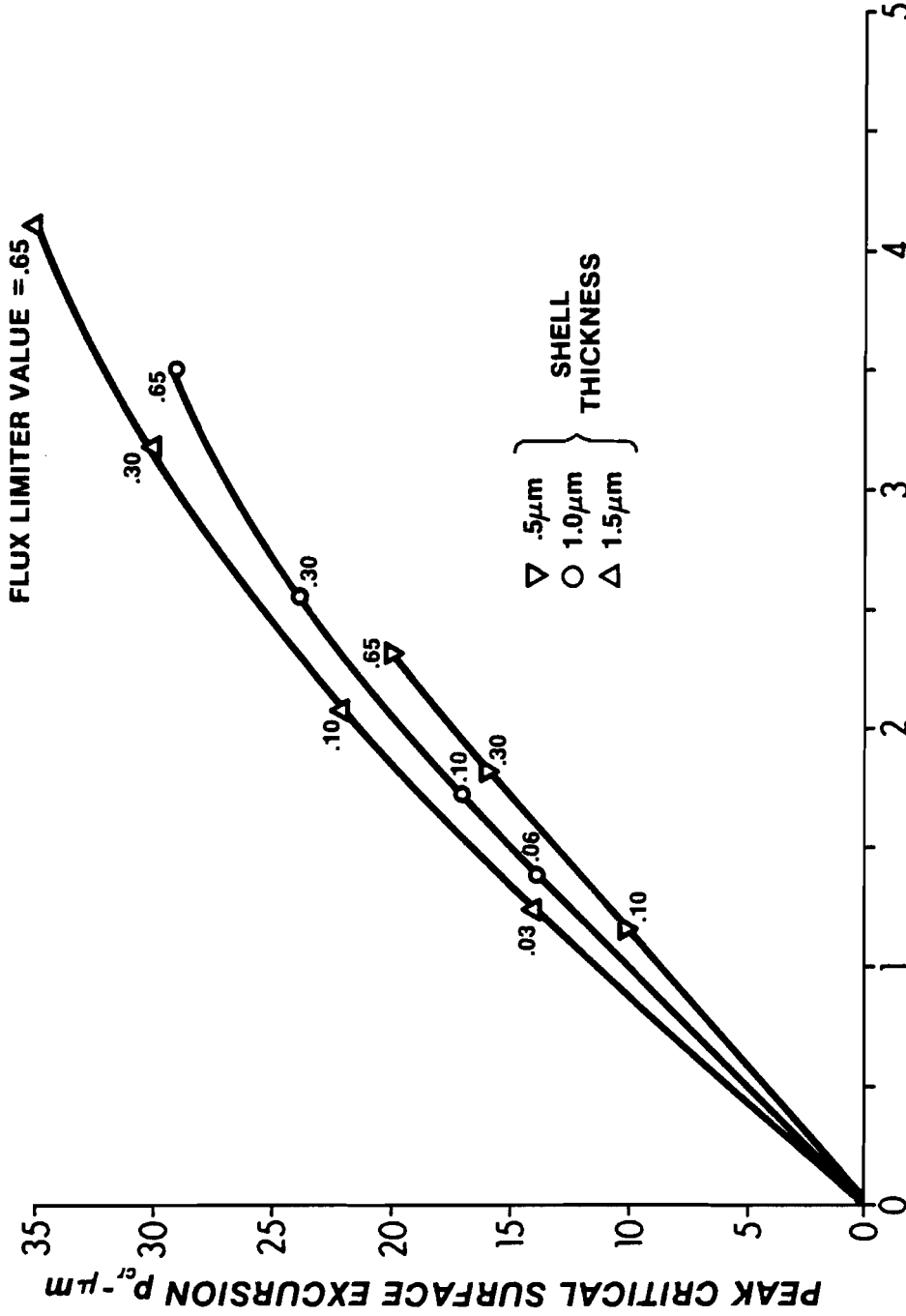
$(r - r_{ABL})$ at the time of peak excursion, is not dependent on the shell thickness. Figure 6-32 shows the dependence of $(r_{cr} - r_{ABL})$ at the peak excursion time as a function of $E_{TH HF}/T_{e cr}$. Note that the points on the three curves of figure 6-31 all lie on the same curve in figure 6-32. The variable effect of shell thickness has, thus, been accounted for. It should be noted, however, that $(r_{cr} - r_{ABL})$ is not an experimentally measured quantity whereas p_{cr} and r_t are measured in the experiment.

Figures 6-31 and 6-32 and equation (6-71) show that greater amounts of energy transport produce greater ablation rates and this leads to larger peak excursions. To directly see the relation between peak excursion and ablation rate, 'p' can be plotted as a function of the mass flow rate through the critical surface at the time of peak excursion (\dot{m}_{cr}). ' \dot{m}_{cr} ' is a maximum at this time. The dependence is a function of the absorption but this can be eliminated by dividing \dot{m}_{cr} by the corona temperature $T_{e cr}^{1/2}$. The resulting plot of ' p_{cr} ' as a function of $\dot{m}_{cr}/T_{e cr}^{1/2}$ is shown in figure 6-33. Source motion variation is taken into account by plotting $(r_{cr} - r_{ABL})$ at the time of peak excursion. The result is the single line relation of figure 6-34.

To see the physical significance of $\dot{m}_{cr}/T_{e cr}^{1/2}$ note that an acoustic velocity ' c_A ' is proportional to $T_{e cr}^{1/2}$ and that this gives a characteristic expansion velocity ' v_{EXP} '.

$$\frac{\dot{m}_{cr}}{T_{e cr}^{1/2}} \sim \frac{\dot{m}_{cr}}{c_A} \sim \frac{\dot{m}_{cr}}{v_{EXP}} \quad (6-73)$$

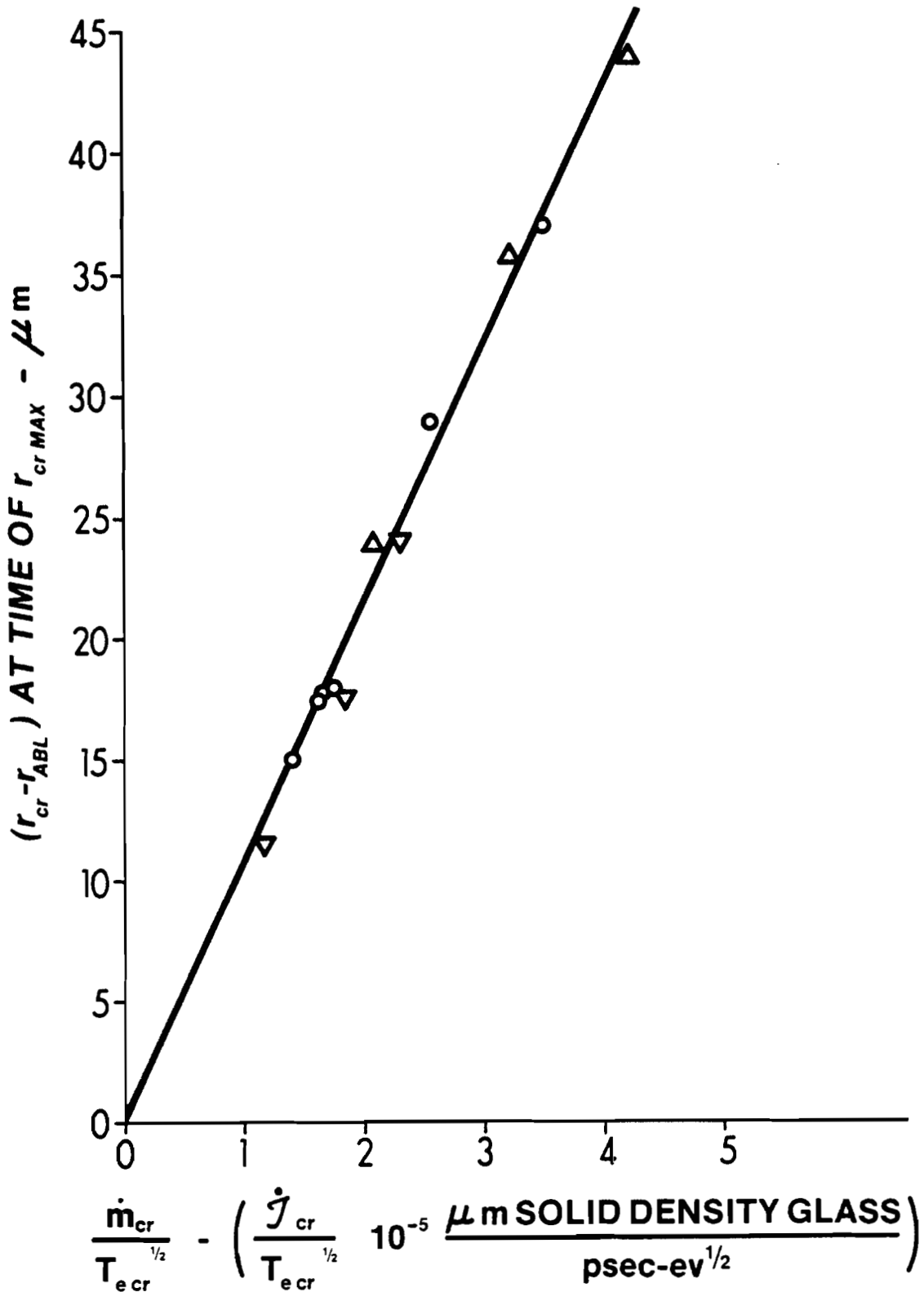
FIGURE 6-33
**PEAK CRITICAL SURFACE EXCURSION DEPENDENCE
 ON ABLATION RATE AND CORONA TEMPERATURE**



$$\frac{\dot{m}_{cr}}{T_{e\ cr}^{1/2}} - \left(\frac{\dot{J}_{cr}}{T_{e\ cr}^{1/2}} \right) 10^{-5} \frac{\mu\text{m}}{\text{psec-ev}^{1/2}}, \quad \dot{m}_{cr} = (\rho_{\text{SOLID GLASS}} \times 4\pi r_{cr}^2) \times \dot{J}_{cr}$$

FIGURE 6-34

**PEAK CRITICAL SURFACE LOCATION DEPENDENCE
ON ABLATION RATE, CORONA TEMPERATURE, AND
SOURCE LOCATION**



For a fixed expansion velocity, larger ablation rates imply more plasma in the corona and larger peak excursions. Fixing the ablation rate while increasing the expansion velocity implies smaller radius since $\dot{m}_{cr} = 4\pi r_{cr}^2 \rho_{cr} v_{cr}$. If v_{EXP} increases v_{cr} will also increase. For constant \dot{m}_{cr} , r_{cr} must decrease as v_{cr} increases.

Up to this point emphasis has been placed on quantifying the dependences of the peak critical surface excursion. Any other density point could have been similarly analyzed. Instead of duplicating the analysis, it is instructive to consider the correlation of one density point peak excursion to another. As an example, the correlation between the critical and quarter-critical peak excursions, the experimentally measured quantities, is considered. Figure 6-35 shows the result. The points for all the computer runs lie along a single line indicating that the peak excursion dependence between the critical and quarter-critical surfaces, and all others in the ablation region, is unique. If the peak excursion for one density is known, then the peak excursion for all other density points in that ablation region profile are uniquely determined and can be obtained via computer results.

Figure 6-35 has the added significance that since it predicts a unique critical - quarter-critical surface peak excursion correlation, an experimental check on the theory can be had without having to independently know the energy transport coefficients or rates. Figure 6-36 shows the comparison. The indication is of good agreement between theory and experiment. The divergence between the

FIGURE 6-35
CRITICAL - 1/4-CRITICAL SURFACE PEAK EXCURSION RELATION

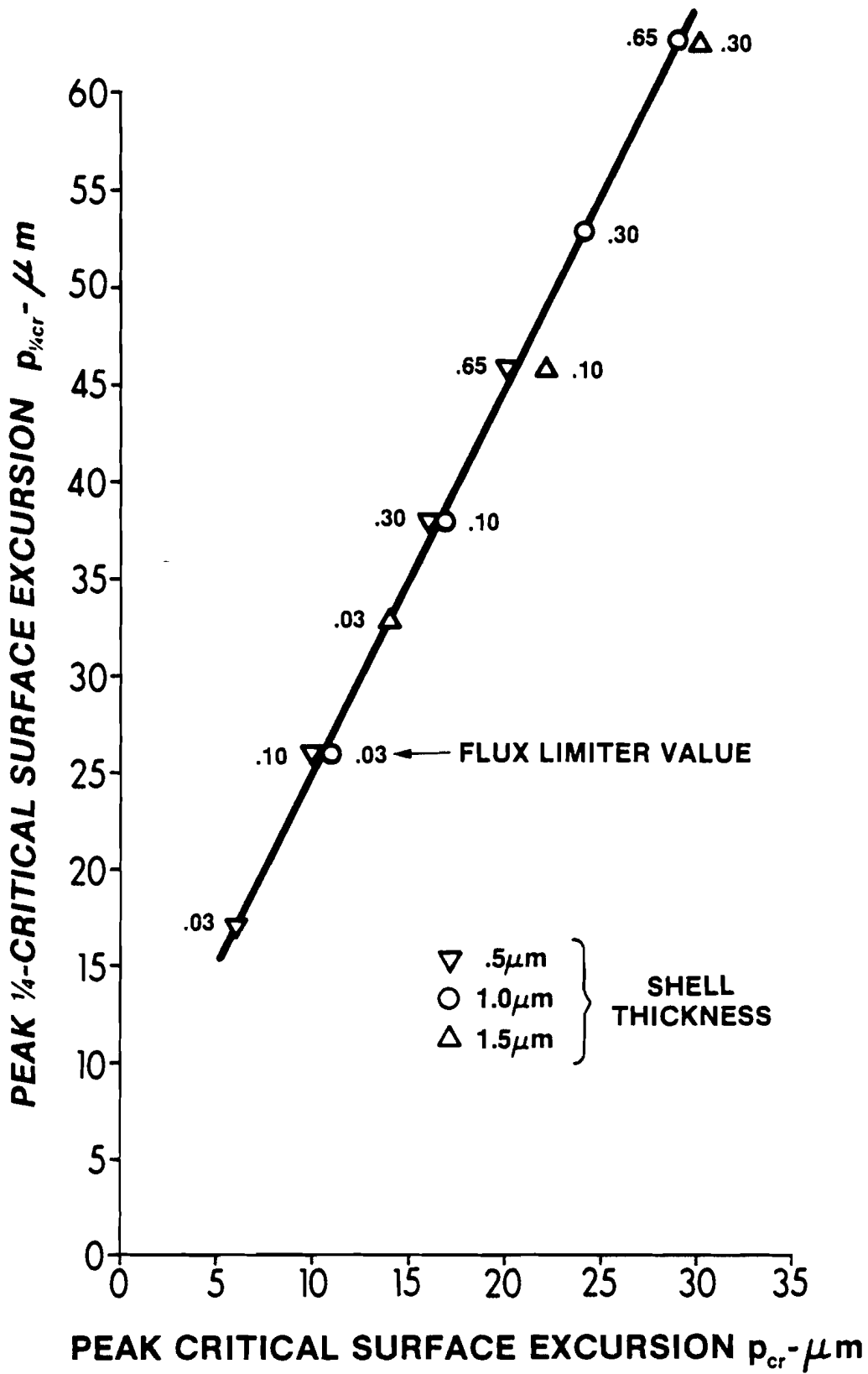
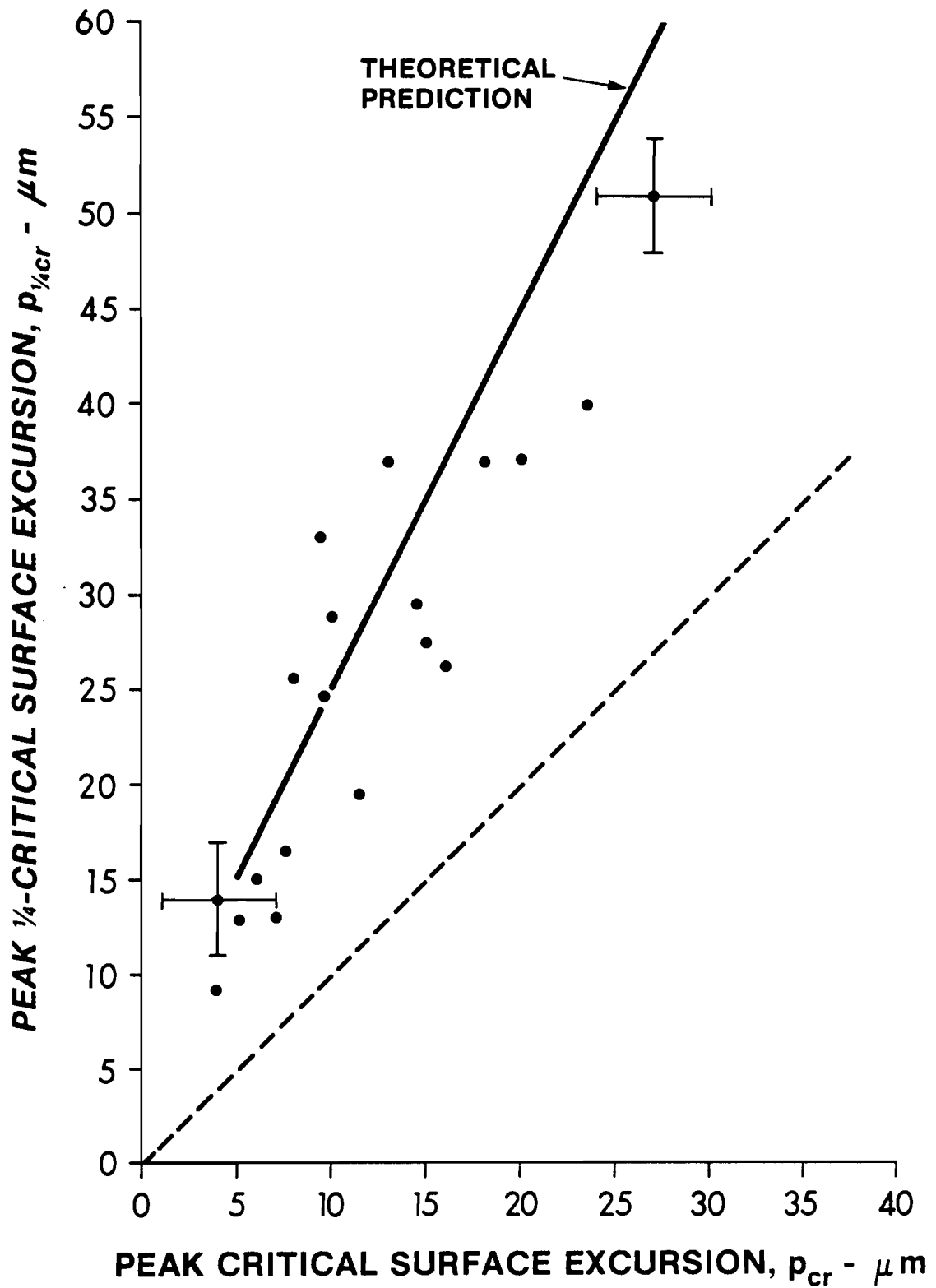


FIGURE 6-36

COMPARISON OF THEORY AND EXPERIMENT

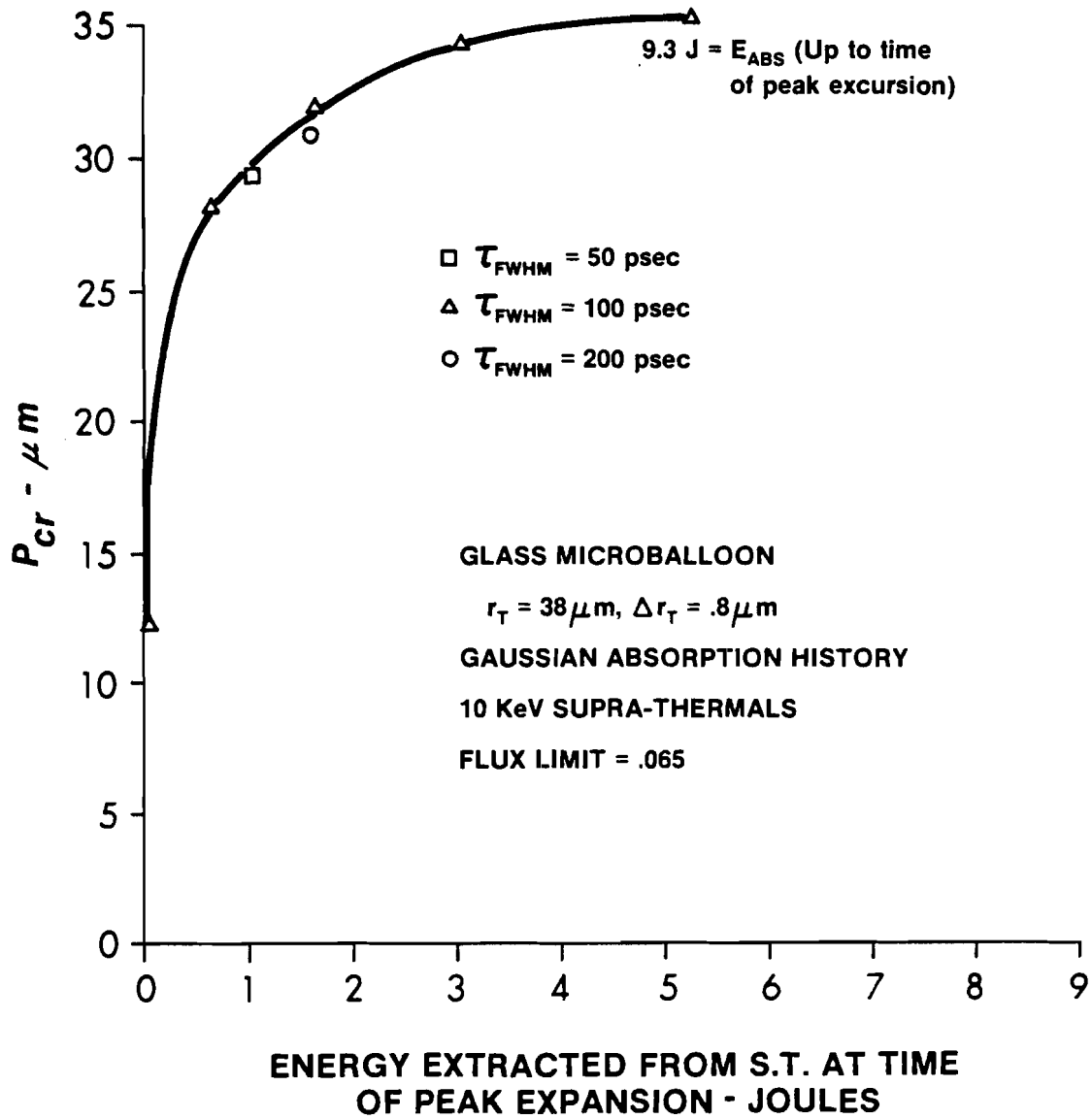
experiment-theory and the dashed line prediction of a pondromotive force steepened density profile should be noted.

At this point the effect of supra-thermal electrons is considered. Many of the conclusions derived from the analysis of thermal electron transport still apply. With the inclusion of supra-thermal electrons, the peak excursions still hold to the unique correlation of figure 6-35. The peak excursions are still a sensitive function of the energy transported into the shell and since supra-thermal electrons act as an additional energy transport channel they cause larger peak excursions than in identical cases without them. This is seen in figure 6-37 where the peak critical surface excursion is plotted as a function of the supra-thermal electron energy deposited into the thermal plasma. The deposited energy appears primarily as electron thermal energy plus ion kinetic energy. (The supra-thermal electrons comprise only about 1% of the total number of electrons in the plasma.)

Plotting ' $E_{TH HF}/T_{e cr}$ ', where the heat front is now defined as the region $n_{ABL} \geq n_e \geq n_{cr}$, gives results nearly equal to figure 6-32 for the ordinate as $(r_{cr} - r_{ABL})$ or as p_{cr} . The near equivalence of $(r_{cr} - r_{ABL})$ and p_{cr} with supra-thermals present, is due to the only several micron motion of the ablation surface at the time of peak excursion. The diminished motion is a consequence of inward ablating material from the shell inner surface heated to a few hundred eV by the supra-thermal electrons.

The computer simulations do predict a peak excursion dependence on the incident pulse parameters. This is because the amount of transport has been directly tied to the incident pulse through the

FIGURE 6-37
**EFFECT OF SUPRA-THERMAL
 ELECTRON ENERGY TRANSPORT
 ON PEAK EXCURSIONS**



energy dumped into the supra-thermals. For a given pulse shape, pulses with higher peak powers deposit more energy in the dump and generate more fast electrons. These transport and deposit more energy into the shell and produce greater peak excursions. A limit is reached when the fast electrons have heated the shell such that half of it goes in and half goes out. The situation here is not one of a uniformly heated shell but of a shell with a temperature minimum roughly at the middle of the wall ($r = r_t - \frac{1}{2} \Delta r_t$). The corona is hot because that is where laser energy is absorbed in a thermal electron distribution. The bulk of the shell is heated to a few hundred eV (300-600 eV) by the supra-thermal electrons. At the inner edge of the shell where there is an interface to the gas fill of the microballoon, the warm shell expands and drives a shock into the gas. Behind this shock the gas heats to about 1 KeV and thermal conduction causes the shell near the interface to also heat up. For a .8 μm thick shell the maximum peak excursion is reached when about 5 joules has been absorbed by the time of peak excursion from a 10 KeV supra-thermal distribution.

For the pulses considered, no clear dependence between the peak critical surface excursion and the rise time was observed.

At this point it can be said that with or without the presence of supra-thermal electrons the peak excursions are a function of the energy transported into the shell to heat and ablate more material. Supra-thermal electrons act as an additional energy transport channel and so increase the peak excursions beyond those expected from thermal electron transport.

Additional insight may be gained by referring to an experimental correlation (Chapter 5) that relates the peak critical surface excursion ' p_{cr} ' to the incident laser pulse rise time ' T_{RISE} ' (figure 6-38). Although this is in apparent contradiction to the computer results, the simulations do not take into account the parameters that affect the energy transport coefficient 'FL' or the actual production rate and spectrum (temperature) of the supra-thermal electrons. The implication is, however, clear that longer rise time laser pulses result in more efficient energy transport.

The experimental $p_{cr} - T_{RISE}$ relationship can be cross-correlated to the computer results to quantify the rise time dependence of energy transport. Using the results derived without supra-thermals, a rise time dependence to the flux limit can be obtained (figure 6-39). With or without supra-thermals the rise time dependence of the energy transport parameter ' $E_{TH HF}/T_{e cr}$ ' can be had (figure 6-40).

The prime usefulness of figure 6-39 is that it shows the energy transport contributing to the heating of outwards ablating plasma to be less than that predicted by classical thermal transport whether or not supra-thermals actually existed in the experiment. Figure 6-39 also allows for a comparison of the results from this study with those of other experiments.^(6-18,19,20) Although the laser pulse rise times for these experiments is not known, the range of flux limiter values is consistent with those of the $2\omega_0 - (3/2)\omega_0$ study.

Figure 6-40 provides the principal result of this energy trans-

FIGURE 6-38
**PEAK CRITICAL SURFACE EXCURSION
RISE TIME DEPENDENCE**

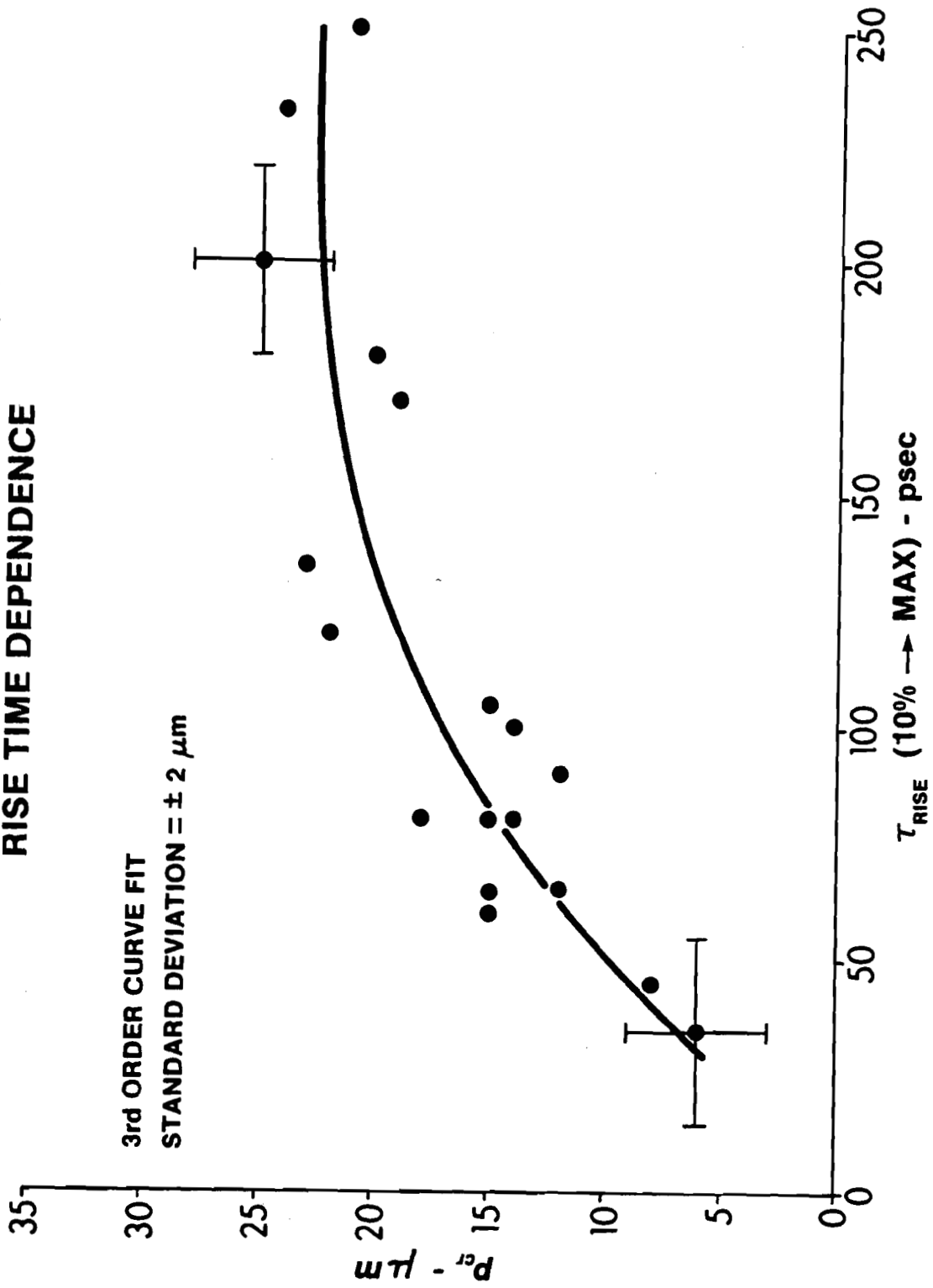


FIGURE 6-39
**FLUX LIMITER—LASER PULSE RISE TIME
CROSS-CORRELATION**

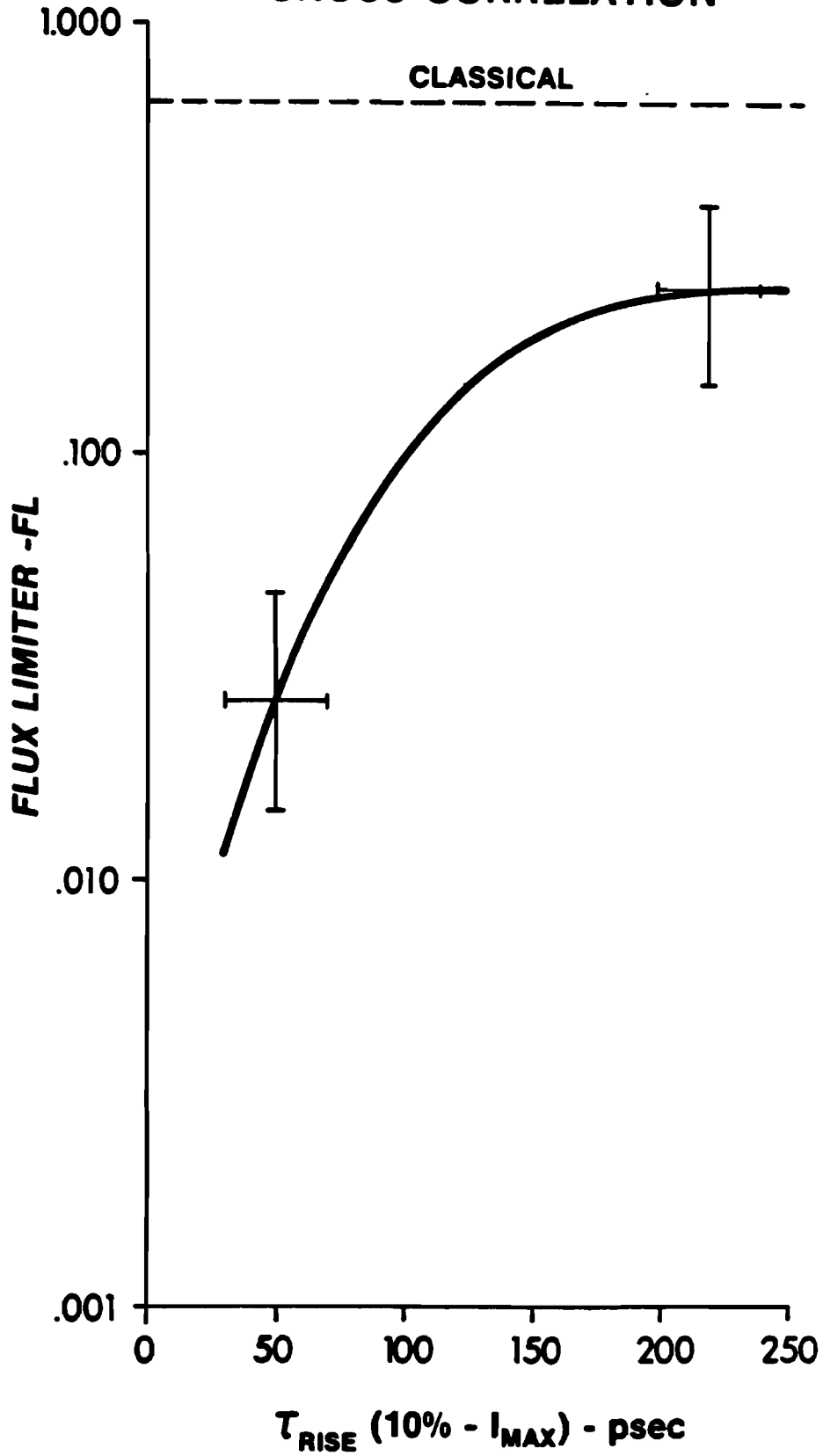
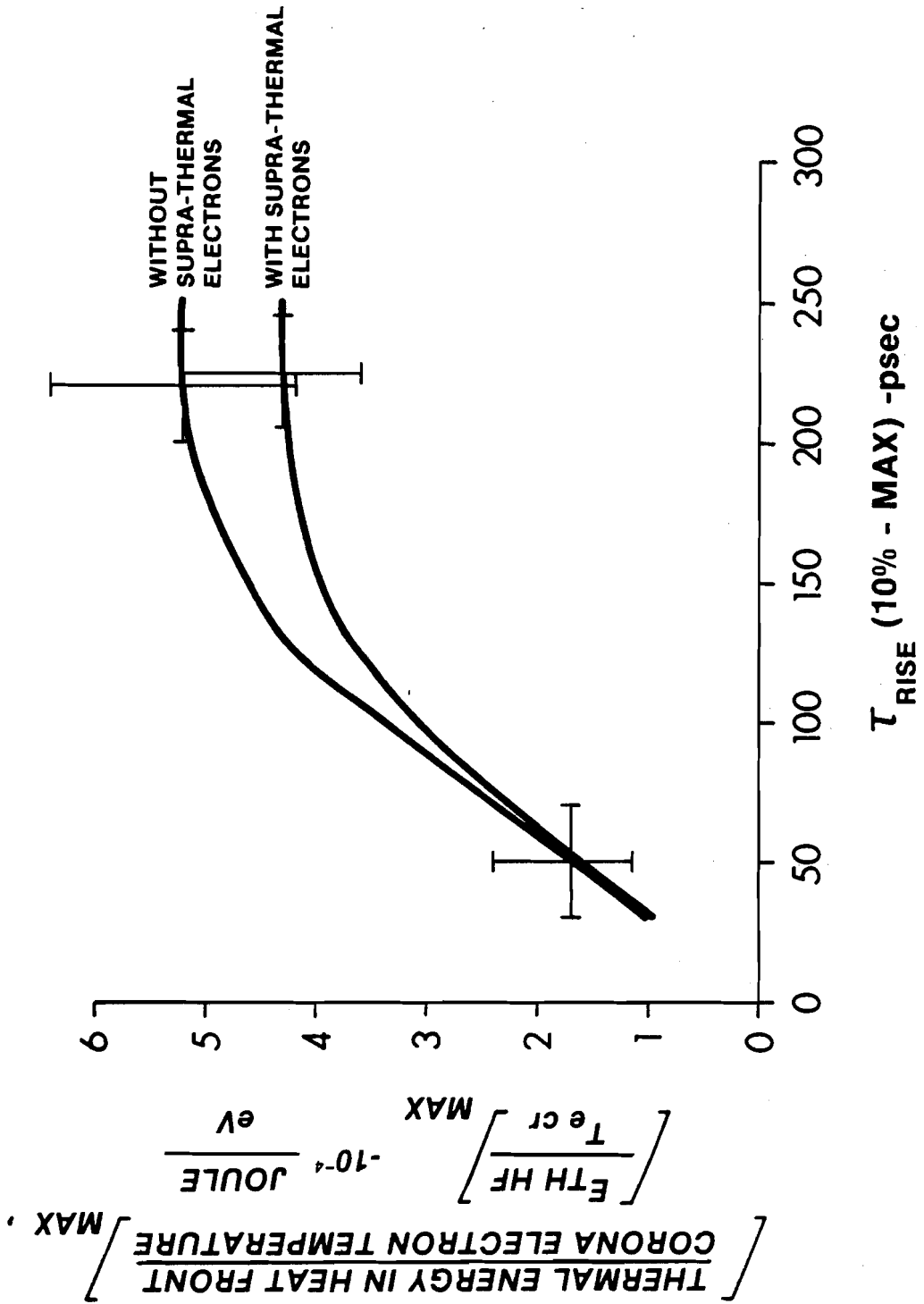


FIGURE 6-40
**CORRELATION BETWEEN ENERGY TRANSPORT
 AND LASER PULSE RISE TIME**



port study. Since the corona electron temperature did not vary substantially from shot to shot (.8 - 1.2 KeV), figure 6-40 gives the variation with laser pulse rise time of energy transport contributing to outwards shell ablation. The increase is linear for pulses with τ_{RISE} up to $\tau_{RISE} \approx 125$ psec. Energy transport appears to have saturated for pulses with $\tau_{RISE} \gtrsim 200$ psec.

It is unknown, at this time, whether the flux limiter varies as a function of rise time, with or without additional transport via supra-thermals, or whether thermal heat conduction is limited to a small amount with the bulk of the energy transported by a variable number of supra-thermal electrons. The supra-thermal spectrum may be a function of laser pulse rise time with the spectrum becoming softer ($T_{e\ HOTT}$ decreasing) for longer rise time pulses. This would enhance the local deposition of energy in the outer shell material and would increase the outwards ablation of material. (For 10 KeV supra-thermal electrons only 1/3 of the supra-thermal energy is deposited into the thermal "heat front".)

7. Discussion of Results

The development of a new diagnostic technique was dealt with in this report. It was shown that the second and three-halves harmonic light emissions could be observed perpendicular to the axis of laser beam irradiation. The harmonic emissions, as predicted by theory, came from distinct and separate zones within the inhomogeneous plasma. The $2\omega_0$ and $(3/2)\omega_0$ harmonics were emitted, according to theory, from the critical and quarter-critical densities. By spatially and temporally resolving the harmonic light emissions, critical and quarter-critical trajectories were obtained.

Time integrated photographs were obtained which had two dimensional spatial resolution and from which peak critical and quarter-critical surface excursions and characteristic plasma density scale-lengths were measured. Streak photographs with spatial resolution along one plasma axis were used to determine critical and quarter-critical surface trajectories and time resolved scalelengths.

In reducing the data it was shown that image analysis could be used to enhance the accuracy of the spatially resolved data. The time integrated and time resolved data had accuracy improvements of factors of three and five respectively.

For the purpose of image analysis it was necessary to determine the point spread function of the streak camera along its axis of spatial resolution. This was done as a function of light intensity into the streak camera. It was found that the shape of the point spread function, exclusive of film response, was relatively insensi-

tive to the input light intensity. The point spread function width at the base intensity level increased with increasing incident intensity. This effect was due to the finite sensitivity level of the streak camera so that more intense incident intensities resulted in greater recorded ranges of the point spread response.

The reduced data was applied to the study of laser light absorption and energy transport. Time integrated scalelengths were found to correlate to the fractional absorption. For laser pulses of 200-500 psec duration and .1 tw peak focused power, the range of scalelengths and fractional absorptions was from 6 μm to 24 μm and from 25% to 57% respectively. The scaling of fractional absorption to scalelength was found to agree with absorption dominated by collisional mechanisms. Time resolved trajectories and scalelengths were used to obtain absorption histories. Resonant absorption was found to be significant at 15% fractional absorption, for about one laser pulse rise time. After this period of time, as the scalelengths increased, collisional absorption increased, and resonant absorption diminished.

Collisional absorption theories predicted absorption via electrons scattering off of ions within the range of a thermal plasma fluctuation, inverse bremsstrahlung absorption, or via electrons scattering off of ions within a nonequilibrium ion structure, absorption off of ion turbulence. The scalelength dependence of these two mechanisms was seen to be similar. Absorption off of ion turbulence was expected to have an ion charge and electron temperature dependence much diminished from that of inverse bremsstrahlung absorption.

Resonant absorption theory applied to linearly polarized light incident on spherical plasmas predicted peak resonant absorption efficiency of 15-20%.

Energy transport was studied and related to experimentally observable effects. Computer simulations were used to determine the relationship between energy transport and mass ablation rates, and the density profile. It was found that the peak excursions could be related to energy and mass transport parameters. An experimental correlation between the peak critical surface excursion and the laser pulse rise time was cross-correlated to the computer simulation results to show an energy transport dependence on laser pulse rise time. In terms of the flux limiter it was seen that energy transport was reduced by a factor of 60 from classical at a laser pulse rise time of 30 psec and by a factor of 2.5 at a laser pulse rise time of 250 psec. Because of the possible presence of supra-thermal electrons, the results were more generally expressed in terms of the maximum energy deposited into the thermal electron heating front.

With varying energy transport coefficients, the codes showed that there existed a critical - quarter-critical surface peak excursion correlation. This was seen to agree with the experimental result. No evidence was observed of a nonhydrodynamically steepened density profile with scalelength consistently less than a micron.

References

- 2-1 J. Dawson, "Advances in Plasma Physics" VI Ed: Simon & Thompson, John Wiley and sons (1968), p. 12.
- 2-2 V. P. Silin, Soviet Physics JETP 20, 1510 (1965).
- 2-3 Catto and Speziale, Laboratory for Laser Energetics Report #42 (1976).
- 2-4 Dawson and Oberman, Physics of Fluids 5, 517 (1962).
- 2-5 Dawson and Oberman, Physics of Fluids 6, 394 (1963).
- 2-6 Faehl and Kruer, Physics of Fluids 20, 55 (1977).
- 2-7 Manheimer, Physics of Fluids 20, 265 (1977).
- 2-8 Ginzburg, "The Propagation of Electromagnetic Waves in Plasmas" 2nd edition, Pergamon Press (1970), pp. 260 - 280.
- 2-9 Omel'chenko, Panchenko and Stepanov, Radiophysics and Quantum Electronics 14, 1166 (1971).
- 2-10 Forsland, Kindel, Lee, Lindman, and Morse, Phys. Rev. A 11, 679 (1975).
- 2-11 Erkkila, University of California/Lawrence Livermore Laboratory Report #UCRL-51914, (1975).
- 2-12 Speziale and Catto, Laboratory for Laser Energetics Report #45, (1976).
- 2-13 Perkins and Flick, Physics of Fluids 14, 2012 (1971).
- 2-14 Kruer and Dawson, in "Laser Interaction and Related Plasma Phenomena" V2, Ed: Schwarz and Hora, Plenum Press (1972), p. 317.
- 2-15 Galeev and Sagdeev, Nuclear Fusion 13, 603 (1973).
- 2-16 Forsland, Kindel and Lindman, Phys. Rev. Letters 16, 739 (1973).
- 2-17 Liu, Rosenbluth, and White, Physics of Fluids 17, 1211 (1974).
- 2-18 DuBois, in "Laser Interaction and Related Plasma Phenomena" V3A Ed: Schwarz and Hora, Plenum Press (1974), p. 267.

- 2-19 Chen, in "Laser Interaction and Related Plasma Phenomena" V3A, Ed: Schwarz and Hora, Plenum Press (1974) p. 291.
- 2-20 Kruer, Valeo, and Estabrook, Phys. Rev. Letters 20, 1076 (1975).
- 2-21 Forsland, Kindel, Lee, Lindman, Phys. Rev. Letters 36, 35 (1976).
- 2-22 Liu, Physics of Fluids 19, 967 (1976).
- 2-23 Spitzer, "Physics of Fully Ionized Gases", Interscience (1962), p. 143.
- 2-24 Bickerton, Nuclear Fusion 13, 457 (1973).
- 2-25 Morse and Nielson, Physics of Fluids 16, 909 (1973).
- 2-26 J. Delettrez, Laboratory for Laser Energetics Report #36 (1977).
- 2-27 Lee, Forsland, Kindel, and Lindman, Physics of Fluids 20, 51 (1977).
- 2-28 Estabrook, Physics of Fluids 19, 1733 (1976).
- 2-29 Siegrist, Optics Communications 16, 402 (1976).
- 2-30 Erokhin, Zakharov, and Moiseev, Soviet Physics JETP 29, 101 (1969).
- 2-31 Vinogradov and Pustovalov, Soviet Physic JETP 36, 492 (1973).
- 2-32 Erokhin, Moisev, and Mukhin, Nuclear Fusion 14, 333 (1974).
- 2-33 Biskamp and Welter, Phys. Rev. Letters 34, 312 (1975).
- 2-34 Bobin, Optics Communications 14, 339 (1975).
- 2-35 Pant, Eidmann, Sachsenmaier, and Sigel, Optics Communications 16, 396 (1976).
- 2-36 M. Lubin, E. Goldman, J. Soures, L. Goldman, W. Friedman, S. Letzring, J. Albritton, P. Koch, and B. Yaakobi, in "Plasma Physics and Controlled Nuclear Fusion Research 1974 VII", International Atomic Energy Agency (1975), p. 459.

- 3-1 W. Smith, "Modern Optical Engineering", McGraw-Hill Book Co. (1966), p. 82-84.
- 3-2 "Kodak Plates and Films for Science and Industry"
- 3-3 D. Bradley, G. New, Proceedings of the IEEE 62, (1974), p. 313-315.
- 3-4 D. Bradley, B. Liddy, A. Roddie, W. Sibbett, W. Sleat, in "Advances in Electronics and Electron Physics V 33b", Ed: L. Marton, Academic press (1972), p. 1145.
- 3-5 High Speed Photography - Proceedings of the 11th International Congress on High Speed Photography, Ed: P. Rolls, Chapman and Hall Ltd., (1975).
- 3-6 Charatis, Downward, Goforth, Guscott, Henderson, Hildum, Johnson, Moncur, Leonard, Mayer, Segall, Siebert, Solomon, Thomas, in "Plasma Physics and Controlled Nuclear Fusion Research 1974 V II", "International Atomic Energy Agency (1975), p. 317.
- 3-7 Lubin, Goldman, Soures, Goldman, Friedman, Letzring, Albritton, Koch, Yaakobi, in "Plasma Physics and Controlled Nuclear Fusion Research 1974 V II", "International Atomic Energy Agency (1975), p. 459.
- 3-8 Haas, Mead, Kruer, Phillion, Kornblum, Lindl, MacQuigg, Rupert, Tirsell, Physics of Fluids 20, 322 (1977).
- 3-9 Ripin, Applied Physics Letters 30, 134 (1977).
- 3-10 J. Stone, "Radiation and Optics", McGraw-Hill Book Co. (1963); p. 168-176, 180-185, 224-230.
- 3-11 W. Smith, "Modern Optical Engineering", p. 63.
- 3-12 M. Born, E. Wolf, "Principles of Optics" Fourth Edition , Pergamon Press (1970), Fig. 9.5.

- 5-1 Bruce Perry, Private communication.
- 5-2 Steve Kumpan, Abe Nee, Private communication; J. Soures, S. Kumpan, J. Hoose, Applied Optics 13, 2081 (1974).
- 5-3 Pelah, Physics Letters 59A, 348 (1976).

- 5-4 Allan Hauer, Private Communication .
- 5-5 T. Bristow, "X-ray Emission and Ionization Dynamics of Laser Produced Plasmas" Ph.D. Thesis, University of Rochester, (1973).
- 6-1 J. Dawson, "Advances in Plasma Physics" VI Ed: Simon & Thompson, John Wiley and Sons, Inc. (1968). p. 12 .
- 6-2 V. P. Silin, Soviet Physics JETP 20, 1510 (1965).
- 6-3 Catto, Speziale, "Strong Field Inverse Bremsstrahlung Via a Lorentz Model" Laboratory for Laser Energetics Report #42, (1976).
- 6-4 Jacques Delettrez - Private communication.
- 6-5 Steve Kumpan and Abe Nee - Private communication;
J. Soures, S. Kumpan, J. Hoos, Applied Optics 13, 2081, (1974).
- 6-6 Faehl and Kruer, Physics of Fluids 20, 55 (1977).
- 6-7 Ginzburg, "The Propagation of Electromagnetic Waves in Plasmas", 2nd edition, Pergamon Press (1970), p. 260- 280.
- 6-8 Omel'chenko, Panchenko, Stepanov, Radiophysics and Quantum Electronics 14, 1166 (1971).
- 6-9 Forsland, Kindel, Lee, Lindman, Morse, Phys. Rev. A 11. 679 (1975).
- 6-10 Speziale and Catto, "Linear Wave Conversion in an Unmagnetized, Collisionless Plasma", Laboratory for Laser Energetics Report #45, (1976).
- 6-11 Erkkila, "Laser Light Scattering and Absorption in Dense Spherically Symmetric Plasmas", University of California/ Lawrence Livermore Laboratory, UCRL-51914 (Dec. 1975).
- 6-12 Born & Wolf, "Principles of Optics" 4th Edition, Pergamon Press (1970), p. 104-124.
- 6-13 E. Goldman, Laboratory for Laser Energetics Report #16, (Feb., 1973).
- 6-14 E. Goldman, Plasma Physics 15, 289 (1973).

- 6-15 E. Goldman, Laboratory for Laser Energetics Internal Report, "Tech. Note: Theory Group Report #6, (August, 1976).
 - 6-16 J. Delettrez, Laboratory for Laser Energetics Internal Report; "Tech. Note: Theory Group Report #8", (Dec. 1976).
 - 6-17 J. Delettrez, Laboratory for Laser Energetics Report #36, (1977).
 - 6-18 Malone, McCrory, and Morse, Phys. Rev. Letters 34, 721 (1975).
 - 6-19 Young, Whittock, Decoste, Ripin, Nagel, Stamper, McMahon, Bodner, Applied Physics Letters 30, 45 (1977).
 - 6-20 Yaakobi and Bristow, Phys. Rev. Letters 38, 350 (1977).
-
- A-1 J. Stone, "Radiation and Optics", McGraw-Hill Book Co. (1963); pp. 168-176, 180-185, 224-230.
 - A-2 W. Smith, "Modern Optical Engineering", McGraw-Hill Book Co., (1966), p. 63.
 - A-3 M. Born, E. Wolf, "Principles of Optics, Fourth Edition", Pergamon Press (1970), fig. 9.5.
 - A-4 D. Bradley, B. Liddy, A. Roddie, W. Sibbett, W. Sleat, in "Advances in Electronics and Electron Physics V 33b", Ed: L. Marton, Academic Press (1972), p. 1145.

Appendix A - Spatial Resolution and Spatial Accuracy

This appendix analyzes the sources of spatial error encountered in spatially and temporally resolved harmonic emission studies (section 3.3). The resolution of microscope systems viewing three-dimensional objects is computed. The performance of the optical system used in the experiment is determined. Particular attention is paid to the streak camera spatial resolution. The possible effect of refraction is estimated. Finally, a simple image analysis technique is developed that accounts for and eliminates most of the systematic error introduced by the finite system resolution.

A.1 Finite Object Thickness

A well corrected optical system images a plane object into a plane image. If a three-dimensional object is being photographed then only one plane in the object can be brought into sharp focus on the photographic film. The rest of the object will be blurred to some extent. Even if only one plane is being studied, the effect of the entire object must be considered since, in general, the out of focus light will overlay the one sharply focused plane.

The amount of blur is a function of the thickness and shape of the object and of the angular spread in the rays that leave the object and are collected by the optics.

Finite object thickness effects (FOT) can be analyzed by treating the object, i.e., the $2\omega_0$ or $(3/2)\omega_0$ emitting surface, as a spherical surface. The goals of the measurement are to determine the position of the emitting surface and to examine the spatial structure of the emissions. The radius of the sphere and the loca-

tion of points on its surface are, thus, to be measured.

It is assumed that the optical system has been focused onto the major circumference of the sphere perpendicular to the optical axis of the viewing system. Light is assumed to be emitted in all directions but attention is restricted to those rays that are emitted at an angle ϕ to the optical axis such that $|\phi| \leq \phi_M$, the maximum acceptance angle of the optical system. The situation is illustrated in figure A-1.

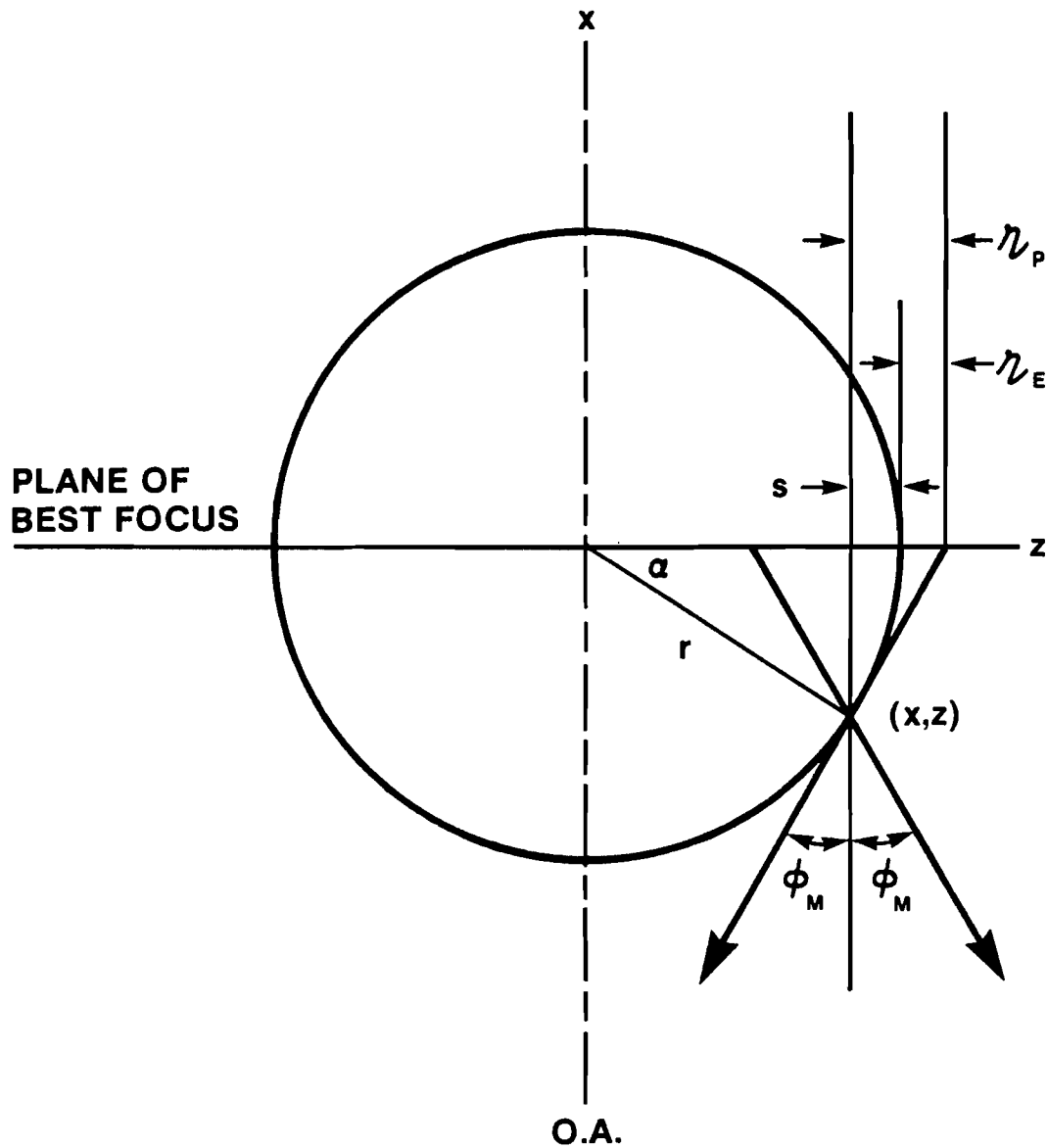
To proceed, note that the amount of blur is determined by the projection onto the z axis of the rays leaving a point (x,z) at an angle ϕ_M to the optical axis (O.A). The edge resolution is determined by the maximum differences between the z coordinate of the ray projection and the radius of the emitting surface. To determine the maximum difference, the difference due to each point of the sphere surface is calculated and $\partial/\partial z$ of the difference is found and set equal to zero. This locates the point producing the maximum difference. The edge resolution is then computed.

With reference to figure A-1, the difference between the ray projection and the sphere's radius 'r' is

$$\begin{aligned} \epsilon &= x \tan \phi_M - s \quad \text{where } s = r-z \\ \epsilon &= z + (r^2 - z^2)^{\frac{1}{2}} \tan \phi_M - r \end{aligned} \tag{A-1}$$

Taking the first derivative with respect to z of (A-1) and setting it equal to zero the location of the point causing the maximum edge blur

FIGURE A-1
**GEOMETRY FOR EMITTING SOURCE WITH
FINITE THICKNESS**



is found.

$$\frac{\partial \nu}{\partial z} = 0 = 1 - \frac{z \tan \phi_M}{(r^2 - z^2)^{1/2}}$$

$$z = r \cos \phi_M \text{ or } \alpha = \phi_M \text{ for maximum } \nu. \quad (\text{A-2})$$

The edge resolution due to finite object thickness ($\nu_{E - FOT}$) is the value of ' ν ' in equation (A-1) for the conditions of equation (A-2).

$$\nu_{E - FOT} = \frac{r(1 - \cos \phi_M)}{\cos \phi_M} \quad (\text{A-3})$$

The f-number of the entrance pupil is related to ϕ_M by:

$$f_c \equiv \frac{1}{2 \tan \phi_M} \quad (\text{A-4})$$

so that (A-3) becomes

$$\nu_{E - FOT} = r \left[\left(1 + \frac{1}{4f_c^2} \right)^{1/2} - 1 \right] \quad (\text{A-5})$$

f_c is typically greater than 1 so that (A-5) can be approximated by

$$\nu_{E - FOT} \approx \frac{r}{8f_c^2} \quad f_c > 1 \quad (\text{A-6})$$

If no other effects are considered, then (A-6) indicates that

for a given emitting surface radius, $r_E - FOT$ is smallest for the largest f_c . The blur is smallest when the cone of rays producing it is most acute.

The point resolution is determined as the difference between the emitting point's marginal ray projection at the z-axis and the z coordinate of the emitting point. The difference is equal to the point resolution $r_p - FOT$.

$$r_p - FOT = x \tan \phi_M = \frac{x}{2f_c} \quad (A-7)$$

The blur is zero for points on the plane of best focus and becomes worse as the emitting point moves away from the focal plane.

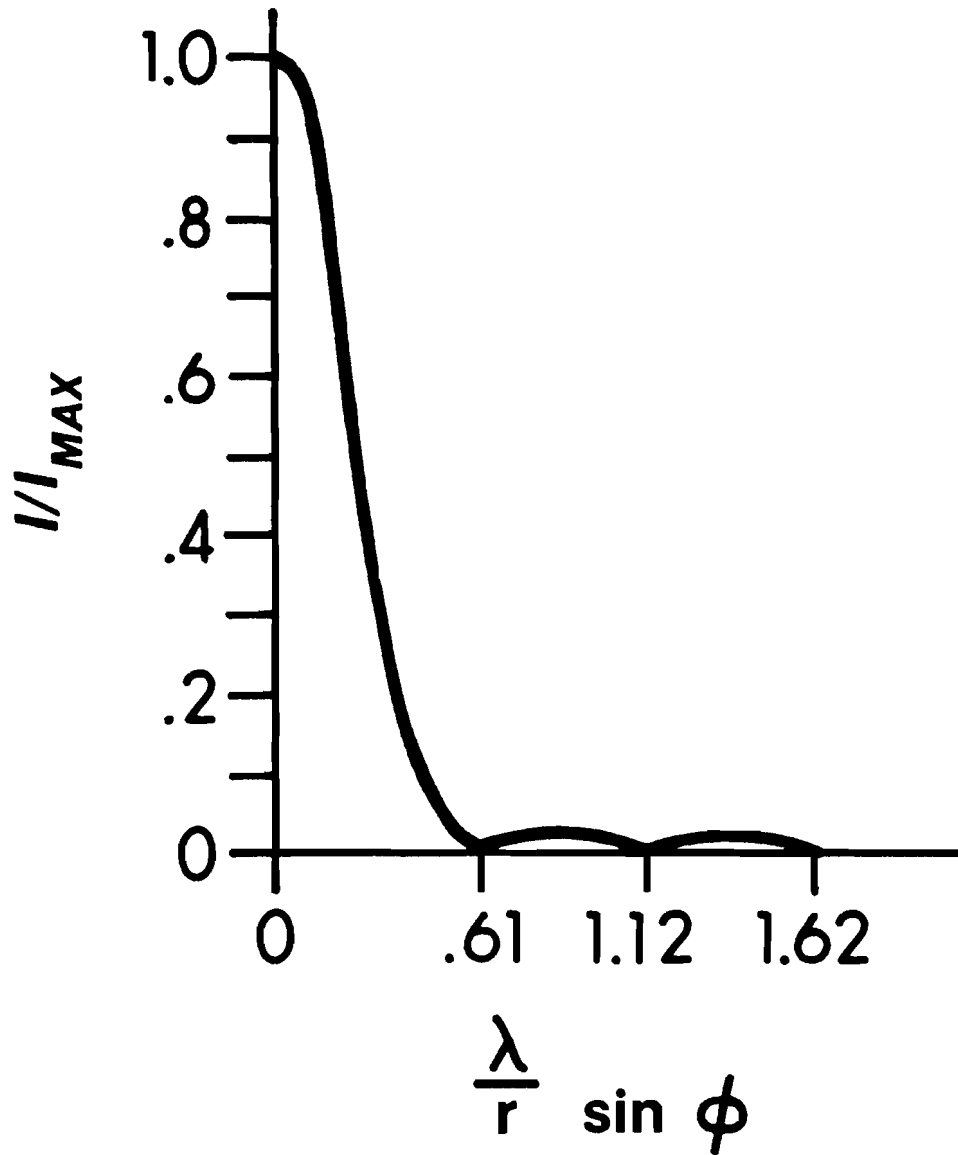
A.2 Diffraction Limited Resolution

Diffraction limited performance is a consequence of the finite acceptance angle (f-number) of an optical system. The limitation on resolution can be most easily seen by considering the diffraction of a plane wave by a circular aperture in an otherwise opaque screen. Although the light entering the aperture is collimated (plane waves), the light leaving the aperture is spread out over a range of angles. ^(A-1) The light pattern is the "Airy diffraction pattern" (figure A-2) and the range in angles is characterized by the first zero of the intensity distribution. This angle is given by

$$\phi_d = .61 \frac{\lambda}{r} \quad (A-8)$$

where 'r' is the radius of the aperture and ' λ ' is the wavelength of

FIGURE A-2

AIRY DIFFRACTION PATTERN

the light. To form a perfect image of the aperture all of the diffracted light has to be collected and to form a "good" image all the light within the angle ' ϕ_M ' needs to be collected. (A-1)

If an optical system is to have a diffraction limited resolution ' κ_D ' then it should collect all the light within the range $\phi \leq \phi_M$ where

$$\phi_M = .61 \frac{\lambda}{\kappa_D} \quad (A-9)$$

solving for ' κ_D ' in (A-9) and noting that $\phi_M \approx 1/2f_c$, the diffraction limited resolution of the optical system is obtained as a function of the entrance pupil f-number and of the wavelength of the light.

$$\kappa_D = 1.22 \lambda f_c \quad (A-10)$$

A.3 Resolution of a Diffraction Limited System for Viewing a Three-Dimensional Object

If flat objects are being viewed then the maximum theoretical resolution is the diffraction limited resolution of equation (A-10). Since the plasmas are three-dimensional the resolution is determined by the combined effects of finite object thickness, equation (A-6) or (A-7), and the diffraction limited optical system performance of equation (A-10). The net resolution for these essentially independent effects is given by:

$$\kappa = (\kappa_{FOT}^2 + \kappa_D^2)^{1/2} \quad (A-11)$$

The edge resolution, ' ν_E ', is:

$$\nu_E = \left[\left(\frac{r}{8f_c} \right)^2 + (1.22 \lambda f_c)^2 \right]^{1/2} \quad (\text{A-12})$$

and the point resolution, ' ν_p ', is:

$$\nu_p = \left[\left(\frac{x}{2f_c} \right)^2 + (1.22 \lambda f_c)^2 \right]^{1/2} \quad (\text{A-13})$$

Plots of ' ν_E ' and ' ν_p ' as functions of f-number, at $\lambda = .53 \mu\text{m}$ for several source sizes comparable to those of the plasma, are found in figures A-3 and A-4. Both ' ν_E ' and ' ν_p ' as functions of f-number have minima. The f-numbers for optimum resolution occur at different places, and below these values the resolution rapidly degrades. The edge resolution is independent of source size, for the radii of interest, at $f_c > 5$. The point resolution is essentially independent of source location ($\Delta\nu_p < 1 \mu\text{m}$ for the source sizes of interest) for $f_c > 12$.

For a system optimized for edge resolution $f_c \approx 3$ and $\nu_E \approx 2 \mu\text{m}$. The point resolution of points on the emitting surface and near the optical axis is poor. For $x = 50 \mu\text{m}$, $\nu_p \approx 9 \mu\text{m}$ and for $x = 100 \mu\text{m}$, $\nu_p \approx 17 \mu\text{m}$. For optimum point resolution $f_c \approx 7 \rightarrow 9$ and the point resolution is $6 \mu\text{m}$ and $8 \mu\text{m}$ for points $50 \mu\text{m}$ and $100 \mu\text{m}$ from the plane of best focus. Edge resolution at these f-numbers is $\nu_E \approx 5 \mu\text{m}$. Overall system performance is best for a system optimized for point resolution.

FIGURE A-3

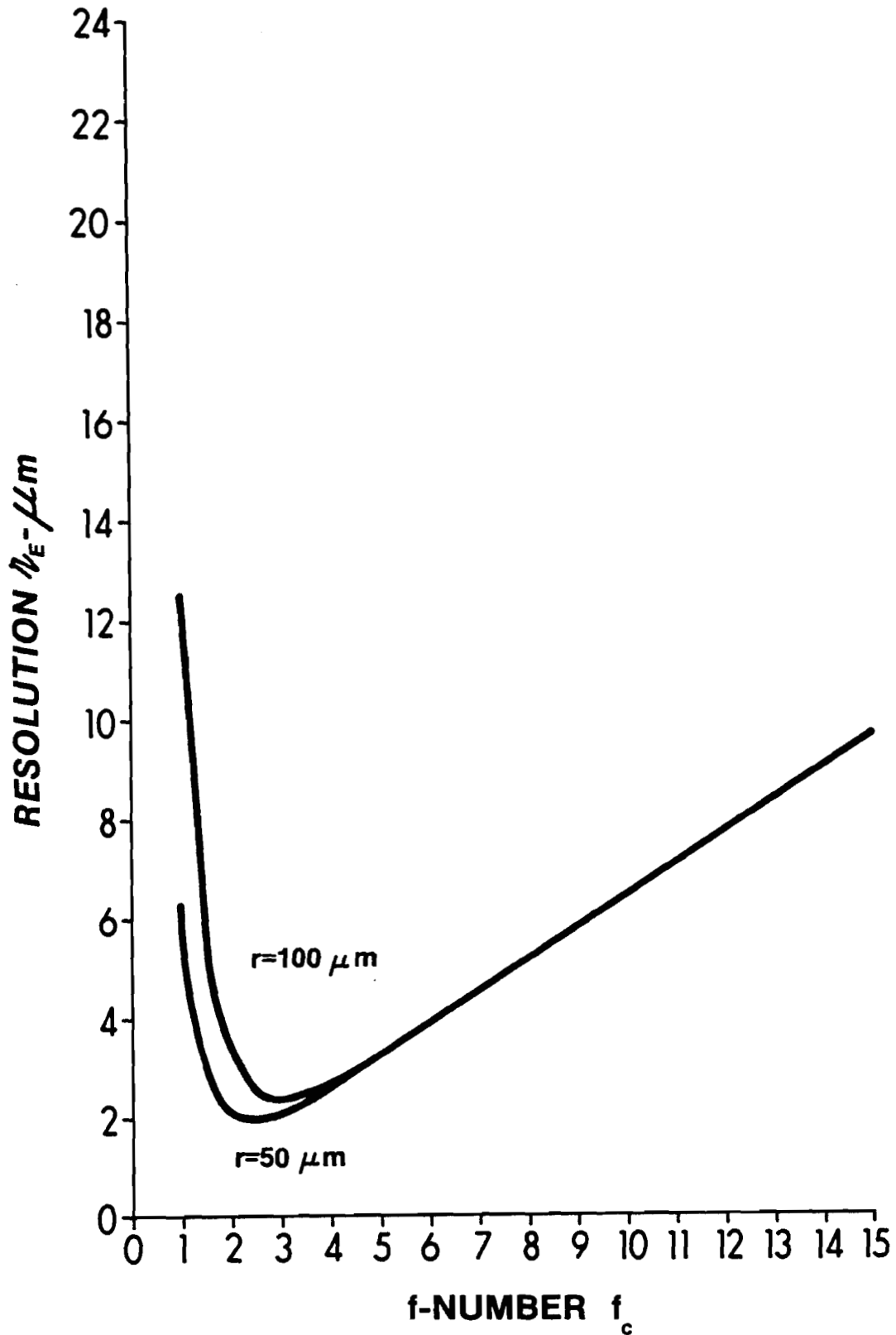
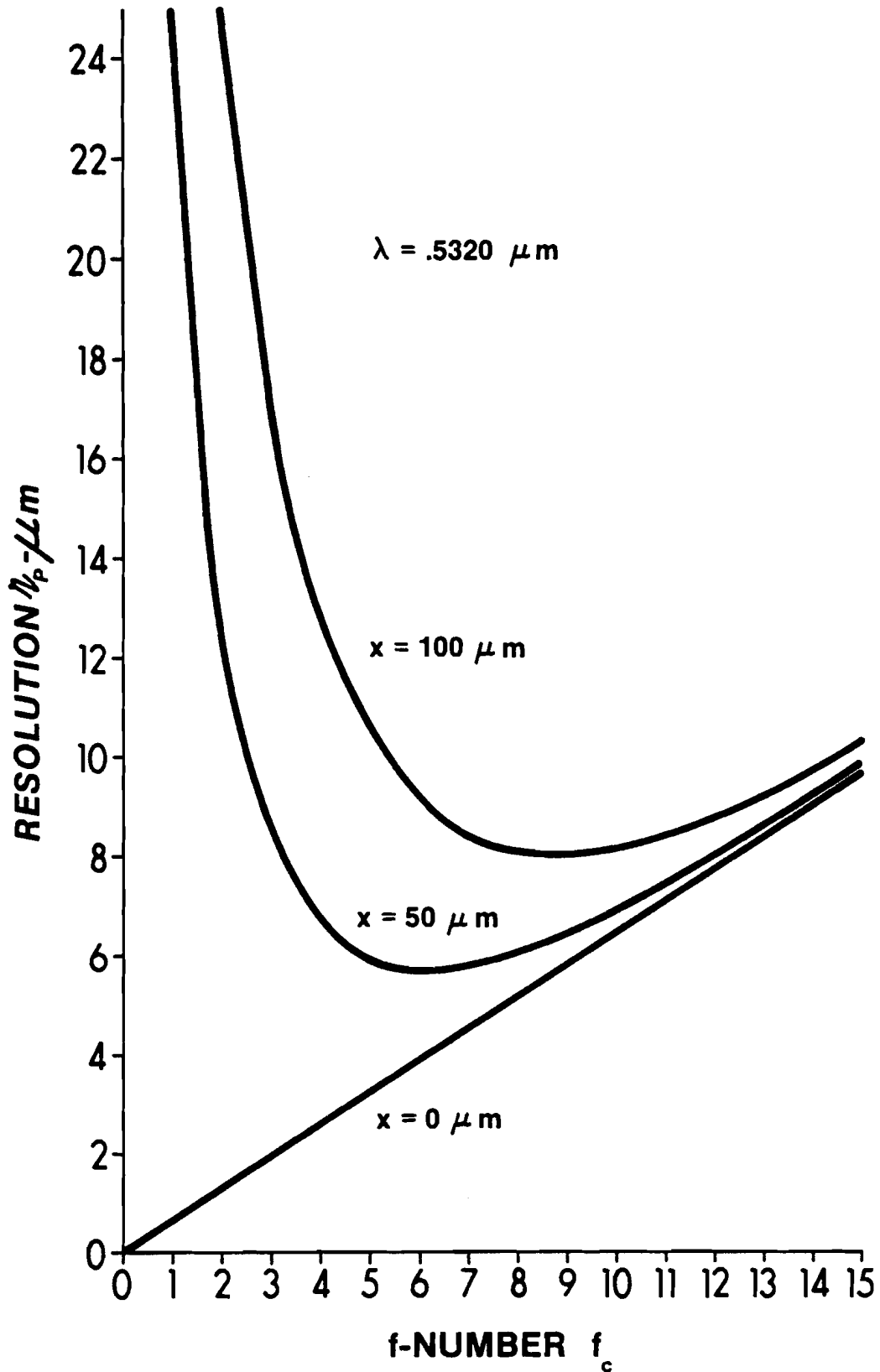
RESOLUTION OF AN EDGE FOR EMITTING SURFACES WITH RADIUS r .

FIGURE A-4

**RESOLUTION OF A POINT AT A HEIGHT x
ABOVE THE PLANE OF BEST FOCUS**

A.4 Real Optical System Performance

The actual optical system was run at an f -number of $f_c = 13$. This was the lowest f -number for which the non-symmetrical aberration of coma was eliminated^(A-2) and for which the symmetrical aberrations of spherical and axial chromatic aberration were reduced^(A-2) to the point where an Airy diffraction pattern could be clearly observed.^(A-3) The resolution for a flat object was nearly diffraction limited, figures A-3 and A-4, and was determined by photographing a resolution chart, figure A-5, and observing which element was "just" resolved. The "just" resolved element for green light ($\lambda \approx .53 \mu\text{m}$) illumination was group 7 element 1 which gave a value for the spatial resolution of $8 \mu\text{m}$. This is in good agreement with the predictions for diffraction limited or near diffraction limited performance. The flat object resolutions for the two wavelengths of interest are shown in table A-1.

WAVELENGTH λ - μm	FLAT OBJECT POINT RESOLUTION μm
.5320	8.
.7093	11.

FLAT OBJECT POINT RESOLUTION FOR THE
OPTICAL SYSTEM

TABLE A-1

Three dimensional object resolutions are obtained using equations (A-12) and (A-13). With the optical system at $f_c = 13$ no chromatic aberration was observed with white light illumination of the bar

FIGURE A-5
RESOLUTION CHART PHOTOGRAPHED THROUGH
THE OPTICAL SYSTEM

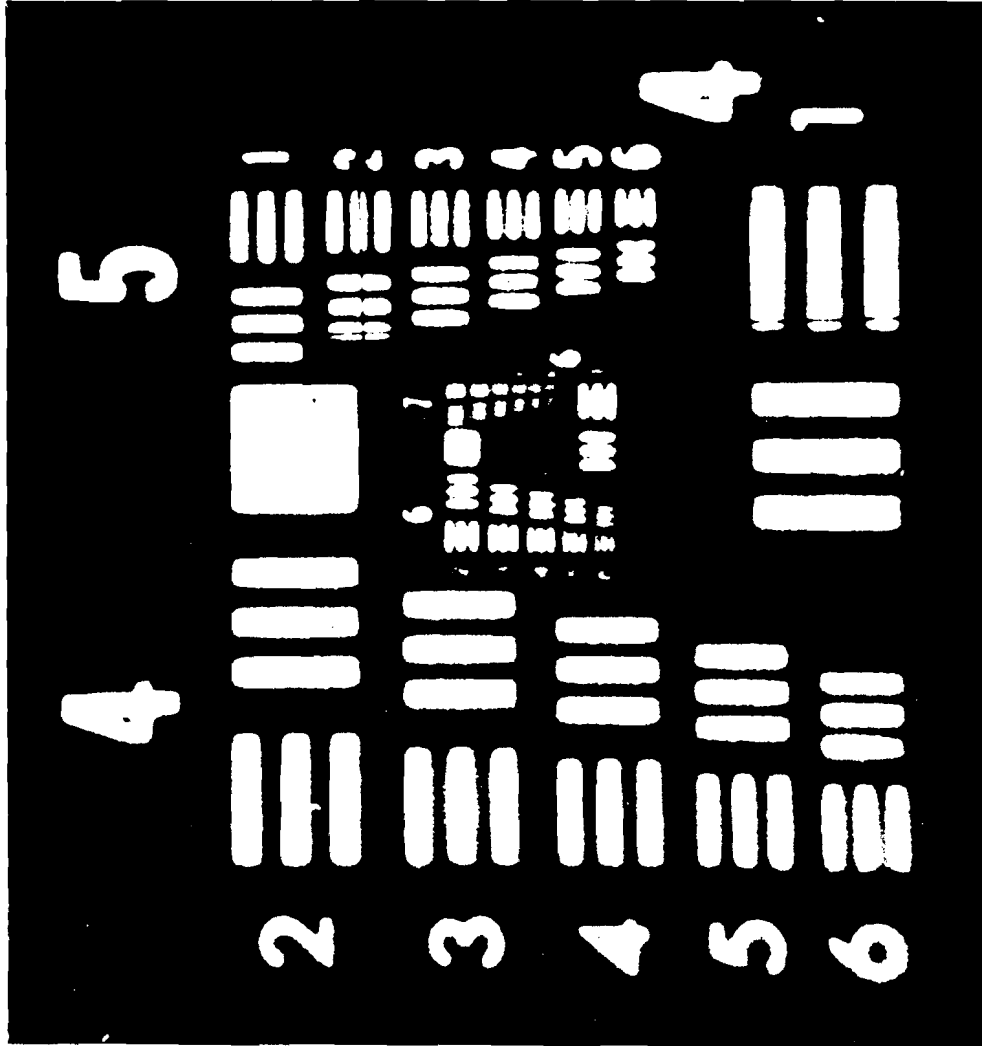


chart and of 100 μm diameter CD_2 and glass spheres used as test objects.

A.5 Streak Camera Spatial Resolution

Spatial resolution of the streaked results was determined in several ways. The first approach was to image a spherical CD_2 target through the optical system and streak camera. With the streak camera in focus mode (images not streaked) and the slits removed, an image of the target was formed at the streak camera output. A photograph of the image was taken and a microdensitometer trace was made across it. The system resolution was determined by analyzing the microdensitometer trace.

The measurements were made with the equipment setup and aligned for a shot, the only exception being the absence of the interference filters. The targets were illuminated from the side with the focused broad-band light of a mercury-arc lamp and the light scattered by 90° was collected by the optical system. The target was translucent but appeared brightest where the focused beam entered and exited the surface.

Figure A-6 shows the data for a typical resolution measurement. 'a' is the image through the streak camera and 'b' is a microdensitometer trace through one of the target images. The trace shows the spatial variation of the film density. For comparison, 'c' shows a CD_2 target illuminated by two mercury-arc lamps and viewed through the time integrated optics. 'd' is the corresponding microdensitometer trace.

FIGURE A-6

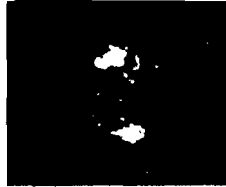
TEST OBJECT IMAGES

IMAGE OF CD₂ TARGET THROUGH STREAK CAMERA IN FOCUS MODE

IMAGE FOR $2\omega_0$ STREAK



IMAGE FOR $(3/2)\omega_0$ STREAK

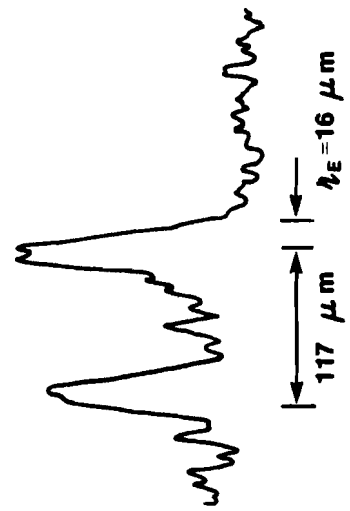


a

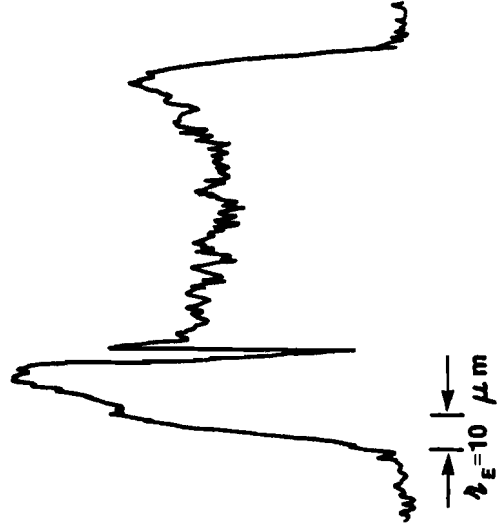
A CD₂ TARGET IMAGED THROUGH THE TIME INTEGRATED OPTICS



c



b



d

The sloped density drop at the outer edge is due to the instrument response. The width of the drop, from the outer edge of the object to the outer point of the instrument response, is the measure of edge resolution. The outermost point in the instrument response is taken as the extrapolation of the density curve in the $.5D_{MAX}$ region to the base density. The slope of the edge response is a straight line for most of the density drop.

The innermost point of the edge response, the outer edge of the object, is taken as the point where the density first reaches a local maximum or first enters a region of slow variation. The selection of this point is subjective and often unclear. For this reason the innermost edge response point is used only in the estimation of the system resolution.

The ideal system magnification is equal to the distance between the inner points of the edge response divided by the target diameter. The edge resolution is equal to the thickness of the edge response divided by the ideal system magnification. The edge resolution for the streak-camera-optics system is $16 \mu\text{m}$. For an optical system resolution of $10 \mu\text{m}$, the streak camera static resolution in the object space is $12 \mu\text{m}$. At the streak camera slits the resolution in focused mode is $.234 \text{ mm}$ or $4.3 \frac{\text{LINE PAIR}}{\text{mm}}$.

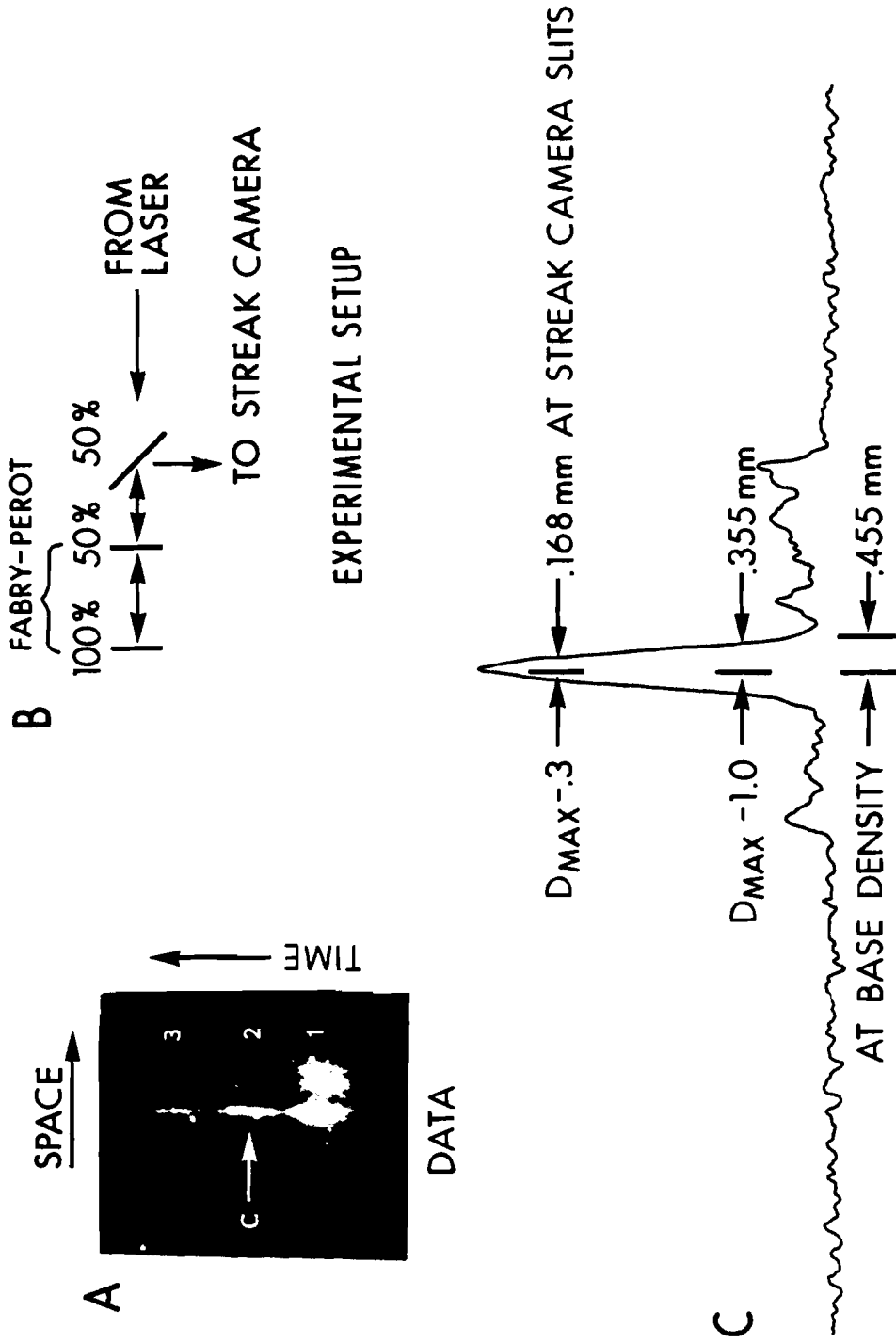
The first techniques for streak camera resolution determination measured the resolution with the camera operated in focused mode. Measurements by Bradley^(A-4) indicate that the dynamic spatial resolution of the streak camera may be degraded from its static spatial

resolution.

To compare the dynamic and static spatial resolution, an experiment was performed in which a 30 μm wide slit was placed perpendicular to the streak camera slits. A point of light with a width less than 1/5 of a resolution element was imaged through the streak camera. The resulting streaked image gave a dynamic point spread function for the streak camera. The illumination was a ~ 200 psec long 1.06 μm pulse from the high power Nd-glass laser system. The pulse was passed through a "leaky" Fabry-Perot interferometer consisting of a 50% and 100% mirror. The output consisted of a train of pulses, each with an amplitude 50% of the previous one. Data with a wide intensity spread was produced so that intensity dependent effects could be observed. The film used in this test was developed as for all data shots.

Figure A-7 shows a photograph of the data. Three reflections covering an intensity range of four are recorded. The intensity of the pulse varies in time so that several points can be measured within each reflection. A density range of 2 (factor of 100 in intensity) is covered in a single shot. 'b' is a schematic of the experimental arrangement and 'c' is a microdensitometer scan in the spatial direction through the center of the second reflection.

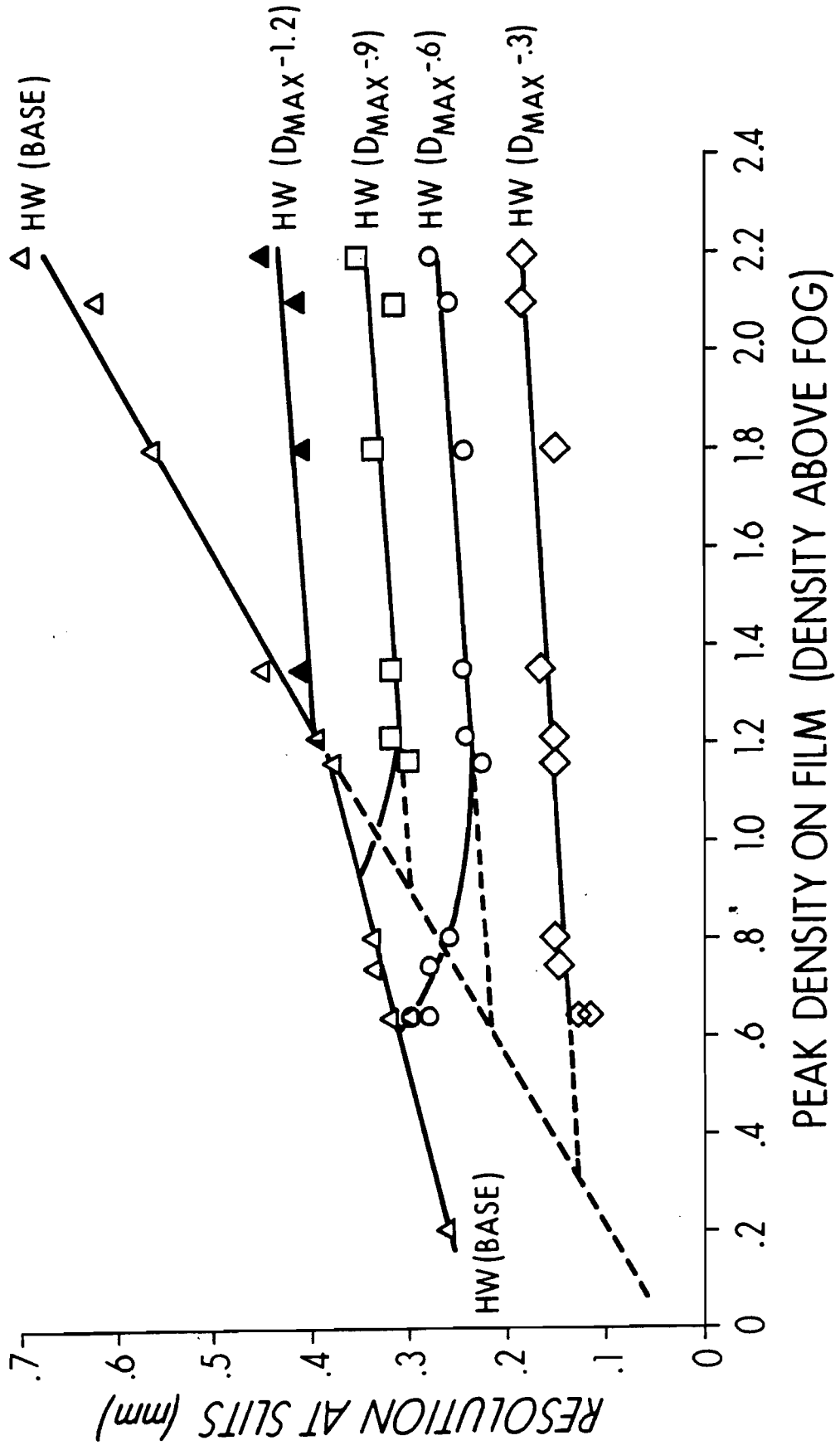
Figure A-8 shows the results with the resolution, referenced to the streak camera slits, plotted as a function of the peak signal density ' D_{MAX} ' (density above fog) for each microdensitometer scan. (Resolution is studied as a function of density because the



MICRODENSITOMETER SCAN ACROSS A SEGMENT OF THE STREAKED SLIT IMAGE

FIGURE A-7

FIGURE A-8
 DYNAMIC STREAK CAMERA SPATIAL RESOLUTION



$2\omega_0 - (3/2)\omega_0$ data is reduced from density plots.) The half-widths of the streak camera point response are plotted for several values of $D = D_{MAX} - D_s = \text{CONST}$, and for the half-width at the base density, i.e., for $D_s = 0$. D_s is the local signal density.

To understand the results it is first necessary to consider the relationship between the measured film density at a point and the amount of energy at the point 'E' (exposure) that generated the signal. In a linear photographic system the signal density is related to the exposure by the relation

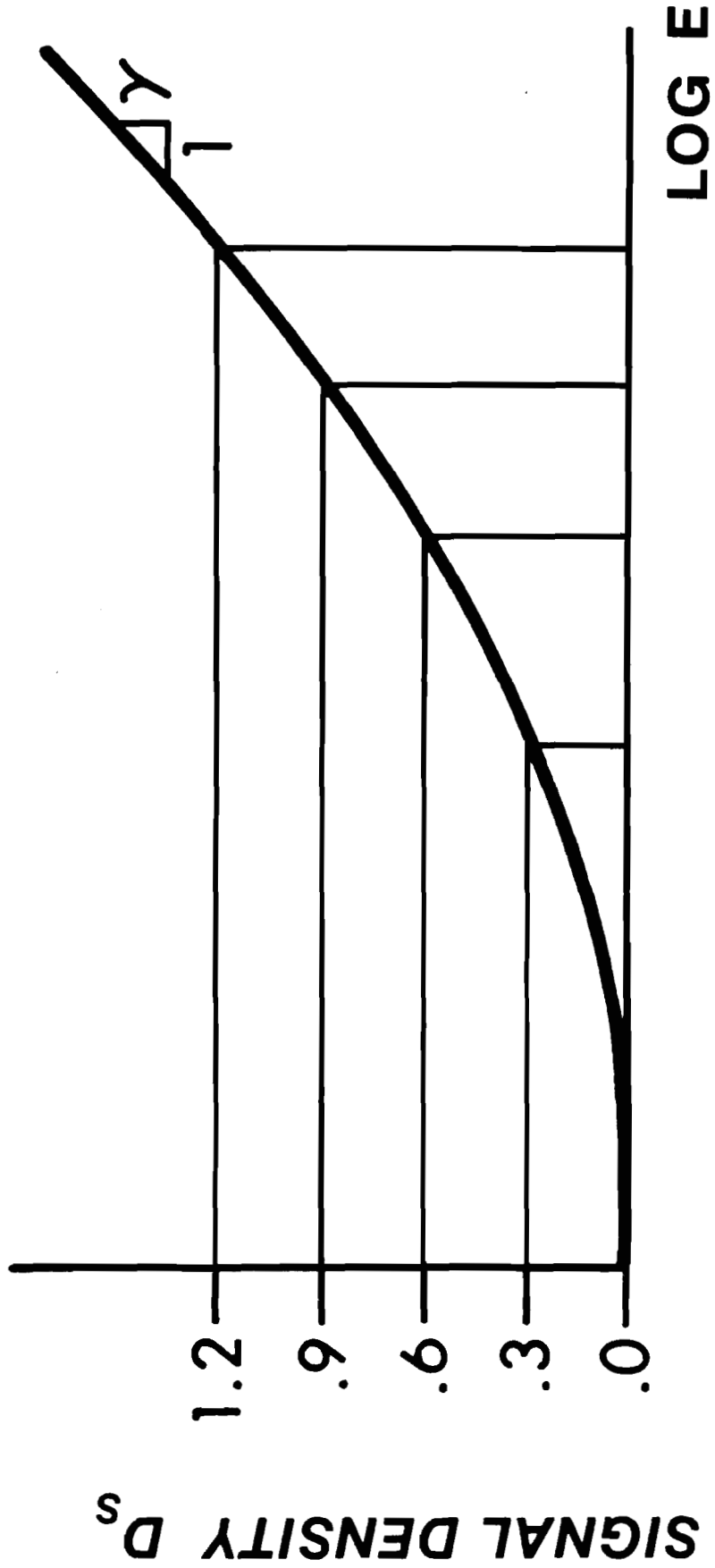
$$D_s = \gamma \log E \quad (\text{A-14})$$

where $\gamma = \text{CONST}$.

At low exposure levels γ is a variable and decreases with decreasing exposure. In figure A-9, a $D - \log E$ curve is sketched.

For constant γ , $D_{MAX} - D_s = \text{CONST}$. corresponds to a constant ratio of local signal exposure to peak response function exposure, i.e., $E_s/E_{MAX} = \text{CONST}$. Comparison of point response widths at $D_{MAX} - D_s = \text{CONST}$. or $E_s/E_{MAX} = \text{CONST}$. for different values of D_{MAX} or E_{MAX} gives the intensity dependence of the point response shape. At low exposures, however, a constant drop in density results in a larger drop in exposure than expected for constant γ . The effect is that low density point response half-widths are measured at lower intensities than expected for constant γ and the widths are larger than expected for constant γ .

FIGURE A-9
**SKETCH OF D-LOG E CURVE
AND EFFECT OF VARIABLE γ**



Even if the point response of the streak camera were constant, non-linear γ would cause the half-width of the $D_{MAX} - \Delta D$ point response curves to vary at low densities. That this is the observed effect is suggested by noting that the half-width curves measured at $D_{MAX} - \Delta D$ for high signal densities ($D_S > .5$) are approximately straight lines. γ is constant in this region. The broadening of the point response at constant E_S/E_{MAX} appears small. The half-width measured at the base density ($D_S = 0$) increases, but this increase is due to the fact that the streak camera has a minimum intensity detectability level. For stronger signals, more of the point response is detected. The half-width at base density increases linearly above $D_{MAX} = 1.2$. (For traces with large D_{MAX} the effect of variable γ is restricted to a relatively small density range around the base. The effect is minimized by extrapolating the response curves from the constant region down to the base.) The HW (BASE) and HW ($D_{MAX} - \Delta D$) curves must intersect when $D_{MAX} - \Delta D = 0$. If the experimental HW ($D_{MAX} - \Delta D$) curves are linearly extrapolated from the high D_S regions to $D_{MAX} = \Delta D$, then points for the HW (BASE) are obtained consistent with the assumption of constant γ . These additional points lie on a straight line which is almost an exact extrapolation of the curve fit for the experimental HW (BASE) points in the high peak density region. The ordinate of this line at $D_{MAX} = 0$ is approximately equal to the combined widths of the crossed slit and the slit on the microdensitometer.

Several conclusions can be made about the streak camera resolution. The first is that the $D_{MAX} - D_S = \text{constant}$ curves show the

intensity distribution of the point response to only weakly broaden with increasing input intensity. The second is that since the shape of the response function is nearly constant, the broadening at the base is due only to the presence of a minimum detectability level. More of the point response function is seen for higher peak intensities. The spatial resolution degrades when an image is streaked. The degradation given by $1 - (R_{\text{STATIC}}/R_{\text{DYNAMIC}})$ is approximately 25%.

In order to see the effect of streak camera resolution on the $2\omega_0 - (3/2)\omega_0$ results, the HW (BASE) curve of figure A-8 is re-plotted as the solid line in figure A-10. Here the resolution is referenced to the object space of the system. The dashed lines are the system resolutions of the streak camera and the optical system at $f_c = 13$ for the $2\omega_0$ and $(3/2)\omega_0$ frequencies.

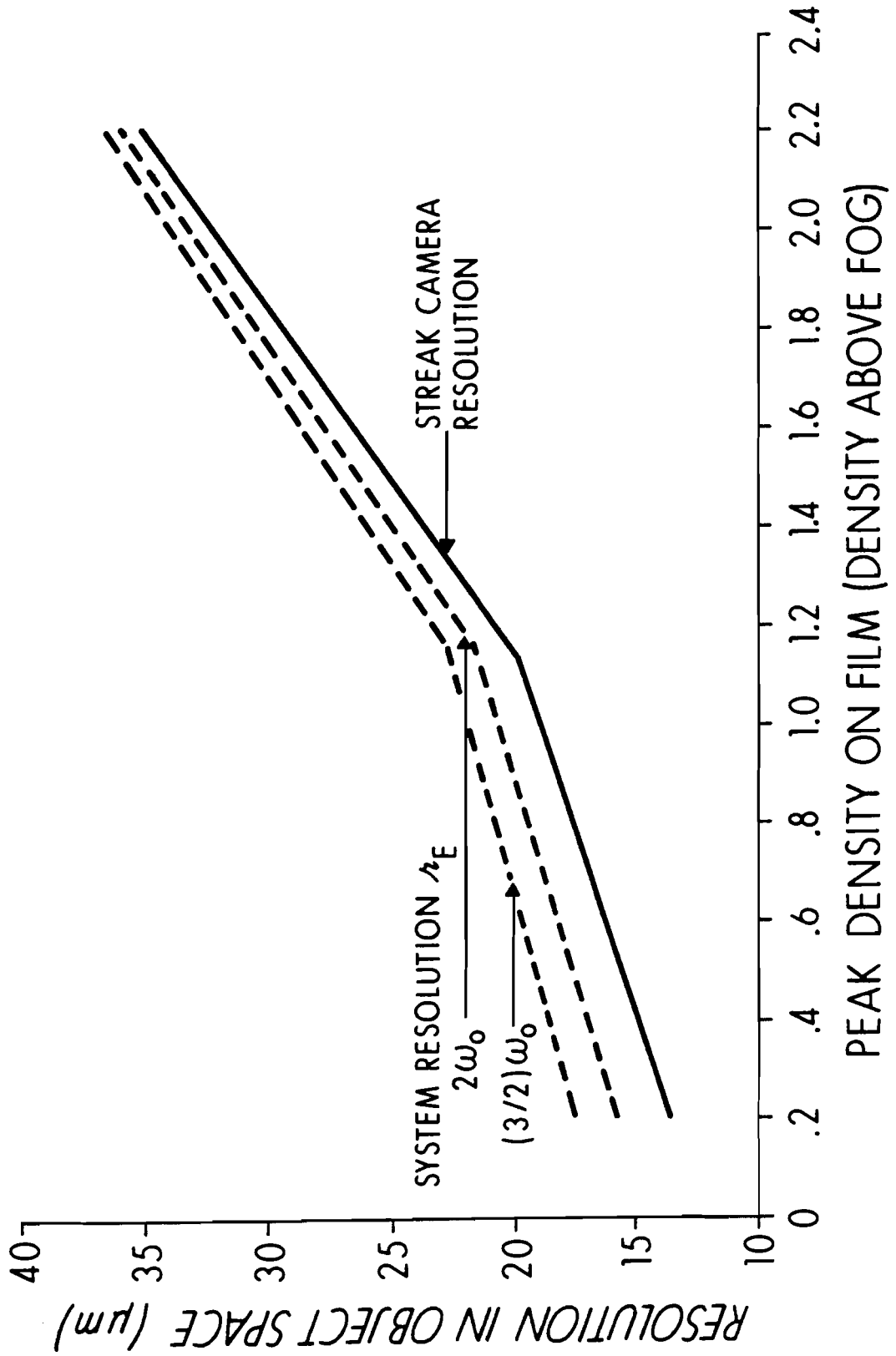
The streaked $2\omega_0 - (3/2)\omega_0$ data usually lies within the peak density range of .3 to 1.0. Within this range the system resolution varies from 16 μm to 21 μm at $2\omega_0$ and from 17 μm to 22 μm at $(3/2)\omega_0$. The average system resolutions and their bounds are $18 \pm 2 \mu\text{m}$ at $2\omega_0$ and $20 \mu\text{m} \pm 2$ at $(3/2)\omega_0$.

A.6 Distortion Due to Refraction

An inhomogeneous plasma has a variable index of refraction and causes light passing obliquely through it to bend. If the goal of an observation is to locate a source of emissions within the plasma then the effect of light refraction must be considered.

Consider the case of refraction through a spherical plasma. The emitting surface is a sphere and, as in the experiment, the goal is

FIGURE A-10
 SPATIAL RESOLUTION OF STREAKED DATA



to determine the sphere's radius. The plasma emissions are viewed from a single direction and since the acceptance angle of the optical system is small, $\phi_M = \pm 2^\circ$ for $f_c = 13$, it is sufficient to treat only those rays which after refraction propagate parallel to the optical axis of the viewing system.

The situation is depicted in figure A-11 which shows the results of a typical ray trace computation. The error introduced by refraction occurs because after a ray has passed out of the plasma its height from the optical axis is less than the height of the emitting point. The image formed by the optical system is equivalent to the straight line projection, into the plane of best focus, of the ray trajectories after refraction. Refraction, thus, causes the emitting point to be shorter than the actual emitting point height.

To determine the magnitude of the error, the ray is found which after refraction has the largest ray height. This ray delineates the outer edge of the image. The error due to refraction is then given by the difference between the actual radius 'r' and the apparent radius 'r_{APP}', i.e.,

$$\Delta r_{REF} \equiv r - r_{APP} \quad (A-15)$$

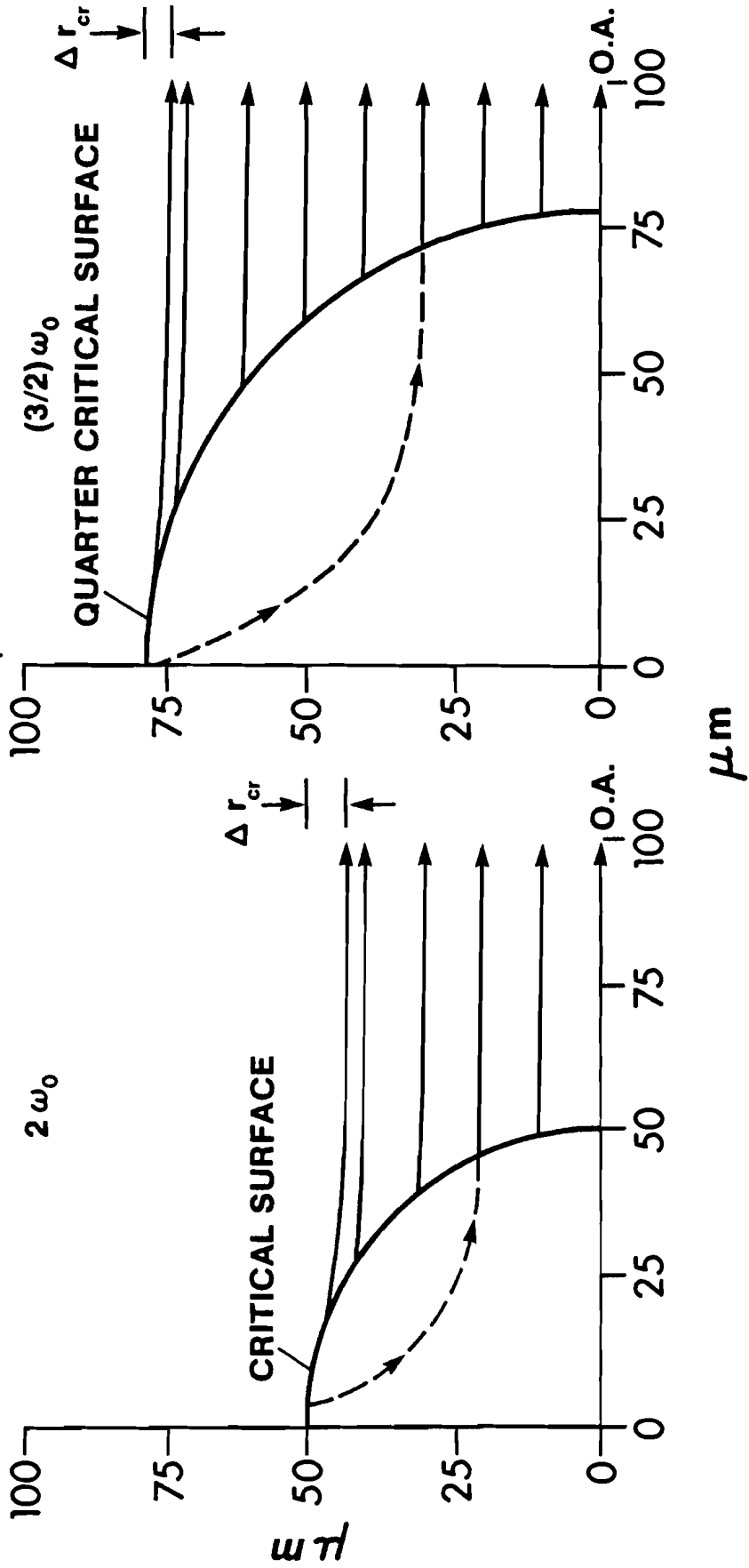
Refraction was studied with the use of a computer code that numerically calculated the ray trajectories and with an analytic model. The refraction theory is developed in chapter 6. Only the results are presented here.

The code was run for an exponential plasma density profile of

FIGURE A-11

REFRACTION OF PLASMA EMISSIONS

CRITICAL DENSITY AT $r_{cr} = 50 \mu\text{m}$
 SCALELENGTH $L = 28 \mu\text{m}$



the form

$$n = n_{cr} e^{-(r - r_{cr})/(\cdot 721\ell)} \quad (\text{A-16})$$

where 'n' is the electron density at radius 'r', $n_{cr} = 10^{21} \text{ cm}^{-3}$ is the critical density of 1.06 μm light, ' r_{cr} ' is the location of the critical density, and ' ℓ ' is the distance between the critical and quarter-critical densities. A parameter map for r was formed for the $2\omega_0$ and $(3/2)\omega_0$ emissions by varying r_{cr} and ℓ .

Plasmas with very short scalelengths were modelled by treating the plasma gradients as sufficiently steep so that the refraction was across a sharp boundary from an index of refraction equal to that at the emitting surface to an index of refraction of a vacuum. Rays were examined which after refraction propagated parallel to the optical axis and the outermost ray was determined.

The results of the study are: The ray that appears at the outer edge of the image is the ray that was generated tangent to the emitting surface. The refraction correction at each frequency is given by a single equation

$$r = \frac{r_{APP}}{\mu} \quad (\text{A-17})$$

where μ is the index of refraction of the emitted light at the source density and is given by

$$\mu = \left[1 - (8.94 \times 10^{-14} \text{ cm}^{-1}) \lambda^2 n_e \right]^{1/2} \quad (\text{A-18})$$

Note that the refraction correction is independent of scalelength.

The possible errors in the measurements due to refraction are given by

$$\Delta r_{\text{cr} - \text{REF}} \equiv r_{\text{cr}} - r_{\text{cr APP}} = .15 r_{\text{cr APP}} \quad (\text{A-19})$$

$$\Delta r_{\frac{1}{4}\text{cr} - \text{REF}} \equiv r_{\frac{1}{4}\text{cr}} - r_{\frac{1}{4}\text{cr APP}} = .06 r_{\frac{1}{4}\text{cr APP}} \quad (\text{A-20})$$

$$\Delta \ell_{\text{REF}} \equiv \ell - \ell_{\text{APP}} = .06 \ell_{\text{APP}} - .09 r_{\text{cr APP}} \quad (\text{A-21})$$

It should be noted that equations (A-19) - (A-21) appear to overestimate the refraction corrections. This is seen from the experimental results (Chapter 5) by first noting that the streak results show an initial critical surface radius equal to, within the $\pm 4 \mu\text{m}$ accuracy of the final results, the initial target radius. Equation (A-17) would have predicted an apparent radius of $.87 r_{\text{T}}$. Secondly, a minimum apparent scalelength of about $4 \mu\text{m}$ to $7 \mu\text{m}$ is predicted from (A-21). $0 \mu\text{m} \pm 6 \mu\text{m}$ scalelengths have often been seen.

A plausible explanation is that the plasma does not have smooth isodensity surfaces but that there exists local structures or turbulence. Such structures, as discussed in Chapter 2, are expected. For a plasma with steep density gradients, refraction of the emissions is dominated by the plasma profile near the source. Under such circumstances the light emitted from within each structure suffers refraction, as per equation (A-17) with $r_{\text{cr APP}}$ and r_{cr} replaced by the local radii of curvature, but there is always some light from each structured region that is refracted towards the optical axis. Thus the entire emitting sphere is seen.

Because of the discrepancy between theory and experiment equations (A-19) to (A-21) can be used only as an upper bound on the refraction error. The actual error is probably smaller.

A.7 Image Analysis

The results of the preceding sections show that the system resolution is substantially larger than the maximum tolerable error required for physical interpretation of the result. The error introduced by finite system resolution turns out to be systematic and is correctable by a simple image analysis technique.

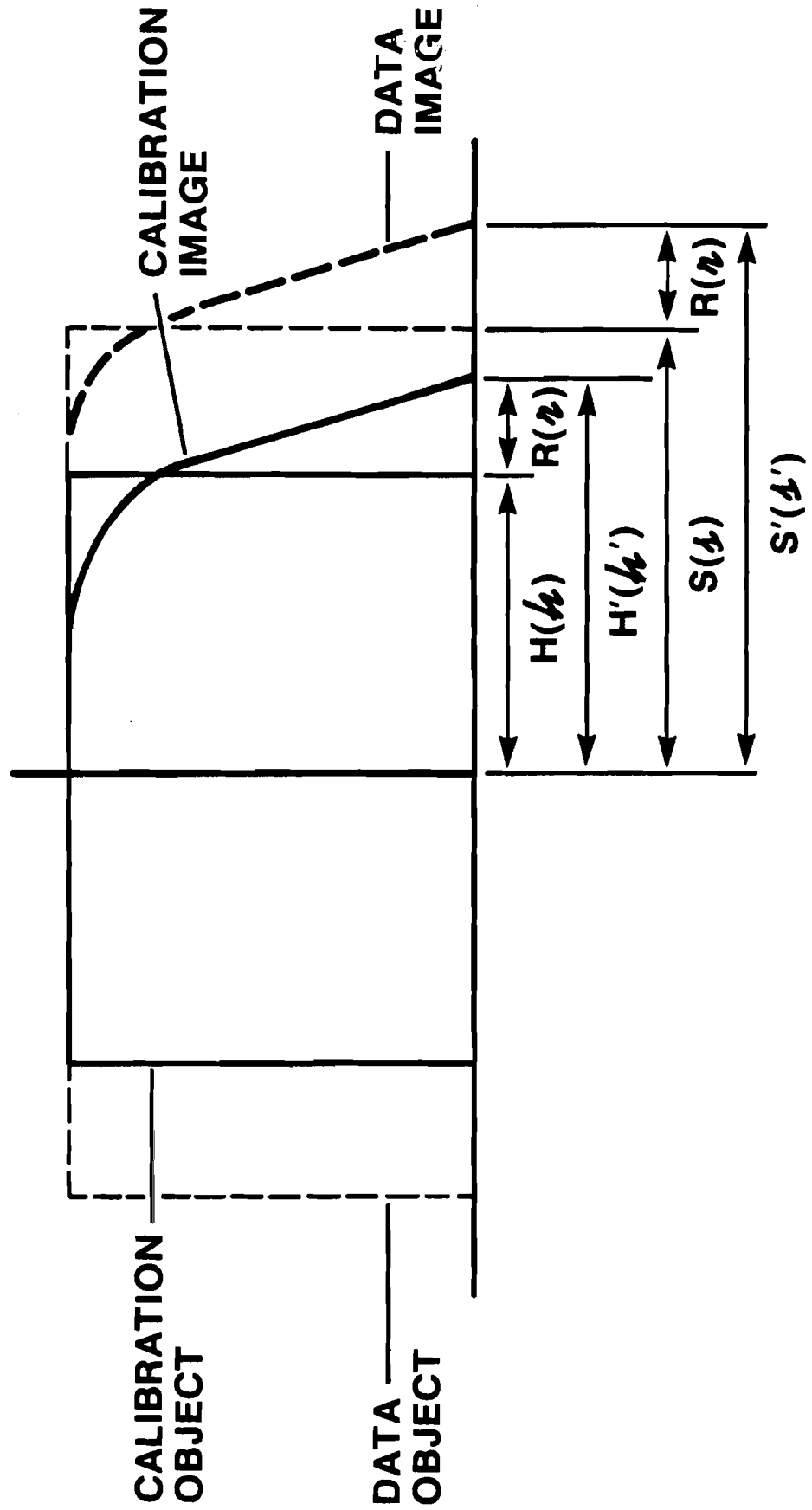
In the experiment, the system magnification is determined by measuring the diameter of a test object and dividing by the known object diameter. The measured magnification contains the finite resolution effects and differs from the theoretical ideal system magnification. Nevertheless, if a subsequent measurement is made with the system of an object the same size as that of the test object, then the image sizes will be the same. Use of the measured magnification accurately gives the object size and the measurement contains no systematic error. For object sizes different from the test object, use of the measured magnification leaves a residual systematic error. This error can be much less than the system resolution. If an estimate of the resolution is available, then most of the residual error can be eliminated.

The situation is depicted in figure A-12. The objects shown are, for convenience, assumed to have flat-top intensity distributions. The images have a more complex intensity distribution due to the finite system resolution. The test object and its image are

FIGURE A-12

IMAGE ANALYSIS GEOMETRY

INTENSITY



shown in solid lines, while the object being measured and its image are shown in dashed lines. Capital letters refer to image dimensions while small letters refer to object dimensions. Unprimed letters refer to actual dimensions while primed letters refer to measured dimensions.

Dimensions, actual and measured, are taken to be from the origin to the point where the signal intensity first equals zero. For an ideal system with perfect resolution $\kappa = 0$ and the magnification of such a system is

$$m = \frac{H}{h} \quad (\text{A-22})$$

For a real system, the resolution is finite and the measured magnification is

$$m = \frac{H'}{h} \quad (\text{A-23})$$

Since $H' = H + R$ and $R = m\kappa$

$$H' = mh \left(1 + \frac{\kappa}{h} \right)$$

Using equation (A-23)

$$\frac{m'}{m} = 1 + \frac{\kappa}{h} \quad (\text{A-24})$$

For $\kappa = 20 \mu\text{m}$ and $h = 60 \mu\text{m}$, $m'/m = 1.33$. The difference between

the actual and theoretical ideal magnifications is large. This large difference does not, however, lead to large errors in the measurement.

If a measurement S' is made and if the measured magnification m' is used, then an object dimension δ' is obtained.

$$\delta' = \frac{S'}{m'}$$

Since $S' = S+R = m(\delta + r)$

$$\delta' = \frac{m}{m'} (\delta + r)$$

Using equation (A-24):

$$\delta' = \frac{(1 + \frac{r}{\delta})}{1 + \frac{r}{h}} \quad (\text{A-25})$$

To compare the measured and actual object dimensions the ratio $\frac{\delta'}{\delta}$ is formed

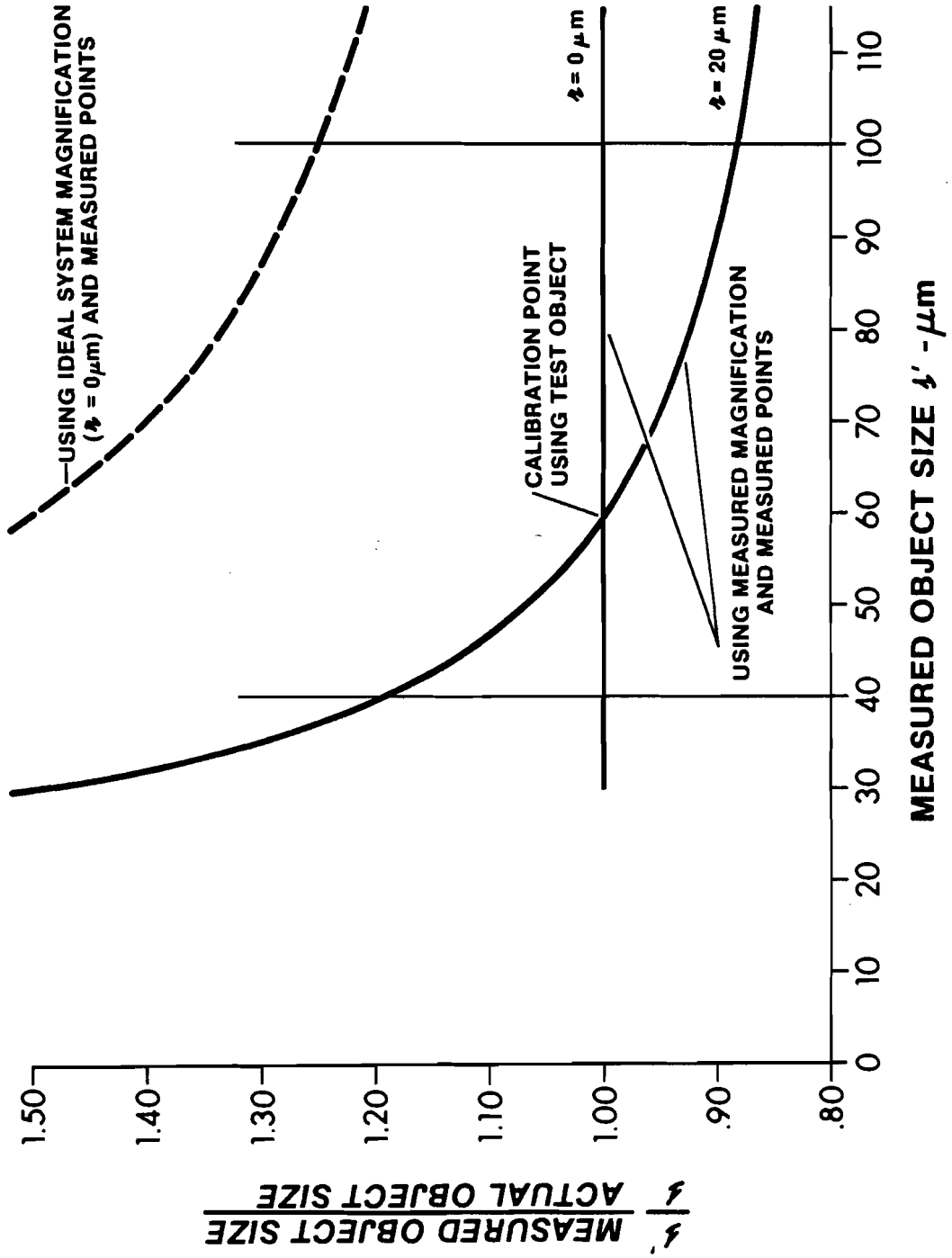
$$\frac{\delta'}{\delta} = \frac{1 + \frac{r}{\delta}}{1 + \frac{r}{h}} = \frac{1}{(1 + \frac{r}{h}) - \frac{r}{\delta'}} \quad (\text{A-26})$$

If equation (A-25) is used to obtain an expression for δ in terms of δ' then a correction formula is obtained for the measured results.

$$\delta = (1 + \frac{r}{h})\delta' - r \quad (\text{A-27})$$

For the measured streaked image resolution of $r \approx 20 \mu\text{m}$ and a test object size of $h = 60 \mu\text{m}$, δ'/δ can be plotted to determine what

FIGURE A-13
EFFECT OF FINITE RESOLUTION ON OBJECT
SIZE MEASUREMENTS



errors exist in the measurements. In figure (A-13) the solid curves show the ratios of measured object size to actual object size ($\frac{s'}{s}$) for resolutions of $\lambda=0$ and 20 μm . For the ideal system the measured size always equals the actual size. For the real system, the measurement is without error only at the calibration point. The maximum error appears for the minimum and maximum object sizes. The plasma dimensions typically range between radii of 40 μm and 100 μm . At these points the errors is +20% (+8 μm) and -12% (-12 μm).

The dashed line in figure (A-13) shows the result of using the ideal system magnification to reduce data with 20 μm resolution. The error is significantly worse than it is using the measured magnification.

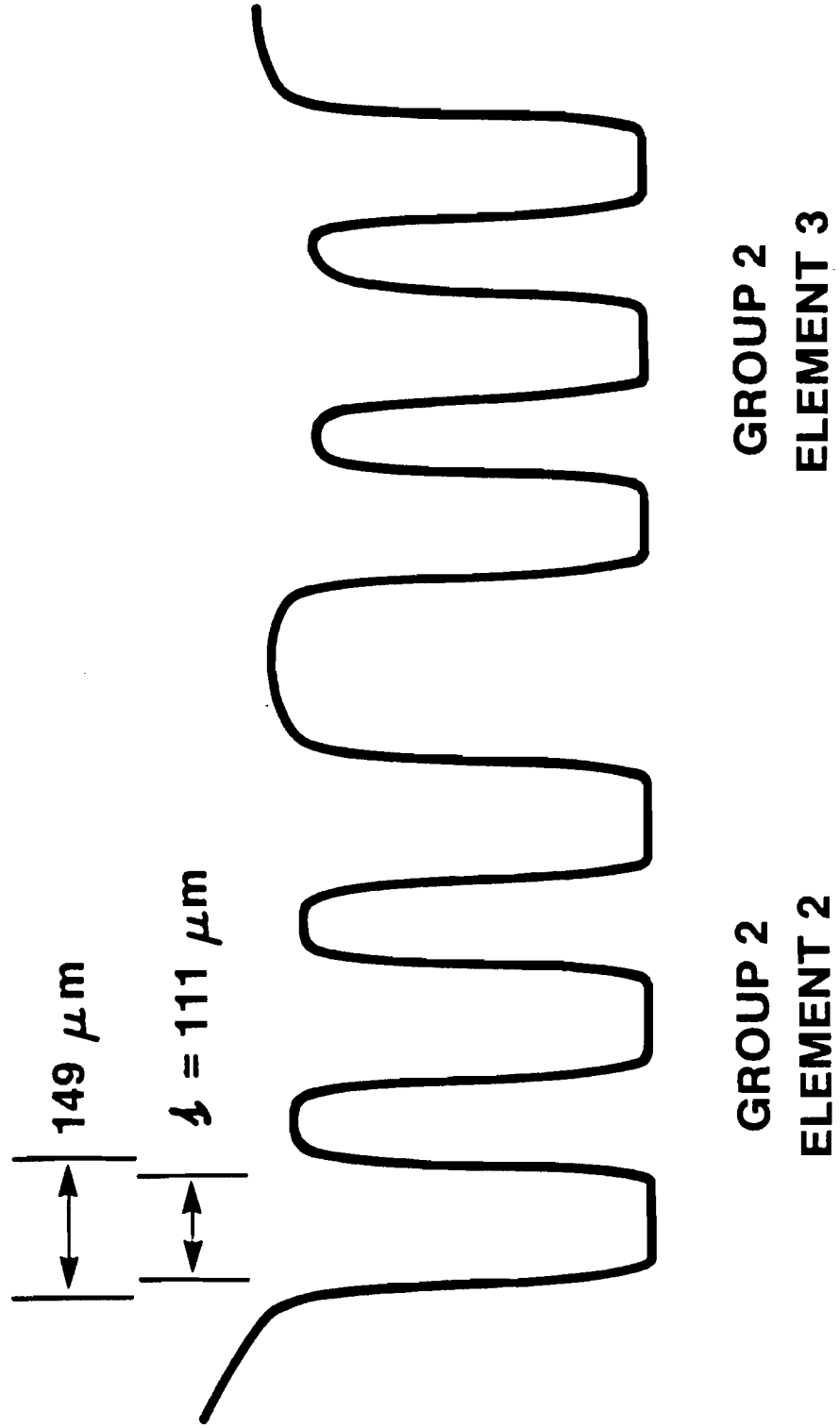
To obtain ± 3 μm resolution the measurements s' must be improved through use of equation (A-27).

To determine how effectively equation (A-27) can be used to improve the measurements' accuracy, an experiment was performed in which a resolution chart was placed in the microdensitometer, the image was defocused, and a scan of the blurred image was made. Several elements were scanned to give a spread in object sizes and one element was chosen to serve as the test object for the magnification calibration.

Figure (A-14) shows a sample scan. Each element consisted of three transparent bars so that six measurements could be made: one width for each of the three individual bars, one width for each group of two bars, and one width for the entire group of three bars. Where several thicknesses were measured the average was taken. The resolu-

FIGURE A-14

OUT OF FOCUS IMAGE
RESOLUTION = 19 μm



tion for the results shown was measured as 19 μm . Object sizes varied from 35 μm to 280 μm ($\frac{1}{2}$ the total width).

The results are presented in the form of correlations between the measured and actual object dimensions. Correlations plotted are $r/\langle s_{\text{MEASURED}} \rangle$ to r/s . For perfect correlation all the points should lie on a 45° straight line. Systematic errors show up as a departure from the line of perfect correlation. Random errors show up as a scatter in the points.

Figure (A-15) shows the error inherent in uncorrected data. Data points obtained using the ideal and actual system magnifications have been plotted along with the predicted curves. Figure (A-16) shows the corrected data. All of the systematic error due to finite resolution has been eliminated. The scatter is due to the $\pm 2 \mu\text{m}$ precision of the measurement technique.

If the resolution of the calibration image differs from that of the measurements, i.e., the focused and streaked mode resolutions differ, then equation (A-27) will not completely correct the systematic error. The measured magnification obtained from a focused mode image should have included all of the streaked image aberrations and if it didn't, then the difference should be included. This difference, through a recalculation of m' , can be taken into account in the correction formula. The result is

$$s = \left(1 + \frac{r_{\text{FOC}}}{h}\right)s' - r_{\text{STR}} \quad (\text{A-28})$$

where r_{FOC} and r_{STR} are the focused and streaked mode resolutions

FIGURE A-15
CORRELATION OF MEASURED EDGE POSITIONS
TO THE ACTUAL EDGE POSITION

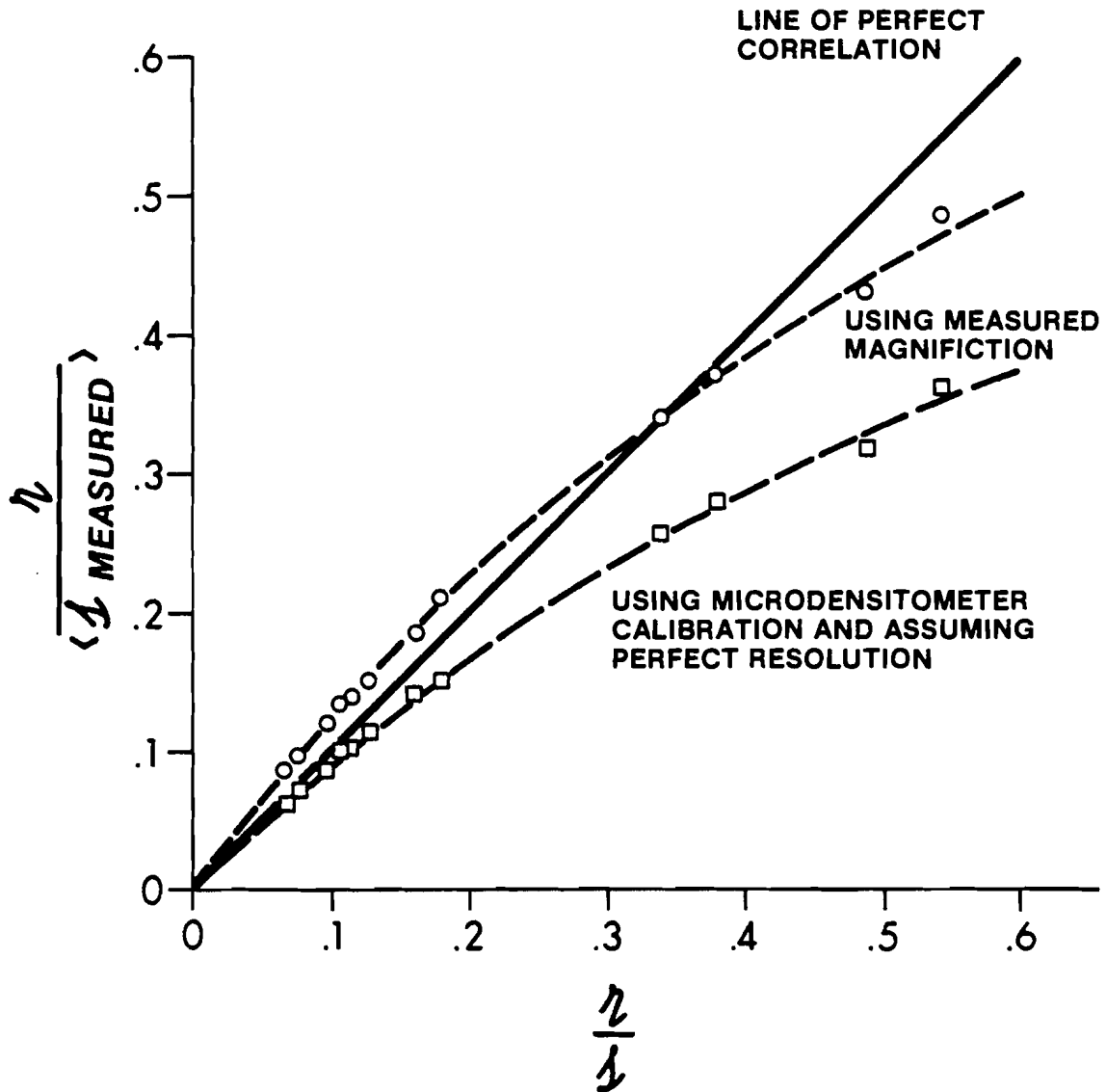
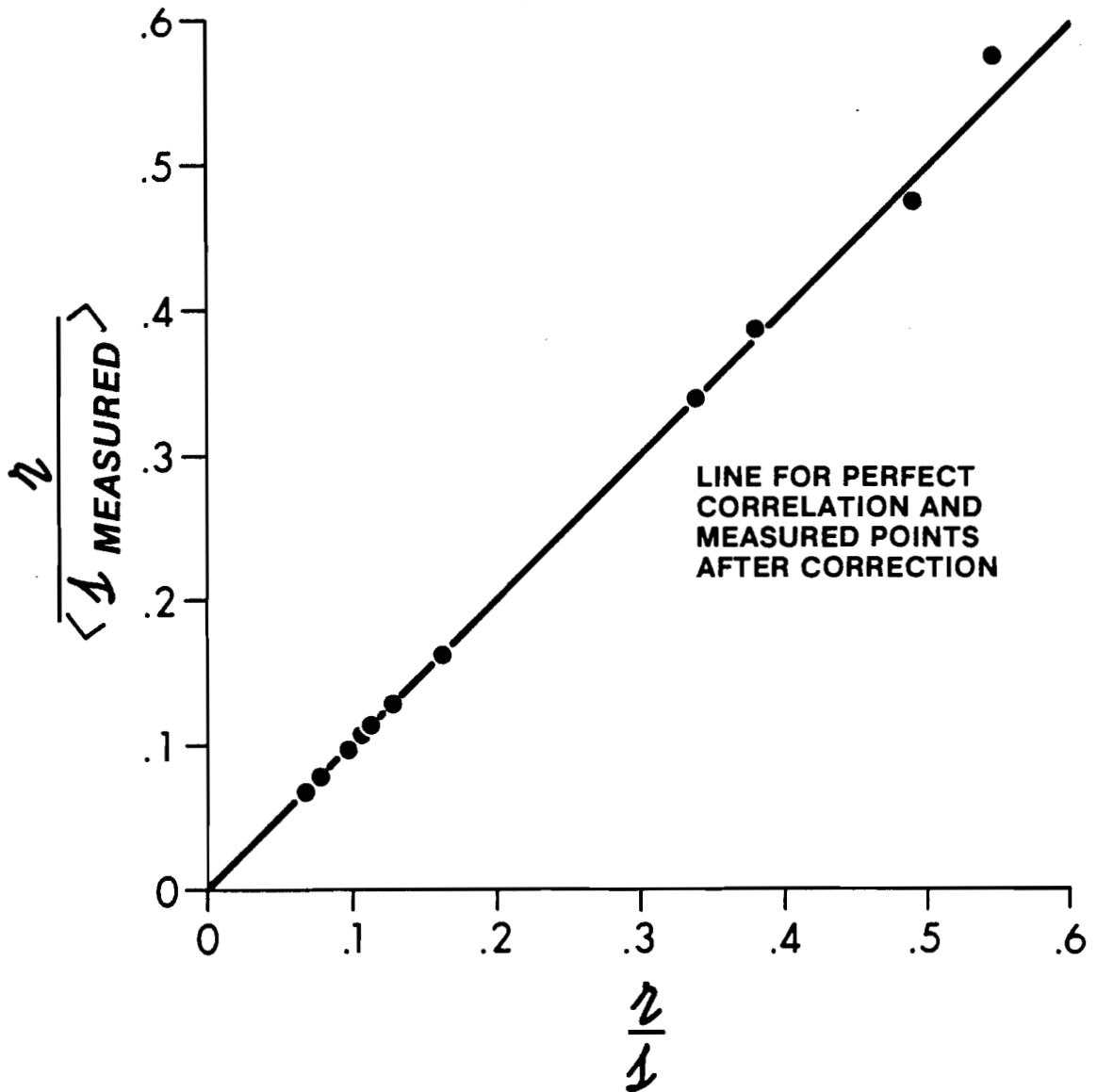


FIGURE A-16

CORRELATION FOR CORRECTED DATA
19 μ m RESOLUTION

and s' is computed using the measured magnification m' obtained from the focused mode test object image.

The image resolution is only known to a certain accuracy. To determine the sensitivity of the results to errors in the resolution estimation $\delta s = \frac{\delta s}{\delta r} \delta r$ is found using equation (A-27) or (A-28).

The result is

$$\delta s = \frac{s'}{h} \delta r_{\text{FOC}} - \delta r_{\text{STR}} \approx \left(\frac{s'}{h} - 1 \right) \delta r \quad (\text{A-29})$$

In section A.5 the streaked data resolution was found to vary by $\pm 4 \mu\text{m}$. At the minimum and maximum values of s' ($40 \mu\text{m}$, $100 \mu\text{m}$) and for a test object radius of $h = 60 \mu\text{m}$. δr equals $-1 \mu\text{m}$ and $+3 \mu\text{m}$. The error due to uncertainties in the streaked data spatial resolutions is approximately $\pm 2 \mu\text{m}$ in the final results.

Appendix B - Density Dependence of the Harmonic Emissions

To see the density dependence of the harmonic emissions, the problem of determining the second order currents that generate the emissions is considered. The current at any point in the plasma is

$$\bar{J} = e (Zn_i \bar{v}_i - en_e \bar{v}_e) \quad (B-1)$$

where n_i and n_e are the ion and electron number densities, \bar{v}_i and \bar{v}_e are the ion and electron velocities, and Z is the ion charge state.

If high frequency electron oscillations are considered then $n_e = Zn_i + n_1$ and $\bar{v}_e = \bar{v}_i + \bar{v}'$. The total current is

$$\bar{J} = -e (Zn_i \bar{v}' + n_1 \bar{v}_i) - e n_1 \bar{v}' \quad (B-2)$$

The last term in equation (B-2) is a second order current. If n_1 and \bar{v}_1 have temporal dependences of $n_1 \sim e^{i\omega_1 t}$ and $\bar{v}' \sim e^{i\omega' t}$ then the temporal dependence of the second order current \bar{J}_2 is $\bar{J}_2 \sim e^{i(\omega_1 + \omega') t}$.

The frequency of the second order current (ω_2) is

$$\omega_2 = \omega_1 + \omega' \quad (B-3)$$

Electrons driven by the laser light electric field oscillate everywhere at a frequency $\omega' = \omega_0$. Only in local regions of the plasma

is n_1 finite. At the critical surface, the resonant fields cause a density fluctuation that oscillates at a frequency $\omega_1 = \omega_0$. The second order current oscillates at a frequency $\omega_2 = 2\omega_0$ and this current generates the $2\omega_0$ light. At the quarter-critical surface, the process of Two-Plasmon Decay generates an $\omega_1 = \omega_0/2$ density fluctuation. The resulting second order current has a frequency $\omega_2 = (3/2)\omega_0$ and is the source of $(3/2)\omega_0$ light.